Hydrogel Machines - Design, Manufacturing, and Applications

by

Xinyue Liu

B.S., Sichuan University, China, 2015

Submitted to the Department of Mechanical Engineering
in partial fulfillment of the requirements for the degree of

Doctor of Philosophy in Mechanical Engineering

at the

MASSACHUSETTS INSTITUTE OF TECHNOLOGY

February 2022

Signature of Author……
Department of Mechanical Engineering
February 01, 2022

Certificated by……...
Xuanhe Zhao
Professor of Mechanical Engineering
Thesis Supervisor

Accepted by...……
Nicolas Hadjiconstantinou
Professor of Mechanical Engineering
Chairman, Department Committee on Graduate Theses

Hydrogel Machines - Design, Manufacturing, and Applications

by

Xinyue Liu

Submitted to the Department of Mechanical Engineering
on January 05, 2022 in Partial Fulfillment of the
Requirements for the Degree of
Doctor of Philosophy in Mechanical Engineering

Abstract

Hydrogels are polymer networks infiltrated with water. Natural hydrogels constitute the major components of the human body such as muscles and cartilages; and synthetic hydrogels have been widely used in applications that closely interact with biological organisms, ranging from tissue engineering, drug delivery, and contact lenses to sensors, actuators, electronics, optics, and other soft machines. As many living tissues undergo dynamic and repeating deformation, natural hydrogels have achieved the extreme mechanical robustness necessary for their survival and well-being through evolution. Mechanical properties of synthetic hydrogels are also required and play crucial roles in maintaining the integration and functionality of hydrogel machines, especially when they interact with the dynamic tissues and organs. In this thesis, I first report the design and manufacturing of tough, fatigue-resistant hydrogel materials and their adhesions with various engineering materials. Based on these hydrogel materials and adhesions, I present three types of hydrogel machines, including hydrogel living devices that incorporate living bacteria in hydrogel matrices, hydrogel ingestible devices that are retained in the gastrointestinal tract, and hydrogel optical fibers that collect the light from and deliver light to nervous systems. The design principles and implementation strategies of each hydrogel machine are described, followed by the theoretical calculation, experimental validation, and proof-of-concept demonstration. In the future, the field of hydrogel machines will enable a paradigm shift in machine design by integrating hydrogels due to physical and physiological matches with biological organisms.

Thesis Supervisor and Committee Chair:
Professor Xuanhe Zhao, Department of Mechanical Engineering

Thesis Committee Members:
Professor Cullen Buie, Department of Mechanical Engineering
Professor Giovanni Traverso, Department of Mechanical Engineering
Professor Timothy K. Lu, Department of Biological Engineering

Acknowledgements

This work would not have been possible without the many people who have supported me along the way. I would first like to thank my thesis advisor Professor Xuanhe Zhao for his invaluable support during my doctoral studies. I thank him for his enthusiasm, guidance, encouragement, understanding, and motivation. I am extremely fortunate to have Professor Zhao as my advisor and could not have imagined having a better mentor for my PhD study.

I express my sincere thanks to my doctoral thesis committee members Professors Cullen Buie, Giovanni Traverso, and Timothy K. Lu for their insightful and supportive feedback on my research. I am very fortunate to have such a wonderful thesis committee who not only helped me improve my thesis work but also gave me insightful advice for my academic career and beyond. I would also like to acknowledge my collaborators, Professors Polina Anikeeva and Robert Langer; it was a great pleasure to work with world-leading experts in biotechnology.

Thank you to my fellow lab mates in the Zhao Lab: Shaoting Lin, Hyunwoo Yuk, German Parada, Yoonho Kim, Xinyu Mao, Heather Bowman, Heejung Roh, Sarah Wu, Mahdi Takaffoli, Jue Deng, Yueying Yang, Jiahua Ni, Jingjing Wu, Xiaoyu Chen, Ji Liu, Baoyang Lu, Guoying Gu, Lingyun Liu, Tao Zhou, Liu Wang, Kai Zhang, Dongchang Zheng, Grace Goon, Yanlei Hu, Jaehun Choe, Hon Fai Chan, Chase Hartquist, Camilo Duque, and Yu Yan. It was wonderful working and getting to know all of them and I hope I have the opportunity to work with them again. I also want to thank Christina Spinelli for wonderfully supporting our lab, Gregory Sands for his nice help in PPSM. I thank Leslie, Saana, and Una from the MechE department for their kindness in the past few years. I want to thank all of my dear friends in Massachusetts, Chengdu, Nanjing, and around the world for not letting me give up when things were tough and for inspiring me every day.

My appreciation also extends to all my collaborators Siyuan Rao and Atharva Sahasrabudhe from Professor Polina Anikeeva's group, Maria Eugenia Inda, Tzu-Chieh Tang, Eleonore Tham, Chang Cheng, Mark Mimee, Dacheng Ma, and Yong Lai from Professor Timothy K. Lu's group, Christoph Steiger, Alison Hayward, Sufeng Zhang, and Shiyi Zhang from Professor Robert Langer and Giovanni Traverso's group, Haipeng Xu from Professor Guoying Gu's group, Jingjing Guo from Professor Andy Yun's group, and Chi Cheng from Professor Rohit Karnik's group. Their expertise in neuroscience, synthetic biology, gastroenterology, and optics sparked my interest in addressing grand challenges in human health, a topic that inspired many chapters of this thesis. My sincere thanks also go to Joy Collins, Siid Tamang, Pierce Hayward, Donna Johnson, Milton Cornwall-Brady, Virginia Spanoudaki, David Bono, and Bogdan Fedeles who provided me immense help and training with my experiments at MIT. I would also like to thank the wonderful undergraduates I have had the pleasure of working with: Minna Z Wyttenbach, Cindy Shi, and Kayla Felix.

Finally, I must express my profound gratitude to my family, including my parents, my grandparents, and my husband, for providing me with support and continuous encouragement

throughout my studies. This accomplishment would not have been possible without them.

Contents

List of Figures

(pH 1.2) over 24 h and in simulated intestinal fluid (pH 6.8) over 10 days. The values correspond to the corroded metal masses from 1 g of the magnetic hydrogel. Dashed lines represent maximum oral doses having no significant toxic effect. (b) Biocompatibility of the magnetic hydrogel in a live/dead assay of Caco-2 cells, using a hydrogel-conditioned medium (conditioning time: 1, 4, 7 days) for cell culture. After culture, the Caco-2 cells are stained with calcein-AM (green) and ethidium homodimer-1 (red) to visualize the viable and dead cells, respectively. (c) Caco-2 cell viability using a hydrogel-conditioned medium with varied conditioning time. (d) Encapsulation and visualization of engineered bacteria (E. coli Nissle 1917) in the magnetic hydrogel for 1–7 days. The encapsulated bacteria are stained with SYTO 9 dye (green) and propidium iodide (red) to visualize the viable and dead bacteria, respectively. (e) Bacterial viability and area occupied by viable bacteria (E. coli Nissle 1917) in hydrogels over time. (f) Bacterial viability (E. coli DH5α) in hydrogels with varied Young's modulus over time. (g) Blood-sensing ability of the magnetic living hydrogels that encapsulated engineered bacteria. Insets: typical images of the luminescent hydrogel (left, blue background) and non-luminescent hydrogel (right, red background; negative control). Dashed red line represents values obtained with the negative control. Data in (a), (c), (e), (f) and (g) are means ± SD, n = 3. Scale bars are 100 μm in (b) and 20 μm in (d). 150

Figure 5-5. In vivo validation of magnet-assisted retention and in vivo heme sensing function of the magnetic living hydrogels. (a) Illustration of an ingested magnetic living hydrogel passing through the whole GI tract of a mouse within ~ 6 h. (b) Illustration of an ingested magnetic living hydrogel retained in the GI tract of a mouse for 7 days by an external magnet attached to the abdomen. (c) CT images of a mouse with an ingested magnetic living hydrogel passing through the whole GI tract of a mouse within ~ 6 h. (d) CT images of a mouse with an ingested magnetic living hydrogel retained in its intestine for 7 days by an extracorporeal magnet attached on the abdomen. Representative histological images stained with haematoxylin and eosin (H&E) for assessment of the small intestine cross-section without (e) and with (f) a magnetic hydrogel after 7-day intestinal retention. (g) Numbers of viable microbes in fecal pellets collected from mice at 12 h post-administration of the hydrogel (containing blood-sensing E. coli Nissle 1917). The fecal samples with and without magnetic hydrogels exhibit significant differences in microbe numbers (*$P < 0.05$; Student's t test; n = 7). Dashed line indicates the limit of detection (LOD) of the assay. (h) CT images of fecal pellets with or without magnetic hydrogels. (i) In vivo blood sensing performance. After the magnetic hydrogel (containing blood-sensing E. coli Nissle 1917) is

iliac crest, hip, knee, ankle, and toe from top to bottom. (d) Pose estimation of mice with an implanted hydrogel fiber-optic device on a running wheel using DeepLabCut. The colored labels represent features of mice including ferrule, neck, back, iliac crest, hip, knee, ankle, and toe. Scale bars: 10 mm. The hydrogel fiber length is calculated from the total length of the segments starting from the ferrule to the middle point between hip and knee. The hydrogel fiber-optic device is stretched and relaxed per running step. (e) Distance between fore toe to hind toe of the mouse on a running wheel varies over time on Day 13. (f) Mechanical strain of the implanted hydrogel fiber-optic device in the mouse on a running wheel varies over time on Day 13. The total time period in (e) and (f) is separated into different gait cycles, and each gait cycle is discomposed to a swing phase (light grey) and a stance phase (white) according to the positive or negative slope in (e). (g) Illustration of the fiber length variation during mouse running. (h) Maximum strain of a hydrogel fiber-optic device in mice on a running wheel over 30,000 cycles of in vivo fiber stretching. Statistical significance is determined by one-way ANOVA and Tukey's multiple comparison test; $*P \leq 0.05$, n.s., not significant..... 197

Figure 7-4. Optogenetic activation enabled by the fatigue-resistant hydrogel fiber optics. (a) Confocal image of transverse section of the mouse sciatic nerve. Scale bar: 100 μm. (b) In vivo study design of implantation and optogenetic stimulation through the hydrogel fiber-optic devices, accompanied by voluntary wheel running of the animal. On Day 0, Day 7, Day 14, Day 21, and Day 28, the subjects have experienced 0, 4,000, 10,000, 20,000, and 30,000 running cycles on a wheel, respectively, and are exposed to optogenetic stimulation. (c) Representative EMG signals recorded by needle electrodes on Day 0. Green bars indicate the optical stimulation periods. (d) Overlay plot of EMG spikes on Day 0, aligned to the time of optogenetic stimulation. The green bar indicates the optical stimulation period. (e) Images of the ankle joint movement in response to optical stimulation through the hydrogel fiber-optic devices. Scale bars: 5 mm. (f) Root mean square voltage of the EMG signals in response to optical stimulation via the hydrogel fiber-optic devices over 30,000 cycles of in vivo fiber stretching. Statistical significance is determined by two-way ANOVA and Tukey's multiple comparison test; $*P \leq 0.05$. Values represent the mean and the standard deviation (n = 3 independent measurements from different animals). ..... **Error! Bookmark not defined.**

Chapter 1

Introduction

Parts of the review presented in this chapter have been published in:

- **Xinyue Liu**, Ji Liu, Shaoting Lin, and Xuanhe Zhao. Hydrogel machines. Materials Today. 36, 2020.
- Xuanhe Zhao, Xiaoyu Chen†, Hyunwoo Yuk†, Shaoting Lin†, **Xinyue Liu**, German Parada. Soft materials by design: Unconventional polymer networks give extreme properties. Chemical Reviews. 121, 2021.

1.1. Hydrogel machines

As hydrophilic polymer networks infiltrated with water, hydrogels behave like both solids and fluids [1, 2]. Owing to their crosslinked polymer networks, hydrogels exhibit the properties of elastic solids with deformability and softness[3]. On the other hand, the high water content in hydrogels leads to liquid-like attributes of hydrogels, including permeability to a wide range of chemical and biological molecules[4], and transparency to optical and acoustic waves[5, 6]. Beyond these, hydrogels also feature other unique properties, such as swelling and responsiveness [7-9], due to the combination of solid (i.e., polymer networks) and liquid (i.e., water). Most building blocks of the human body are biological hydrogels (**Figure 1-1**), which are soft, deformable, and contain 60 – 90 wt% water[2, 10-12]. In some sense, the human body is a living machine mainly comprised of hydrogels and skeletons[13]. The nervous system transmits electrical signals and acts as a controller; the digestive and circulatory system transports nutrients, water, and wastes; and the musculoskeletal system functions as motors and actuators. The fact that the human body's functions mainly rely on hydrogels raises an intriguing question in science and technology. While conventional machines are mostly made of rigid elements (e.g., metals, silicon,

plastics, and ceramics, **Figure 1-1**), can hydrogels constitute a new class of machines that harness hydrogels' unique properties?

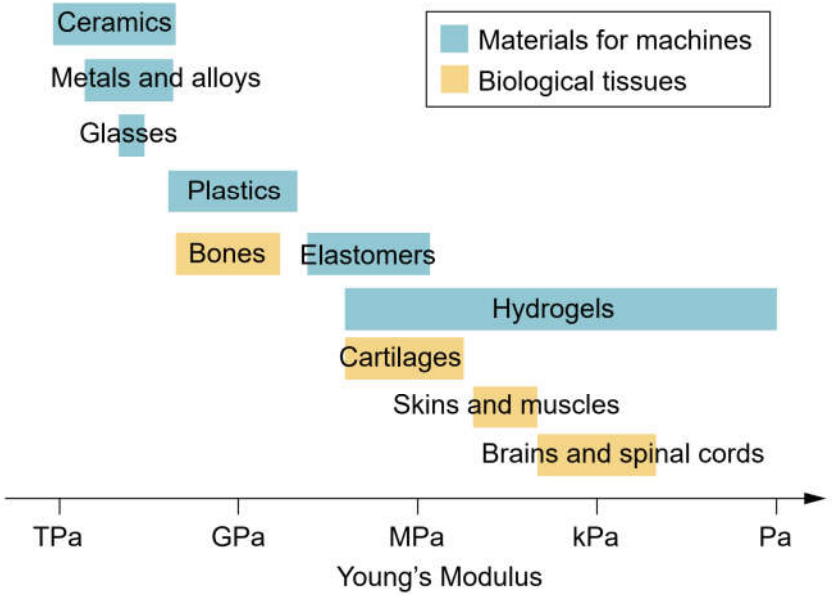

Figure 1-1. Young's moduli of biological tissues and common materials for machines.

Hydrogels have been widely used in the fields of tissue engineering cell culture[14-20], and drug delivery[4, 21-26], in which the hydrogels intimately interact with biological organisms (**Figure 1-2**). Moreover, the unique properties of hydrogels, such as superior softness, wetness, responsiveness, biocompatibility, and bioactivity [10], indeed suggest the possibility of their crucial functions in devices and machines, such as sensors, actuators, coatings, optics, electronics, and water harvesters[27]. In order to ensure the stable operation of hydrogel machines, it usually requires that the hydrogels are robust in terms of mechanical performance and functionality. Recent innovations in the design of tough hydrogels[28, 29], tough adhesion of hydrogels to other engineering materials[30, 31], and advanced fabrication methods for hydrogels[32-35] have made hydrogels a promising material candidate for next-generation machines. A nascent field named hydrogel machines rapidly evolves, exploiting hydrogels as key components for devices and machines to potentially replace or complement many conventional machines based on rigid materials.

Whereas individual hydrogel machines such as hydrogel sensors and actuators have been reviewed[27, 36, 37], we overview various categories of hydrogel machines that systematically correlate hydrogels' properties to machines' functions is still absent in the field. This introduction

is aimed to provide such a panoramic discussion of existing hydrogel machines and a set of rational guidelines for the design of future hydrogel machines based on fundamental thermodynamics, kinetics, chemistries, and mechanics of hydrogels. We classify various hydrogel machines developed so far into a number of categories according to their major applications, including sensors, actuators, coatings, optics, electronics, and water harvesters (**Figure 1-2**). For each category, we discuss the working principles of hydrogel machines, the unique properties of hydrogels that enable specific functions of the machines, and the challenges faced by hydrogel machines and potential solutions.

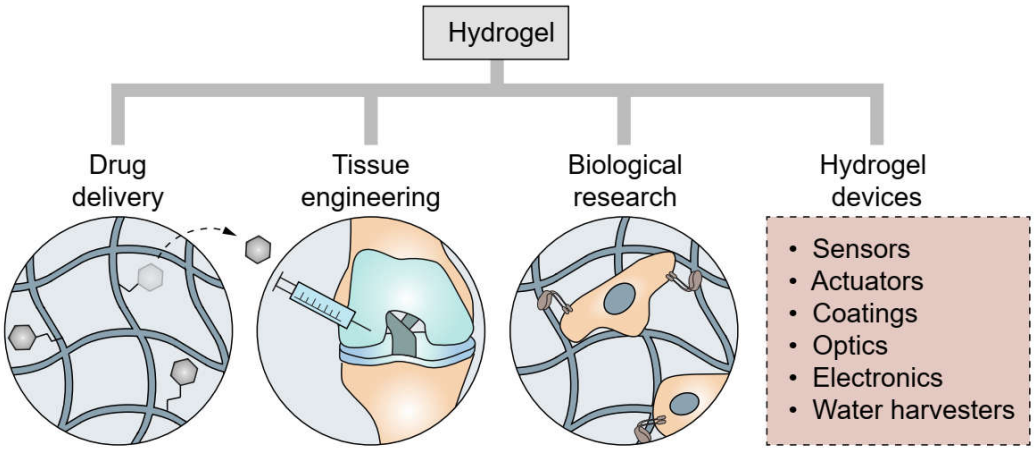

Figure 1-2. Hydrogels have been widely used in the fields such as drug delivery[21, 22], tissue engineering[38], and biological research[14]; and they are being intensively investigated for crucial functions in devices and machines such as sensors, actuators, coatings, optics, electronics, and water harvesters[33].

1.1.1. Hydrogel sensors

By definition, a sensor is a machine or part of a machine that detects and responds to signals in the environments[36]. The human body harbors numerous sensors that can receive environmental signals for perception, such as the eyes for vision, the ears for hearing, the tongue for taste, the nose for smell, and the skin for touch[39]. Conventional sensors, such as electronic sensors and electrochemical sensors, are able to convert environmental inputs to electrical outputs based on semiconductors and/or metallic electrodes. In contrast to conventional sensors made of rigid materials and electrical circuits, hydrogel sensors rely on hydrogels' unique attributes, such as high compliance, high water content, stimuli-responsiveness, and high permeability to a wide range of molecules.

Hydrogel sensors can be classified into two types according to hydrogels' functions in the sensors: (a) stimuli-responsive hydrogels as sensors that can exhibit volume and/or phase changes according to environmental inputs[40-49]; and (b) passive hydrogels as matrices to host responsive substances (e.g., free ions, nanoparticles, biomolecules, and living cells) that respond to environmental inputs[50-52]. The environmental inputs detected by hydrogel sensors include both chemical (e.g., pH, ions, and antibodies)[41, 42] and physical (e.g., temperature, light, mechanical stress, and electric field)[44, 47, 51, 53] stimuli. The sensing process of hydrogel sensors usually takes place by first receiving the chemical or physical inputs through chemical diffusion or physical fields, respectively; and then the hydrogel sensors transduce the input signals into measurable outputs[36, 54]. The output signals are displayed in the form of geometric, mechanical[41], optical[48], electrical[51], and biological responses of the hydrogel sensors[55]. Hydrogel sensors are becoming practical tools for diverse applications including point-of-care detection, medical diagnostics, and environmental monitoring[56-58].

Stimuli–responsive hydrogels as sensors. The polymer chains and/or polymer networks of stimuli-sensitive hydrogels can be regulated by chemical (e.g., ions, biomolecules)[41, 42, 59-62] and physical (e.g., temperature, light, mechanical forces, electric fields)[44, 45, 47, 63] stimuli, leading to conformational transformation of polymer chains (e.g., random coil, extended chain, or collapsed globule) and/or changes in the polymer networks (e.g., high or low crosslink density)[36] (**Figure 1-3a**). The molecular level changes of polymer chains and networks result in the micro-/macro-scopic volume change and/or phase transition of the hydrogels, which can be quantified by instruments such as piezoresistors and transmitted light detectors[54]. Two classical examples of stimuli-responsive hydrogel sensors involve poly(N-isopropylacrylamide) (PNIPAM) hydrogels which have been widely used as temperature sensors[64, 65], and polyelectrolyte hydrogels which have been adopted to detect variations in pH, ion concentration and electrical potential[40, 41, 44, 53]. In both examples, the polymer chains in the hydrogels experience collapse or extension in response to input signals. As another example, a hydrogel crosslinked by antigens and corresponding antibodies is sensitive to free antigens in the solution, which can bind with antibodies in the network to vary the crosslinking density of the hydrogel and trigger a dramatic change in the hydrogel's volume[42].

Passive hydrogel matrices for sensors. As another strategy for hydrogel sensors, hydrogels can be adopted as inert matrices to accommodate active or responsive elements, such as free ions[51, 52], nanomaterials (i.e., metal and carbon nanomaterials)[66], biomolecules (i.e., enzymes[67-69], antigens/antibodies[70, 71], nucleotides[62, 72], and fluorescence/luminescence probes[50, 73]), and living cells (i.e., bacteria and mammalian cells)[33, 55, 74]. These active elements are either physically entrapped in or chemically anchored to the hydrogel matrices, and the hydrogel matrices are permeable to chemical inputs (e.g., ions, proteins, carbohydrates, and nucleic acids)[4], thus allowing the interactions between these input signals and the active elements (**Figure 1-3b**). Synthetic hydrogels made of polyethylene glycol (PEG)[75], polyacrylamide (PAAm)[51], or polyvinyl alcohol (PVA)[76, 77] are commonly utilized as the passive matrices for active elements. Furthermore, conducting polymer hydrogels are used as matrices to enable rapid electron transfer towards electrodes after the redox reactions between enzymes in hydrogels (e.g., glucose oxidase, lactate oxidase, and uricase) and various biomolecules (e.g., glucose, lactate, and uric acid)[69, 78-80]. In contrast to the stimuli-responsive hydrogels, the volume and phase of passive hydrogel matrices usually remain constant during sensing processes. These passive hydrogel matrices can be designed and optimized to achieve desirable properties and structures, such as porosity, biocompatibility, conductivity, and mechanical performance[12, 81, 82]. For example, Liu et al. reported the encapsulation of genetically engineered bacteria within a tough, stretchable hydrogel-elastomer hybrid[55]. In this living hydrogel sensor, the encapsulated bacteria with programmed genetic circuits are able to express green fluorescent proteins in response to different chemicals. The passive hydrogel matrix for the living sensor allows diffusion of water, nutrients, and chemical inputs to the bacteria, and prevents the bacteria leakage toward the environment[55]. As another example, a work by Kim et al. demonstrated that a highly transparent and stretchable touch panel can be designed with free moving ions in a PAAm hydrogel. The finger position on the touch panel can be interpreted by the current flow in the ionically conductive hydrogels[51].

High-performance sensors commonly exhibit short response time, high sensitivity (i.e., high ratio between output and input signals), low detection limit (i.e., low lower bound of detectable input signals), and high reversibility (i.e., no memory effect caused by previous measurements). Since many hydrogel sensors rely on diffusion of input signals and water in hydrogels, a hurdle for these hydrogel sensors is the long response time, limited by the chemical diffusion across the typical dimensions of hydrogel sensors[83]. To address this challenge,

enhancing the chemical's diffusion coefficient in the hydrogel D or decreasing the typical dimension of a hydrogel L can dramatically reduce the diffusion time τ, according to the scaling of diffusion kinetics $\tau \sim L^2 / D$ [3]. For a homogeneous, nonporous hydrogel, the mesh size of the hydrogel's polymer network can affect a chemical's diffusion coefficient in the hydrogel, as the mesh size can control steric interactions between the chemical and the polymer network. By reducing polymer and crosslinker concentration in the hydrogel, one can increase the mesh size. The diffusion coefficients of macromolecules in hydrogels can be tuned from 10^{-11} to 10^{-9} m^2 s^{-1} by varying the mesh sizes of the polymer networks[4, 84]. On the other side, small-molecule chemicals are usually much smaller than the mesh sizes, so that their diffusion coefficients are almost independent of the mesh sizes, and can be estimated via the Stokes-Einstein equation[4]. Besides the diffusion coefficient, the typical dimension of a hydrogel is another key parameter that controls the response time. For example, a hydrogel antigen sensor with a diameter of 3 mm required more than 1 h to sense biomolecules[42], while hydrogel ion sensors in the form of photonic crystal with a feature size of 500 nm exhibited the color shift in Bragg diffraction within 10 s in response to varied ion concentration[46, 85]. To enhance the sensitivity of hydrogel sensors, one strategy is to establish selective and specific interactions (e.g., enzyme-substrate or antigen-antibody interaction) between input signals and stimuli-responsive hydrogels or active elements in passive hydrogels, instead of unspecific interactions. In addition, an abrupt volume change in response to a small change in input signal (e.g., a first-order phase transition such as PNIPAM hydrogels at the lower critical solution temperature) can be introduced to give extreme sensitivity at the critical point[86-88]. For more detailed discussions, please refer to a few reviews on hydrogel sensors[36, 54], and specifically on the stimuli-responsive hydrogels[7, 89-91] or passive hydrogels that carry nanomaterials[92] and free ions[93].

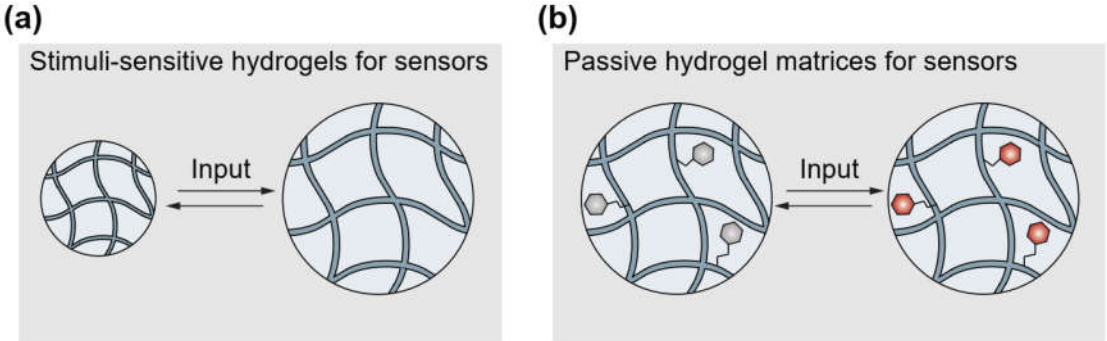

Figure 1-3. Hydrogel sensors based on (a) stimuli-responsive hydrogels as sensors that can exhibit the volume and/or phase change according to the environmental inputs[47, 48], and (b) passive

hydrogel matrices for accommodating responsive elements (e.g., free ions, nanoparticles, biomolecules, and living cells)[51, 55].

1.1.2. Hydrogel actuators

An actuator is a machine or a component of a machine that converts other forms of energy into mechanical energy to generate forces and motions. Complex movements of the human body are enabled by the musculoskeletal system as living actuators, in which the skeletal muscles induce forces and motions with short response time (0.1 s) and a large deformation (~ 40% in strain)[94]. Conventional actuators adapted for mechanical systems usually comprise rigid materials (e.g., metals and ceramics), and their actuation usually relies on relatively small deformations of the rigid materials such as shape memory alloys and piezoelectric ceramics[13, 95]. In contrast, actuators made of hydrogels provide mechanical motions commonly driven by relatively large deformations of the hydrogels[96, 97]. In the light of different mechanisms for actuation, hydrogel actuators can be divided into three types: (a) stimuli-responsive hydrogels driven by osmotic pressure change[32, 47, 97-105]; (b) hydrogels matrices incorporating active elements (such as magnetic particles or free ions) in response to varying external fields (such as magnetic or electric fields)[96, 106-109]; and (c) hydrogel structures with chambers actuated by hydraulic or pneumatic pressures[5].

Osmotic pressure driven actuators. Osmotic pressure driven hydrogel actuators rely on similar swelling/de-swelling mechanisms as the stimuli-responsive hydrogel sensors discussed above. A wide range of external stimuli, including water[32, 110], pH[41, 98], biomolecules[42, 43, 100, 111], temperatures[47, 65, 101, 112-115], light[102, 116, 117], and electric field[44, 98, 103], can induce the osmotic pressure change of solvents in hydrogels and/or environments, leading to water diffusion in/out of the hydrogels and their corresponding expansion/contraction (**Figure 1-4a**).

Assuming only two species of ions, of valences +1 and -1, are mobile in the hydrogel and in the external solution, the osmotic pressure Π in the hydrogel can be expressed as[118]

$$\Pi = \frac{kT}{v^s}\left[\frac{C^+ + C^-}{C^s} - 2v^s c_0 - \log\frac{v^s C^s}{1+v^s C^s} - \frac{1}{1+v^s C^s} - \frac{\chi}{\left(1+v^s C^s\right)^2}\right] \tag{1-1}$$

where v^s is the volume of a water molecule, C^s, C^+ and C^- are the numbers of water molecules, free cations, and free anions per unit volume of the dry polymer of the hydrogel, c_0 is the number

of either specie of ions per unit volume of the external solution, and χ is the interaction parameter between polymer and water. Assuming the fixed charges on the polymer of the hydrogel have valence -1, we further have $C_0 + C^- = C^+$ for charge neutrality inside the hydrogel, where C_0 is the numbers of fixed charges per unit volume of the dry polymer of the hydrogel.

Therefore, osmotic pressure depends on the concentrations of water and various charges, and the interaction parameter between polymer and water. The osmotic pressure of hydrogel can be measured through two methods. A direct method to measure the osmotic pressure involves a semipermeable membrane but is limited by the membrane strength, so that hydrogels of low polymer concentrations or low osmotic pressure can be measured[119, 120]. In addition, the osmotic pressure can be indirectly calculated through a few equations of state of hydrogels (e.g., volume conservation and free energy conservation) by subjecting hydrogels to different deformations[121, 122].

Tanaka et al. carried out a series of pioneer studies on both thermodynamics and kinetics for volume changes of hydrogels (e.g., PNIPAM, PAAm, and PAA) driven by osmotic pressure [83, 86-88]. To further achieve the targeted deformation, such as elongation, bending, folding, twisting, and locomotion, researchers adopted various asymmetric shapes as well as heterogeneous structures for hydrogel actuators through layering, patterning, and alignments[32, 49, 101, 112, 123]. For instance, Beebe et al. used patterned hydrogel structures as flow control valves in microfluidic channels[99]. Gladman et al. created shape-morphing hydrogel actuators by 3D printing and nanofibril alignment, which can transform into prescribed complex 3D structures upon immersion in water[32]. As another example, Liu et al. developed an ingestible hydrogel device composed of a PVA hydrogel membrane[124] and encapsulated small superabsorbent particles to achieve high swelling ratio, high swelling speed, and long-term robustness. The device can be ingested as a standard-sized pill, swell rapidly into a large soft sphere, and maintain robustness under repeated mechanical loads in the stomach for up to one month[97].

The actuation force and response time are commonly coupled for the osmotic pressure driven hydrogel actuators, where a higher actuation force requires a larger dimension of the hydrogel, leading to longer response time[5]. Therefore, the stimuli-responsive hydrogel actuators are generally hindered by low actuation speed (response time 10 min – 10 h) and/or low actuation force (1 – 10 mN)[101, 103, 117].

Magnetic or electrical field driven actuators. One approach to decouple the actuation forces and times of osmotic pressure driven hydrogel actuators is to embed ingredients that have shorter response time to external inputs in hydrogels, such as magnetic particles in hydrogels in response to magnetic fields[106-108], free ions in ionic conductors in response to electric fields (**Figure 1-4b, c**)[96, 109]. The response time of magnetic or electric field driven hydrogel actuators can be as low as 10^{-3} s. In many cases, the short response time may only depend on the mechanical inertia of the hydrogels, instead of their magnetic or electrical properties[96, 125, 126].

Magnetic hydrogels are hydrogels containing magnetic particles (e.g., magnetite, carbonyl iron, and neodymium-iron-boron) and exhibit unique magnetoelastic properties. Subject to a non-uniform magnetic field, a magnetic hydrogel experiences a body force proportional to the gradient of the applied field, resulting in deformation or motion (**Figure 1-4b**)[106, 127]. Zhao et al. showed that the deformation of porous magnetic hydrogels induced by applied magnetic fields could be utilized for controlled drug release. The magnetic hydrogel actuators are able to not only complete fast shape transformation (response time 0.1 s) under a constant magnetic field, but also achieve continuous movement according to a rotating magnetic field with the frequency of 2 Hz[106-108]. Ionic conductors composed of free ions in hydrogel matrices (e.g., PAAm) can also exhibit a large deformation actuated by an electric field, when they are assembled with dielectric elastomers[96, 109, 128]. As illustrated in **Figure 1-4c**, a membrane of a dielectric elastomer is sandwiched between two membranes of hydrogel ionic conductors. When a voltage is applied between the hydrogel ionic conductors, ions of different charge polarities collect on the two surfaces of the dielectric elastomer. The oppositely charged ions attract each other and cause the sandwich to reduce its thickness and increase its area[96].

One challenge for the magnetic and electric field driven actuators is the ability to achieve complex deformation under uniform magnetic and electric fields. To address this, Kim et al. attempted to program ferromagnetic domains in soft materials by 3D printing an elastomeric ink containing ferromagnetic particles, resulting in multiple complex modes of transformation and functions such as jumping, crawling, and rolling[126]. As another example, by assembling an ionically conductive hydrogel film, pre-stretched dielectric elastomers and silicone bodies, Li et al. constructed an untethered soft electronic fish with the ability of fast forward motion underwater, in which the hydrogel and surrounding water served as ionically conductive electrodes.

Hydraulic/pneumatic pressure driven actuators. Another approach to address the force-speed coupling challenge of osmotic pressure driven hydrogel actuators is to introduce chambers and channels inside hydrogels that can inflate like balloons for actuation (**Figure 1-4d**). Consisting of a bladder (e.g., silicone elastomer) covered in a shell of braided, strong, inextensible fibers (e.g., nylon or metal), the McKibben-type actuators developed by McKibben in the late 1950s is simultaneously strong and fast, similar to muscles[129, 130], but their actuation mode is limited to contraction/extension. The elastomer based pneumatic actuators developed by Whitesides group can give multiple modes of actuation such as contraction, elongation, bending, or rotation by varying the geometry and stiffness of elastomer components[131, 132]. Yuk et al. reported the first hydraulic hydrogel actuators, which are made of tough hydrogels with embedded hydraulic chambers and channels. The hydraulic hydrogel actuators showed a much higher actuation force (> 1 N) and speed (response time < 1 s) than osmotic pressure driven hydrogel actuators[5]. The hydraulic or pneumatic actuation requires mechanical robustness of the assembled hydrogel structures to prevent leakage or failure in the bodies and interfaces[31, 133].

Overall, compared to their rigid counterparts, hydrogel actuators have attracted growing interests due to their high flexibility, water contents, and biocompatibility, and resulted in multiple applications, including artificial muscles[102, 128], soft robot[5, 44], biomedical devices[47, 97, 106, 110], and microfluidics[40, 99]. However, the mechanical properties of hydrogels pose significant challenges to the accuracy, reproducibility, and durability of hydrogel actuation. Specifically, unlike the linear elastic materials (e.g., metals and ceramics), the stiffness of hydrogels can vary substantially with increased strain due to the nonlinear elasticity of hydrogels[134], which greatly increases the complexity in modeling and controlling hydrogel actuators. In addition, the design and operation of hydrogel actuators can be further challenged by the viscoelasticity and poroelasticity[134, 135], Mullins effect[136], and instability[137] of hydrogels. A better understanding of the fundamental mechanical properties of responsive hydrogels could advance the development of hydrogel actuators with high strain resolution, reproducibility, and robustness, especially for long-term cyclic operations. Please refer to specific reviews for more detailed discussions on hydrogel actuators driven by osmotic pressure[27, 49, 138, 139], magnetic field[140, 141], and electric field[93].

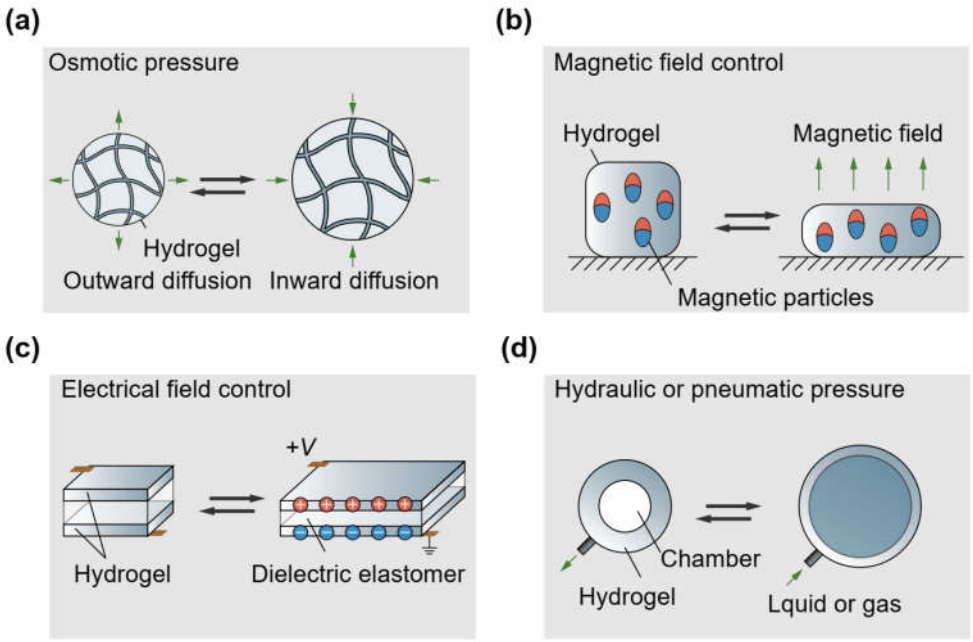

Figure 1-4. Hydrogel actuators based on (a) stimuli-responsive hydrogels driven by osmotic pressure change, (b) hydrogels matrices incorporating magnetic particles controlled by varying magnetic field, (c) hydrogels matrices incorporating free ions controlled by varying electric field, and (d) hydrogel structures with chambers actuated by hydraulic or pneumatic pressures.

1.1.3. Hydrogel coatings

In physically attached hydrogel coatings, only non-covalent interactions, such as electrostatic interactions, van der Waals interactions, hydrogen bonds, and hydrophobic interactions, exist at the interface between the hydrogel coatings and engineering materials (**Figure 1-5a**). The energies of these interactions are orders of magnitude lower than that of covalent bonds, leading to relatively low interfacial toughness (i.e., lower than 10 J m^{-2})[30, 142] and thus weak adhesion that is easy to detach. The simple attachment and detachment of physically attached hydrogel coatings have enabled several commercial products, such as ultrasound hydrogel pads (e.g., HydroAid) and hydrogel coatings on ECG electrodes (e.g., TenderTrode Plus). These hydrogel coatings can reduce skin irritation and/or increase signal-to-noise ratios, owing to their water contents, compliance, and conformal adhesion on skins[143]. On the other hand, due to the weak adhesion, most of the hydrogel coatings based on non-covalent interactions are limited to short-term applications (e.g., seconds to hours)[144, 145].

Physically attached coatings. In physically attached hydrogel coatings, only non-covalent interactions, such as electrostatic interactions, van der Waals interactions, hydrogen bonds, and

hydrophobic interactions, exist at the interface between the hydrogel coatings and engineering materials (**Figure 1-5a**). The energies of these interactions are orders of magnitude lower than that of covalent bonds, leading to relatively low interfacial toughness (i.e., lower than 10 J m^{-2})[30, 142] and thus weak adhesion that is easy to detach. The simple attachment and detachment of physically attached hydrogel coatings have enabled several commercial products, such as ultrasound hydrogel pads (e.g., HydroAid) and hydrogel coatings on ECG electrodes (e.g., TenderTrode Plus). These hydrogel coatings can reduce skin irritation and/or increase signal-to-noise ratios, owing to their water contents, compliance, and conformal adhesion on skins[143]. On the other hand, due to the weak adhesion, most of the hydrogel coatings based on non-covalent interactions are limited to short-term applications (e.g., seconds to hours)[144, 145].

Covalently anchored coatings. Bonding of hydrogels to diverse engineering materials via covalent anchorage can be achieved through different ways of surface functionalization and covalent bonding chemistry (**Figure 1-5b**). Compared to the physical attachment, the covalent anchorage is stronger and more stable under physiological conditions, allowing hydrogel coatings for relatively long-term applications, such as hydrogel coatings on neural implants[146, 147]. The robust hydrogel coatings on rigid biomedical devices can provide not only mechanical compliance that matches the tissue modulus and surface lubrication with minimal friction and wear, but also biofunctionalities such as antifouling, minimal immune response, selective permeability, and drug delivery[143, 148]. Besides the research advances, covalently anchored hydrogel coatings have been commercialized with products, such as hydrogel coated latex Foley catheter (e.g., Dover) and surgical gloves (e.g., Protexis).

Although covalent anchorage gives more chemically and mechanically stable hydrogel coatings than physically attached ones, the interfacial toughness between the hydrogel layer and the substrate can still be low. As depicted by the Lake-Thomas theory[149], the interfacial adhesion energy is equal to the energy required to fracture a layer of polymer chains, which is in the range of 1-100 J m^{-2}. Such weak and brittle interfaces still induce fracture and/or debonding of hydrogel coatings under high mechanical loads. Yuk et al. first reported a strategy for tough bonding of hydrogels on diverse nonporous solid materials, including metals, ceramics, glasses, and elastomers, by covalently anchoring tough dissipative hydrogels onto the substrates[30]. The energy required for fracturing anchored polymer chains and the energy dissipated in deforming the

bulk tough hydrogel synergistically give an interfacial toughness over 1,000 J m^{-2}. More recently, Yuk et al. further reported a dry-crosslinking strategy for fast (within 5 s), tough, and long-term stable adhesion of hydrogels on solid materials and tissues[150].

Interfacial interpenetrated coatings. Both mechanisms of physical attachment and covalent anchorage for hydrogel coatings described above rely on the introduction of functional groups in hydrogels and/or substrates for adhesion. When the substrate surface is permeable to the polymer chains of hydrogels or bonding agents, interpenetration can form between two polymer networks at the hydrogel-solid interface, resulting in entanglement at the molecular level (**Figure 1-5c**). Yuk et al. proposed that benzophenone treatment of polymers and elastomers can activate their surfaces and make them permeable to hydrophilic polymers and monomers to allow the interpenetration of hydrogel polymer networks into the polymeric and elastomeric substrates[31, 151]. As another example, Yang et al. reported that adhesion between two hydrogels can be achieved through the interpenetration of stitching polymers (such as chitosan) into both hydrogels[152].

Mechanical interlocked coatings. A rough and porous surface of a machine can enable the mechanical interlocking of hydrogel coatings, which not only increases the interfacial area, but also creates numerous locked snap-fits at the microscale (**Figure 1-5d**). Based on this mechanism, Kurokawa et al. for the first time anchored double network hydrogels to hard, dry, porous substrates, including glass, polyethylene, and sponge[153]. A continuous hydrogel was formed both on top of and in the voids of the porous solid substrates[153]. Inspired from the geometry of Clingfish adhesive disc, Rao et al. fabricated hydrogels with microscale facets and grooves, in which the grooves acted as water drainage channels to facilitate fast contact between the hydrogels and substrates underwater, and the discontinuous facets prevented interfacial crack propagation[154]. Notably, in many cases, mechanical interlocking alone cannot give robust adhesion of hydrogel coatings, since the soft and deformable hydrogels can easily be detached from the snap-fit connectors[142]. Thus, the interlocking mechanism is commonly exploited together with covalent and/or non-covalent interactions for synergistic adhesion[153].

Despite the great advances in hydrogel coatings onto various substrates, there are still some unresolved challenges. One is the ability to conformally and uniformly adapt the hydrogel coatings to devices with complex surface geometries and fine features. Hydrogel coatings fabricated by

molding or dip-coating typically result in relatively thick and non-uniform hydrogel layers (over 50 μm), and only applicable for relatively simple surface geometries. A potential solution was reported by Yu et al. by interpenetrating hydrophilic polymers into the surface of diverse polymers with arbitrary shapes to form naturally integrated "hydrogel skins"[151]. Owing to the unique combination of hydrophobic initiators absorbed to the polymer surfaces and hydrophilic initiators dissolved in the hydrogel pre-gel solution, the hydrogel skins with a thickness of 5-25 μm can be formed in situ on the substrates, conformally adapting to complex and fine geometries of diverse polymer materials and devices, such as a pacemaker, a Foley catheter, and a swimming robot[151]. More elaborate discussions on different types of hydrogel adhesions and coatings can be found in books and reviews[142, 155].

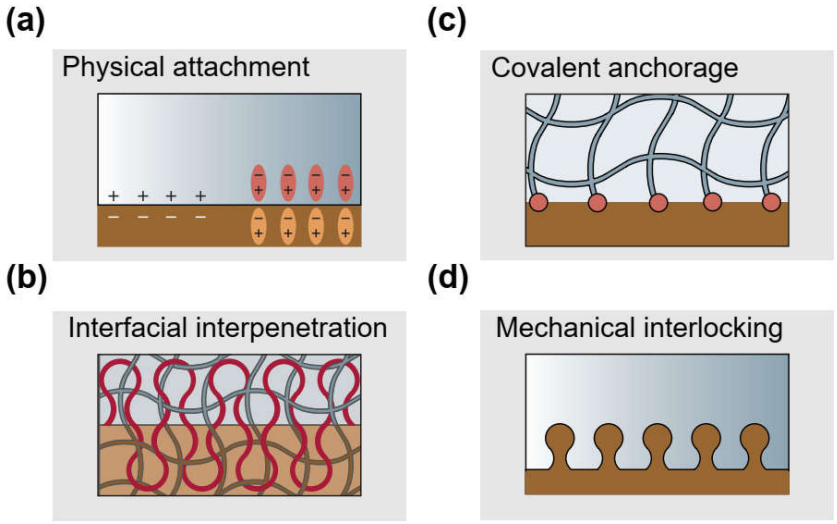

Figure 1-5. Hydrogel coatings based on different mechanisms of hydrogel adhesion, including (a) physical attachment, (b) covalent anchorage, (c) interfacial penetration, and (d) mechanical interlocking.

1.1.4. Hydrogel optics

Light and optical techniques have found particular importance in imaging, diagnosis, therapy, surgery, and biological research such as optogenetics and photometry[156]. The eye is a living optical machine, in which the cornea and crystalline lens refract the incoming light rays and focus them on the retina[157]. Cornea and crystalline lens are biological hydrogels containing 78 wt% and 65 wt% water, respectively[158, 159]. The high compliance, high water content, and biocompatibility make hydrogels an ideal material candidate for optic devices, especially for those in close contact with biological organisms. Efficient hydrogel optics rely on high transparency (low light absorption and scattering) and high refractive index (low bending loss) of

hydrogels[160]. High transparency of hydrogels requires them to be free of light absorbents such as conjugated molecular structures[161], and light scattering domains such as nanoscale inhomogeneity[48]. On the other hand, it usually involves introducing nanostructures or polymers with high molar refractivity to reach a high apparent refractive index of hydrogels[162]. According to their applications, there are four representative types of hydrogel optics developed so far, including (a) ophthalmic lenses[163-167], (b) smart windows and displays[48, 51, 168], (c) optical fibers[45, 74, 169], and (d) bioassay matrices[9, 170-173].

Ophthalmic lenses. Ophthalmic lenses, including wearable contact lenses[164, 165, 174], implantable artificial corneas[167], intraocular lens[163], and artificial vitreous body[175, 176], are traditionally made of rigid transparent materials such as glass, poly(methyl methacrylate), and polycarbonate. Owing to the softness, transparency, oxygen permeability, biocompatibility, and high water content of hydrogels[177, 178] (**Figure 1-6a**), the new generation of ophthalmic lenses are mostly based on hydrogels. For example, the contact lenses made of hydrogels offer an increased level of comfort and hydration for long wearing time (such as 1 day), compared to the traditional poly(methyl methacrylate) ones. In addition, the adaptive hydrogel lenses with adjustable focus lengths have been developed to mimic the lens shape change during eye accommodation[47].

One key challenge in hydrogel lenses is the refractive index of hydrogels. Hydrogels with high water content (60 – 90 wt%) typically exhibit a refractive index similar to that of water (1.333). However, high refractive indices of lens materials (> 1.38) are required in order to make thin lenses, which not only provide the desirable optical correction with a thin film, but also ensure sufficient oxygen permeability and minimal discomfort thanks to low thickness (e.g., ~30 μm)[162]. Therefore, silicone hydrogels, poly(2-hydroxyethyl methacrylate) hydrogels, and their derivatives are selected for ophthalmic lenses owing to the reconciled properties of high refractive index (1.380~1.400) and high water content (> 60 wt%)[178]. Other strategies that give rise to a high refractive index of hydrogels include the incorporation of inorganic nanoparticles or organic nano-phases featuring high molar refractivity[167, 179]. However, the refractive index mismatch between nano-domains/fillers and hydrogel matrices may lead to substantial undesirable light scattering, thus inferior transparency. Downsizing the nano-domains/fillers to less than one-tenth of the wavelength (e.g., zinc sulfide nanoparticles, 3 nm) has been proved to effectively diminish

light scattering, and thus achieve a high refractive index of 1.49 and high transparency at the same time[167].

Smart windows and displays. Light management based on smart window technologies is promising, as it can theoretically lead to annual energy savings of more than 1.055×10^{15} kJ in the United States (i.e., 1% of annual total energy consumption)[180]. Materials that can switch light absorption, scattering, and transmission properties in response to external stimuli offer new mechanisms to create smart windows for privacy, comfort, and energy efficiency (**Figure 1-6b**). Traditional transmission modulation mainly relies on inorganic thermochromic or electrochromic materials (e.g., vanadium dioxide, VO_2), which face challenges of high critical temperature (e.g., 68 °C for VO_2) and small transparency change[181, 182]. Temperature-responsive hydrogels (e.g., PNIPAM hydrogels) emerge as a promising alternative to inorganic thermochromic materials due to the dramatic phase transition around its lower critical solution temperature (~ 32 °C, close to the room temperature)[86, 101]. For example, Li et al. achieved the tunable scattering of PNIPAM-based hydrogel particles, resulting in thermo-responsive light rejection over the infrared region[48]. That is, the hydrodynamic diameter of these hydrogel particles decreased from 1388 nm at 25 °C to 546 nm at 35 °C, leading to significant infrared light scattering at 35 °C[48]. Furthermore, temperature-regulated solar transmission utilizing PNIPAM hydrogels demonstrated excellent stability, reversibility, and the ability of mass production[48].

In addition, the reversible modulation of light absorption, transmission, or reflection in hydrogels by external signals offers great opportunities in hydrogel based pressure-sensitive touch screen[51, 168], and electroluminescent displays[183]. The hydrogel smart windows and displays are soft and stretchable, potentially allowing seamless interfaces for human-machine interactions.

Optical fibers. Optical scattering and absorption of tissues limit the depths of light penetration in tissues, for example, only 50–100 μm for blue light (wavelength of 400-500 nm) and 1–3 mm for red and near infrared light (wavelength of 650-1000 nm) under skin[156]. Optical fibers can be embedded deep in the body to deliver light to or collect optical signals from the body (**Figure 1-6c**). The traditional optical fibers based on glasses and plastics are rigid and static, and thus fail to accompany the natural micro- and/or macro-motions of biological tissues[184]. Owing to the high transparency, low modulus and biocompatibility, hydrogels represent an attractive material

candidate for optical fibers in the body, especially for long-term applications. Light-guiding hydrogel fibers enable bidirectional, real-time transmission of optical signals between internal organs and external light sources/detectors[74, 169]. Hydrogel optical fibers have recently been implanted in the nervous system for optogenetic modulation and potentially treatment of neuropsychiatric disorders[185, 186]. In addition, laser surgeries (e.g., deep tissue ablation, photocoagulation in the retina, and destruction of cardiovascular plaques) and light-activated therapies (e.g., photodynamic therapy) can harness the light delivered through hydrogel fibers[156]. By using PEG hydrogels with high crosslinking density, Choi et al. invented hydrogel optical fibers for in vivo optical sensing and therapy[74, 169]. While the PEG hydrogels exhibited high biocompatibility and favorable light-guiding properties[74], they were mechanically brittle and lacked stretchability. Guo et al. used a highly stretchable and tough hydrogel (PAAm-alginate hydrogel) to fabricate optical fibers, attempting to address the low stretchability and brittleness of previous ones[45]. Hydrogel optical fibers with optimized guiding efficiency, mechanical stability, and softness are qualified for light recording and stimulation across an organ-scale distance, and applicable to dynamic and/or fragile tissues such as the brain and spinal cord[74, 169].

The applications of hydrogel optical fibers are still facing a number of challenges in terms of long-term optical and mechanical performances. First, when the hydrogel is brought into contact with tissues at its equilibrium state, the refractive index of the fully hydrated hydrogel is usually similar to that of water (1.333), and thus the light can hardly achieve total internal reflection at the interface between hydrogel and the surrounding tissues, leading to severe light leakage. Second, the tissues and hydrogel fibers are in a mechanically dynamic environment, and thus curvatures are generated along the deformed hydrogel fibers, causing aggravated light loss. To address these limitations, various hydrogel fiber structures (e.g., core-cladding geometry[45, 169]), hydrogel formulations (e.g., nanodomains or nanofillers with high refractive indices[167]), fabrication methods (e.g., hydrogels with smooth surfaces[45]), and mechanically robust hydrogels (e.g., anti-fatigue hydrogels[124]) were developed.

Bioassay matrices. Owing to the optical transparency, molecule permeability, and swelling capability of hydrogels, biologists use them as transparent matrices to fix tissues (**Figure 1-6d**). Two recently invented technologies (i.e., CLARITY[170] and expansion microscopy[9]) transform intact tissues with lipids into hydrogel-hybridized forms (i.e., PAAm and PAA

hydrogels). Together with antibody or gene based labeling, the resultant hydrogels enable a fine structural analysis of proteins, nucleic acids, and cells in tissues[9, 170, 171]. Especially, the PAA hydrogels used in the expansion microscopy allow the high-ratio, homogeneous swelling of the tissue specimens when immersed in water for structural observation and analysis with a nanoscale spatial resolution[9]. Besides fixing tissues for imaging, hydrogels are also adopted as a matrix for gel electrophoresis to separate macromolecules (e.g., DNA, RNA, and proteins) based on their sizes and charges under electric fields[172, 173]. After electrophoresis, the macromolecules in the transparent hydrogels can be visualized by staining and then viewed under a UV light[172, 173].

For more discussions on each type of hydrogel optics, please refer to some specific reviews on contact lenses[177, 187], smart windows[188, 189], optical fibers[190], and bioassay matrices[191] based on hydrogels.

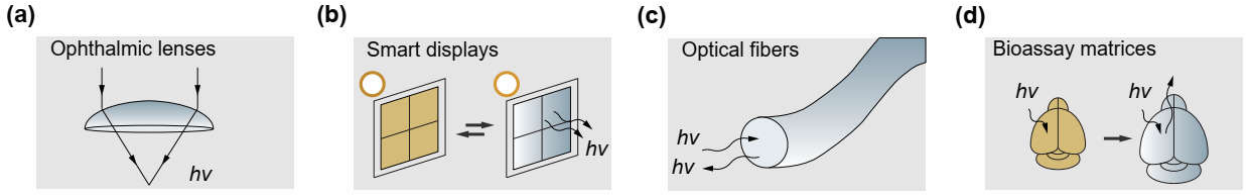

Figure 1-6. Hydrogel optics based on different applications, including (a) ophthalmic lenses, (b) smart windows and displays, (c) optical fibers, and (d) bioassay matrices. *hv*, photon.

1.1.5. Hydrogel electronics

The central and peripheral nervous systems in the human body receive, transmit, and generate electrical signals throughout the complex network of neurons in order to collect, process, and respond to information from the environments[192]. While nervous systems in biological organisms are composed of hydrogels (73 wt% water, modulus < 3 kPa), existing electronic devices that interact with nervous tissues are mostly based on hard and dry materials such as silicon and metals (0% water, modulus > 100 GPa)[143, 184]. Due to their similarities to biological tissues and versatility in electrical, mechanical, and biofunctional engineering, hydrogels have recently attracted growing attention in bioelectronics to potentially provide a seamless interface between biology and electronics.

Hydrogels are generally considered as electrical insulators due to the absence of mobile charges or charge carriers. The electrical conductivity of hydrogels in the physiologically relevant conditions is similar to that of tissue media, and much inferior to common electronic conductors such as metals, limiting their applications in electronics[193, 194]. To overcome such limitation

and enable the possibility of hydrogel electronics for improved tissue-electrode interfaces, a few strategies have been developed to enhance the electrical conductivity of hydrogels, including (a) addition of ionic salts in the hydrogels to achieve ionically conductive hydrogels[51, 96, 195-198], (b) incorporation of electrically conductive micro- and nano-materials within hydrogel matrices to endow electronic conductivity[66, 199-202], and (c) introduction of conducting polymers into hydrogels to enhance electronic conductivity[203-208].

Ionically conductive hydrogels. Ionically conductive hydrogels are enabled by the movement of mobile ionic salts such as Na^+, Li^+, and Cl^- in the hydrogel matrices activated by an electric field (**Figure 1-7a**). The resultant hydrogels can not only maintain the original mechanical compliance and optical transparency, but exhibit high ionic conductivity (~ 10 S m^{-1} when the salt concentration is ~ 3 M)[96, 195]. A series of electronic machines have been developed utilizing the ionically conductive hydrogels, including diodes[209], sensors[51], actuators[96], signal transmitters[125], memristors[210], photovoltaic cells[211], and power sources[197]. For example, a power source was created by stacking a high-salinity hydrogel, a cation-selective hydrogel, a low-salinity hydrogel, an anion-selective hydrogel and a second high-salinity hydrogel in sequence[197]. Upon contact with each other, they formed ionically conductive pathways, generating ~ 150 mV at open-circuit voltage.

One major challenge for applications of ionically conductive hydrogels inside biological organisms is the biocompatibility. The salt concentration in those hydrogels is an order of magnitude higher than the electrolyte concentration in the body fluids (~ 0.15 M), causing disorders of water and salt metabolism, as well as the loss of conductivity when salts diffuse from hydrogel to extracellular fluid[96, 195]. Thereafter, the ionically conductive hydrogels could only be used for non-invasive bioelectronics and machines that do not directly contact with body fluids.

Conductive micro and nanocomposite hydrogels. A variety of carbon and metal micro- and nano-materials, such as silver nanowires[66, 212], gold nanoparticles[66], carbon nanotubes[200, 213], graphene[201, 202], and liquid metals[214] have been incorporated into hydrogels as conductive fillers (**Figure 1-7b**). In those composites, the hydrogel matrices maintain the mechanical properties, while the conductive fillers provide electronic conductivity. Conductive hydrogel-nanomaterial composites have enabled various applications in electronics, including

underwater acoustic detectors by depositing silver nanowires on PAAm hydrogel[66], cardiac patches based on gold nanowires in alginate hydrogel or carbon nanotubes in gelatin methacrylate hydrogel[199], skin patches enabled by incorporating wavy titanium wires in PAAm-alginate hydrogel[215], and electrodes for EMG and ECG recording based on graphene nanocomposite hydrogel[216].

However, one obstacle remains in composite hydrogels due to the trade-off between electrical and mechanical properties. To achieve a high electrical conductivity through the micro- or nano-fillers dispersed in the hydrogel matrix, filler concentration above a critical concentration (i.e., percolation threshold) is required[66, 202]. On the other hand, a substantially high carbon or metal fraction may give rise to nano-/micro-scale aggregates, leading to deteriorated mechanical performances of the hydrogel composite[216].

Conducting polymer hydrogels. The electrical conductivity of conducting polymer hydrogels originates from the high electron mobility within a one-dimensional electronic band formed by the conjugated p-orbitals of conducting polymer chains (**Figure 1-7c**)[217]. Several types of conducting polymers, including poly(3,4-ethylenedioxythiophene) (PEDOT)[203, 204, 206], polypyrrole (PPy)[205], and polyaniline (PANI)[207, 208], become promising candidates in hydrogel electronics due to their favorable mechanical and electrical properties, electrochemical stability, biocompatibility, and processability for chemical modification[218]. The conducting polymers can either form interpenetrating networks with non-conducting polymer chains/networks[206], or form pure hydrogels without any non-conducting components[203, 204]. Poly(3,4-ethylenedioxythiophene):poly(styrene sulfonate) (PEDOT:PSS) hydrogels particularly provide a promising electrical interface with biological tissues for recording and stimulation, in which the coexistence of ionic and electrical conduction ensures a low interfacial impedance[203, 204, 206]. Existing methods to prepare PEDOT:PSS hydrogels mostly rely on mixing or in situ polymerization of PEDOT:PSS within non-conductive hydrogel templates to form interpenetrating polymer networks (IPN). Feig et al. reported that the interpenetration of a soft and stretchable polymer network within the loosely-crosslinked PEDOT:PSS network led to a conductive IPN hydrogel with low PEDOT:PSS content (1.1 wt%), high conductivity ($> 10\ S\ m^{-1}$), and high stretchability (> 100%)[206].

However, many IPN based conducting polymer hydrogels sacrifice their electrical conductivity and/or electrochemical performances since the non-conductive hydrogel network acts as an electrical insulator (e.g., electrical conductivity is typically below 100 S m^{-1} in deionized water)[143, 219]. A few strategies have been developed to convert pure PEDOT:PSS solutions into well-dispersed and connected networks, including increasing ionic strength[220], lowering pH[221], and adding ionic liquids[203, 222] and co-solvents[223, 224]. Recently, Lu et al. showed that the addition of volatile dimethyl sulfoxide in aqueous PEDOT:PSS solutions followed by controlled dry-annealing, and subsequent rehydration can yield pure PEDOT:PSS hydrogels, which exhibited high electrical conductivity (~2,000 S m^{-1} in PBS, ~4,000 S m^{-1} in deionized water), high stretchability (> 35% strain), low Young's modulus (~2 MPa), superior mechanical, electrical and electrochemical stability, and tunable isotropic/anisotropic swelling in wet physiological environments[204]. Moreover, Liu et al. synthesized and used the PEDOT:PSS hydrogels as elastic microelectronics for low-voltage electrical stimulation of the sciatic nerve in mice[203].

More examples and detailed mechanisms of hydrogel electronics and ionotronics can be found in recent reviews by Yuk et al.[143], Yang et al.[93], Koo et al.[225], and Guo et al[226].

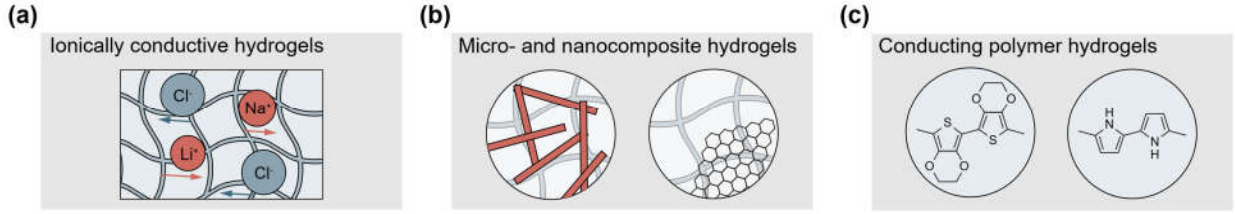

Figure 1-7. Hydrogel electronics based on (a) addition of ionic salts in the hydrogels to achieve ionically conductive hydrogels, (b) incorporation of electrically conductive micro or nanocomposites to endow electronic conductivity, and (d) introduction of conducting polymers into the polymer networks of hydrogel to enhance electronic conductivity.

1.1.6. Hydrogel water harvesters

Water is critical to the survival of all living organisms. However, only 2.5% of the water on Earth is fresh, and the rest is saline. Furthermore, only 1% of the freshwater is easily accessible, and the majority is trapped in glaciers and groundwater[227]. To enhance accessibility to fresh water, a number of technologies have been developed for water harvesting, including distillation, ion exchange, membrane filtration, and reverse osmosis[228]. Besides these, hydrogels provide alternative methods for water harvesting, owing to the high water content and reversible

swelling/dehydration process. Three strategies have been summarized below to harvest freshwater from different sources by hydrogels, including (a) contaminant removal to purify water from polluted water[229-232], (b) desalination by forward osmosis from salt water[233-237], and (c) vapor condensation from atmospheric water[238-241]. All three strategies rely on hydrogels' capability of absorbing and releasing water and/or other molecules.

Contaminant adsorption. Each year 1.2 trillion gallons of untreated sewage, stormwater runoff, and industrial waste are dumped into the aquatic system[242]. Heavy metals from mineral processing and dyes from the textile industry are toxic or carcinogenic to aquatic life, and imperil water environment for fishing, swimming, and drinking[243]. A few techniques have been widely adopted to remove the chemical wastes from polluted streams, such as precipitation, adsorption, oxidation, and nanofiltration[244], among which adsorption is viewed as an effective method due to the facile operation, low cost, and adsorbent diversity[244]. Hydrogels have been recognized as a versatile material platform for contaminant adsorption owing to the high water content, rapid ion diffusion, and the ability to incorporate varied functional receptors (**Figure 1-8a**). For example, hydrogels with negatively charged polymer networks (e.g., PAA hydrogel[245], chitosan hydrogel[231, 232], and nanocomposite hydrogel[229]) are able to selectively adsorb water-soluble heavy metal ions (e.g., Cu^{2+}, Pb^{2+}, As^{5+}, and Cr^{6+}) and cationic dyes (e.g., malachite green, methylene blue, basic fuchsin, and crystal violet), while hydrogels with positively charged polymer networks (e.g., poly(diallyldimethylammonium chloride))[246] can adsorb anionic toxins and dyes (e.g., nitrate, phosphate, and methyl orange) via electrostatic interaction. Besides, specific receptors of metal ions and dyes incorporated into the hydrogel networks allow selective recognition and adsorption of these contaminants[230]. The contaminant adsorption from polluted water by hydrogels leads to purified water with a minimal number of contaminants and hydrogels loaded with concentrated contaminants.

The removal efficiency of contaminants depends on the binding affinity between receptors in hydrogels and contaminants in water[230], amounts of receptors, as well as the mesh size of the hydrogels[247]. A high-performance adsorbent requires the hydrogel to exhibit not only high adsorption capacity and rate, but also the regeneration ability for repeated use[230]. A few methods have been reported to regenerate the hydrogel adsorbents after separation of hydrogels from the purified water, such as decreasing pH to release the bounded heavy metal ions from sodium

polyacrylate hydrogels[230], and solvent exchange to extract the adsorbed dyes[248]. A few reviews summarized the contaminant and toxin adsorption by hydrogels[249-251].

Desalination. For saline water, the most abundant water source on Earth, hydrogels are used as draw agents for forward osmosis to obtain desalinated water[252]. The hydrogel drawn desalination is accomplished through two steps (**Figure 1-8c**)[234]: First, driven by the osmotic pressure, the hydrogel absorbs clean water from the saline water, in which the hydrogel should possess a higher osmotic pressure than that of saline water. Then, for the purpose of pure water recovery and hydrogel re-usage, the captured pure water is subsequently expelled out of the hydrogel by temperature change, applied pressure, or solar irradiation[252]. In a typical work, Li et al. developed a hydrogel composed of PAA-co-PNIPAM, in which the negatively charged polymer chains induce hydrogel swelling with high water flux. Moreover, the swollen hydrogel can release the captured water during the subsequent thermo-induced deswelling[233]. Different hydrogel draw agents, including hydrogel blended with carbon particles for enhanced water recovery[252], hydrogel loaded with magnetic particles for easy retrieval[253], and hydrogels with ionic liquid[254], have been used to increase the desalination efficiency. For more examples, readers can refer to the reviews by Li et al.[255] and Cai et al[256].

The two separated steps of water absorbing and recovery, however, require repeated swelling/deswelling of the hydrogels, and cannot give continuous desalination process. Zhao et al. demonstrated that a hydrogel with microchannels composed of PVA and polypyrrole allowed continuous purification (**Figure 1-8b**)[237]. In this system, the hydrogel floated in a container of brine, and the capillary microchannels ensured adequate water supply from the bottom to the hydrogel upper surface. Besides, solar irradiation acted as a stimulus for water evaporation from the hydrogel, while polypyrrole as solar absorbers effectively converted solar energy to evaporate water in the hydrogel, leading to a stable, high water vapor collection rate (i.e., 3.2 kg m^{-2} h^{-1} for up to 28 days). The stable evaporation rate revealed that the hydrogel exhibits promising performances for practical long-term solar desalination with antifouling functionality in brine [257-259]. Similar desalination systems based on continuous water supply and solar vapor generation were reported by Yu group using different solar absorbers, including reduced graphene oxide[236], Ti_2O_3 nanoparticles[258], and activated carbon[259].

Atmospheric water condensation. The Earth's atmosphere holds approximately 13 trillion tons of freshwater distributed all over the world with fast replenishment[227]. Atmospheric water harvesting relies on condensing the gaseous water to liquid water, which requires the ability to absorb moisture and then release them in the form of vapor or liquid (**Figure 1-8c**). Deliquescent salts, such as calcium chloride and lithium chloride, exhibit a strong affinity with water and can capture moisture 5-6 times its own weight at low humidity (e.g., 10–25% relative humidity), which is significantly higher than other porous sorbents, such as metal-organic frameworks, molecular sieves, silica gels, zeolite, and activated alumina[260-262]. However, hydration of deliquescent salts after moisture absorption leads to an aqueous solution, which is practically difficult to handle. As an alternative, incorporation of these deliquescent salts within a hydrogel matrix can maintain the hydrated salts in a solid form, without sacrificing the capability of moisture absorption[238, 239]. The collected water can be released from the hydrogel at 80–100 °C, assisted by solar irradiation[238, 239, 263].

The introduction of carbon nanotubes as solar absorbers in the hydrogel enabled almost 100% release of the captured water under regular and even weak sunlight[264]. In order to further lower the energy required for water release, PNIPAM hydrogel was selected as a matrix for the moisture capture due to its drastic change in the hydrophilicity/hydrophobicity by a subtle temperature variation near its lower critical solution temperature. Matsumoto et al. reported that the freeze-dried PNIPAM-alginate hydrogel was able to absorb moisture at 27 °C and 80% RH, while the liquid water oozed out of the hydrogel at 50 °C[240]. Zhao et al. incorporated solar absorbing and hygroscopic polypyrrole chloride into thermo-responsive PNIPAM hydrogels[241]. In these hydrogel systems, liquid water was collected by an oozing process using the thermo-responsive hydrogels with low energy consumption, because this process got rid of repeated evaporation and condensation for water collection[240, 241].

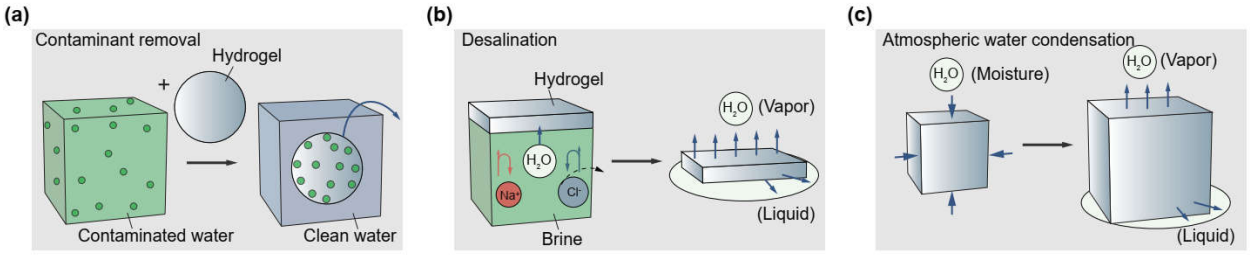

Figure 1-8. Hydrogels water harvesters based on (a) contaminant adsorption, (b) desalination, and (c) atmospheric water condensation.

1.2. Research methodology

This thesis presents an integrated approach to material and machine design using manufacturing, theoretical calculation, numerical modeling, experimental characterization, and in vitro and in vivo demonstration (**Figure 1-9**). The methods are briefly discussed here with specifics and further detail given in subsequent chapters when needed.

1.2.1. Manufacturing

The manufacturing of hydrogel materials, adhesions, and devices involves versatile methods including molding, electrospinning, and strain engineering for single-component materials, and coating, assembly, two-dimensional (2D) patterning, and three-dimensional (3D) printing for multi-component machines. Specific fabrication techniques used will be discussed in the coming chapters.

1.2.2. Theoretical calculation

Finite element analysis is adopted as a numerical tool to predict the mechanical responses of hydrogels and hydrogel machines under large deformation. We also used MATLAB and other software to calculate the kinetics and thermodynamics of the hydrogel responses, including chemical diffusion, cellular induction, swelling, magnetic attraction, and optical transmission. The theoretical and numerical calculation is used for optimized design and fabrication of hydrogel machines, and verified by the experimental results.

1.2.3. Experimental characterization

Experimental characterization of the hydrogel-based materials and machines is used to validate the proposed design principles. The microstructure and surface morphology of hydrogels are imaged using versatile microscale technologies, such as scanning electron microscope (SEM) and atomic force microscope (AFM). The mechanical properties of hydrogels in the short term and long term are usually characterized. The biocompatibilities of hydrogel machines with bacteria, mammalian cells, and tissues are evaluated. The functions and applications of hydrogel machines generally require the hydrogel to possess a set of specific properties. Therefore, we conduct optical

characterization for hydrogel optical fibers, magnetic characterization for magnetic hydrogels, swelling characterization for hydrogel balloons, and fluorescent signal detection for hydrogel living devices.

1.2.4. Demonstration

We conduct in vitro and ex vivo demonstrations to evaluate the functionality of the hydrogel materials and machines in a simulated physiological environment. In vivo experiments are used as a preclinical test to validate the efficacy and safety of the hydrogel machines, in which mice and pigs are adopted as animal models.

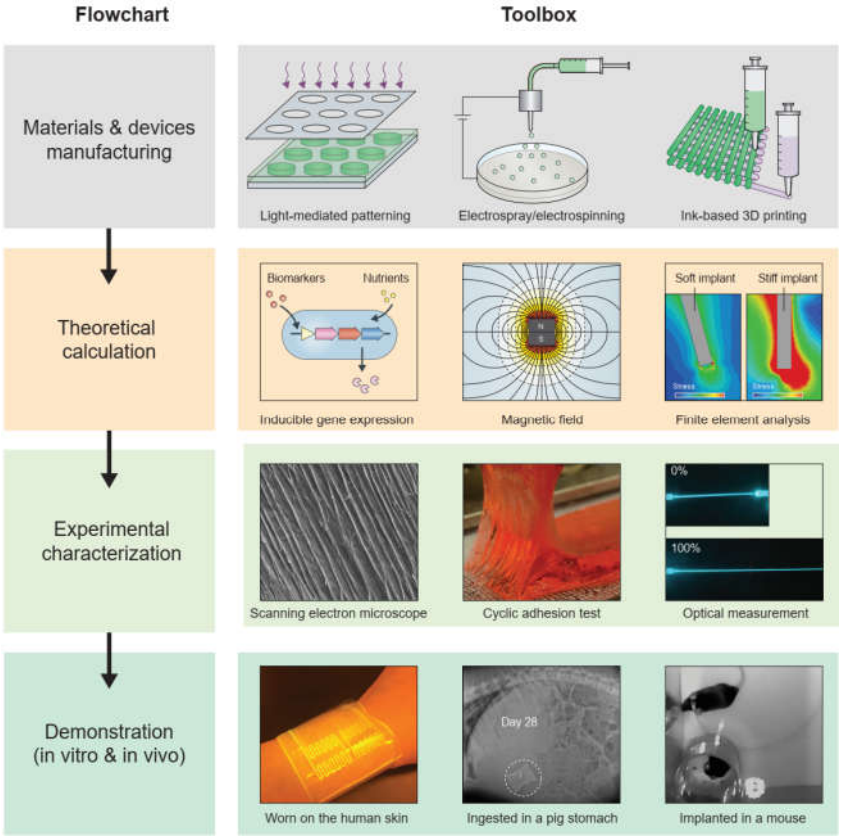

Figure 1-9. Flow chart of hydrogel machines and available toolbox.

1.3. Thesis structure

After an introduction to hydrogel machines and the research approach, this thesis specifically focuses on two aspects: (a) designing tough, fatigue-resistant hydrogel materials and adhesions, and (b) designing hydrogel machines that interact with biological organisms. We first report the design and manufacturing of tough, fatigue-resistant hydrogel materials and their adhesion with

other engineering materials. Building on these hydrogel materials and adhesions, we next present three types of hydrogel machines in series, including hydrogel living devices that incorporate living bacteria in hydrogel matrices, hydrogel ingestible devices that are retained in the gastrointestinal tract, hydrogel optical fibers that collect and deliver light from/to the nervous system. The design principles and implementation strategies of each hydrogel machine are described, followed by the theoretical calculation and experimental validation. Therefore, the thesis is organized as follows:

- Chapter 1 reviews general hydrogel machines and research methodology.
- Chapter 2 considers the design and synthesis of tough, fatigue-resistant hydrogel materials.
- Chapter 3 considers the design and synthesis of tough, fatigue-resistant hydrogel adhesions.
- Chapter 4 explores the design and manufacturing of hydrogel living devices and how they can be implemented as wearable devices.
- Chapter 5 explores the design and manufacturing of hydrogel gastric retentive devices and how they can be implemented as ingestible devices.
- Chapter 6 explores the design and manufacturing of hydrogel intestinal retentive devices and how they can be implemented as ingestible devices.
- Chapter 7 explores the design and manufacturing of hydrogel optical fibers and how they can be implanted in the nervous systems.
- Chapter 8 concludes the thesis and discusses challenges and opportunities for future research.

This thesis aims to provide new perspectives and tools for the design and optimization of next-generation machines based on hydrogel materials for a variety of applications in health, environment, and robotics, among others.

Chapter 2

Fatigue-resistant hydrogel materials

The research presented in this chapter has been published in:

- Shaoting Lin†, **Xinyue Liu†**, Ji Liu†, Hyunwoo Yuk, Jake Song, Hyun-chae Loh, German A. Parada, Charles Settens, Admir Masic, Gareth McKinley, and Xuanhe Zhao. Anti-fatigue-fracture hydrogels. Science Advances. 5, 2019.
- Shaoting Lin†, Ji Liu†, **Xinyue Liu**, and Xuanhe Zhao. Muscle-like fatigue-resistant hydrogels by mechanical training. Proceedings of the National Academy of Sciences. 116, 2019.
- Jiahua Ni, Shaoting Lin, Zhao Qin, David Veysset, **Xinyue Liu,** Yuchen Sun, Alex J. Hsieh, Raul Radovitzky, Keith A. Nelson, Xuanhe Zhao*, Strong fatigue-resistant nanofibrous hydrogels inspired by lobster underbelly, Matter. 5, 2021.
- Xuanhe Zhao, Xiaoyu Chen†, Hyunwoo Yuk†, Shaoting Lin†, **Xinyue Liu**, German Parada. Soft materials by design: Unconventional polymer networks give extreme properties. Chemical Reviews. 121, 2021.

2.1. Introduction

As hydrophilic polymer networks infiltrated with water[2], hydrogels are the major components of animal bodies, constituting most of their cells, extracellular matrices, tissues, and organs. The mechanical properties of biological hydrogels are crucial to the survival and wellbeing of animals. For example, cartilage is a tough connective tissue that covers the surfaces of joints to provide reduced friction [265]. The human knee joint cartilage (i.e., articular cartilage) typically needs to sustain compressive stresses of 4-9 MPa for 1 million cycles per year, while maintaining high fracture toughness around 1,000 J m^{-2}[266]. The high fracture toughness of articular cartilage is mainly attributed to its abundant strong collagen fibers interpenetrated with proteoglycan macromolecules. Tendon is a strong connective tissue that connects muscle to bone and muscle to

muscle. The human patellar tendon can sustain a high tensile strength over 50 MPa and fracture toughness of 20-30 kJ m^{-2}[267, 268], owing to its unique hierarchical fibrous structure that enables the simultaneous stiffening of bundles of collagen fibers before their tensile failure[269, 270]. Heart valves generally possess high fracture toughness around 1,200 J m^{-2}[271, 272]. Under large deformation, the stiffening and fracture of the collagen fibers in heart valves dissipate substantial mechanical energy, making the heart valve tough[273].

On the other hand, hydrogels have been widely used in biomedical applications such as vehicles for drug delivery [4, 26, 274, 275], scaffolds for tissue engineering [10, 276, 277], medical implants [187, 278], wound dressings[279-281], and contact lenses [278, 282]. More recently, intensive efforts have been devoted to exploring hydrogels' emerging applications in devices and machines [283] such as hydrogel sensors [42, 47, 55, 85], actuators [5, 96, 99, 106], soft robots [5, 101, 109], electronic devices [66, 203, 204], and bioadhesive devices [150, 284], and coatings [151, 285], as elaborated in Chapter 1. The abovementioned applications of hydrogels generally require the hydrogels to possess mechanical robustness. For example, the use of hydrogels as artificial cartilages and spinal discs requires the hydrogels to be fatigue-resistant under cyclic mechanical loading [124, 286-288]. High-power and high-force hydrogel actuators require them to exhibit high values of strength and fracture toughness[5].

However, fracture and fatigue are common in soft materials, severely limiting their applications in devices and machines; fatigue fracture has been reported to occur in medical implants and tissue scaffolds made of hydrogels. Most hydrogels are brittle, with fracture energies of about 10 J m^{-2}, as compared with 1,000 J m^{-2} for cartilage and 10,000 J m^{-2} for natural rubbers. Intense efforts are devoted to synthesizing hydrogels with improved mechanical properties. Following the pioneering work by Gong et al. [28], hydrogels have been made tough to resist crack propagation under a single cycle of mechanical load [29, 289-291]. The toughening of hydrogels is achieved by integrating mechanisms for dissipating mechanical energy such as fracture of short polymer chains and reversible crosslinks into stretchy polymer networks [1, 292]. These tough hydrogels have reached fracture energy of 100–1,0000 J m^{-2}. However, existing tough hydrogels still suffer from fatigue fracture under multiple cycles of mechanical loads [93, 293, 294], because the resistance to fatigue-crack propagation after prolonged cycles of loads is the energy required to fracture a single layer of polymer chains (i.e., the intrinsic fracture energy of the hydrogel), which is unaffected by the additional dissipation mechanisms introduced in tough hydrogels [293,

294]. The reported fatigue thresholds of various tough hydrogels are 8.4 J m^{-2} for PAAm-PVA [294] and 53.2 J m^{-2} for PAAm-alginate [293], the same order as their intrinsic fracture energies. The highest fatigue threshold for hydrogels reported so far is 418 J m^{-2} for a double network hydrogel, poly(2-acrylamido-2-methyl-1-propanesulfonic acid) (PAMPS)-PAAm, which possibly can be attributed to the PAAm network with very long polymer chains and thus high intrinsic fracture energy [28, 295].

A general strategy toward the design of anti-fatigue-fracture hydrogels has remained a critical need and a central challenge for long-term applications of hydrogels in devices and machines. The architectures of various biological hydrogels to achieve extreme mechanical properties can inspire the design of synthetic hydrogels with high fracture energy and fatigue threshold. In this chapter, we will introduce the structural design principles for polymer networks to achieve resistance to a single cycle (high fracture toughness) and multiple cycles of mechanical load (high fatigue threshold). Then, we will focus on three different implementation strategies for fatigue-resistant hydrogels, including nanocrystalline domains by thermal annealing, polymer nanofibers formed by phase separation and polymer nanofibers deposited by electrospinning. We will describe the manufacturing and characterization of the three types of tough, fatigue-resistant hydrogels. Specifically, we will characterize the microstructures and mechanical properties, and reveal how the microstructures of hydrogels can resist the crack propagation during single and repeated mechanical deformation.

2.2. Design principles

2.2.1. Toughness: build dissipation into stretchy polymer networks

Fracture toughness. Fracture toughness has been widely used to characterize a material's capability to resist fracture under mechanical loads. One common definition for the fracture toughness of a material is the energy required to propagate a crack in the material over a unit area measured in the undeformed state (**Figure 2-1a**) which can be quantitatively expressed as,

$$\Gamma = G_c = -\frac{dU}{dA} \tag{2-1}$$

where U is the total potential energy of the system, A is the crack area measured in the undeformed state, and G_c is the critical energy release rate that drives crack propagation.

According to **Equation 2-1**, the unit for the fracture toughness is joule per meter squared (i.e., J m^{-2}).

The fracture toughness of soft materials such as elastomers and hydrogels has been measured with many experimental methods such as the pure-shear test and the single-notch test, which have been summarized in a few recent review papers[1, 296, 297]. For example, in the pure-shear test, two identical pieces of a hydrogel are fabricated with the same thickness T, width W and height H, where W >> H >> T (**Figure 2-1a**). Both pieces of the samples are clamped along their long edges (i.e., along the width direction) with rigid plates. A notch with a length of ~0.5W is introduced into the first sample, which is then gradually pulled to a stretch of λ_c times of its undeformed height until a crack begins to propagate from the notch (**Figure 2-1a**). The second sample without notch is uniformly stretched above the critical stretch λ_c to measure the nominal stress s vs stretch λ relation (**Figure 2-1a**). Thereafter, the fracture toughness of the hydrogel can be calculated as $\Gamma = H\int_1^{\lambda_c} s d\lambda$, based on the measured λ_c and stress vs stretch relation in the pure-shear tests.

The fracture toughness of a conventional polymer network is its intrinsic fracture energy Γ_0 , which is the energy required to fracture a layer of polymer chains over a unit area (**Figure 2-2a**). Evaluated with typical parameters of conventional polymer networks, the fracture toughness of the corresponding hydrogels is commonly limited to a few tens of joule per meter squared. In addition, the fracture toughness of hydrogels with conventional polymer networks is also coupled with their stretch limits and shear moduli (**Equation 2-2**)

$$\lambda_{\text{lim}} \sim \Gamma_0 \sim G^{-1/2} \tag{3-2}$$

For example, in order to increase the fracture toughness of a conventional polymer network, the chain length (i.e., N) and thus the stretch limit of the polymer network need to be increased. Consequently, the chain density (i.e., n) and thus the shear modulus of the polymer network will be decreased.

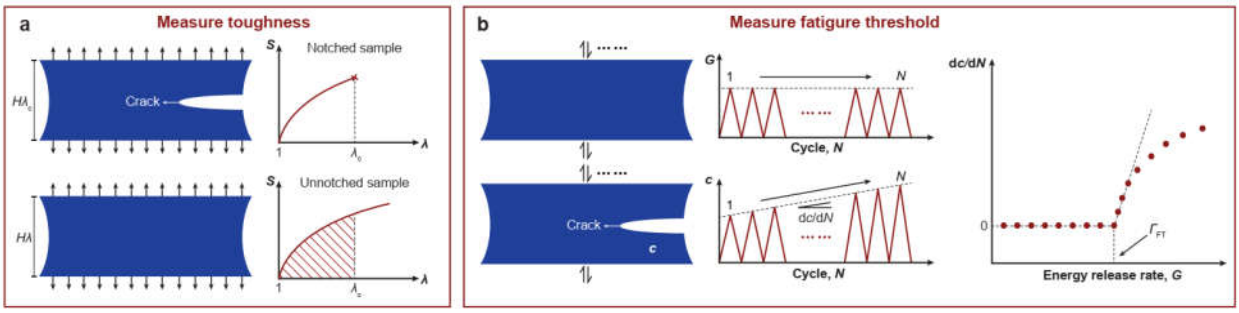

Figure 2-1. Definition and measurement of fracture toughness and fatigue threshold. (a) Definition of fracture toughness, and the pure-shear test to measure the fracture toughness. When a notched sample with height H at the undeformed state is stretched by a critical ratio of λ_c under the pure-shear deformation, the crack begins to propagate (top). The relation of the nominal stress S and the stretch λ is measured for an un-notched sample (otherwise the same as the notched sample) under the pure-shear deformation (bottom). The fracture toughness can be calculated as $\Gamma = H\int_1^{\lambda_c} s d\lambda$ based on the measured λ_c and S - λ relation in the pure-shear tests. (b) Definition of fatigue threshold, and the pure-shear method to measure fatigue threshold. G is the energy release rate, c is the crack length, and N is the cycle number. The fatigue threshold Γ_{FT} is determined by intersecting the curve of dc/dN vs G with the G axis.

Design principle. The design principle for tough hydrogels is the same as the principle for toughening various engineering materials (such as metals[298], ceramics [299], composites[300] and polymers[301]) and various biological tissues (such as tendons, cartilages, muscles and blood vessels[302]). That is to integrate both ductility and mechanical dissipation in the same material, so that a process zone with substantial mechanical dissipation develops around the crack tip prior to crack propagation (**Figure 2-2e**). The mechanical dissipation of a material manifests as the hysteresis loop on its stress-stretch curve under a loading-unloading cycle (**Figure 2-2f**). The ductility of hydrogels generally relies on the high stretchability (or the high stretch limit) of their polymer networks. Overall, the design principle for tough hydrogels is to build dissipation into stretchy polymer networks[1, 292]. Quantitatively, the total fracture toughness of a hydrogel with the capability of mechanical dissipation can be expressed as [1, 136]

$$\Gamma = \Gamma_0 + \Gamma_D \tag{2-3}$$

where Γ, Γ_0, and Γ_D are the total fracture toughness, the intrinsic fracture energy, and the contribution of mechanical dissipation in the process zone to the total fracture toughness, respectively. While the intrinsic fracture energy for hydrogels is usually limited to a few tens of joule per meter squared (**Figure 2-2a-c**), the contribution of the process-zone dissipation can be extremely high because both the dissipated energy per volume of the process zone and the size of

the process zone can be large values (**Figure 2-2e-g**). Indeed, the fracture toughness of tough hydrogels has exceeded 10,000 J m^{-2}, orders of magnitude higher than that of hydrogels with conventional polymer networks[1].

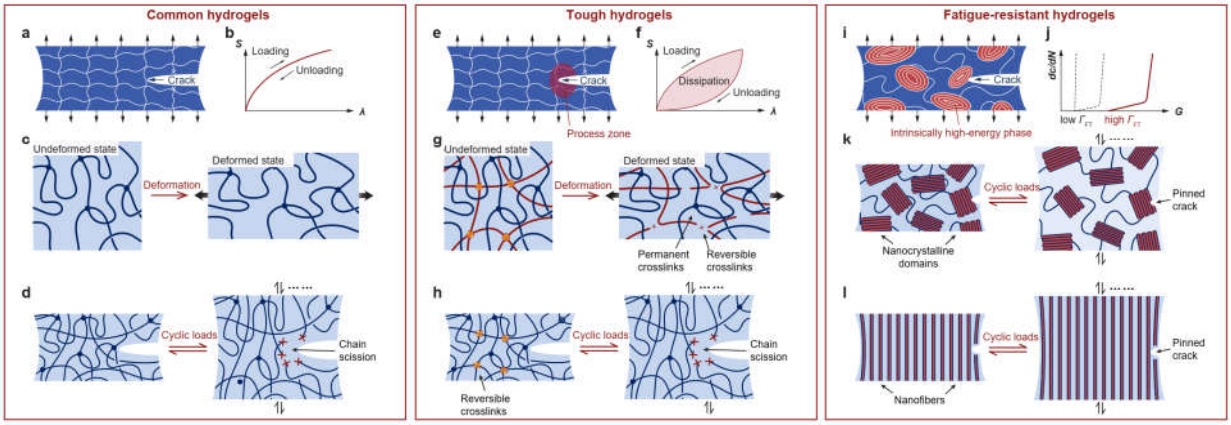

Figure 2-2. Design principles of hydrogels with extreme mechanical properties. (a) Design principles for common hydrogels. (b) Stress versus strain curve of common hydrogels with no hysteresis. (c) The sparsely-crosslinked long-chain polymer network ensures the high stretchability of the polymer network in common hydrogels. (d) Fatigue crack in common hydrogels propagates over cyclic loads. (e) Design principles for tough hydrogels through building dissipation into stretchy polymer networks. (f) Stress versus strain curve of tough hydrogels with large hysteresis. (g) An implementation strategy of tough hydrogels: reversible crosslinks dissociate to dissipate substantial mechanical energy and the sparsely-crosslinked long-chain polymer network still sustains the high stretchability of the polymer network. (h) Fatigue crack in tough hydrogels propagates over cyclic loads. Dissipation mechanisms such as reversible crosslinks in tough hydrogels are depleted over cyclic loads, not contributing to the fatigue threshold. (i) Design principles for fatigue-resistant hydrogels through pinning fatigue cracks with intrinsically high-energy phases. (j) Crack propagation rate versus energy release rate curves of common (dash), tough (dash), and fatigue-resistant (solid, red) hydrogels. (k) An implementation strategy of fatigue-resistant hydrogels: fatigue crack is pinned by nanocrystalline domains. (l) An implementation strategy of fatigue-resistant hydrogels: fatigue crack is pinned by nanofibers.

2.2.2. Fatigue-resistance: pin fatigue cracks with intrinsically high-energy phases

Fatigue threshold. The word "fatigue" has been used to describe many symptoms observed in materials under prolonged loads, including materials with or without precut cracks under prolonged static or cyclic loads[303, 304]. In this section, we will focus on the fatigue fracture of hydrogels with precut cracks under cyclic loads (**Figure 2-1b**), because this is one of the most common failure modes of hydrogels in mechanically dynamic environments such as artificial cartilages[305] and soft robots[5]. Fatigue threshold has been commonly used to characterize a material's resistance to fatigue crack propagation under cyclic loads. The fatigue threshold is

defined as the minimal fracture energy at which fatigue crack propagation occurs under infinite cycles of loads[149, 306]. Quantitatively, the fatigue threshold Γ_{FT} can be expressed as,

$$\Gamma_{FT} = G_c\left(dc/dN \to 0\right) \tag{2-4}$$

where G is the energy release rate to drive crack propagation under each cycle of load, G_c is the minimal energy release rate at which crack propagation occurs under infinite cycles of loads (i.e. $dc/dN \to 0$), c is the length of the crack, N is the cycle number of the applied load, and dc/dN gives the crack extension per cycle.

The fatigue threshold of soft materials such as elastomers and hydrogels have been measured with various experimental methods such as the pure-shear fatigue-fracture test and the single-notch fatigue-fracture test[124]. For example, in the pure-shear fatigue-fracture test, two identical pieces of a hydrogel are fabricated with the same thickness T, width W and height H, where W >> H >> T (**Figure 2-1b**). Both pieces of samples are clamped along their long edges (i.e., along the width direction) with rigid plates. The first sample is repeatedly pulled to a stretch of $\lambda_{applied}$ times of its undeformed height to measure the nominal stress s vs stretch λ relation, and the corresponding energy release rate can be calculated as $G = H\int_1^{\lambda_{applied}} s d\lambda$, which is a function of the cyclic number N (**Figure 2-1b**) . Thereafter, a notch with a length of ~0.5W is introduced into the second sample, which is then repeatedly pulled to the same stretch $\lambda_{applied}$ to measure the crack length c as a function of the cyclic number N. The pure-shear fatigue-fracture tests are repeated for different values of the applied stretch $\lambda_{applied}$ (i.e., different energy release rate G), and a curve of dc/dN vs G can be obtained (**Figure 2-1b**). The fatigue threshold Γ_{FT} is then determined by intersecting the curve of dc/dN vs G with the G axis (i.e., when $dc/dN \to 0$). Notably, the fatigue-fracture tests of hydrogels are commonly carried out in aqueous environments to avoid dehydration of the hydrogels under prolonged loads[124, 288]. For further discussion on the theory and experiments for the fatigue of hydrogels, a comprehensive review paper on this topic is recommended[304].

Design principle. As discussed above, a hydrogel can be designed tough by building mechanical dissipation into stretchy polymer networks[1]. The mechanical dissipation in the process zone

around the crack tip can dramatically enhance the fracture toughness of the hydrogel. However, the mechanisms for irreversible dissipation such as fracturing polymer chains in the process zone are usually depleted under cyclic loads. The mechanisms for reversible dissipation such as reversible crosslinks, once depleted, usually cannot recover in time to resist fatigue crack propagation in future cycles of loads (**Figure 2-2h**)[149, 293, 306]. Consequently, the fatigue threshold of hydrogels and elastomers is their intrinsic fracture energy[149, 293, 306],

$$\Gamma_{FT} = \Gamma_0 \tag{2-5}$$

Therefore, it is clear that the design of fatigue-resistant hydrogels usually cannot rely on mechanical dissipation in the bulk hydrogel matrices.

The design principle for fatigue-resistant hydrogels is to make the fatigue crack encounter and fracture objects with energies per unit area much higher than that for fracturing a single layer of polymer chains, or in short, to pin fatigue crack by intrinsically high-energy phases (**Figure 2-2i**)[124]. The intrinsically high-energy phases that have been exploited for the design of fatigue-resistant hydrogels include nanocrystalline domains (**Figure 2-2k**)[124], nano-/micro-fibers (**Figure 2-2l**)[288], microphase separations[304, 307], and macroscale composites[308]. In addition, because the design of fatigue-resistant hydrogels does not rely on mechanical dissipation in the bulk hydrogels, fatigue-resistant hydrogels usually demonstrate low hysteresis ratio and high resilience[124, 288, 309]. Notably, biological hydrogels such as muscles, tendons and ligaments commonly possess intrinsically high-energy phases such as nano-/micro-fibers, usually arranged in hierarchical architectures, to achieve high fatigue threshold.

2.2.3. Implementation strategies for fatigue-resistant hydrogels.

The design principle for fatigue-resistant hydrogels has been implemented with hydrogel structures that possess intrinsically high-energy phases[124, 288, 304, 307, 308]. In order to effectively pin fatigue cracks, the density of the intrinsically high-energy phases in the hydrogels should be sufficiently high[124]. Two types of high-energy phases including nanocrystalline domains and nano-/micro-fibers are presented below.

High-functionality crosslinks such as nanocrystalline domains can effectively play the role of intrinsically high-energy phases in the hydrogels (**Figure 2-2k**). The energy required to pull out a polymer chain from a nanocrystalline domain can be multiple times higher than that to fracture the same polymer chain, and the energy required to mechanically damage the nanocrystalline

domains can be multiple times higher than that to fracture the corresponding amorphous polymer chains (**Figure 2-2d,h**)[310]. Consequently, it has been shown that enhancing the crystallinity of a PVA hydrogel from 0.2 wt% to 18.9 wt% by dry-annealing the hydrogel can increase its fatigue threshold from 10 J m^{-2} to 1,000 J m^{-2}, reaching the level of fatigue-resistant biological hydrogels such as cartilages[124]. Since the size of the crystalline domains in the PVA hydrogel has been measured to be a few nanometers, it is the nanocrystalline domains that play the role of intrinsically high-energy phases.

Nano-/micro-fibers can also act as intrinsically high-energy phases in the hydrogels to implement the design principle for fatigue-resistant hydrogels (**Figure 2-2l**). The energy required to fracture a nano-/micro-fiber can be much higher than that to fracture the corresponding amorphous polymer chains, because of the synergistic elongation and stiffening of the bundled polymer chains in the fiber[288]. Based on this implementation strategy, it has been shown that introducing nanofibers into a PVA hydrogel by freeze-thawing the hydrogel can enhance its fatigue threshold from 10 J m^{-2} to 310 J m^{-2}. In particular, if the nanofibers are aligned perpendicular to the fatigue crack by pre-stretching the hydrogel, the measured fatigue threshold further increases to 1,250 J m^{-2} [288]. In addition, because the nanofibers can be made compliant, stretchable and strong by using a low density of nanocrystalline domains to bundle polymer chains, the resultant nanofibrous hydrogel integrates high compliance, stretchability and strength together with high fatigue threshold – mimicking the combinational mechanical properties of biological muscles [288]. Besides the nanofibrous hydrogels formed by freeze-thawing, the nanofibrous PVA hydrogels have also been obtained by electrospinning and welding [311]. The final bouligand-type nanofibrous structure closely mimic the bouligand structure of the natural membrane in the lobster underbelly [311]. The strong welded interface between nanofibers and high crystalline nanofibers work synergistically to resist propagation of fatigue crack. The resultant nanofibrous hydrogel can reach high nominal strength up to 8.4 MPa and high fatigue threshold up to 770 J m^{-2} [311].

2.3. Materials and methods

2.3.1. Fabrication of hydrogels

All types of our PVA hydrogels were synthesized from 10 wt% PVA (molecular weight, 146,000 to 186,000; 99+% hydrolyzed) solution. The solution was heated in a water bath at 100°C with stirring for 5 hours.

Chemically crosslinked PVA hydrogels. We added 100 μL of glutaraldehyde (25 vol%) as a cross-linker to 1 mL of 10 wt% PVA solution and added 100 μL of hydrochloric acid (36.5 wt%) as an accelerator into the other 1 mL of 10 wt% PVA solution. We then mixed and defoamed each of them by using a centrifugal mixer (AR-100, Thinky). The final mixtures, obtained by mixing and defoaming the two solutions together, were then cast into a mold and allowed to cure for 2 hours. The chemically cross-linked PVA hydrogels were immersed in deionized (DI) water for 2 days to remove unreacted chemicals.

Annealed PVA hydrogels. 10 wt% PVA solutions after mixing and defoaming were poured into a mold, frozen at −20°C for 8 hours, and thawed at 25°C for 3 hours. The freeze-thawed hydrogels were further dried at room temperature for 8 hours and then annealed at 100°C for a controlled time (i.e., 0, 1, 3, 5, 10, or 90 min). All as-prepared PVA hydrogels were immersed in water to achieve their equilibrium-swollen state.

Freeze-thawed PVA hydrogels with randomly distributed nanofibers. 10 wt% PVA solutions after mixing and defoaming were poured into a mold, frozen at −20°C for 8 hours, and thawed at 25°C for 3 hours. The freeze-thawing process was repeated five times. The as-prepared PVA hydrogels were immersed in water to achieve their equilibrium-swollen state.

Mechanically trained PVA hydrogels with aligned nanofibers. 10 wt% PVA solutions after mixing and defoaming were poured into a mold, frozen at −20°C for 8 hours, and thawed at 25°C for 3 hours. The freeze-thawing process was repeated five times. Then, we cyclically prestretched the freeze-thawed hydrogel in a water bath using a mechanical tester (CellScale, Canada). The sufficiently aligned nanofibers were achieved by applying the maximum applied stretch of 4.6 for 1000 cycles.

2.3.2. Measurement of water content

We measured the water content in swollen PVA hydrogels using thermal gravimetric analysis (TGA; TA Instrument). We first cut a disk shape of swollen PVA hydrogels of ~ 5 mg. The swollen

hydrogels weighing m_S in a titanium pan without any water droplet on the surface of the samples. The samples were thereafter heated up from 30 °C to 150 °C at the rate of 20 °C min^{-1}, and then 150 °C to 160 °C at the rate of 5 °C min^{-1} under a nitrogen atmosphere at a flow rate of 30 mL min^{-1}. The measured mass of the sample was recorded. The mass of the sample decreases with the increase of temperature and gradually reaches a plateau m_D when the all residual water in the sample evaporates. The water contents of the swollen PVA hydrogels were identified as

$\phi_{water} = 1 - m_D / m_S$

2.3.3. Measurement of crystallinity

We measured the crystallinities of the PVA hydrogels using differential scanning calorimetry (DSC; TA Instrument). Before drying the PVA hydrogels for DSC measurements, we first used excess chemical cross-links to fix the amorphous polymer chains to minimize the further formation of crystalline domains during the air-drying process. Specifically, we soaked the samples (thickness of 1 mm) in the aqueous solution consisting of 10 mL of glutaraldehyde (25 vol%), 500 μL of hydrochloric acid (36.5 wt%), and 100 mL of DI water for 1 hour. Thereafter, we soaked the samples in a deionized water bath for 1 hour to remove the extra glutaraldehyde and hydrochloric acid. The samples were further dried at 37 °C for 2 hours.

In a typical DSC measurement, we first weighed the total mass of the dry sample (with residual water). The sample was thereafter placed in a Tzero Pan and heated up from 50° to 250°C at a rate of 20°C min^{-1} under a nitrogen atmosphere with a flow rate of 30 mL min^{-1}. The curve of heat flow shows a broad peak from 60° to 180°C, indicating that the sample contains a small amount of residual water. The integration of the endothermic transition ranging from 60° to 180°C gives the enthalpy for evaporation of the residual water per unit mass of the dry sample (with residual water) H_r. Therefore, the mass of the residual water m_R can be calculated as

$$m_R = m H_R / H^0_{water} \quad (2\text{-}6)$$

where $H^0_{water} = 2260$ J g^{-1} is the latent heat of water evaporation, and m is the total mass of the dry sample. The curve of heat flow shows another narrow peak ranging from 200 °C to 250 °C, corresponding to the melting of the crystalline domains. The integration of the endothermic transition ranging from 200 °C to 250 °C gives the enthalpy for melting the crystalline domains per unit mass of the dry sample (with residual water) H_C. Therefore, the mass of the crystalline domains m_C can be calculated as

$$m_R = m\, H_C / H^0_C \quad (2\text{-}7)$$

where $H^0_C = 138.6\ J\ g^{-1}$ is the enthalpy of fusion of 100 wt% crystalline PVA measured at the equilibrium melting point. Therefore, the crystallinity in the ideally dry sample X_{dry} (without residual water) can be calculated as

$$X_{dry} = m_C/(m-m_R) \quad (2\text{-}8)$$

With measured water content ϕ_{water}, the crystallinity in the swollen state can be calculated as

$$X_{gel} = X_{dry}\,(1- \phi_{water}) \quad (2\text{-}9)$$

2.3.4. Imaging of morphology

X-ray scattering. We investigated nanocrystalline morphologies in PVA hydrogels through small-angle X-ray scattering (SAXS) and wide-angle X-ray scattering (WAXS). The X-ray scattering measurements were performed with a Pilatus3R 300K detector (Bruker Nanostar SAXS). We used a small-angle 2-mm beamstop with a sample-detector distance of 1059.1 mm for SAXS measurements and a wide-angle 2-mm beamstop with a sample-detector distance of 109.1 mm for WAXS measurements. The exposure time was set as 300 s. Raw SAXS and WAXS patterns were processed with corrections by MATLAB-based GIXSGUI software before analysis. The measured scattering intensity of PVA hydrogels in the swollen state was corrected by subtracting the water background. A customized linear stretcher was designed to hold the samples at the various stretches for in situ X-ray scattering measurements.

Confocal imaging. To visualize the microstructures of PVA nanofibrous hydrogels, a fluorescent dye, 5-([4,6-dichlorotriazin-2-yl]amino) fluorescein hydrochloride (5-DTAF), was used to label the hydroxyl groups in PVA.33 Specifically, 1.0 mL of 0.5 wt% 5-DTAF in anhydrous dimethyl sulfoxide was added into 100 mL of sodium bicarbonate aqueous solution (0.1 M [pH 9.0]) to form a reactive dye solution. The PVA nanofibrous hydrogels were immersed in the dye solution for 12 h at 4°C in the dark to conjugate fluorochrome to PVA. Finally, the nanofibrous hydrogel samples were rinsed several times with water to wash away the non-conjugated dyes before fluorescence imaging. To achieve in situ fluorescent imaging of the nanofibrous hydrogels, the hydrogel samples were stretched under uniaxial tension using a linear stretcher (MicroVice Holder, STJ-0116). The microstructures of nanofibrous hydrogel were imaged using a confocal microscope

(Leica TCS SP8). Laser intensity, filter sensitivity, and grayscale threshold were adjusted in each application to optimize the contrast of the images.

SEM imaging. For the freeze-thawed and mechanically trained PVA hydrogels, a notched sample was gradually elongated to a stretch of 2 without obvious crack propagation in order to delaminate the fibrils near the notch. The PVA sample was immediately immersed in a 2.5 wt% glutaraldehyde solution for 3 hours to fix the structure, and dehydrated through a series of alcohol solutions in ascending concentration (30, 50, 70, 90, 95, and 100 vol% twice) in order to avoid non-uniform shrinkage. The dehydrated PVA sample was fractured along the notch using forceps immediately after being frozen in liquid nitrogen. The fractured samples were kept in ethanol and dried in a supercritical dryer (Automegasamdri Series C, Tousimis). The dried fracture surfaces were then sputter coated with gold and observed by a SEM (JEOL 5910).

AFM phase imaging. AFM phase images were acquired with an atomic force microscope (Asylum Research MFP-3D) in tapping mode. Dry PVA films were directly attached onto the sample stage with a doublesided carbon tape. The probe lightly taps on the sample surface with a recorded phase shift angle of the probe motion relative to a driving oscillator. The bright regions with high phase angle correspond to regions with relatively high modulus, and the dark regions with low phase angle correspond to regions with relatively low modulus.

2.3.5. Mechanical characterization

Measurement of stress-stretch curve. All the mechanical tests were performed on notched and unnotched samples in a water bath at $c(N)$. The applied energy release rate can be calculated by $G(\lambda_a, N) = 2k(\lambda_a)c(N)W(\lambda_a, N)$, where $k = 3/\sqrt{\lambda_a}$, c is the crack length measured by the camera, and W is the stored strain energy density, which can be identified from the measured nominal stress versus stretch curves of an unnotched sample at different stretches over cycles, i.e., $W(\lambda_a, N) = \int_1^{\lambda_a} S(N)\, d\lambda$. The unnotched sample shares the identical geometrical dimensions with the notched sample. By varying the applied stretch of λ_{max}, we acquired the curve of crack extension per cycle dc/dN versus the applied energy release rate G. The fatigue threshold was obtained by linearly extrapolating the curve of dc/dN vs. G to the intercept with the abscissa.

2.4. Results and discussion

2.4.1. Structural characterization of annealed PVA hydrogels.

We first measure the crystallinities of the resultant PVA hydrogels in their dry state by differential scanning calorimetry (DSC). For the chemically-crosslinked and freeze-thawed PVA hydrogels, we use excess chemical crosslinks to fix the amorphous polymer chains before air-drying them in an incubator at 37 °C (see Materials and Methods). The excess chemical crosslinks minimize the formation of further crystalline domains during the air-drying process [312, 313]. As shown in **Figure 2-3a**, both the chemically-crosslinked and freeze-thawed PVA hydrogels show negligible endothermic peaks with measured crystallinities in the dry state of 0.2 wt% and 2.1 wt%, respectively. However, when the freeze-thawed PVA (without excess chemical crosslinks) is dried in air, the crystallinity in the dry state increases to 37.7 wt% (**Figure 2-3a**). The increase of the crystallinity implies that substantially more crystalline domains nucleate during the air-drying process [314]. The crystallinity further increases gradually by increasing the annealing time. When the sample is annealed for 90 min at 100 °C, the crystallinity in the dry state reaches 47.3 wt%. In addition to the crystallinities in the dry state measured from DSC, we further measure the water contents in the fully swollen samples shown in **Figure 2-3b** and calculate the corresponding crystallinities in the swollen state shown in **Figure 2-3c**. It is well-known that the as-prepared dry PVA samples may contain residual water bonded with polymer chains [313]. The amount of residual water can be calculated from the endothermic transition ranging from 60 °C to 180 °C on the DSC curves (**Figure 2-3a**) [315]. The above reported crystallinities in the dry state (without residual water), water contents and crystallinities in the swollen state have been corrected to account for the weights of residual water in the as-prepared dry samples (see Materials and Methods).

To quantify the evolution of crystalline morphology, we measure the average distance between adjacent crystalline domains L through SAXS and the average size of crystalline domains D through WAXS (see Materials and Methods). We first perform SAXS measurements on the samples in the swollen state after subtracting the water background, measuring the scattering intensity I (q) versus the scattering vector q. To identify the location of the peak intensity, we correct the intensity by multiplying the scattering intensity with the scattering vector q [316]. As shown in **Figure 2-3d**, there is no peak in the plot of the corrected intensity Iq versus the scattering

vector q for the freeze-thawed hydrogel, which implies negligible interference between adjacent crystalline domains. For the hydrogel dry-annealed for 0 min, there is a slight shoulder shown in the corrected intensity curve, which indicates stronger interference between adjacent domains. The average distance between adjacent crystalline domains L can be estimated from the critical vector corresponding to the peak intensity q_{max}, following the Bragg expression $L = 2\pi / q_{max}$ [316]. The average distance for the hydrogel dry-annealed for 0 min is estimated to be 21 nm in the swollen state. As the annealing time increases to 90 min, the average distance L decreases to 13 nm in the swollen state (**Figure 2-3g**). As a control case, we also measure SAXS profiles of the hydrogel dry-annealed 90 min in the dry state. As shown in **Figure 2-3f**, the average distance between adjacent crystalline domains in the dry state is around 9 nm, smaller than the distance in the same hydrogel in the swollen state (i.e., 13 nm). This is because swelling of the interstitial amorphous polymer chains increases the distance between adjacent crystalline domains.

We further perform WAXS measurements on the hydrogels in their dry state using Ni-filtered CuKα1 radiation with X-ray wavelength $\lambda = 1.54$ Å. As shown in **Figure 2-3e**, all dry-annealed PVA hydrogels show a strong diffraction peak at 2θ = 19.7 °, which corresponds to the typical reflection plane of $(1\,0\,\bar{1})$ in semi-crystalline PVA [317]. In addition, small peaks at 2θ = 11.5 ° and 23.1 ° are also observed in the hydrogel dry-annealed for 90 min, suggesting a high crystallinity in the hydrogel, which is consistent with the DSC measurement. By identifying the half-width of the maximum diffraction peak β, the average size of crystalline domains D can be approximately calculated using Scherrer's equation [318]

$$D = k\lambda / (\beta \cos\theta) \tag{2-10}$$

where k is a dimensionless shape factor varying with the actual shape of the crystalline domain; λ is the wavelength of X-ray diffraction; and θ is the Bragg angle. Here, β is identified after subtracting the instrumental line broadening; and the dimensionless shape factor k is set as 1, approximating the spherical shape of the crystalline domains [319]. As shown in **Figure 2-3g**, by increasing the annealing time from 0 min to 90 min, the average size of the crystalline domains increases from 3.8 nm to 6.5 nm. This trend is consistent with the decrease of the average distance between adjacent crystalline domains with annealing time, since the growth of the crystalline domains consumes the interstitial amorphous polymer chains.

To further validate the tuning of crystalline domains in the PVA hydrogel with annealing time, we use tapping-mode AFM to obtain phase images of the hydrogels dry-annealed for 0 min and 90 min, respectively. The bright areas in **Figure 2-3h** correspond to the regions with relatively high modulus (mainly crystalline domains), whereas the dark areas represent the regions with relatively low modulus (mainly amorphous domains). As shown in **Figure 2-3h**, the morphology of isolated crystalline domains is observed in the hydrogel dry-annealed for 0 min, while the hydrogel dry-annealed for 90 min shows larger aggregated crystalline domains.

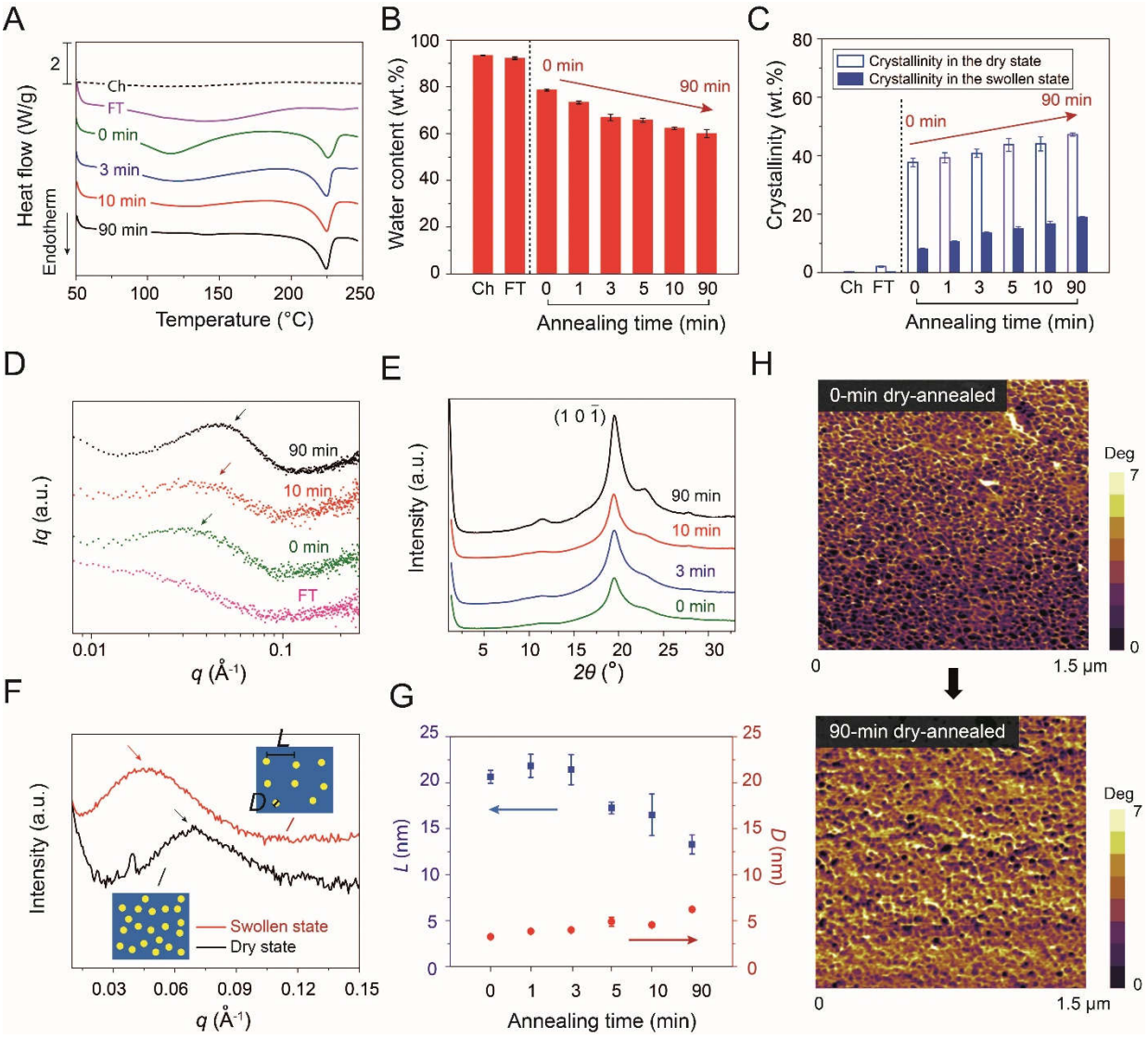

Figure 2-3. Characterization of crystalline domains in PVA hydrogels. (a) Representative DSC thermographs of chemically-crosslinked (Ch), freeze-thawed (FT) and dry-annealed PVA with annealing time of 0, 3, 10, 90 min. (b) Water contents of chemically-crosslinked (Ch), freeze-thawed (FT) and dry-annealed PVA with annealing time of 0, 1, 3, 5, 10, 90 min. (c) Measured crystallinity in the dry and swollen states of Ch, FT and dry-annealed PVA with annealing time of 0, 1, 3, 5, 10, 90 min. (d) Representative SAXS profiles of FT hydrogel and dry-annealed PVA

with annealing time of 0, 10, and 90 min. (e) Representative WAXS profiles of annealed PVA with annealing time of 0, 3, 10, and 90 min. (f) SAXS profiles of 90-min dry-annealed PVA in the dry state and the swollen state. Insets: the distance between adjacent crystalline domains increases due to swelling of amorphous polymer chains. (g) The estimated average distance between adjacent crystalline domains L and average crystalline domain size D of dry-annealed PVA with annealing time of 0, 1, 3, 5, 10, 90 min. (h) AFM phase images of dry-annealed hydrogel with annealing time of 0 min and 90 min. Data in (b), (c) and (g) are means ± SD, n = 3.

2.4.2. Mechanical characterization of annealed PVA hydrogels.

To measure the fatigue threshold of PVA hydrogels, we adopt the single-notch method, which has been widely used in fatigue tests of rubbers [320, 321]. Notably, all fatigue tests in this study are performed on fully-swollen hydrogels immersed in a water bath, to prevent the dehydration-induced crack propagation. We use dogbone-shaped samples and perform cyclic tensile tests on both notched and unnotched samples, which are otherwise the same. The nominal stress versus stretch curves (i.e., S vs. λ) of unnotched samples are obtained over N cycles of applied stretch λ^A. The strain energy density W of the unnotched sample under the N_{th} cycle of applied stretch λ^A can be calculated as

$$W\left(\lambda^A, N\right) = \int_1^{\lambda^A} S d\lambda \tag{2-11}$$

where S and λ are the measured nominal stress and stretch, respectively. Thereafter, the same cyclic stretch λ^A is applied on the notched sample, measuring the evolution of the cut length in undeformed state c with the cycle number N. The applied energy release rate G in the notched sample under the N_{th} cycle of applied stretch λ^A can be calculated as [320, 321]

$$G\left(\lambda^A, N\right) = 2k\left(\lambda^A\right) \cdot c\left(N\right) \cdot W\left(\lambda^A, N\right) \tag{2-12}$$

where k is a slowly varying function of the applied stretch expressed as $k = 3/\sqrt{\lambda^A}$, c the current crack length at undeformed configuration, and W the strain energy density measured in the unnotched sample (**Equation 2-11**). By systematically varying the applied stretch λ^A, we can obtain a plot of crack extension per cycle versus the applied energy release rate (i.e., dc/dN vs. G). By linearly extrapolating the curve of dc/dN vs. G to the intercept with the abscissa, we can approximately obtain the critical energy release rate G_c, below which the fatigue crack will not propogate under infinite cycles of loads. By definition, the fatigue threshold Γ_0 is equal to the critical energy release rate G_c. To validate that this extrapolated value G_c is indeed the fatigue

threshold Γ_0, we further apply G_c to the notched sample over 30,000 cycles (to approximate infinite cycles of loads) and observe no crack extension (**Figure 2-4h**). In addition, we also measure the fatigue thresholds using the pure-shear test to validate the results from the single-notch test[124, 293].

For cyclic tensile tests on unnotched samples (**Figure 2-4a,b**), both chemically-crosslinked PVA and freeze-thawed PVA show negligible Mullins effect, and their S vs. λ curves reach steady states after only a few cycles (i.e., 10 for chemically-crosslinked PVA at an applied stretch of 1.6, and 200 for freeze-thawed PVA at an applied stretch of 2.2). On the other hand, the dry-annealed PVA hydrogels exhibit a more significant Mullins effect, due to mechanical dissipation caused by melting and reorientation of crystalline domains [316]. As the stretch further increases, the crystalline domains may transform into aligned fibrils along the loading direction [316]. The energy required to damage the crystalline domains and fibrils is much higher than that to fracture a single layer of the same polymer in amorphous state. The hydrogel dry-annealed 90 min reaches steady state after 1,000 cycles of applied stretches of $\lambda^A = 2$ (**Figure 2-4c**). Despite the Mullins effect, the steady-state maximum nominal stress of the hydrogel dry-annealed for 90 min is much higher than that of both the chemically-crosslinked PVA and the freeze-thawed PVA at the same applied stretch of $\lambda^A = 2$ (e.g., 2.3 MPa for hydrogel dry-annealed 90 min, 15 kPa for chemically-crosslinked PVA, and 3 kPa for freeze-thawed PVA in **Figure 2-4a-c**).

For cyclic tensile tests on notched samples, a pre-crack is cut using a razor blade with tip radius of around 200 μm and initial crack length around 1 mm, smaller than one-fifth of the width of the sample [321]. A digital microscope (AM4815ZT, Dino-Lite, resolution 20 μm pixel^{-1}) is used to record the cut length under cyclic loads. We first apply cyclic loads with a small applied stretch (i.e., $\lambda^A = 1.3$) on a notched sample. If the crack remains quasi-stationary with crack extension per cycle (dc/dN) smaller than 20 nm cycle^{-1} (i.e., no detectable crack extension in 1,000 cycles), the applied cyclic stretch is increased by the increment of $\Delta\lambda^A = 0.1$ for other notched samples until crack propagation greater than 20 nm cycle^{-1} is captured. As shown in **Figure 2-4d,e**, the fatigue thresholds of chemically-crosslinked PVA and freeze-thawed PVA are measured to be 10 J m^{-2} and 23 J m^{-2}, respectively. The fatigue threshold for the hydrogel dry-annealed 0 min increases to 110 J m^{-2}. As the annealing time increases, the fatigue threshold further increases. In particular, for the hydrogel dry-annealed 90 min, the fatigue threshold can achieve 1000 J m^{-2} (**Figure 2-4f**). The measured fatigue threshold of the hydrogel dry-annealed 90 min

from the pure-shear test is 918 J m^{-2}. The dependence of fatigue threshold on the crystallinity is summarized in **Figure 2-4g**. The fatigue theshold increases with the crystallinity and demonstrates a sharp jump when the crystallinity in the swollen state reaches approximate 15 wt%.

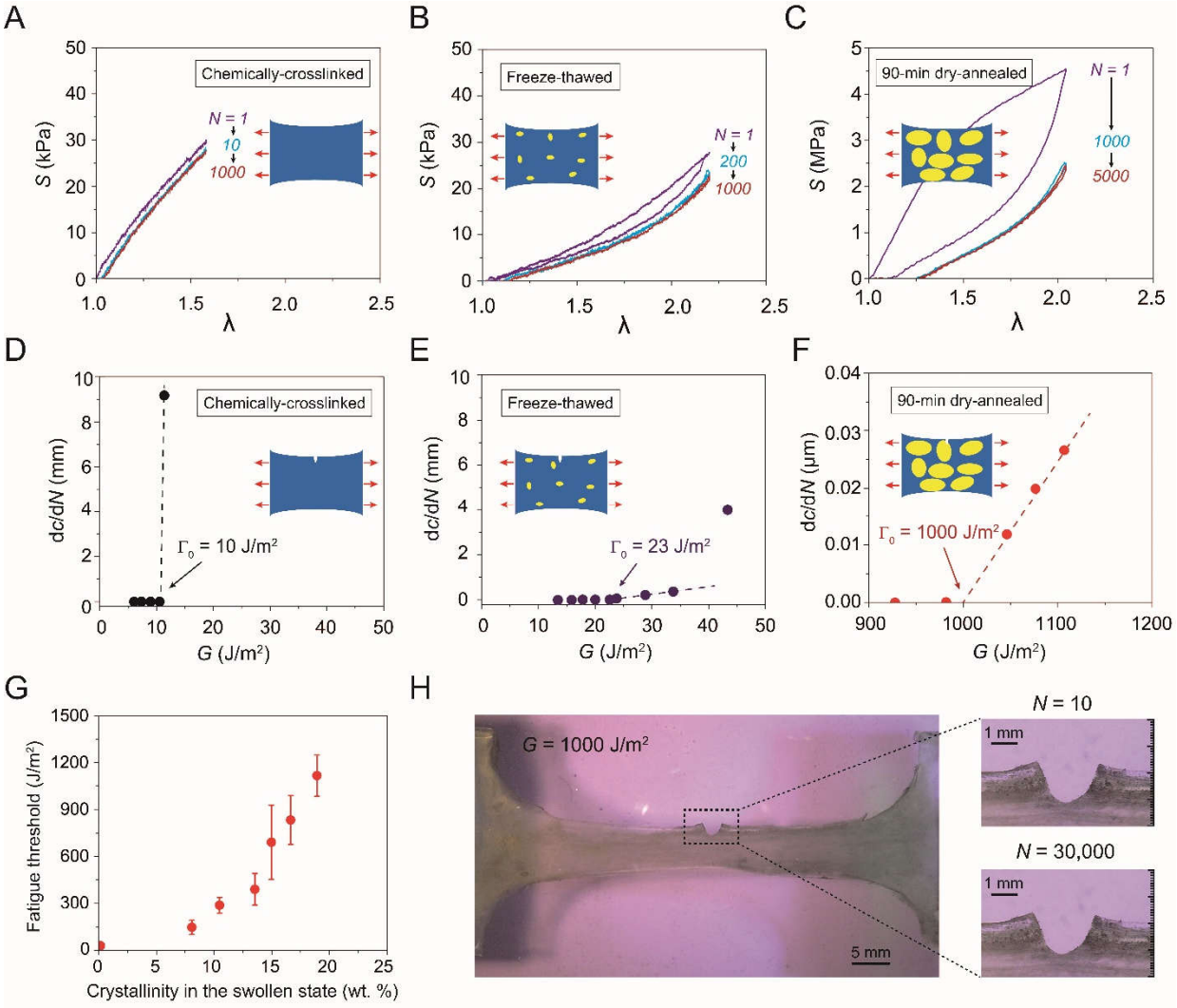

Figure 2-4. Measurement of fatigue thresholds of PVA hydrogels. Nominal stress S vs. stretch λ curves over cyclic loads for (a) chemically-crosslinked hydrogel at an applied stretch of $\lambda^A = 1.6$, (b) freeze-thawed hydrogel at an applied stretch of $\lambda^A = 2.2$, and (c) 90-min dry-annealed hydrogel at an applied stretch of $\lambda^A = 2.0$. Crack extension per cycle dc/dN vs. applied energy release rate G for (d) chemically-crosslinked hydrogel, (e) freeze-thawed hydrogel, and (f) dry-annealed hydrogel with annealing time of 90 min. (g) The fatigue threshold increases with the crystallinity of the hydrogel in the swollen state. (h) Validation of fatigue threshold as high as 1000 J m^{-2} in 90-min dry-annealed hydrogel using the single-notch test. Data in (g) are means ± SD, n = 3. Scale bars are 5 mm in (h, left) and 1 mm for the right images in (h, right).

In addition to fatigue tests, we also measure the nominal stress versus stretch curves of all hydrogels to obtain their Young's moduli and tensile strengths[124]. As shown in **Figure 2-5a,b**,

both the Young's modulus and tensile strength increase with the hydrogels' crystallinity and show dramatic enhancements when the crystallinity in the swollen state reaches approximate 15 wt% [322]. This sharp jump in Young's modulus and tensile strength is consistent with the dramatic increase of fatigue threshold of the hydrogel at approximate 15 wt% crystallinity in the swollen state (**Figure 2-4g**). Whereas annealing the whole PVA hydrogel can significiantly enhance its fatigue threshold, the annealing treatment also increases the modulus and decreases the water content of the hydrogel (**Figure 2-5c**).

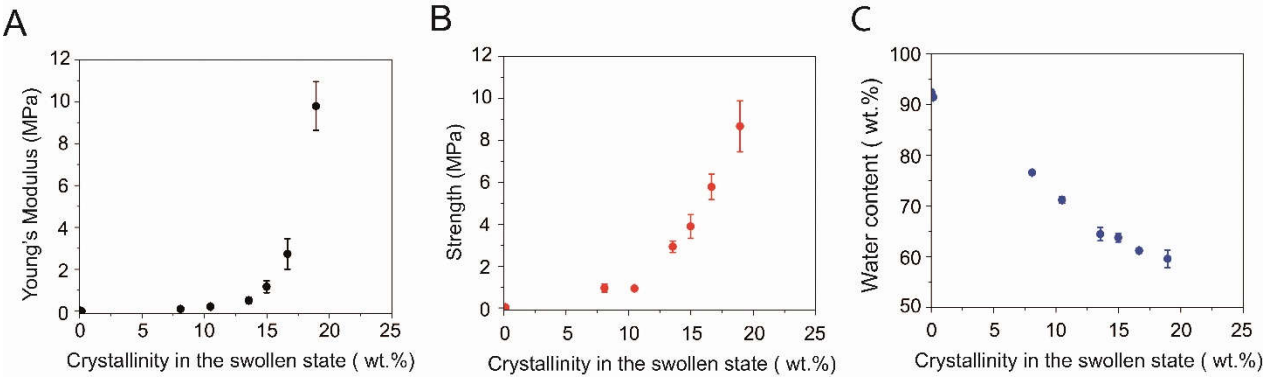

Figure 2-5. Young's moduli, tensile strengths and water contents of PVA hydrogels. (a) Young's modulus versus crystallinity in the swollen state. (b) Tensile strength versus crystallinity in the swollen state. (c) Water content versus crystallinity in the swollen state. Data in (a), (b) and (c) are means ± SD, n = 3.

2.4.3. Structural characterization of mechanically trained PVA hydrogels

We first use the confocal laser scanning microscopy to visualize the nanofibers in the pristine freeze-thawed PVA hydrogel. Fluorochrome is conjugated to the PVA macromolecules by immersing the freeze-thawed hydrogels in a reactive dye solution [323]. With the conjugated fluorochromes, the PVA-rich phases are visible in green in the form of randomly-distributed nanofibers (**Figure 2-6a**), while regions with relatively low concentrations of PVA polymers (i.e., water-rich phase between adjacent nanofibers) are dark.

We next show that the freeze-thawed PVA hydrogel can form aligned nanofibrous structures by repeated pre-stretches in a water bath (**Figure 2-6a**). The confocal images of the pre-stretched PVA hydrogel in **Figure 2-6a** confirm that the randomly-distributed nanofibers gradually reorient and align towards the direction of the applied pre-stretches. The alignment of nanofibers reaches a steady state after sufficient cycles of pre-stretches (i.e., 1000 cycles of pre-stretches of 4.6). The alignment of the nanofibers in the pre-stretched PVA hydrogels is also validated through SEM images (**Figure 2-6c**) and AFM phase images (**Figure 2-6d**). SAXS patterns (**Figure 2-6b**)

further reveal that the nanocrystalline domains in nanofibers have been reoriented during the pre-stretches. In addition, the measured diameters of the nanofibers range from ~200 nm to ~1 μm (**Figure 2-6a,c**).

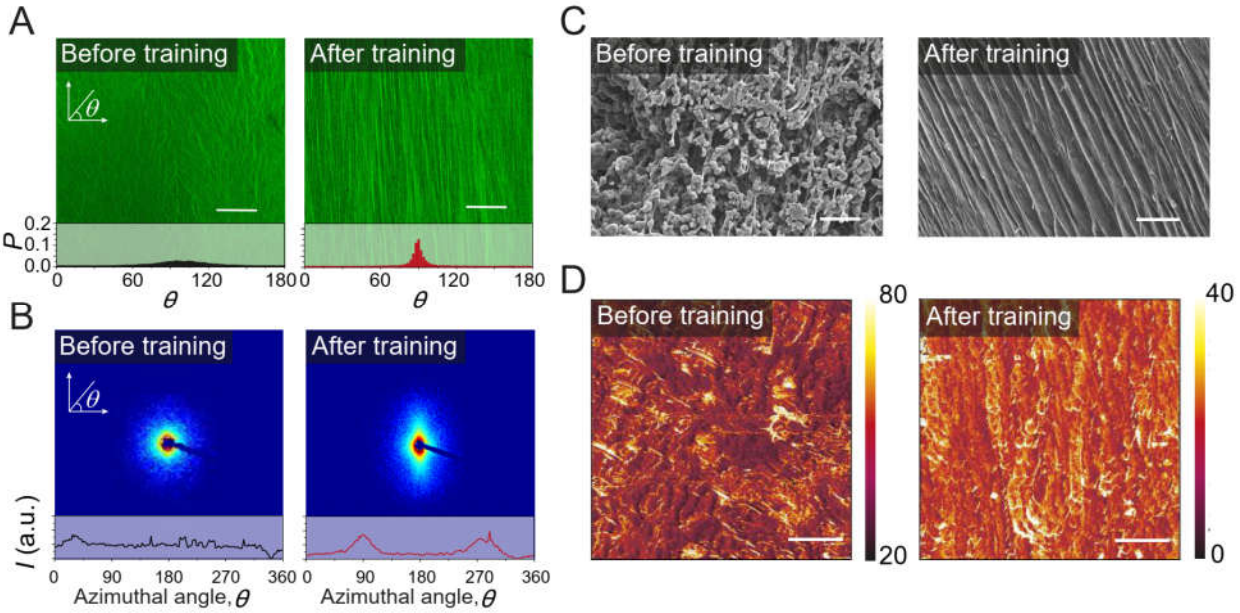

Figure 2-6. Microstructures of PVA hydrogels before and after mechanical training. (a) Confocal images and corresponding histograms of a hydrogel with randomly-oriented nanofibers before training (i.e., freeze-thawed PVA) and a hydrogel with aligned nanofibers after training (i.e., pre-stretched PVA). P in the histograms represents the probability of nanofibers at each aligned direction θ. (b) SAXS patterns and corresponding scattering intensity I versus azimuthal angle θ curve of a hydrogel with randomly-oriented nanofibers before training (i.e., freeze-thawed PVA), and hydrogel with aligned nanofibers after training (i.e., pre-stretched PVA). a.u., arbitrary units. (c) SEM images of a hydrogel with randomly-oriented nanofibers before training (i.e., freeze-thawed PVA) and a hydrogel with aligned nanofibers after training (i.e., pre-stretched PVA). (d) AFM phase images of a hydrogel with randomly-oriented nanofibers before training (i.e., freeze-thawed PVA) and a hydrogel with aligned nanofibers after training (i.e., pre-stretched PVA). Scale bars are 50 μm in (a), 20 μm in (c, left) 10 μm for right image in (c, right), and 100 nm in (d).

Existing approaches to introduce ordered nanocrystalline domains and aligned structures in hydrogels include cold-drawing [324], pre-stretching in air [325], and constrained air-drying [326], which fail to retain their original high water contents, due to the formation of additional excessive nanocrystalline domains. By contrast, the pre-stretched PVA hydrogel obtained from our strategy can still maintain a high water content of 84 wt% (**Figure 2-7c**), close to the pristine freeze-thawed PVA samples (88 wt%). The differential scanning calorimetry (DSC) results further show that the crystallinity in the swollen state of the pre-stretched PVA hydrogel is only 2.8 wt%, slightly higher than the pristine freeze-thawed PVA hydrogel (1.8 wt%) (**Figure 2-7c**). The slightly

increased crystallinity could be attributed to the newly-formed nanocrystalline domains during the nanofibrillar alignments under cyclic pre-stretches [327]. Both high water content and low crystallinity in our pre-stretched PVA hydrogel indicate that our strategy could substantially suppress the undesirable excessive crystallization while maintaining water contents and compliances of the hydrogels.

2.4.4. Mechanical characterization of mechanically trained PVA hydrogels

We further demonstrate the combinational muscle-like mechanical properties in the pre-stretched PVA hydrogel (**Figure 2-7**). At small stretches, the pre-stretched PVA hydrogel demonstrates a low Young's modulus along directions both parallel (210 kPa) and perpendicular (140 kPa) to the aligned nanofibers, similar to the pristine freeze-thawed PVA hydrogels (100 kPa) (**Figure 2-7a,d**). At high stretches, the pre-stretched PVA hydrogel stiffens drastically parallel to the aligned nanofibers, exhibiting a J-shaped stress versus stretch curve, similar to that of skeletal muscles [328]. In addition, the pre-stretched PVA hydrogel shows an extremely high ultimate nominal tensile strength of 5.2 MPa parallel to the aligned nanofibers, which is 4.3 times of the pristine freeze-thawed hydrogel's strength (1.2 MPa) and 26 times of the chemically cross-linked hydrogel's strength (0.2 MPa) (**Figure 2-7a,d**). The ultimate nominal tensile strength of the pre-stretched PVA hydrogel perpendicular to nanofibers is measured to be 1.1 MPa, close to the value of the pristine freeze-thawed hydrogel (i.e., 1.2 MPa). The fatigue threshold of the pre-stretched PVA hydrogel measured along the aligned nanofibers reaches a record-high value of 1,250 J m^{-2} (**Figure 2-7b**), orders of magnitude higher than those of existing tough hydrogels (10~100 J m^{-2}) [293, 295, 329]. By contrast, the fatigue threshold perpendicular to the aligned nanofibers is 233 J m^{-2}, which is on the same order as that of the pristine freeze-thawed PVA hydrogel (i.e., 310 J m^{-2}, **Figure 2-7d**), but still much larger than that of the chemically cross-linked PVA hydrogel (i.e., 10 J m^{-2}, **Figure 2-7d**).

To compare our results with existing hydrogels and biological tissues, we summarize the nominal tensile strengths, Young's moduli, fatigue thresholds, and water contents of various tough hydrogels [28, 29, 124, 289, 326, 330-333] and biological tissues [328] in **Figure 2-7e,f**. The strength-modulus ratios S/E of existing tough hydrogels such as PAAm-alginate [29], PVA-PAAm [332], dry annealed PVA [124], freeze-thawed PVA [334], polyampholyte hydrogels [289], fiber reinforced hydrogel composites [330, 335], wood hydrogels [331], and constrained air-drying

hydrogels [326] are in the range of 0.1 to 10 (**Figure 2-7e**). Remarkably, the strength-modulus ratio S/E of the pre-stretched PVA hydrogel is as high as 50, since the high strength of the pre-stretched PVA hydrogel is accompanied by its low Young's modulus.

In addition to the challenge in designing synthetic hydrogels with superior compliances and high strengths, the combinational properties of high fatigue threshold and high water content have not been achieved in existing hydrogels (**Figure 2-7f)**. By following our strategy, the fatigue threshold of the pre-stretched PVA hydrogel can achieve a high value of 1,250 J m^{-2} along with a high water content of 84 wt%, outperforming existing hydrogels and biological tissues.

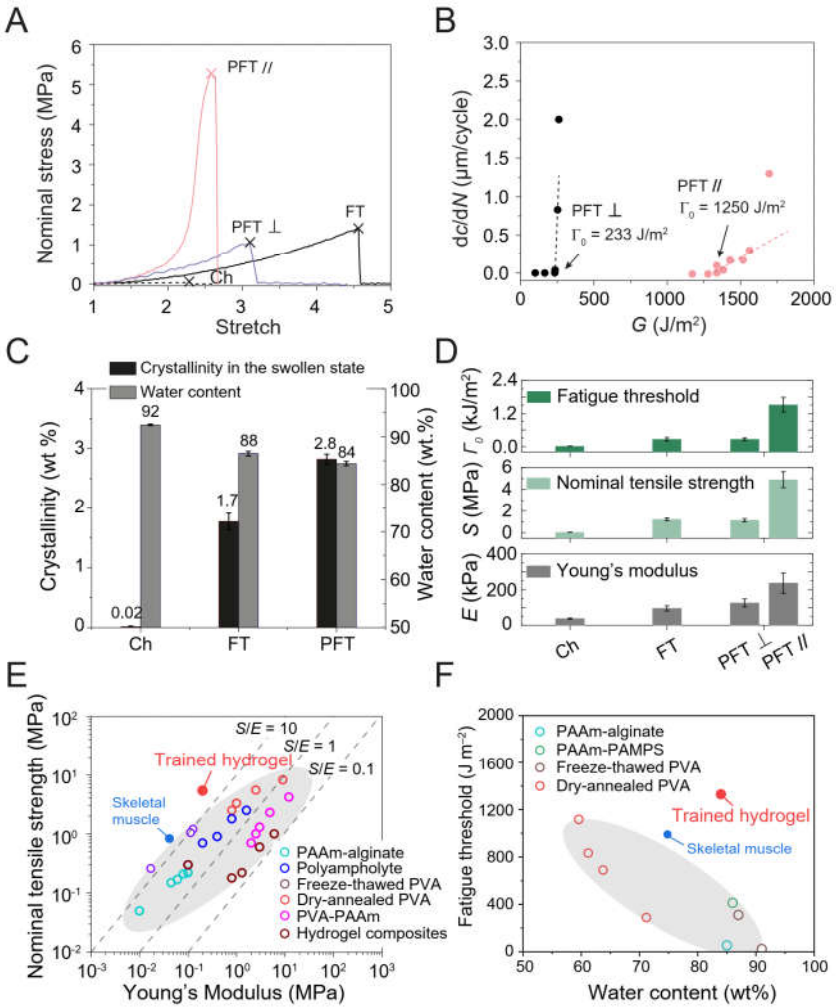

Figure 2-7. Mechanical properties of PVA hydrogels before and after mechanical training. (a) Nominal stress versus stretch curves of chemically cross-linked (Ch), freeze-thawed (FT), and pre-stretched PVA hydrogels parallel to (PFT //) and perpendicular to (PFT ⊥) nanofibers. The X mark indicates the point of fracture. (b) Crack extension per cycle dc/dN versus applied energy release rate G of pre-stretched PVA hydrogels parallel to (PFT //) and perpendicular to (PFT ⊥) nanofibers.

(c) Summarized water contents and crystallinities in the swollen state of chemically cross-linked PVA (Ch), freeze-thawed PVA (FT), and pre-stretched PVA (PFT). (d) Summarized Young's moduli E, ultimate nominal tensile strengths S, and fatigue thresholds Γ_0 of chemically cross-linked (Ch), freeze-thawed (FT) and pre-stretched PVA hydrogels parallel to (PFT //) and perpendicular to (PFT ⊥) nanofibers. (e) Comparison chart in the plot of nominal tensile strength and Young's modulus among tough hydrogels (e.g., PAAm-alginate [29], polyampholyte [289], freeze-thawed PVA [124], dry-annealed PVA [124], PVA-PAAm [332], and hydrogel composites [335]), biological tissues (e.g., skeletal muscle [328, 336]) and trained hydrogel (i.e., pre-stretched PVA). The dashed lines denote the linear relation between strength and modulus with strength-modulus ratio S/E of 0.1, 1, and 10. (f) Comparison chart in the plot of fatigue thresholds and water contents among tough hydrogels [329] (e.g., PAAm-alginate, PAAm-PAMPS, freeze-thawed PVA) and nanocrystalline hydrogels (e.g., dry-annealed PVA) [124], biological tissues (e.g., skeletal muscle), and trained hydrogel (i.e., pre-stretched PVA). Data in (c) and (d) are means ± SD, n = 3.

2.4.5. Mechanisms for mechanical properties of mechanically trained PVA hydrogels

In situ SAXS measurements offer insights into the mechanism for the superior compliance of the pre-stretched PVA hydrogel at small deformations (**Figure 2-8a**). The nanocrystalline morphology in the pre-stretched PVA hydrogel (in the swollen state) is investigated by SAXS analysis at the applied stretch of 1, 1.4, 1.8, and 2.2. As shown in **Figure 2-8b,d**, the average distance between neighboring nanocrystalline domains parallel to aligned nanofibers L∥ (i.e., $\theta = 0°$) for the pre-stretched PVA hydrogel at undeformed state (i.e., $\lambda = 1$) is estimated to be 13.2 nm. As the applied stretch increases to 2.2, the average distance between neighboring nanocrystalline domains increases to 15.5 nm (**Figure 2-8d**), which indicates the stretching of interstitial amorphous chains between the adjacent nanocrystalline domains in the nanofibers. Since the stretch of interstitial amorphous chains (e.g., 15.5 nm/13.2 nm) is much lower than the corresponding applied stretch (e.g., 2.2), sliding between nanofibers may also occur during stretching. In comparison, the scattering curves show negligible difference at different stretches perpendicular to the aligned nanofibers L⊥ (i.e., $\theta = 90°$) (**Figure 2-8c**), which implies the average distance between neighboring nanocrystalline domains perpendicular to the aligned nanofibers L⊥ (i.e., $\theta = 90°$) remains constant with negligible lateral contraction as the stretch increases.

We further plot the scattering intensity I versus direction θ to quantify the degree of orientation of nanocrystalline domains during stretching (**Figure 2-8e**). At the undeformed state (i.e., $\lambda = 1$), there are peaks along the pre-stretched direction (i.e., $\theta = 0°$), implying that the orientation of nanocrystalline domains along the pre-stretched direction exists in the undeformed sample. As the applied stretch increases, the peaks along the pre-stretched direction (i.e., $\theta = 0°$)

become more pronounced, indicating that the applied stretch can drive additional orientation of nanocrystalline domains. Overall, the stretch of interstitial amorphous chains, orientation of nanocrystalline domains and sliding between nanofibers account for the superior compliance of the pre-stretched PVA hydrogel at moderate deformations along the aligned nanofibers.

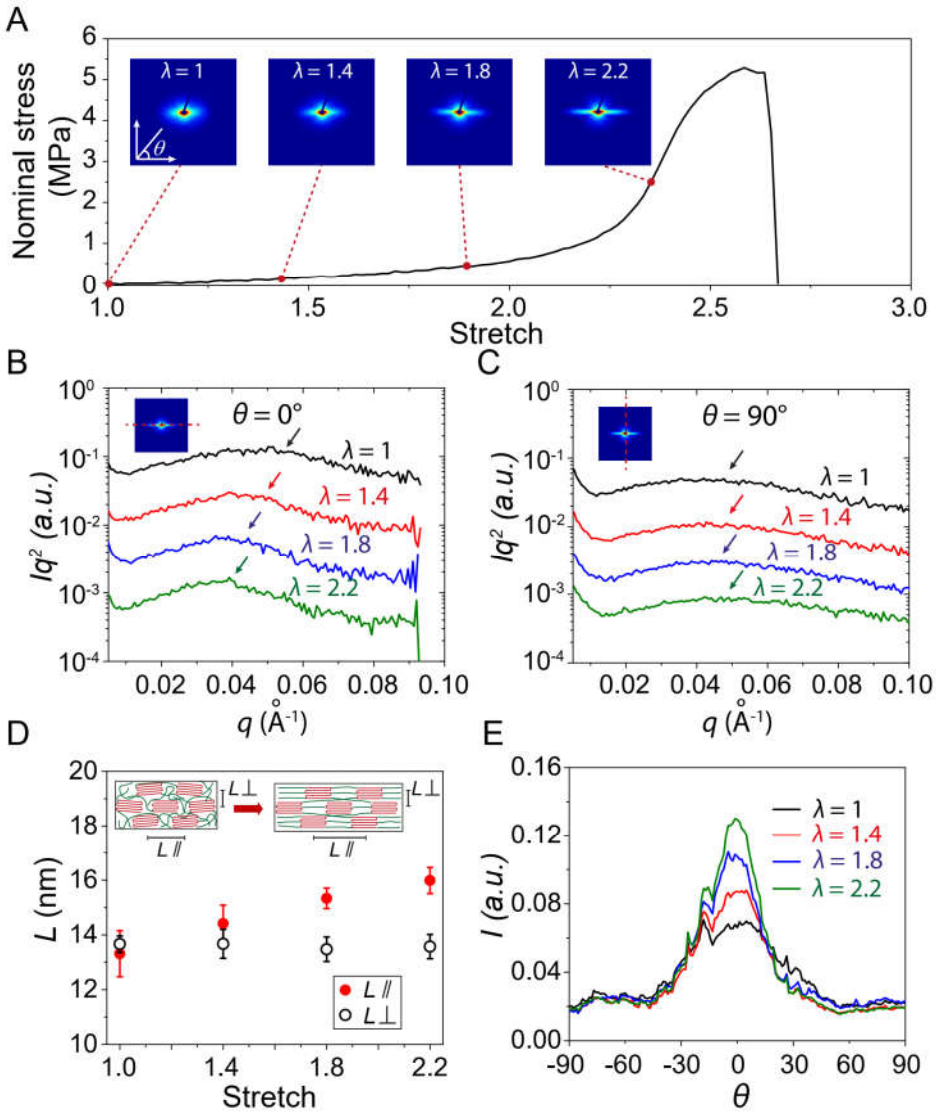

Figure 2-8. Mechanisms for high compliances of pre-stretched PVA hydrogels with aligned nanofibers. (a) Nominal stress versus stretch curve of pre-stretched PVA hydrogel with aligned nanofibers and corresponding SAXS pattern at the stretch of 1, 1.4, 1.8, and 2.2. (b) The corrected scattering intensity Iq^2 versus vector q parallel to nanofibers (i.e., $\theta = 0°$) of pre-stretched PVA hydrogel at the stretch of 1, 1.4, 1.8, and 2.2. Inset: a scattering pattern showing the direction of interest (dashed red line) is parallel to nanofibers. (c) The corrected scattering intensity Iq^2 versus vector q perpendicular to nanofibers (i.e., $\theta = 90°$) of pre-stretched PVA hydrogel at the stretch of 1, 1.4, 1.8, and 2.2. Inset: a scattering pattern showing the direction of interest (dashed red line) is perpendicular to nanofibers. (d) Calculated average distance between adjacent nanocrystalline

domains of pre-stretched PVA hydrogel parallel to nanofibers L∥ (i.e., θ = 0°) and perpendicular to nanofibers L⊥ (i.e., θ = 90°) at the stretch of 1, 1.4, 1.8, and 2.2. (e) The measured scattering intensity I vs. Azimuthal angle θ curves of pre-stretched PVA hydrogel at the stretch of 1, 1.4, 1.8, and 2.2. Data in (d) are means ± SD, n = 3.

Furthermore, the high compliances of the pristine freeze-thawed PVA hydrogel and the pre-stretched PVA hydrogel stretched perpendicularly to the aligned nanofibers can be attributed to the orientation of randomly-distributed nanofibers and the stretching of amorphous polymer chains between adjacent nanofibers, respectively.

In situ confocal laser scanning microscopy further explains the mechanism for the high fatigue threshold of the pre-stretched PVA hydrogel. As shown in **Figure 2-9a,b**, the aligned nanofibers are perpendicular to the crack path and pin the crack due to the high strength of the nanofibers. There is no observable crack propagation at the applied stretch of 2.4. As the applied stretch further increases to 2.6, the nanofibers at the crack tip are pulled out from the hydrogel but still bridge the crack tip. As the crack propagates, the rupture of the nanofibers requires a much higher energy per unit area than fracturing the corresponding amorphous polymer chains, giving rise to a much higher fatigue threshold (1250 J m^{-2}) than that of the amorphous polymer networks (10 J m^{-2}). Notably, the crack pinned by the aligned nanofibers does not branch or tilt under high static and cyclic loads (e.g., **Figure 2-9b**), assuring the hydrogel's high fatigue threshold. By contrast, crack branching and tilting has been observed in hydrogels reinforced by microscale phase separation [304] and in elastomers reinforced by macroscale fibers [309]. It will be interesting to study the effects of the reinforcements across different length scales in future.

When the crack is parallel to the aligned nanofibers, the crack begins to propagate in between neighboring nanofibers at the applied stretch of 1.5, fracturing interstitial amorphous chains between the adjacent nanofibers (**Figure 2-9c,d**). Similarly, in freeze-thawed PVA hydrogel, the initially randomly-oriented nanofibers gradually align parallel to the crack contour with the increase of the applied stretch, followed by fracturing interstitial amorphous chains (**Figure 2-9e,f**). In addition, due to the very long amorphous chains between the adjacent nanofibers [149], the fatigue thresholds of the pristine freeze-thawed PVA hydrogel and the pre-stretched PVA hydrogel with a crack along the aligned nanofibers are still moderately high (310 J m^{-2} and 233 J m^{-2}, respectively).

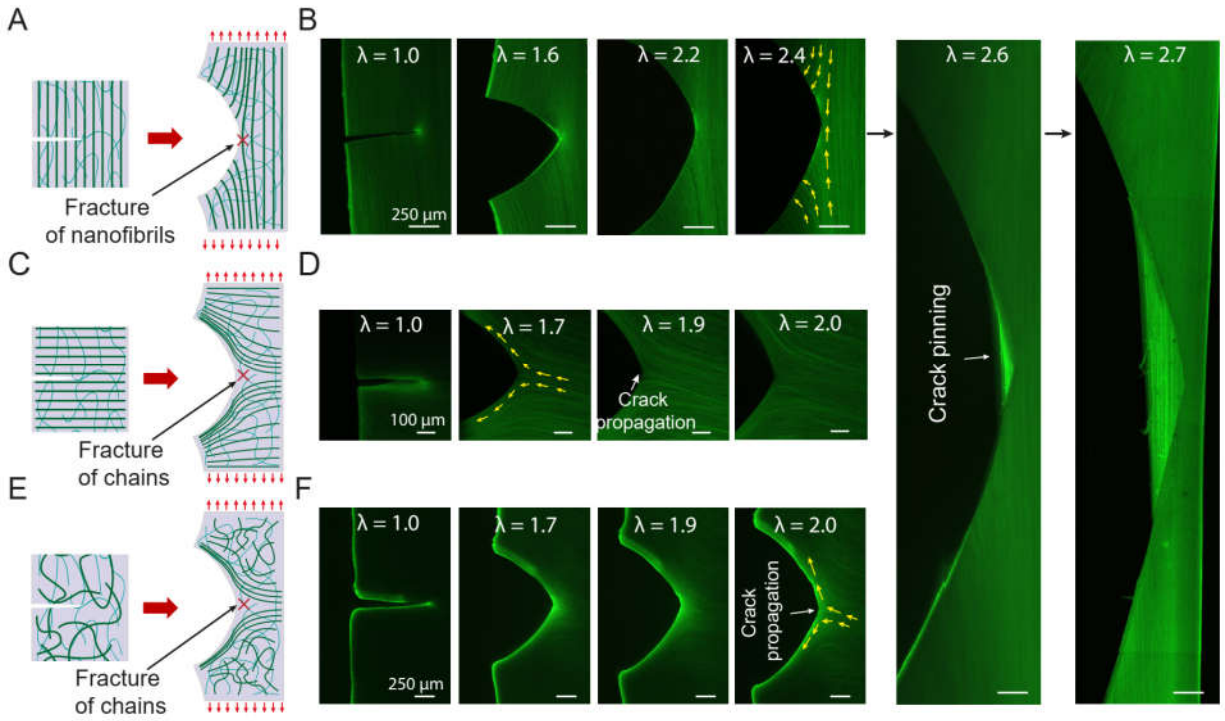

Figure 2-9. Mechanisms for high fatigue thresholds of pre-stretched PVA hydrogels with aligned nanofibers. Schematic illustration of nanofibril morphology in (a) notched pre-stretched PVA hydrogel where crack is perpendicular to the longitudinal direction of nanofibers, (c) notched pre-stretched PVA hydrogel where crack is parallel to the longitudinal direction of nanofibers, and (e) freeze-thawed PVA hydrogel. Corresponding confocal images of notched samples under different stretches for (b) pre-stretched PVA hydrogel where crack is perpendicular to the longitudinal direction of nanofibers, (d) pre-stretched PVA hydrogel where crack is parallel to the longitudinal direction of nanofibers, and (f) freeze-thawed PVA hydrogel. The yellow arrows in confocal images indicate the direction of aligned nanofibers around crack tip. Scale bars are 250 μm in (b), 100 μm in (d), and 250 μm in (f).

2.5. Conclusions

We have discussed the design principles and implementation strategies for tough, fatigue-resistant hydrogels. We have demonstrated that the toughness of hydrogels can be enhanced by building dissipation into stretchy polymer networks, and the fatigue threshold of hydrogels can be greatly enhanced by pinning fatigue cracks with intrinsically high-energy phases. Inspired by the architectures of biological tissues, different structures of PVA hydrogels were manufactured and used as a model material to validate the design principles for anti-fatigue-fracture hydrogels. Three types of fatigue-resistant hydrogels, including annealed PVA hydrogels with nanocrystalline domains [124], mechanically trained PVA hydrogels with aligned nanofibers [288], bouligand-

type PVA hydrogels with helicoidally stacked nanofibers [311] exhibit the fatigue threshold of 1,000 J m^{-2}, 1,250 J m^{-2}, and 770 J m^{-2}, respectively.

The capability to enhance the fracture-resistance and fatigue-resistance of synthetic hydrogels makes a number of future research directions and applications possible. For example, anti-fatigue hydrogels can be used for hydrogel-based gastric retentive devices and implantable tissue replacements of menisci, intervertebral disks, and cartilages, which require long-term mechanical robustness when interacting with the human body. In Chapter 4, we adopt tough hydrogels in living devices. In Chapters 5-7, we use fatigue-resistant hydrogels for ingestible devices and optical fibers.

Chapter 3

Fatigue-resistant hydrogel adhesions

The research presented in this chapter has been published in:

- Ji Liu†, Shaoting Lin†, **Xinyue Liu†**, Zhao Qin†, Yueying Yang, Jianfeng Zang, Xuanhe Zhao, Fatigue-resistant adhesion of hydrogels. Nature Communications. 11, 2020.
- Xuanhe Zhao, Xiaoyu Chen†, Hyunwoo Yuk†, Shaoting Lin†, **Xinyue Liu**, German Parada. Soft materials by design: Unconventional polymer networks give extreme properties. Chemical Reviews. 121, 2021.
- Yan Yu†, Hyunwoo Yuk†, German A. Parada†, You Wu, **Xinyue Liu**, Christoph S. Nabzdyk, Kamal Youcef-Toumi, Jianfeng Zang, and Xuanhe Zhao, Multifunctional "hydrogel skins" on diverse polymers with arbitrary shapes. Advanced Materials. 31, 2019.
- Hyunwoo Yuk, Teng Zhang, German Alberto Parada, **Xinyue Liu**, and Xuanhe Zhao, Skin-inspired hydrogel-elastomer hybrids with robust interfaces and functional microstructures. Nature Communications. 7, 2016.
- Shaoting Lin, Yueying Yang†, Jiahua Ni†, Yoichiro Tsurimaki†, **Xinyue Liu**, Yaodong Tu, Baoyang Lu, Jiawei Zhou, Jianfeng Zang, Xuanhe Zhao, and Gang Chen. Stretchable anti-fogging wrap for diverse transparent surfaces. Advanced Functional Materials. Under revision.

3.1. Introduction

In nature, the adhesions of tendons, ligaments, and cartilages to bones are commonly achieved through a transitional interface (**Figure 3-1a**), from the uncalcified collagen nanofibrils (i) to the calcified collagen nanofibrils (ii) to the bones (iii) (**Figure 3-1b**) [337]. At the interface (ii), nanostructured composites of aligned collagen nanofibrils and ordered hydroxyapatite nanocrystals [337-342] are anchored on the bones, leading to fatigue-resistant adhesions of tendons, ligaments, and cartilages to the bones (**Figure 3-1b**) [341]. For example, the cartilage-bone

interface in the human knee joint can sustain compressive stresses of 1 MPa along with an interfacial toughness around 800 J m^{-2} over 1 million cycles of loading per year [266, 343, 344].

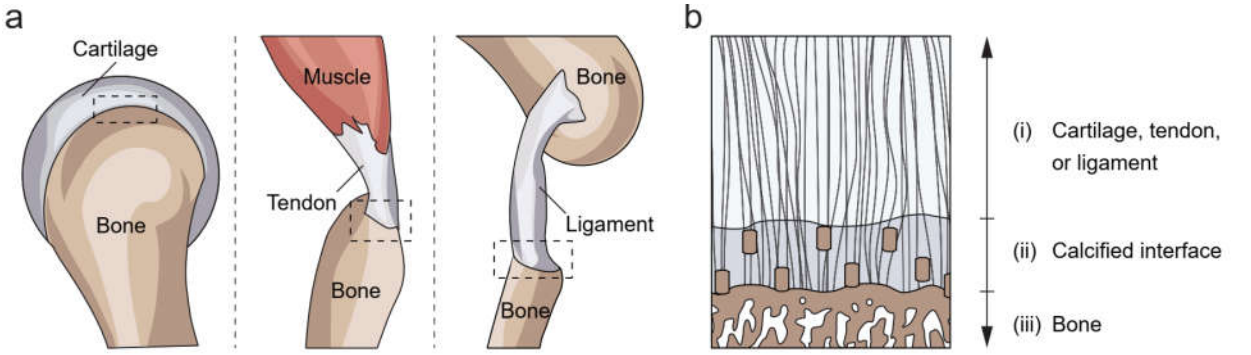

Figure 3-1. Fatigue-resistant hydrogel adhesion in nature. (a) Schematic illustration of the fatigue-resistant adhesions between soft connective tissues (cartilage, tendon, ligament) and bones. (b) The transitional interface from uncalcified collagen nanofibrils (i) to calcified nanofibers (ii) to the bone (iii). The nanostructured composites of aligned collagen nanofibrils and ordered hydroxyapatite nanocrystals contribute to the fatigue-resistant adhesions of the cartilages, tendons, and ligaments to the bones.

On the other hand, hybrid combinations of hydrogels and solid materials, including metals, ceramics, silicon, elastomers, and polymers, are used in areas as diverse as biomedicine [10, 275], adaptive and responsive materials [345], antifouling [346], actuators for optics and fluidics [47, 99], soft electronics [96] and machines [347], as discussed in Chapter 1.

Although hydrogels with extraordinary physical properties have been recently developed [28, 29, 289, 348], the weak and brittle bonding between hydrogels and solid materials often severely hampers their integration and function in devices and systems. Whereas intense efforts have been devoted to the development of tough hydrogel–solid interfaces, previous works are generally limited to special cases with porous solid substrates [153]. Robust adhesion of dry elastomers to non-porous solids has been achieved [349, 350], but such adhesion is not applicable to hydrogels that contain significant amounts of water [351]. The need for general strategies and practical methods for the design and fabrication of tough hydrogel bonding to diverse solid materials has remained a central challenge for the field. Tough adhesions between hydrogels and engineering materials have been achieved by covalently anchoring polymer chains of tough hydrogels on solid surfaces [30]. When the hydrogel is peeled from the solid under a single cycle of the mechanical load, the energy required for fracturing anchored polymer chains and the energy dissipated in deforming the bulk hydrogel synergistically give an interfacial toughness over 1,000 J m^{-2}. However, such tough hydrogel adhesion suffers from fatigue failure over multiple cycles of

mechanical loads, in which the effect of bulk dissipation has been depleted. The resultant interfacial fatigue threshold (i.e., the minimal fracture energy at which interfacial crack propagation occurs under cyclic loads) is equal to the energy for fracturing a single layer of bonded amorphous polymer chains, on the order of 1–100 J m^{-2} [149, 288, 293, 306, 352, 353].

In this chapter, we will introduce the structural design principles for synthetic hydrogel adhesions to achieve resistance to a single cycle (high interfacial toughness) and multiple cycles of mechanical loads (high interfacial fatigue threshold). Then, we will focus on the implementation strategy for fatigue-resistant adhesion of hydrogels, that is, anchoring ordered nanostructures (e.g., nanocrystalline domains) on engineering materials. We will describe the manufacturing, characterization, and deployment of the fatigue-resistant hydrogel adhesions. Specifically, we reveal how the hydrogel-substrate interface is able to resist crack propagation in the nano- and molecular scale.

3.2. Design principles

3.2.1. Tough adhesion: integrate tough dissipative hydrogels and strong interfacial linkages

Interfacial toughness. Interfacial toughness, or so-called practical work of adhesion, has been commonly used to characterize the capability of the interface of two adhered materials to resist fracture under mechanical loads. One common definition for the interfacial toughness between two adhered materials is the energy required to propagate a crack along the interface or in either material over a unit area measured in the undeformed state of the materials (**Figure 3-2a**)[354]. Depending on whether the crack propagates along the interface or in either material, the failure mode is called an adhesive failure or cohesive failure, respectively (**Figure 3-2a**). Quantitatively, the interfacial toughness Γ^{inter} can be expressed as,

$$\Gamma^{\text{inter}} = G_c = -\frac{dU}{dA} \tag{4-1}$$

where U is the total potential energy of the system, A is the crack area measured in the undeformed state, and G_c is the critical energy release rate that drives interfacial crack propagation. According to **Equation 3-1**, the unit for the interfacial toughness is joule per meter squared (i.e., J m^{-2}).

The interfacial toughness of soft materials such as elastomers and hydrogels has been measured with many experimental methods such as the 90-degree peeling test, the T-peeling test and the lap-shear test[296, 354]. For example, in the 90-degree peeling test, a layer of a hydrogel

with thickness T, width W and length L (L >> W >> T) is bonded on a substrate, and a notch is introduced on the interface along the length direction (**Figure 3-2a**). The detached part of the hydrogel is further peeled off the substrate, while maintaining vertical to the substrate (**Figure 3-2a**). The measured force reaches a plateau $F_{plateau}$ as the peeling process enters the steady state, and the interfacial toughness is determined by dividing the plateau force $F_{plateau}$ by the width of the hydrogel sheet W, i.e.,

$$\Gamma^{\text{inter}} = F_{plateau} / W \tag{5-2}$$

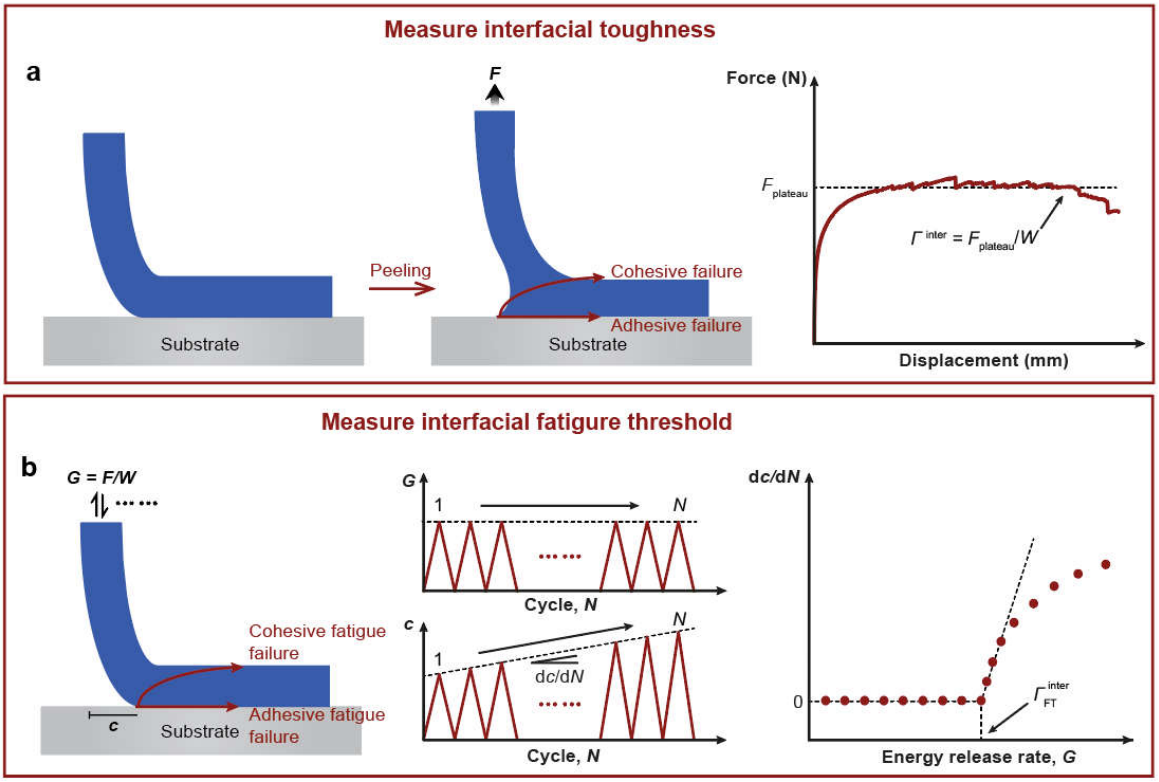

Figure 3-2. Definition and measurement of interfacial toughness and interfacial fatigue threshold. (a) Definition of interfacial toughness, and the 90-degree peeling test to measure the interfacial toughness. F is the peeling force, $F_{plateau}$ is the plateau peeling force, and W is the width of the sample. The interfacial toughness can be calculated as $\Gamma^{inter} = F_{plateau}/W$ based on the values of $F_{plateau}$ and W measured in the 90-degree peeling test. (b) Definition of interfacial fatigue threshold, and the 90-degree cyclic peeling test to measure the interfacial fatigue threshold. F is the applied peeling force, W is the width of the sample, G is the energy release rate, c is the crack length, and N is the cycle number. The interfacial fatigue threshold Γ_{FT}^{inter} is determined by intersecting the curve of dc/dN vs G with the G axis.

Design principle. If a hydrogel with a conventional polymer network is strongly bonded on a substrate (e.g., via covalent bonds), the interfacial toughness is on the level of the hydrogel's fracture toughness or intrinsic fracture energy Γ_0. This is because the fracture toughness of the hydrogel poses an upper limit for the interfacial toughness, since the cohesive failure mode may occur (**Figure 3-3a**)[45]. Therefore, evaluated with typical parameters of conventional polymer networks, the interfacial toughness of the hydrogel is bounded by a few tens of joule per meter squared. The design of tough adhesion of hydrogels first requires high fracture toughness of the hydrogel matrices[30]. If the hydrogel is adhered on the substrate via a low density of weak physical crosslinks such as hydrogen bonds and electrostatic interactions, the interfacial toughness can be even lower, since the adhesive failure mode may occur (**Figure 3-3a**)[355]. Therefore, the design of tough adhesion of hydrogels further requires strong interfacial linkages between the hydrogels and the adhered substrates, such as covalent bonds (**Figure 3-3c**)[30, 31, 356], strong physical crosslinks[310, 355, 357], connector polymers (**Figure 3-3d**)[5, 133, 152, 284], and mechanical interlocks[153, 154].

Overall, the design principle for tough adhesion of hydrogels is to integrate tough dissipative hydrogel matrices and strong interfacial linkages[30]. When attempting to detach the tough hydrogel from the substrate, the strong interfacial linkages will hold the interfacial crack tip, allowing the bulk hydrogel to develop a process zone with substantial mechanical dissipation (**Figure 3-3b**). Quantitatively, the total interfacial toughness can be expressed as[30, 356]

$$\Gamma^{\text{inter}} = \Gamma_0^{\text{inter}} + \Gamma_D^{\text{inter}} \tag{6-3}$$

where Γ^{inter}, Γ_0^{inter}, and Γ_D^{inter} are the total interfacial toughness, the intrinsic interfacial toughness due to strong interfacial linkages, and the contribution of mechanical dissipation in the process zone to the total interfacial toughness, respectively.

Tough adhesion of biological hydrogels in animal bodies such as cartilages, tendons and ligaments on bones generally relies on the integration of tough hydrogels and strong interfacial linkages. However, only recently has this design principle been proposed[30] and implemented[5, 30, 31, 133, 142, 150, 152, 284] for tough adhesion of synthetic hydrogels on diverse substrate materials, including metals, ceramics, glass, silicone, elastomers, hydrogels and biological tissues. This is because the role of tough dissipative hydrogel matrices has been underexplored or underestimated in adhesion of hydrogels[30, 358, 359]. Notably, strong interfacial linkages and/or

bulk dissipation of the adherents have also been widely employed for tough bonding of engineering materials such as metals[360] and rubbers[361, 362] on substrates.

3.2.2. Fatigue-resistant adhesion: strongly bond intrinsically high-energy phases on interfaces

Interfacial fatigue threshold. The interfaces of adhered materials can suffer from fatigue failure under prolonged loads, including interfaces with or without precut cracks under prolonged static or cyclic loads. In this section, we will focus on the fatigue fracture of hydrogels adhered on substrates with precut cracks on their interfaces under cyclic loads (**Figure 3-2b**). Depending on whether the fatigue crack propagates along the interface or tilts into the hydrogel under cyclic loads, the failure mode is called adhesive failure or cohesive failure, respectively (**Figure 3-2b**)[310]. Interfacial fatigue threshold has been commonly used to characterize the capability of adhered materials to resist interfacial fatigue crack propagation following either failure mode under cyclic loads. The interfacial fatigue threshold is defined as the minimal fracture energy at which interfacial crack propagation occurs under infinite cycles of loads[310, 352, 363, 364]. Similar to the fatigue threshold, the interfacial fatigue threshold $\Gamma_{FT}^{\text{inter}}$ can be expressed as,

$$\Gamma_{FT}^{\text{inter}} = G_c\left(dc/dN \to 0\right) \tag{3-4}$$

where G is the energy release rate to drive interfacial crack propagation under each cycle of load, G_c is the minimal energy release rate at which interfacial crack propagation occurs under infinite cycles of loads (i.e. $dc/dN \to 0$), c is the length of the crack, N is the cycle number of the applied load, and dc/dN gives the crack extension per cycle.

The interfacial fatigue threshold of soft materials such as elastomers and hydrogels has been measured with many experimental methods such as the cyclic 90-degree peeling test, the cyclic T-peeling test and the cyclic lap-shear test[310, 352, 363, 364]. For example, in the cyclic 90-degree peeling test[310, 363], a layer of a hydrogel with thickness T, width W and length L (L >> W >> T) is bonded on a substrate, and a notch is introduced on the interface along the length direction (**Figure 3-2b**). A force F is repeatedly applied on the detached part of the hydrogel, while maintaining the detached part vertical to the substrate (**Figure 3-2b**). The applied force F gives the energy release rate $G = F/W$, where W is the width of the hydrogel sheet. The interfacial crack length c is then measured as a function of the cyclic number N. The cyclic 90-degree peeling tests

are repeated for different values of the applied force F (i.e., different energy release rate G), and a curve of dc/dN vs Gcan be obtained (**Figure 3-2b**). The interfacial fatigue threshold Γ_{FT}^{inter} is determined by intersecting the curve of dc/dN vs G with the G axis (i.e., when $dc/dN=0$). Notably, the interfacial fatigue fracture tests of hydrogels are commonly carried out in aqueous environments to avoid dehydration of the hydrogels under prolonged loads[310].

Design principle. As discussed above, tough adhesion of hydrogels on substrates relies on the integration of tough dissipative hydrogel matrices and strong interfacial linkages (**Figure 3-3b**)[30]. The strong interfacial linkages can hold the interfacial crack tip, while the mechanical dissipation in the process zone around the crack tip can dramatically enhance the total interfacial toughness of the adhesion. However, similar to the situation in fatigue fracture of hydrogels[149, 293, 306], because the mechanical dissipation in bulk hydrogel matrices is usually depleted or not timely accessible after cyclic loads, such dissipation usually cannot contribute to resisting interfacial fatigue crack propagation (**Figures 3-3e**)[310, 352]. Consequently, the interfacial fatigue threshold of hydrogels and elastomers is their intrinsic interfacial toughness[310, 352],

$$\Gamma_{FT}^{inter}=\Gamma_{0}^{inter} \tag{3-5}$$

Because interfacial cracks can tilt into bulk hydrogels and develop the cohesive failure mode (**Figure 3-3e**), the design of fatigue-resistant adhesion of hydrogels first requires fatigue-resistant hydrogel matrices that possess sufficiently high densities of intrinsically high-energy phases[124]. Notably, hydrogel matrices that are only tough but not fatigue-resistant are unsuitable for the design of fatigue-resistant adhesion, owing to the depletion of dissipation over cyclic loads (**Equation 3-5**). To further avoid the adhesive failure mode under cyclic loads (**Figure 3-3e**), fatigue cracks on the interfaces also need to be pinned by intrinsically high-energy phases strongly bonded on the interfaces as well (**Figure 3-3f**).

Therefore, the design principle for fatigue-resistant adhesion of hydrogels, in short, is to strongly bond intrinsically high-energy phases on interfaces[310]. While the intrinsically high-energy phases that have been exploited for the design of fatigue-resistant adhesion include nano-crystalline domains[310] and long polymer chains[364], other candidates such as nano-/micro-fibers can be explored in the future. Not surprisingly, biological hydrogels including tendons, ligaments and cartilages all rely on strongly bonding nano-crystalline domains and nano-/micro-fibers on their interfaces with bones to achieve fatigue-resistant adhesion[365].

3.3.3. Implementation strategies for fatigue-resistant hydrogel adhesion.

The design of fatigue-resistant hydrogels relies on achieving sufficiently high densities of intrinsically high-energy phases in the hydrogels. In this section, we will focus on how to strongly bond the intrinsically high-energy phases on substrates to implement the design principle for fatigue-resistant adhesion.High-functionality crosslinks such as nano-crystalline domains usually can play the role of intrinsically high-energy phases in the UPNs. For example, nano-crystalline domains in PVA hydrogels have been strongly bonded on diverse substrates including glass, ceramics, metals and elastomers via high-density hydrogen bonds (**Figure 3-3g**)[310].

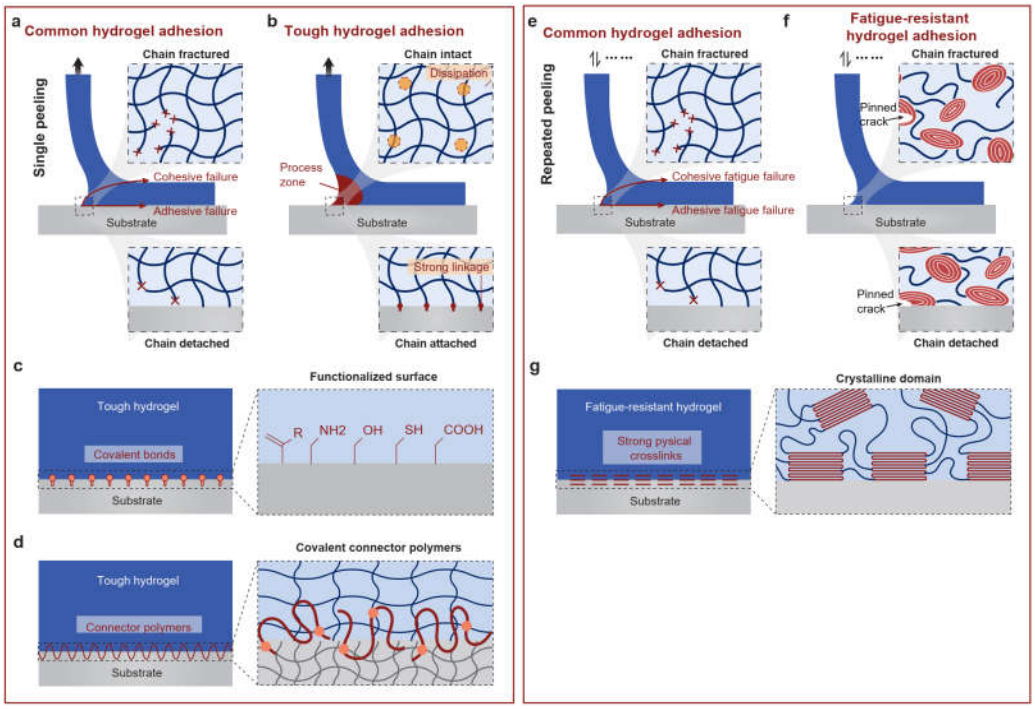

Figure 3-3. Design principles of hydrogels with extreme interfacial mechanical properties. (a) Under a single cycle of load, weak interface can give the adhesive failure mode, and brittle hydrogel matrix can give the cohesive failure mode in the common hydrogel adhesion. (b) Under a single cycle of load, integration of tough dissipative hydrogels and strong interfacial linkages gives tough adhesion of hydrogels. The contributions of strong interfacial linkages and mechanical dissipation in the process zone to the total interfacial toughness are Γ_0^{inter} and Γ_D^{inter}, respectively. The total interfacial toughness of the tough adhesion is $\Gamma^{inter} = \Gamma_0^{inter} + \Gamma_D^{inter}$. (c-d) Implementation strategies of tough hydrogel adhesions: the tough hydrogels are bonded on substrates via various types of strong interfacial linkages: covalent bonds (c) and connector polymers (d). (e) Under cyclic loads, adhesive or cohesive fatigue failure occurs. Dissipation mechanisms such as reversible crosslinks in tough hydrogels are depleted over cycles, not contributing to the fatigue

threshold. (f) Under cyclic loads, fatigue crack is pinned by intrinsically high-energy phases in fatigue-resistant hydrogels. (g) An implementation strategy of fatigue-resistant hydrogel adhesions: the intrinsically high-energy phases can be strongly bonded on the substrates via high-density physical bonds such as hydrogen bonds.

3.3. Materials and methods

3.3.1. Fabrication of hydrogel adhesions

Brittle hydrogel adhesion to glass. Following the same surface functionalization, PAA precursor solution (20 wt% acrylic acid (AA), 0.023 wt% N,N-methylenebisacrylamide (MBAA), and 0.043 wt% ammonium persulphate (APS)) and PAAm precursor solution (20 wt% acrylamide (AAm), 0.023 wt% MBAA, 0.043 wt% APS, and 0.1 wt% N,N,N',N'-tetramethylethylenediamine (TEMED)) were poured onto the 3-(trimethoxysilyl)propyl methacrylate (TMSPMA)-functionalized substrate within an acrylic frame (Plexiglass, 45 mm × 20 mm × 1.5 mm), covered with a glass slide (75 mm × 25 mm × 1 mm), and incubated at 50 °C for 1 h to achieve hydrogel adhesion. The brittle hydrogel adhesions were immersed in water to reach the swollen state before testing.

Tough hydrogel adhesion to various substrates. The tough hydrogel adhesion to various substrates was fabricated following the previous protocol[27]. Briefly, the surface of substrates (i.e., glass, ceramics, titanium, aluminium, and stainless steel) was functionalized with TMSPMA by incubating the substrates in the functional silane solution for 2 h at room temperature. Substrates were washed with ethanol and completely dried with nitrogen flow. The PAAm-alginate tough hydrogel adhesion was fabricated by mixing a carefully degassed aqueous precursor solution (12 wt% AAm, 2 wt% sodium alginate, 0.023 wt% MBAA, and 0.043 wt% APS) with calcium sulphate slurry (0.27 wt% in the mixture) and TEMED (0.1 wt% in the mixture). The mixture was poured onto the TMSPMA-functionalized substrate within an acrylic frame (Plexiglass, 45 mm × 20 mm × 1.5 mm), covered with a glass slide (75 mm × 25 mm × 1 mm), and incubated at 50 °C for 1 h to achieve tough hydrogel adhesion. The Young's modulus of the tough hydrogel is 40 kPa[37]. The tough hydrogels adhered to diverse substrates were immersed in water to reach the swollen state before testing.

Fatigue-resistant hydrogel adhesion to various substrates. 10 g of PVA powders were dispersed in 90 mL deionized water, and dissolved at 100 °C for 5 h, followed by defoaming with a centrifugal mixer (AR-100, Thinky). All the substrates (i.e., glass, ceramic, titanium, aluminium, stainless steel, polydimethylsiloxane (PDMS), and polyurethane (PU)) were thoroughly cleaned with ethanol and deionized water, and then completely dried with nitrogen flow. For the stainless steel substrates, they were first polished to remove the surface oxidation layer prior to the cleaning. Cleaned substrates were then treated by oxygen plasma (30 W at a pressure of 200 mTorr, Harrick Plasma PDC-001) for 5 min. Immediately after the plasma treatment, the PVA solution was poured onto the substrate within an acrylic spacer (Plexiglass, 45 mm × 20 mm × 1.5 mm), fully covered with an acrylic plate (Plexiglass, 75 mm × 50 mm × 1.5 mm), frozen at -20 °C for 8 h, and thawed at 25 °C for 3 h. Multiple cycles of freeze-thawing (cycle number = 1 – 5) could be done, but unless otherwise specified, we only perform one freeze-thawing cycle. Then, the acrylic cover and spacer were removed, and the freeze-thawed hydrogels were air-dried on the substrate for 8 h and then annealed at 100 °C for 90 min to obtain the fatigue-resistant adhesion between PVA hydrogels and substrates. The annealing time was varied when investigating the effect of annealing time on the PVA hydrogel adhesion. The Young's modulus of PVA hydrogels increases from 200 kPa to 10 MPa as the annealing time increases from 0 min to 90 min[36]. All PVA hydrogels adhered to diverse substrates were immersed in water to reach the swollen state before testing.

Fatigue-resistant hydrogel coatings on various substrates. The devices, including glass optical fiber, glass tube, stainless steel spring, Ecoflex elastomer, and ball-and-socket metallic joints, were cleaned with ethanol and deionized water, dried with nitrogen flow, and treated by oxygen plasma for 5 min. Immediately after the plasma treatment, the devices were dipped in the 10 wt% PVA solution and hung in a sealed container at room temperature and relative humidity of 90% for 1 h to drain excess PVA solution. The subsequent freeze-thawing, dry-annealing, and swelling were conducted following the above-mentioned procedure.

To visualize the PVA hydrogel coating on diverse substrates and shapes, 0.01 wt% of fluorescein sodium salt for fluorescent labelling was added into the PVA solution prior to dip-coating. The obtained PVA hydrogel-coated substrates were rinsed with deionized water to remove excess dye solution from the surface before imaging. Macroscopic images were taken by a digital camera (D7000, Nikon) under blue light excitation at 480 nm. The hydrogel coating was also

imaged using an upright confocal laser scanning microscope (CLSM; Leica TCS SP8), where the laser intensity, filter sensitivity, and grayscale threshold were adjusted in each application to optimize the contrast of images. A z-stack acquisition program (~20 μm in slice thickness, 50 steps) was used for 3D scanning, and 3D reconstruction images were created using the LAS X 3D visualization software.

3.3.2. Mechanical characterization

Grazing-incidence wide-angle X-ray scattering (GIWAXS) measurement. Samples for GIWAXS measurements were prepared by spin-coating (3000 rpm, 45 s) of a PVA solution (10 wt%) on a clean glass slide (1 cm × 1 cm), freeze-thawing of the thin hydrogel layer in a humidified chamber and dry-annealing, resulting in a dry film of PVA (~300 nm in thickness) on a glass substrate for GIWAXS measurement. On the other hand, PVA dry film on a glass substrate without annealing, was used as controls. GIWAXS patterns of the PVA samples were obtained with a Pilatus3R 300K detector (Bruker Nanostar), at a radiation wavelength of 1.157 Å and bandwidth of 1.5%. The angle of incidence was kept constant at ~0.2°, while the reflection angle 2θ was scanned from 3 to 90° in angular steps of 0.1°.

3.3.3. Mechanical characterization

Measurement of interfacial toughness. The interfacial toughness of various hydrogel adhesion was measured using the standard 90-degree peeling test (ASTM D2861) with a mechanical testing machine (2 kN load cell; Zwick/Roell Z2.5) and 90-degree peeling fixture (TestResources, G50). As a rigid backing during peeling, a nylon film was bonded on the top of hydrogel with superglue (Loctite, 1405419). All 90-degree peeling tests were performed on swollen hydrogels immersed in a deionized water bath or DPBS at a constant loading speed of 120 mm min^{-1}. The interfacial toughness was measured as $\Gamma = F_s/W$, where F_s is the steady-state peeling force and W is the width of the hydrogel sample [36].

Measurement of interfacial fatigue threshold. To quantify the interfacial fatigue threshold of the hydrogel adhesion to various substrates, we further performed the 90-degree peeling test under cyclic loading (force control mode) using the same experiment setup as the standard 90-degree peeling test. In a multiple-cycle peeling test, we applied the cyclic peeling force with an amplitude

of F_a ($F_a < F_s$) over N cycles, and the interfacial crack extension c were recorded from the testing machine as a function of cycle number N. Accordingly, the applied energy release rate was calculated as $G = F_a/W$, and the interfacial crack propagation rate as dc/dN. The multiple-cycle peeling test was performed at varied applied force amplitudes to give a plot of dc/dN versus G. By linearly extrapolating the plot of dc/dN versus G to the x-intercept, we obtained the interfacial fatigue threshold Γ_0, measured under this condition [39].

3.4. Results and discussion

3.4.1. Mechanical characterization of fatigue-resistant hydrogel adhesion

We first form the PVA hydrogels with low crystallinity on diverse solid substrates including glass, ceramics, titanium, aluminium, stainless steel, PU and PDMS through a freeze-thawing process[18]. Then, we dry and anneal the samples to substantially increase the crystallinity within the hydrogels (see Materials and Methods)[19, 20]. The dry-annealing process also induces the formation of hydrogen bonds between the ordered nanocrystalline domains and the solid surfaces (**Figure 3-3g**)[21]. As control samples, we fabricate tough hydrogel adhesion (e.g., PAAm-alginate hydrogel) and common hydrogel adhesion (e.g., PAAm hydrogel and polyacrylic acid (PAA) hydrogel) to solid substrates by covalently anchoring the polymer networks of hydrogels on the substrates (see Materials and Methods)[22].

Next, we carry out the standard 90-degree peeling tests on the adhered hydrogel samples under a single cycle and multiple cycles of loads to measure the interfacial toughness Γ (**Figure 3-4a**) and interfacial fatigue threshold Γ_0 (**Figure 3-4c**), respectively. From a single-cycle peeling test, the interfacial toughness is measured as

$$\Gamma = F_s/W \tag{3-6}$$

where F_s is the steady-state peeling force and W is the width of the hydrogel sample (**Figure 3-4a**)[4]. In a multiple-cycle peeling test, we apply the cyclic peeling force with an amplitude of F_a ($F_a < F_s$) over N cycles, and measure the interfacial crack extension c as a function of cycle number N. Accordingly, the applied energy release rate G can be calculated as

$$G = F_a/W \tag{3-7}$$

and the interfacial crack propagation rate as dc/dN. The multiple-cycle peeling test is performed at varied amplitudes of applied forces to give a plot of dc/dN versus G (**Figure 3-4c**). By linearly extrapolating the plot of dc/dN versus G to intercept the G-axis, we can obtain the interfacial

fatigue threshold Γ_0, measured under this condition[23] (**Figure 3-4d**). Notably, the hydrogel samples are immersed in an aqueous bath and maintain their swollen state throughout the peeling tests to prevent dehydration. In addition, a thin and rigid nylon film is attached to the surface of the hydrogel sample as a backing to prevent its elongation along the peeling direction (see Methods and Materials).

As shown in **Figure 3-4b**, while the measured interfacial toughnesses for both tough hydrogel adhesion (PAAm-alginate with 1,500 J m^{-2}) and fatigue-resistant hydrogel adhesion (PVA with 7,500 J m^{-2}, **Figure 3-4b**) on glass are high, their interfacial fatigue thresholds are dramatically different. The interfacial fatigue threshold of tough hydrogel adhesion (PAAm-alginate) is as low as 68 J m^{-2} (**Figure 3-4d**), similar to that of common hydrogel adhesion (9 J m^{-2} for PAA and 32 J m^{-2} for PAAm) [310], and comparable with the energy required for fracturing a layer of amorphous polymer chains (1-100 J m^{-2})[24-26]. By contrast, the fatigue threshold of fatigue-resistant hydrogel adhesion is 800 J m^{-2} in deionized water (**Figure 3-4d**), approximating the value for tendon-to-bone adhesion[10, 26, 27]. To further validate the high interfacial fatigue threshold, we apply an energy release rate of 800 J m^{-2} on the fatigue-resistant hydrogel adhesion over 30,000 cycles, and observe no interfacial crack propagation using a camera with a resolution of 20 μm per pixel. This result means that the speed of any possible crack propagation should be lower than 0.6 nm $cycle^{-1}$, consistent with the previous validation of fatigue thresholds for hydrogels[28] (**Figure 3-4f**). On the contrary, when the tough hydrogel adhesion is subjected to an energy release rate of 200 J m^{-2} over 5,000 cycles, substantial propagation of the interfacial cohesive crack can be identified (**Figure 3-4e**).

Furthermore, when the applied energy release rate is higher than the interfacial fatigue threshold, the interfacial fatigue cracks in both cases (i.e., PAAm-alginate and PVA) may gradually tilt into the bulk hydrogel and induce fatigue fracture of the bulk hydrogel (**Figure 3-4e**). This failure mode indicates that the interfacial fatigue thresholds of hydrogel adhesion also depend on the intrinsic fracture toughness of the bulk hydrogel, due to possible crack tilting and cohesive failure of the bulk hydrogel. The high density of nanocrystalline domains in the bulk PVA hydrogel gives it a high intrinsic fracture toughness (i.e., 1,000 J m^{-2}) [29] and guarantee its high interfacial fatigue threshold (i.e., 800 J m^{-2}).

In addition to glass, the fatigue-resistant hydrogel adhesion is also applicable to diverse solid substrates (**Figure 3-4g**), including ceramics ($\Gamma_0 = 470$ J m^{-2}), titanium (225 J m^{-2}), aluminium (370 J m^{-2}), stainless W (330 J m^{-2}), PU (420 J m^{-2}), and PDMS (150 J m^{-2}).

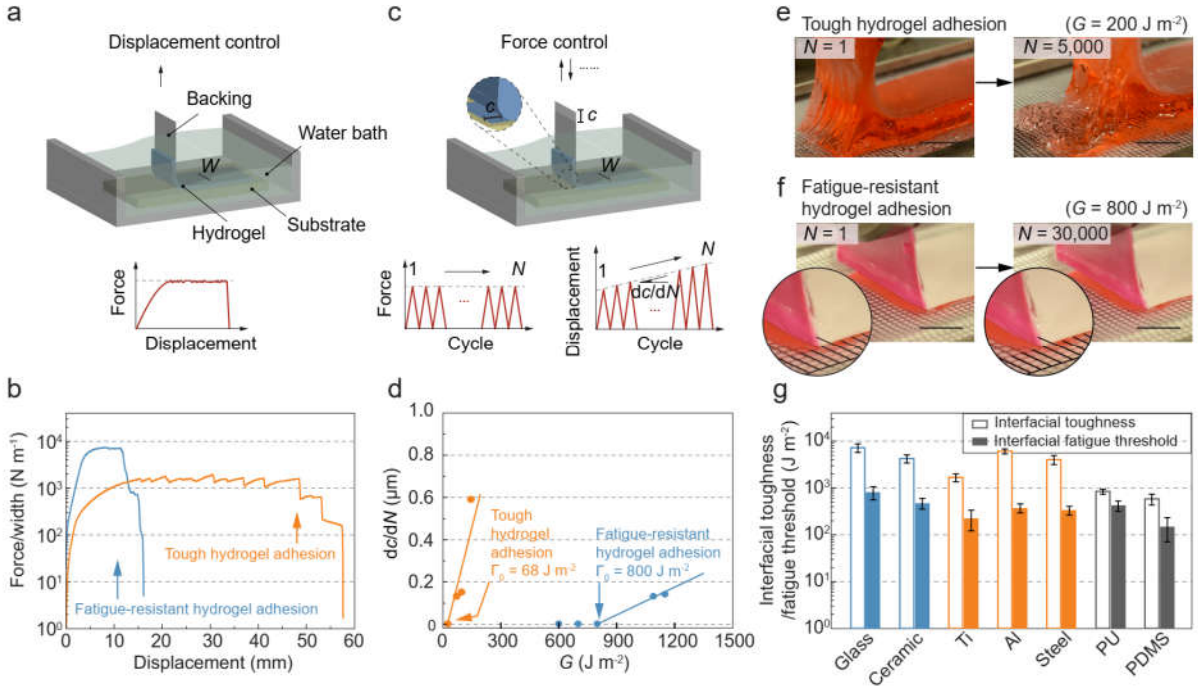

Figure 3-4. Mechanical characterization of fatigue-resistant hydrogel adhesion. (a) Schematic illustration of measuring nominal peeling force F versus displacement curve during a single cycle of loading within a water bath. (b) Representative curves of the peeling force per width of the hydrogel (F/W) versus displacement for the tough hydrogel adhesion (i.e., PAAm-alginate) and fatigue-resistant hydrogel adhesion (i.e., PVA) on a glass substrate. (c) Schematic illustration of measuring the interfacial crack extension c versus cycle number N during a cyclic peeling test at a peeling force of F_a. (d) Plot of crack extension rate (dc/dN) versus applied energy release rate $G = F_a/W$ for the tough hydrogel adhesion and fatigue-resistant hydrogel adhesion on a glass substrate. The linear extrapolation to the x-intercept gives the fatigue threshold Γ_0. (e) Images of interfacial crack propagation during a cyclic peeling test for tough hydrogel adhesion with a thickness around 3 mm (swollen state) at an energy release rate of 200 J m^{-2}, showing substantial interfacial crack propagation within 5,000 cycles. (f) Images of interfacial crack propagation during a cyclic peeling test for fatigue-resistant hydrogel adhesion with a thickness around 100 μm (swollen state) at an energy release rate of 800 J m^{-2}, showing no interfacial crack propagation within 30,000 cycles. (g) Summary of measured interfacial toughness and interfacial fatigue threshold for fatigue-resistant hydrogel adhesion on various substrates, including glass, ceramic, titanium, aluminium, stainless steel, PU, and PDMS. Data in (g) are means ± SD, n = 3. Scale bars are 10 mm in (e) and (f).

3.4.2. Mechanism of fatigue-resistant hydrogel adhesion

To understand the mechanism for fatigue-resistant hydrogel adhesion, we vary the annealing time for the PVA hydrogels on glass substrates, and then measure the interfacial fatigue thresholds and

characterize the nanocrystalline domains in the hydrogels. The hydrogel without annealing easily detaches from the substrates upon hydration. However, by increasing the annealing time from 0 to 90 min, the interfacial fatigue threshold of the hydrogel adhesion is greatly enhanced from 0 to 800 J m^{-2} [310]. Correspondingly, the prolonged annealing time (from 0 to 90 min) leads to the significantly increased crystallinity (from 12.1 wt% to 33.7 wt% at the swollen state) and reduced water content (from 67 wt% to 37 wt%) in the PVA hydrogels [310]. In addition, although the freeze-thawing process is crucial for nanocrystal nucleation in hydrogels, varying the freeze-thawing cycles of PVA hydrogels does not change the adhesion performance significantly [310], since the subsequent dry-annealing process increases the crystallinity much more dramatically than the freeze-thawing process [30].

We further carry out two-dimensional (2D) grazing-incidence wide-angle X-ray scattering (GIWAXS) measurements on the PVA samples adhered to glass substrates before and after annealing (100 °C, 90 min). Before annealing, the 2D pattern of GIWAXS (**Figure 3-5c,e**) exhibits a uniform scattering ring with equal intensity at all different azimuthal angles (θ), suggesting random orientation of the nanocrystalline domains (**Figure 3-5a**) [31]. By contrast, an arc-like scattering feature prominently appears in the 2D pattern of GIWAXS for samples after annealing, where the intense scattering is dominantly aligned along the normal direction of the hydrogel-solid interface (**Figure 3-5d,f**). This pattern implies that the preferred orientation of nanocrystalline domains is parallel to the interface in annealed PVA hydrogel samples (**Figure 3-5b**) [32]. The densely-packed and oriented nanocrystalline domains at the interface can collectively and effectively pin the crack propagation on the hydrogel-solid interface.

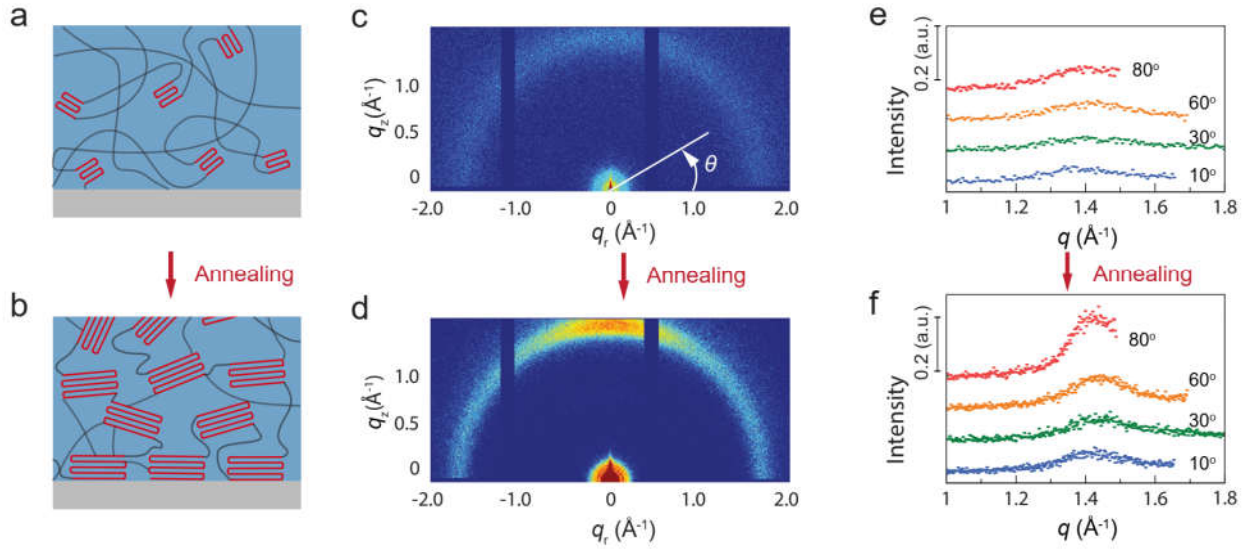

Figure 3-5. Mechanisms for fatigue-resistant hydrogel adhesion. Schematic illustration of the nanocrystalline structures of fatigue-resistant hydrogel adhesion before (a) and after (b) annealing (100 °C, 90 min). GIWAXS patterns of fatigue-resistant hydrogel adhesion before (c) and after annealing (d). GIWAXS scattering profiles at azimuthal angles of 10°, 30°, 60° and 80° for PVA hydrogel before (e) and after (f) annealing.

3.4.3. Fatigue-resistant hydrogel adhesion on various shapes

Materials and devices with complex shapes can be exposed to repeated mechanical loads, which pose a challenge to their coating materials in terms of fabrication method and long-term robustness. We demonstrate that the fatigue-resistant hydrogel adhesion can potentially provide a facile and versatile solution towards this challenge. We first present a set of materials and devices, including a glass optical fiber (**Figure 3-6a** before and **Figure 3-6b** after coating), a glass tube (**Figure 3-6c,d**), a stainless steel spring (**Figure 3-6e,f**), a leaf-shaped elastomer (**Figure 3-6g,h**), and a ball-and-socket metallic joint (**Figure 3-6i-l**), which are coated with a hydrogel layer through a dip-coating, freeze-thawing, and dry-annealing process. The thin (~20 μm in thickness, insets in **Figure 3-6b,d**) and uniform hydrogel coatings are applicable to devices with various feature sizes (from 200 μm in **Figure 3-6a** to 35 mm in **Figure 3-6i**), curvatures (convex surface in **Figure 3-6a,e,i**, concave surface in **Figure 3-6k**, and inner and outer surfaces in **Figure 3-6c**) and diverse materials (glass in **Figure 3-6a,c**, stainless steel in **Figure 3-6e,i,k**, and silicone elastomer in **Figure 3-6g**).

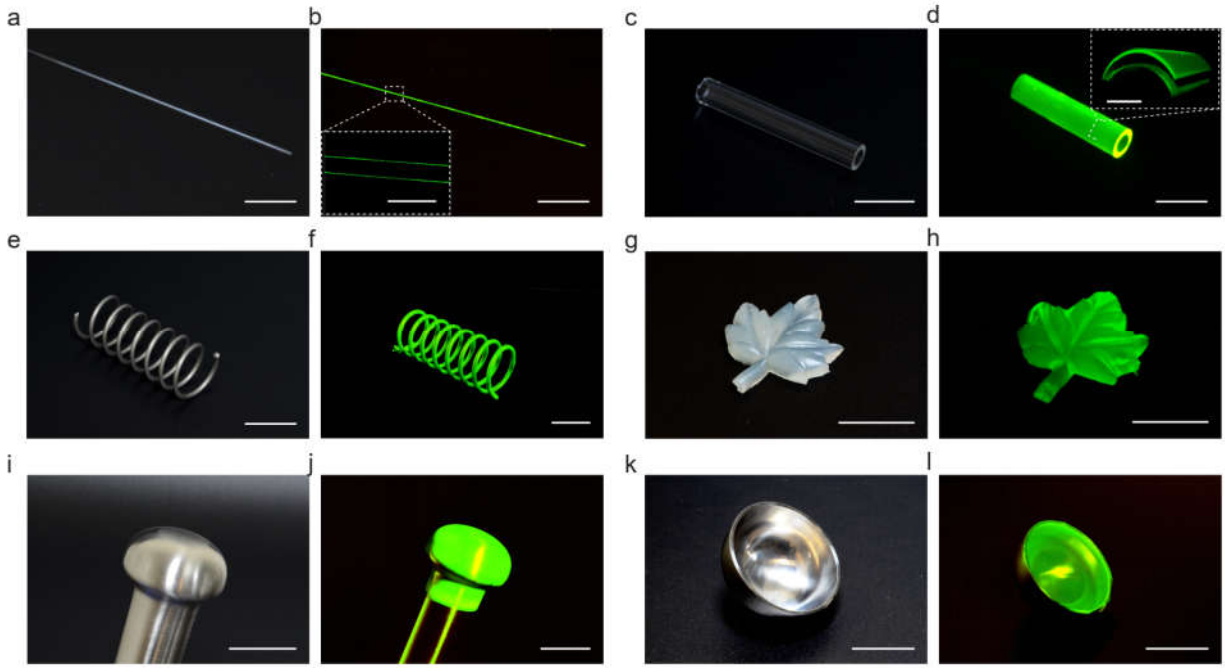

Figure 3-6. Fatigue-resistant hydrogel coatings on various materials with complex geometries. A glass optical fiber (200 μm in diameter) with (b) and without (a) fatigue-resistant hydrogel coatings. Inset in (b): confocal microscopic image of the hydrogel coating (~20 μm in thickness) on the glass optical fiber. A glass tube with (d) and without (c) fatigue-resistant hydrogel coatings on the inner and outer surfaces. Inset in (d): 3D CLSM image of the hydrogel coating on both inner and outer surfaces. A stainless steel spring with (f) and without (e) fatigue-resistant hydrogel coatings. A leaf-shaped elastomer with (h) and without (g) fatigue-resistant hydrogel coatings. A convex end of the ball-and-socket metallic joint with (j) and without (i) fatigue-resistant hydrogel. A concave end of the ball-and-socket metallic joint with (l) and without (k) fatigue-resistant hydrogel. The hydrogel coatings are colorized with fluorescein sodium salt dye for visualization and all the images of (b), (d), (f), (h), (j), (l) are taken under a blue light excitation (480 nm in wavelength). Scar bars: 20 mm in (a-l), 500 μm in the inset of (b), and 2 mm in the inset of (d).

3.5. Conclusions

We have discussed the design principle and implementation strategy for tough, fatigue-resistant hydrogel adhesions. We have demonstrated that the interfacial toughness of hydrogel adhesions can be enhanced by integrating tough dissipative hydrogels and strong interfacial linkages, and the interfacial fatigue threshold of hydrogel adhesions can be greatly increased by strongly bonding intrinsically high-energy phases on interfaces. Inspired by the adhesion between bones and tendons/ligaments/cartilages in the human body, we developed an implementation strategy for the fatigue-resistant adhesion of hydrogels on diverse engineering materials through bonding ordered nanostructures in the hydrogels on the engineering materials. This hydrogel-solid adhesion achieves a record-high interfacial fatigue threshold up to 800 J m^{-2}, and enables applications such as long-lasting hydrogel coatings on devices with various feature sizes, curvatures, and substrate materials.

The reported strategy for achieving fatigue-resistant adhesion of synthetic hydrogels to various engineering materials makes a number of future research directions and applications possible by providing a soft cushion between rigid machines and the human body. For example, as a mechanically and biologically compatible interface, the fatigue-resistant hydrogel coatings on machines can not only transmit electrical, optical, acoustic, chemical, and mechanical signals between tissues and external devices (e.g., electrodes, optical fibers, ultrasound transducers, prosthetics, and robots), but also show robust performances over the long term. In Chapter 4, we adopted tough hydrogel adhesions in living devices. In Chapter 7, we used fatigue-resistant hydrogel adhesions for optical fibers. In other papers, we also applied the tough hydrogel adhesives

and coatings for medical tubing, catheters, cardiac pacemaker leads, soft robots[151], goggles[366], and plastic linings in solar stills[366].

Chapter 4

Hydrogel living devices

The research presented in this chapter has been published in:

- **Xinyue Liu†,** Tzu-Chieh Tang†, Eléonore Tham†, Hyunwoo Yuk†, Shaoting Lin, Timothy K Lu, and Xuanhe Zhao. Stretchable living materials and devices with hydrogel–elastomer hybrids hosting programmed cells. Proceedings of the National Academy of Sciences. 114, 2017.
- **Xinyue Liu†,** Hyunwoo Yuk†, Shaoting Lin, German Alberto Parada, Tzu-Chieh Tang, Eléonore Tham, César de la Fuente, Timothy K. Lu, and Xuanhe Zhao. 3D printing of living responsive materials and devices. Advanced Materials. 30, 2017.
- Tzu-Chieh Tang†, Eleonore Tham†, **Xinyue Liu†**, Kevin Yehl, Alexis J. Rovner, Hyunwoo Yuk, Farren J. Isaacs, Xuanhe Zhao, and Timothy K. Lu. Tough hydrogel-based biocontainment of engineered organisms for continuous, self-powered sensing and computation. Nature Chemical Biology. 2021.

4.1. Introduction

Genetically engineered cells enabled by synthetic biology have accomplished multiple programmable functions, including sensing [367-369], responding [370-372], computing [373-375], and recording [376-378]. Powered by this emerging capability to program cells into living computers [367-380], the integration of genetically encoded cells into freestanding materials and devices will not only provide new tools for scientific research but also lead to unprecedented technological applications [381, 382]. However, the development of such living materials and devices has been significantly hampered by the demanding requirements for maintaining viable and functional cells in materials and devices, plus biosafety concerns towards the release of genetically modified organisms into environments [383, 384]. Meanwhile, to sustain the

functionality, the device should be mechanically robust and flexible when it frequently undergoes deformations during applications [215].

Intensive efforts have been made to provide a niche for the living components. For example, gene networks embedded in paper matrices have been utilized for low-cost rapid viruses detection and protein manufacturing [368, 369], but their gene networks are based on freeze-dried extracts from genetically engineered cells to operate, partially because the paper substrates cannot sustain long-term viability and functionality of living cells or prevent their leakage. As another example, by seeding cardiomyocytes on thin elastomer films, bio-hybrid devices have been developed as soft actuators [385, 386] and biomimetic robots [387, 388]. Since the cells are not protected or isolated from the environment, the bio-hybrid devices need to operate in media and the cells may detach from the elastomer films. Thus, despite progresses in the field, it remains a grand challenge to integrate genetically encoded cells into practical materials and devices that can maintain long-term high viability and functionality of the cells, allow for efficient chemical communications between cells and with external environments, and prevent cells from escaping out of the materials or devices. A versatile material system and a general method to design living materials and devices capable of diverse functions [368, 369, 385, 387-390] remain a central need.

As polymer networks infiltrated with water, hydrogels have been widely used as scaffolds for tissue engineering [10] and vehicles for cell delivery [26, 106], owning to their high water content, biocompatibility, biofunctionality, and permeability to a wide range of chemicals and biomolecules [391, 392]. The great success of hydrogels as cell carriers in tissue engineering and cell delivery demonstrates their potential as an ideal matrix for living materials and devices to incorporate genetically engineered cells. Combining programmed cells with robust biocompatible hydrogels has the potential to enable an avenue to create new living materials and devices, but this promising approach has not been explored yet.

On the other hand, 3D printing is an emerging technology to fabricate customized structures of responsive materials including hydrogels[32], liquid crystals[393], shape-memory polymers[394], and aqueous droplets[395]. 3D printed architectures, which can accurately define the networks of signal transmission for active elements, allow one to mimic highly organized, time-evolving biological constructs (e.g., microbial biofilms, gut microbiota, and tumor tissue) [395, 396]. However, the potential benefits of harnessing programmable living cells as active components in 3D printing have not been explored yet.

Here we demonstrate the design of living materials and devices using hydrogels as matrices, including hydrogel-elastomer hybrids and 3D printed hydrogel structures. Both of them host genetically engineered bacterial cells in the living devices. We show that the living devices can sustainably provide water and nutrients to the cells to maintain the long-term viability and functionality of the bacteria. Communication between different types of genetically engineered cells and with the environment is achieved via passive transportation of signaling molecules in hydrogels. The high stretchability and robustness of the hydrogel-elastomer hybrids prevent leakage of cells from the living materials and devices even under large deformations. We demonstrate multiple wearable devices enabled by our living materials and devices, including a skin patch, a glove with living chemical detectors, and a living tattoo. A quantitative model that couples transportation of signaling molecules and responses of cells is developed to guide the design of living materials and devices.

4.2. Results and discussion

4.2.1. Design of hydrogel–elastomer hybrids

General Design. We propose that encapsulating genetically engineered cells in biocompatible, stretchable and robust hydrogel-elastomer hybrid matrices represents a general strategy for the design of living materials and devices with powerful properties and functions. The design of a generic structure for the living materials and devices is illustrated in **Figure 4-1a** (see Methods and Materials). In brief, layers of robust and biocompatible hydrogel and elastomer are assembled and bonded into a hybrid structure [31]. Patterned cavities of different shapes, sizes and connections are introduced on the hydrogel-elastomer interfaces in order to host living cells in subsequent steps. The hydrogel-elastomer hybrid is then immersed in culture media for 12 h, so that the hydrogel can be infiltrated with nutrients. Thereafter, genetically engineered bacteria suspended in media are infused into the patterned cavities through the hydrogel layer, and the injection points are then sealed with drops of fast-curable pre-gel solution. Since the hydrogel is infiltrated with media and the elastomer is air permeable, hydrogel-elastomer hybrids with proper dimensions can provide sustained supplies of water, nutrient and oxygen (if needed) to the cells. By tuning the dimensions of hydrogel walls between different types of cells and between cells and external environments, we can control the transportation times of signaling molecules for cell communication. Furthermore, the high mechanical robustness of the hydrogel, elastomer and their

interface confer structural integrity to the matrix even under large deformations, thus preventing cell escape in dynamic environments.

Fabrication. In the current study, we choose PAAm-alginate interpenetrating network hydrogel [29, 31] and PDMS (Sylgard 184, Dow Corning) or Ecoflex (Smooth-On) silicone elastomer, to constitute the robust hydrogel and elastomer, respectively. The biocompatibility of these materials has been extensively validated in various biomedical applications [397, 398]. The sufficient gas permeation of the silicone elastomer enables oxygen supply for the bacteria [399-401]. If higher level of oxygen is required, one may choose elastomers with higher permeability such as Silbione [402] or microporous elastomers [400]. The covalently-crosslinked PAAm network is highly stretchable and the reversibly-crosslinked alginate network dissipates mechanical energy under deformation, leading to tough and stretchable hydrogels [1, 5, 29]. More robust devices can be fabricated by using fiber reinforced tough hydrogel [335, 403, 404]. Robust bonding between the hydrogel and elastomer can be achieved by covalently anchoring the PAAm network on the elastomer substrate [5, 30, 31]. The Escherichia coli (E. coli) bacterial strains are engineered to produce outputs (e.g., expressing green fluorescent protein (GFP)) under control of promoters that are inducible by cognate chemicals. For example, the $DAPG_{RCV}$/GFP strain produces GFP when the chemical inducer DAPG is added and received by the cells. The cell strains used in the current study include $DAPG_{RCV}$/GFP, AHL_{RCV}/GFP, $IPTG_{RCV}$/GFP, $Rham_{RCV}$/GFP, and aTc_{RCV}/AHL. The 2,4-diacetylphloroglucinol (DAPG), N-acyl homoserine lactone (AHL), isopropyl β-D-1-thiogalactopyranoside (IPTG), rhamnose (Rham), and anhydrotetracycline (aTc) are small molecules with biochemical activities, and used as the signaling molecules in this chapter.

4.2.2. Bacterial evaluation in hydrogel–elastomer hybrids

Bacterial viability. To evaluate the viability of cells in living materials and devices, we place the hydrogel-elastomer hybrid illustrated in **Figure 4-1a** containing $Rham_{RCV}$/GFP bacteria at 37°C and relative humidity of 90%, or immerse this living device in LB media at 37°C. Thereafter, we perform flow cytometry analysis of bacteria retrieved from the hydrogel-elastomer hybrids using the live-dead stain. As compared to live and dead bacterial controls, it is shown that the bacteria in the hydrogel-elastomer hybrid are mostly viable after 12 h (**Figure 4-1c**). To approximate more realistic applications, we further test relatively long-term viability of bacterial cells in the device

placed in humid chamber at room temperature (25 °C) over 3 days. As shown in **Figure 4-1c**, the viability of bacterial cells in the device maintains over 90% over 3 days without addition of media to the device. This viability is similar to that of cells in the device immersed in media or cells directly cultured in media at room temperature (25 °C) over 3 days (**Figure 4-1c**). The self-sustainable living material and device are more facile for wearable and portable applications, as compared with microfluidics with pumps or electronics with power source.

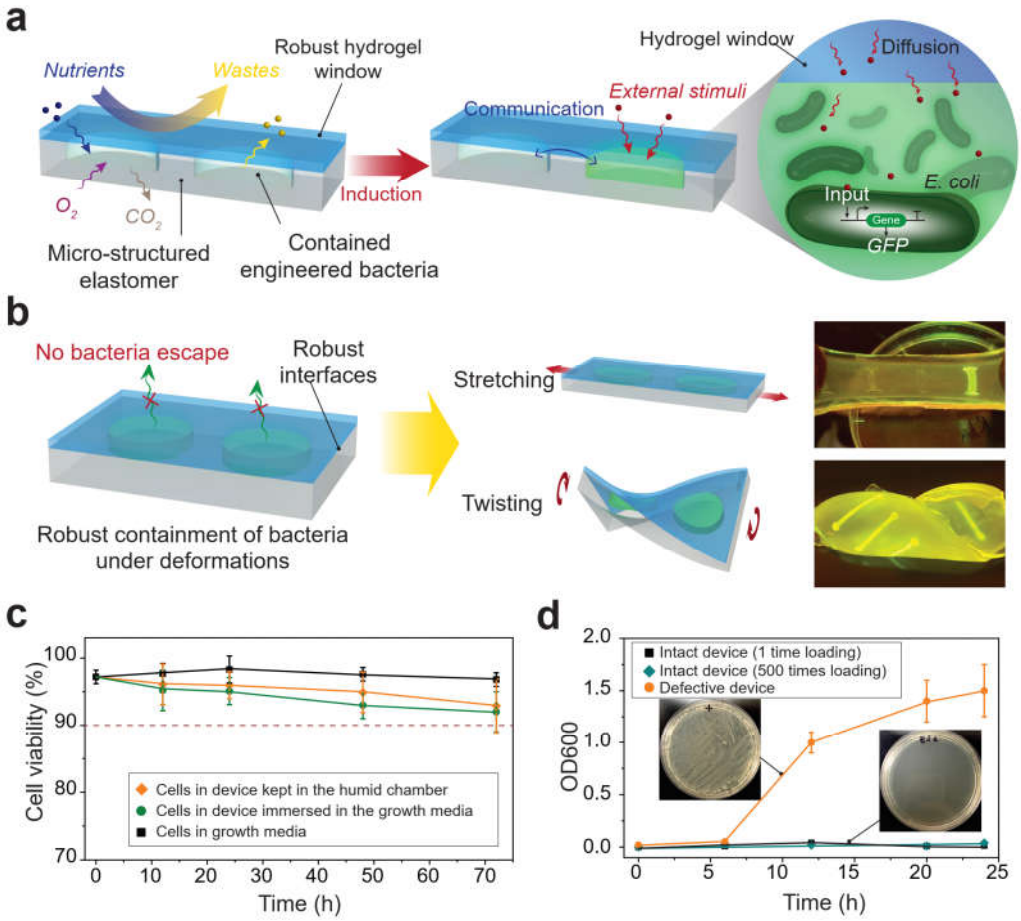

Figure 4-1. Design of hydrogel–elastomer hybrids. (a) Schematic illustration of a generic structure for living materials and devices. Layers of robust and biocompatible hydrogel and elastomer are assembled and bonded into a hybrid structure, which can transport sustained supplies of water, nutrient and oxygen to genetically engineered cells at hydrogel-elastomer interface. Communication between different types of cells and with the environment is achieved by diffusion of small molecules in hydrogels. (b) Schematic illustration of the high stretchability and high robustness of the hydrogel-elastomer hybrids that prevent cell leakage from the living device, even under large deformations. Images shows that the living device can sustain uniaxial stretching over 1.8 times and twisting over 180° while maintaining its structural integrity. (c) Viability of bacterial cells at room temperature over 3 days. The cells are kept in the device placed in the humid chamber without additional growth media (yellow), in the device immersed in the growth media (green) as a control, and in growth media as another control (black). (d) OD_{600} of the media surrounding the

defective devices (yellow) and intact devices at different times after once (black) or 500 times (green) deformation of the living devices and immersion in media. Insets: streaked agar plate of the surrounding media of the defective and intact devices. Data in (c) and (d) are means ± SD, n = 3.

Bacterial escape. To test whether bacteria could escape from the living devices, we deform the hydrogel-elastomer hybrids illustrated in **Figure 4-1b** containing $Rham_{RCV}$/GFP bacteria in different modes (i.e., stretching and twisting), and then immerse the device in media for a 24 h period. The living device made of Ecoflex and tough hydrogel sustains a uniaxial stretch over 1.8 times of its original length[55] and a twist over 180° while maintaining its structural integrity. Furthermore, after immersing the device in media for 6, 12, 20, and 24 h, we collect the media surrounding the device and measured the cell population in the media over time via OD_{600} by UV spectroscopy (**Figure 4-1d)**. 200 μL of media are transferred on agar plates after 24 h to check for cell escape and growth (**Figure 4-1d**, inset**)**. **Figure 4-1d** demonstrates that bacteria do not escape the hydrogel-elastomer hybrid despite large deformations (**Figure 4-1b**). As controls, we intentionally create defective devices (with weak hydrogel-elastomer bonding) and observe significant escape and overgrowth of bacteria after immersing the samples in media (**Figure 4-1d**). To further study the robustness of the device under repeated mechanical loads, the cell escape from the device is measured after stretching it to 1.8 times for 500 cycles. The green curve in **Figure 4-1d** shows negligible cell escape after repeated deformation of the living device, indicating the robustness of the living device under repeated mechanical load.

4.2.3. Prototypes of hydrogel–elastomer hybrids

Orthogonal sensors. We next demonstrate novel functions and applications enabled by the living materials and devices. **Figure 4-2a** illustrates a hydrogel-elastomer hybrid with four isolated chambers that each hosts a different bacterial strain, $DAPG_{RCV}$/GFP, AHL_{RCV}/GFP, $IPTG_{RCV}$/GFP, and $Rham_{RCV}$/GFP. The genetic circuits in these bacterial strains can sense their cognate inducers and express GFP, which can be visible under blue light illumination (488 nm). As mentioned above, the $DAPG_{RCV}$/GFP strain exhibits green fluorescence when receiving (RCVing) DAPG, but is not responsive to other stimuli. Similarly, the AHL_{RCV}/GFP strain expresses GFP only induced by AHL; IPTG selectively induces GFP expression in the $IPTG_{RCV}$/GFP strain; and Rham selectively induces the green fluorescence output of the $Rham_{RCV}$/GFP strain (**Figure 4-2b**) (see details of

strain engineering in Materials and Methods). We show that each inducer, diffusing from the environment through the hydrogel into cell chamber, can trigger GFP expression of its cognate strain inside the device, which could be visualized by microscopy or the naked eye (**Figure 4-2c,d**). This orthogonality makes the hydrogel-elastomer hybrid with encapsulated bacteria into a living sensor that can simultaneously detect multiple chemicals in the environment (**Figure 4-2c**). About two hours are required for each strain to produce significant fluorescence (e.g., 0.5 of the maximum fluorescence). Parameters that affect response times for the living sensor are discussed in Modeling.

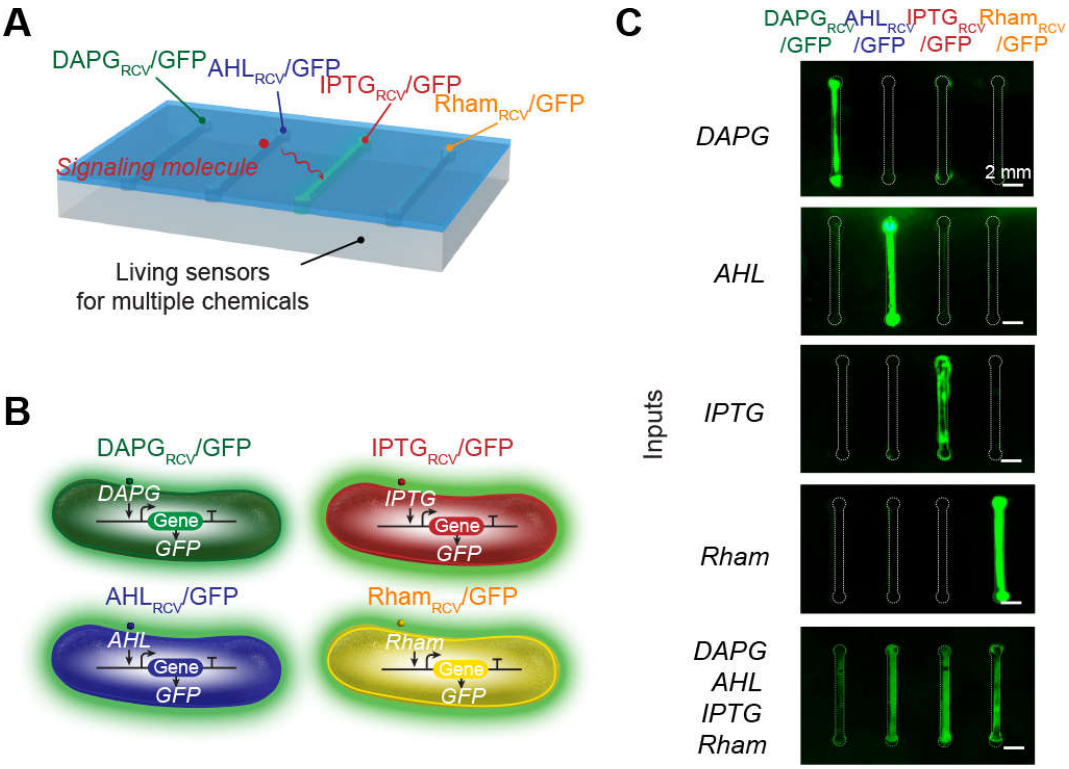

Figure 4-2. Hydrogel–elastomer hybrids as stretchable living sensors. (a) Schematic illustration of a hydrogel-elastomer hybrid with four isolated chambers to host bacterial strains, including DAPG$_{RCV}$/GFP, AHL$_{RCV}$/GFP, IPTG$_{RCV}$/GFP, and Rham$_{RCV}$/GFP, respectively. Signaling molecules diffused from the environment through the hydrogel window into cell chambers, where they are detected by the bacteria. (b) Genetic circuits are constructed in bacterial strains to detect cognate inducers (i.e., DAPG, AHL, IPTG, and Rham), and produce GFP. (c) Images of living devices after exposure to individual or multiple inputs. Cell chambers hosting bacteria with the cognate sensors show green fluorescence while the non-cognate bacteria in chambers are not fluorescent. Scale bars are 2 mm in (c).

Signal propagation in the sensors. Next, we integrate cells containing different genetic circuits into a freestanding living device to study cellular signaling cascades. We design two bacterial

strains can communicate via the diffusion of signaling molecules through the hydrogel even though both are separated by an elastomer barrier within discrete chambers of the device (**Figure 4-3a**). Specifically, we use a transmitter strain (aTc_{RCV}/AHL) that produces the quorum-sensing molecule AHL when induced by aTc, and a receiver strain (AHL_{RCV}/GFP) with an AHL-inducible GFP gene [371, 383, 405]. We trigger this device with aTc from the environment to induce the transmitter cells, which results in AHL production and stimulation of receiver cells to synthesize GFP (**Figure 4-3c**). In **Figure 4-3b**, we plot the normalized fluorescence of bacteria in different cell chambers (i.e., transmitter and receiver in **Figure 4-3a**) as a function of time after aTc (200 ng mL^{-1}) is added outside the device. Due to no GFP gene in the transmitter cells (aTc_{RCV}/AHL), their chambers show no fluorescence over time (**Figure 4-3b**). It takes longer response time (~5 h) for the receiver cells in the middle chamber to exhibit significant fluorescence, as compared with the cells in simple living sensors (**Figure 4-3a**). Two diffusion processes (i.e., aTc from the environment to the two side chambers, and AHL from the two side chambers to the central chamber) and two induction processes (i.e., AHL production induced by aTc in transmitters, and GFP expression induced by AHL in receivers) are involved in the current interactive genetic circuits. As a control, when the transmitters (aTc_{RCV}/AHL) in the device is replaced by a cell strain containing aTc-inducible GFP (aTc_{RCV}/GFP) that cannot communicate with AHL_{RCV}/GFP, no fluorescence is observed in the receiver (AHL_{RCV}/GFP) chamber (**Figure 4-3d**). Overall, the integrated devices containing interactive genetic circuits provide a new platform for the detection of various chemicals and the investigation of cellular interaction among physically isolated cell populations [406, 407]. In addition, these living devices illustrated in **Figure 4-3a** can be mechanically stretchable and robust, preventing cell escape even under large deformations, as illustrated in **Figure 4-1b**.

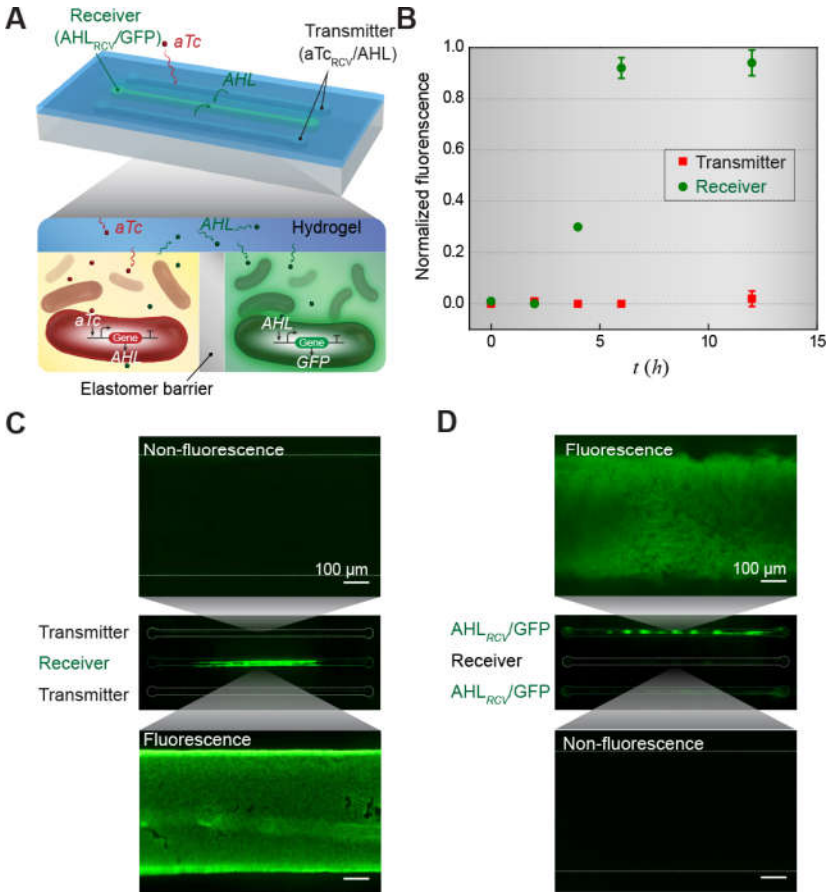

Figure 4-3. Hydrogel–elastomer hybrids as interactive genetic circuits. (a) Schematic illustration of a living device that contains two cell strains: the transmitters (aTc$_{RCV}$/AHL strain) produce AHL in the presence of aTc, and the receivers (AHL$_{RCV}$/GFP strain) express GFP in the presence of AHL. The transmitters could communicate with the receivers via diffusion of the AHL signaling molecules through the hydrogel window, even though the cells are physically isolated by elastomer. (b) Quantification of normalized fluorescence over time. All data are measured by flow cytometry with cells retrieved from the device at different times. (c) Images of device and microscopic images of cell chambers 6 h after addition of aTc into the environment surrounding the device. The side chambers contain transmitters, while middle one contains receivers. (d) Images of device and microscopic images of cell chambers, 6 h after aTc addition in the environment. The side chambers contain aTc$_{RCV}$/GFP instead of transmitters, while middle one contains receivers. Data in (b) are means ± SD, n = 3. Scale bars are 100 μm in (c) and (d).

Skin patches as wearable living sensors. To further demonstrate practical applications of living materials and devices, we fabricate a living wearable living patch that detects chemicals on the skin (**Figure 4-4a-d**). The sensing patch matrix consists of a bilayer hybrid structure of tough hydrogel and silicone elastomer. The wavy cell channels could cover a larger area of the skin with a limited number of bacterial cells (**Figure 4-4a)**. The living patch can be fixed on the skin by clear Scotch tape, with the hydrogel exposed to the skin and the elastomer to the air. The

compliance and stickiness of the hydrogel promotes conformal attachment of the living patch to human skin, while the silicone elastomer cover effectively prevents the dehydration of the sensor patch [31]. As shown in **Figure 4-4b-d**, the inducer Rham (12 mM) is smeared on the skin of a forearm prior to adhering the living patch. The channels with $Rham_{RCV}$/GFP in the living patch become fluorescent within 4 h, while channels with AHL_{RCV}/GFP do not show any difference.

Gloves as wearable living sensors. As another application, a glove with chemical detectors integrated at the fingertips is fabricated (**Figure 4-4e**). The stretchable hydrogel and tough bonding between hydrogel and rubber allow for robust integration of living monitors on flexible gloves. To demonstrate the capability of this living glove, a glove-wearer holds cotton balls which have absorbed inducers. Those chemicals from the cotton ball would diffuse through the hydrogel and induce fluorescence in the engineered bacteria. For example, gripping a wet cotton ball that contains IPTG and Rham results in fluorescence at two of the three bacterial sensors that contains $IPTG_{RCV}$/GFP (indicated as *) and $Rham_{RCV}$/GFP (indicated as ***) on the glove within 4 h. The middle sensor containing AHL_{RCV}/GFP (indicated as **) remains unaffected (**Figure 4-4f-h**). Thus, from the fluorescence at fingertips of gloves, you can read out the substances contained in the cotton balls you have grabbed. Both prototypic living wearable devices, including the living patch and biosensing glove, demonstrate the potential of living materials as low-cost and mechanically flexible platforms for healthcare and environmental monitoring.

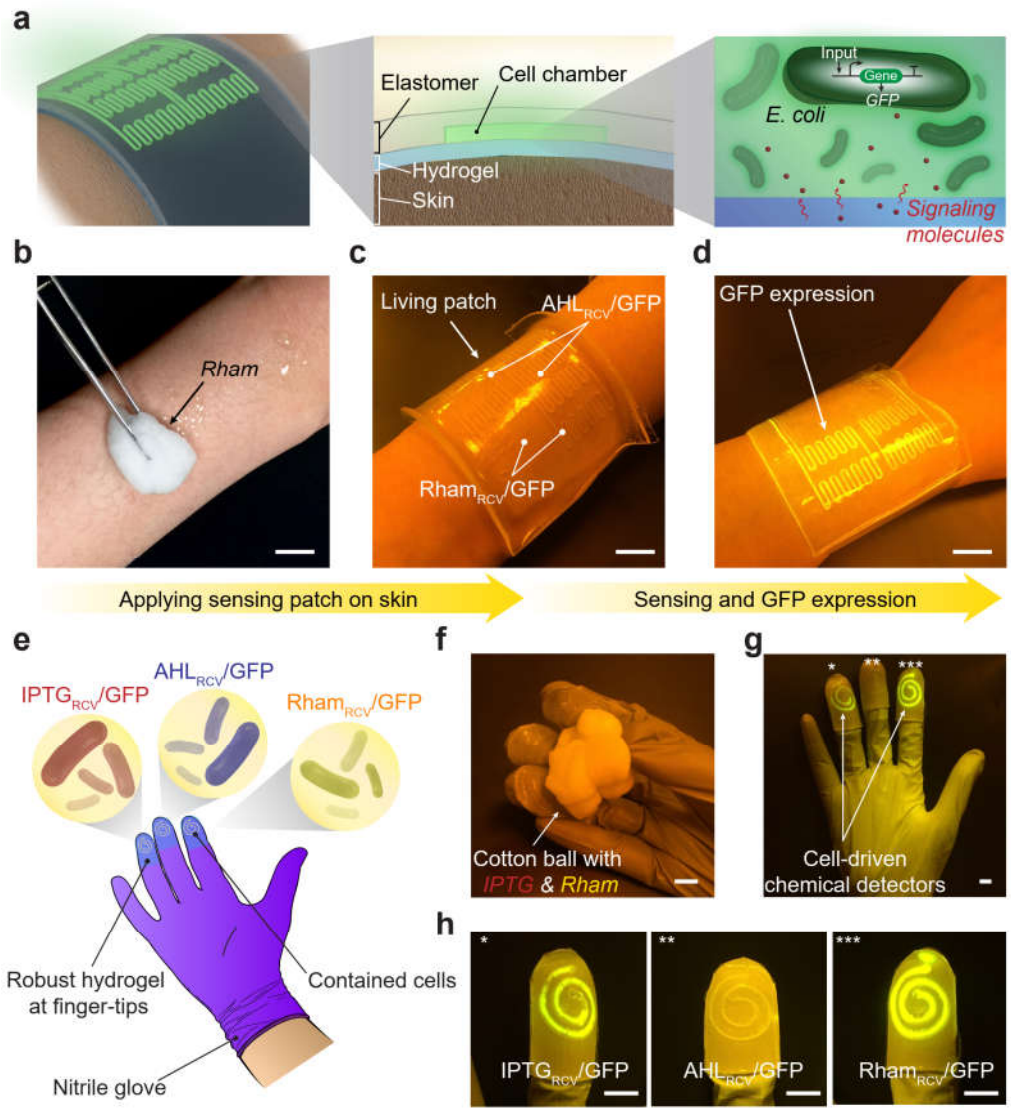

Figure 4-4. Hydrogel–elastomer hybrids as living wearable devices. (a) Schematic illustration of a living patch. The patch adhered to the skin with the hydrogel side and the elastomer side is exposed to the air. Engineered bacteria inside can detect signaling molecules. (b-d) Rham solution is smeared on skin and the sensor patch is conformably applied on skin. The channels with Rham$_{RCV}$/GFP in the living patch became fluorescent, while channels with AHL$_{RCV}$/GFP do not show any differences. (e) Schematic illustration of a glove with chemical detectors robustly integrated at the fingertips. Different chemical-inducible cell strains, including IPTG$_{RCV}$/GFP, AHL$_{RCV}$/GFP, and Rham$_{RCV}$/GFP, are encapsulated in the chambers. (f-h) When the living glove is used to grab a wet cotton ball containing the inducers, GFP fluorescence is shown in the cognate sensors on the gloves. In contrast, the non-cognate sensor does not show any fluorescence. Scale bars are 10 mm in (b), (c) and (d), and 10 mm in (f), (g) and (h).

4.2.4. Design of 3D printed hydrogel structures

General design. The design principle for 3D printing of living materials and devices is illustrated in **Figure 4-5a**. On one hand, living cells as responsive components can be genetically engineered

to possess various functions, including biosensing[408], drug production[409], chemical secretion[410], and programmed cell death[372]. On the other hand, the architectures of living materials and devices can be programmed by 3D printing, including the microstructures of the hydrogel matrices, and the distribution of cells and chemicals within the matrices[395, 396]. We can simulate the chemical diffusion and cell reaction in the 3D printed living networks and predict the behaviors of living materials under various conditions[411, 412]. In turn, the spatiotemporal responses of cells and matrices can provide rational feedback and guidance for the design of living materials and devices, thus enabling the programmable customization of living materials with predictable responsiveness.

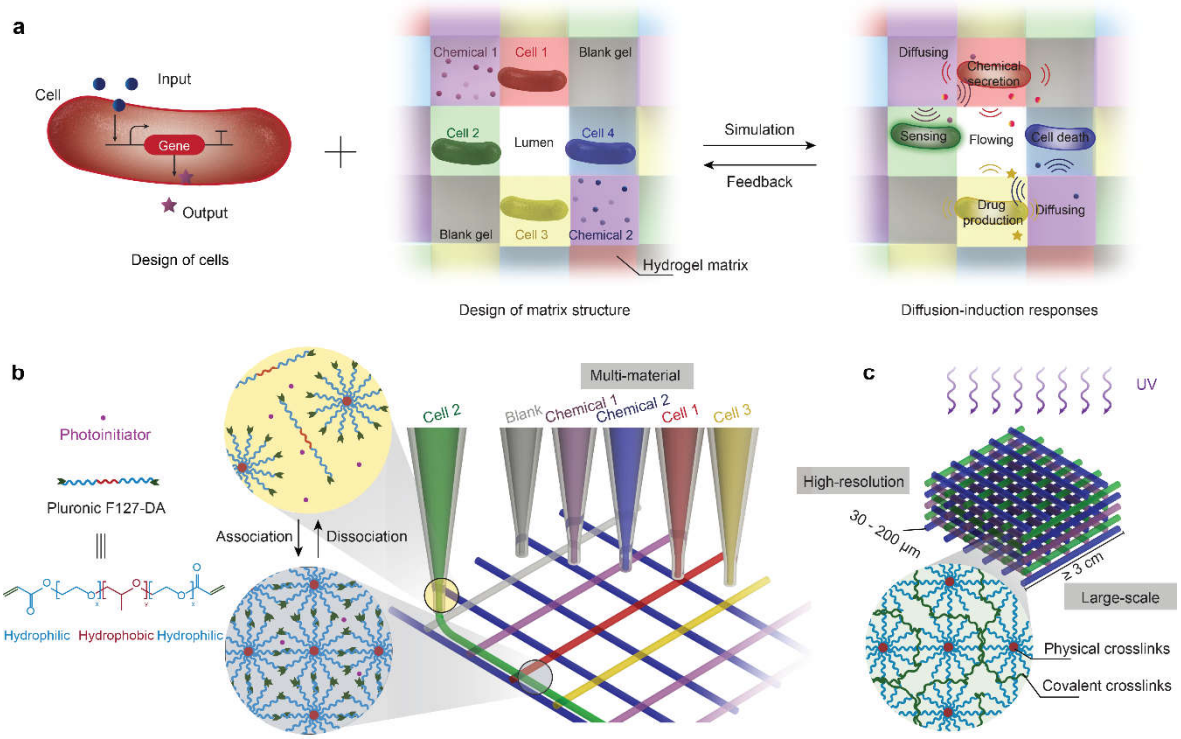

Figure 4-5. Design of 3D printed hydrogel structures. (a) Schematic workflow of living material design, which can be achieved by combined genetic circuit design in the encapsulated cells and structural design of living materials. The responses of living materials, including chemical diffusion and cell induction, can be predicted by simulation, which can provide feedback for living material design. (b) Schematic illustration shows direct writing of hydrogel inks. The packing of Pluronic F127-DA micelles in the ink leads to a physically crosslinked hydrogel, which is fluidized by shear force during ink extrusion and recovers to the packing state right after printing. (c) Schematic illustration shows that covalent crosslinks form among micelles after UV crosslinking. The fabrication process from (b) to (c) results in a large-scale, high-resolution, and multi-ink living material.

4.2.5. Fabrication of 3D printed hydrogel structures

Printing ink. Ink design is critical to ensure the viability and responsiveness of cells in living networks. Our ink system for 3D direct ink writing is based on a well-dispersed mixture of photoinitiator and polymeric micelles in water, with the addition of certain engineered bacterial cells, signaling chemicals, and nutrients. The components serve different purposes in the printing ink: Pluronic F127 diacrylate (Pluronic F127-DA) micelles provide ideal rheological behaviors required for direct ink writing, and the packing of Pluronic F127-DA micelles in the ink leads to a physically crosslinked hydrogel after printing[413]; Irgacure 2959 as a photoinitiator allows post-photocrosslinking of the living structures after printing; engineered bacterial cells are programmed to sense the signaling chemicals and respond with fluorescence and chemical secretion; signaling chemicals, including AHL, IPTG, Rham, and aTc, are allowed to diffuse in the matrices and interact with different cell types; LB broth is used as the nutrient to maintain the viability and functionality of cells presented within matrices. Bacterial cells used in this study are engineered with different responsive functions: GFP+ strain expresses GFP constitutively; AHL/GFP+, Rham/GFP+, or IPTG/GFP+ strain produces GFP when chemical inducer AHL, Rham, or IPTG is received by the cognate cell strain, respectively; aTc/AHL+ strain secretes AHL when aTc is detected by the cell strain; AHL/GFP− strain can repress GFP production in cell when AHL is detected.In all, the living ink system provides a nourishing, biocompatible environment for cell survival and function (**Figure 4-5b,c**).

Printing process. The 3D printing process for living materials consists of two steps: (i) direct writing of multiple hydrogel inks with various types of cells and chemicals (**Figure 4-5b**), and (ii) ultraviolet (UV) curing of the printed constructs (**Figure 4-5c**). During the direct ink writing, the nozzle diameter we adopt ranges from 30 μm to 200 μm, the nozzle feed rate is fixed at 5 mm/s, and the printing pressure is set as 90 kPa. We show that the mechanically reversible, rapidly responsive dissociation/association of Pluronic F127-DA micelles in water (**Figure 4-5b**) endows the ink with a strong shear-thinning effect during printing, and a plateau storage modulus (G') orders of magnitude higher than loss modulus (G") after printing[33]. Thus, the Pluronic F127-DA micelles provide suitable rheological behaviors for 3D living printing. During UV irradiation, the printed sample is exposed to 1 J m^{-2} UV for 5 min. The photocrosslinking is carried out under a humid nitrogen atmosphere to prevent hydrogel dehydration and oxygen inhibition of

polymerization. The reactive end groups in Pluronic F127-DA enable the formation of covalent crosslinks among micelles after UV crosslinking (**Figure 4-5c**). The resultant hydrogel is mechanically robust and stretchable, with shear modulus of 50 kPa, toughness of 77 J m^{-2}, failure stretch of 162%, and fast recovery of elasticity within 1 min[33]. The mechanical robustness and structural integrity of hydrogel matrices can potentially enable applications of living devices that require mechanical reliability under cyclic deformation and robust integration with other engineering materials[30, 31, 414].

Printability. To systematically evaluate the printability of the living ink, we vary the printing pressure and Pluronic F127-DA concentration in the ink, while fixing other parameters including nozzle diameter, nozzle feed rate, and ink compositions (e.g., cells, nutrients). We find the ink can be printed into 3D structures when the concentration of Pluronic F127-DA is between 18 wt% and 36 wt% and the pressure is above a certain threshold, as shown in **Figure 4-6a**. When Pluronic F127-DA concentration is below 18 wt% or above 36 wt%, the ink cannot be printed due to liquid spreading or nozzle clogging, respectively; and when the printing pressure is below the threshold value, the ink cannot flow out of the nozzle (**Figure 4-6a**). In addition, we find that the printability of the ink is independent of nozzle dimensions (30-200 μm) for the ink composition used in this study (**Figure 4-6a**).

Printed structures. To demonstrate the capability of printing large-scale and complex structures with multi-material inks, various 3D architectures are printed (**Figure 4-6b-f**), including a cuboid, a pyramid, a dome, and hollow pyramids. The overall dimensions of the printed architectures can reach up to 3 cm. The first three cases (cuboid, pyramid and dome, **Figure 4-6b-d**) show the capability of printing any solid constructs. In addition, the last two examples (hollow pyramids, **Figure 4-6e,f**) show that overhanging beams can be printed and the printed structures can be self-supporting due to the high yield stress of the ink materials. The multiple materials (red and green inks, **Figure 4-6f**) printed in selective regions of the last hollow pyramid demonstrate that our 3D printing technique is capable of integrating various types of cells and chemicals into a single construct. In addition, the 3D printing method can achieve very high spatial resolution as demonstrated in the printed grid microstructures with different local dimensions (**Figure 4-6g-j**). With encapsulated GFP+ bacterial cells, the grid microstructures of hydrogel matrices are clearly

visualized under confocal microscope, with feature sizes varying from 200 μm (**Figure 4-2g**), 100 μm (**Figure 4-6h**), 50 μm (**Figure 4-6i**), to 30 μm (**Figure 4-6j**). Therefore, we can create complex macroscopic structures (3 cm) with microscopic precision (30 μm) through the 3D multi-material printing method.

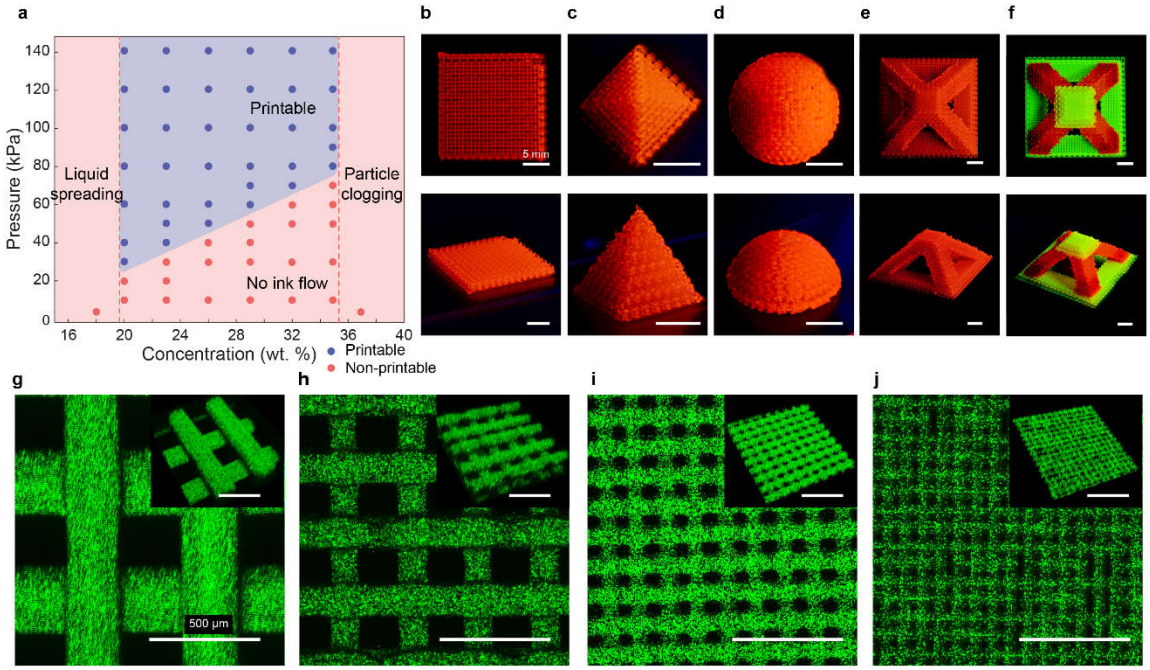

Figure 4-6. High printability of the hydrogel ink into large-scale, high-resolution living structures. (a) Phase diagram for the printability of Pluronic F127-DA ink. The ink can be printed into structures when the concentration of Pluronic F127-DA is between 18 wt% and 36 wt% and the pressure is above a certain threshold. When Pluronic F127-DA concentration is below 18 wt% or above 36 wt%, the ink cannot be printed due to liquid spreading or particle clogging, respectively; and when the printing pressure is below the threshold value, the ink cannot flow out of the nozzle. (b-f) Optical images of various architectures generated by 3D printing, including a cuboid (b), a pyramid (c), a dome (d), and hollow pyramids (e-f). Red color denotes hydrogel ink with rhodamine B, and green color denotes hydrogel ink with fluorescein. (g-j) Confocal top-view images of GFP+ bacterial cell-laden hydrogel scaffolds with a wide range of printing resolutions, including 200 μm (g), 100 μm (h), 50 μm (i), and 30 μm (j). Insets: 3D reconstructed images of GFP+ bacterial cell-laden hydrogel scaffolds. Scale bars are 5 mm in (b)-(f), and 500 μm in (g)-(j).

4.2.6. Bacterial evaluation in 3D printed hydrogel structures

Bacterial viability. The 3D printing method and the ink materials can also give very high viability of bacterial cells in the printed living networks[33], due to the following reasons. First, all ink components including Pluronic F127-DA and Irgacure 2959 are biocompatible[413, 415]. Second, the fabrication processes, including microextrusion (i.e., 90 kPa pressure) and UV irradiation (i.e.,

1 J m^{-2} UV for 5 min) are mild for the encapsulated bacterial cells[396]. Bacterial cells with protective cell walls are able to survive relatively harsh conditions (such as shear force during extrusion and UV exposure during crosslinking) compared with more susceptible mammalian cells[34]. Third, hydrogel matrices can supply water and nutrients to cells, and ensure diffusion of signaling chemicals in the encapsulated multicellular system[55], while fine features (30~200 μm) of the matrices allows for sufficient gas permeation[416]. To test cell viability in the hydrogel matrices, we use live/dead stain and fluorescence imaging for the cells in hydrogel matrices (200 μm and 100 μm in feature sizes). Bacterial cells are highly viable (i.e., viability >95%) 24 h after printing[33]. Therefore, the 3D printed microstructures provide a biocompatible, mechanically soft and robust matrix that supply nutrients and water for genetically engineered microorganisms, and ensure the successful operation of living materials over time.

4.2.7. Prototypes of hydrogel–elastomer hybrids

The 3D printing of living materials and devices enable us to explore novel functions, including logic gates, spatiotemporally responsive patterning, and wearable devices.

Logic gates. With the rapid development in synthetic biology, single cells have now been engineered to have new functions such as logic, memory, oscillator, and classifier[377, 408, 417]. To enable multicellular logic and guide signaling transmission for cell-cell communication, we print multiple types of cells and chemicals into 3D architectures and allow communication between different cell types to follow the well-defined structures of hydrogel matrices, thus achieving logic gates in the 3D printed living materials and devices (**Figure 4-7a,b**). Each cell in the structure performs a simple computational operation. However, combined with their spatial distributions in the 3D architectures, the interactions among different cell types and chemicals in different locations can induce the emergence of informative patterns and achieve complex logic programs. For example, to perform one-input-one-output logic computation, we print orthogonally distributed hydrogel filaments; the rows contain chemicals which act as input, while the columns contain cells which act as output (**Figure 4-7a,c**). For two-input-one-output Boolean logic gate, we print three types of crossed hydrogel filaments; the top rows contain input a, the bottom rows contain input b, and the columns in between contain cells which act as output (**Figure 4-7b,c**). The input hydrogels remain dark no matter if they are 0 or 1, while the output hydrogel columns can be either green (1) or dark (0). As shown in **Figure 4-7c**, Buffer, NOT, AND, OR, and NAND

gates are implemented by depositing different cells and chemicals in the constructs. In the Buffer gate, the output (AHL/GFP+ cells) is originally dark in the absence of AHL, while the presence of AHL can activate fluorescence in cells. In the NOT gate, the output (AHL/GFP− cells) is originally green in absence of NOT input, while the presence of an inhibitor (AHL) can repress GFP synthesis. In the AND gate, the AHL/GFP+ cells become green only when both input a (aTc) and input b (aTc/AHL+ cells) are present. In the OR gate, the output, containing two cell types, AHL/GFP+ cells and Rham/GFP+ cells, turns on when either AHL or Rham are present. In the NAND gate, aTc and aTc/AHL+ cells act as two inputs which can induce the disappearance of green fluorescence in the output (AHL/GFP− cells). While logic gates that use non-living chemical and hydrogels have been reported[418, 419], here we demonstrate the first set of 3D-printed living logic gates using hydrogels and programmed cells. These intricate structures, enabled by 3D multi-material printing, provide well-organized, higher-level living cell networks that integrate multiple input signals for intelligent applications, including decision making and actuation in complex environments[417].

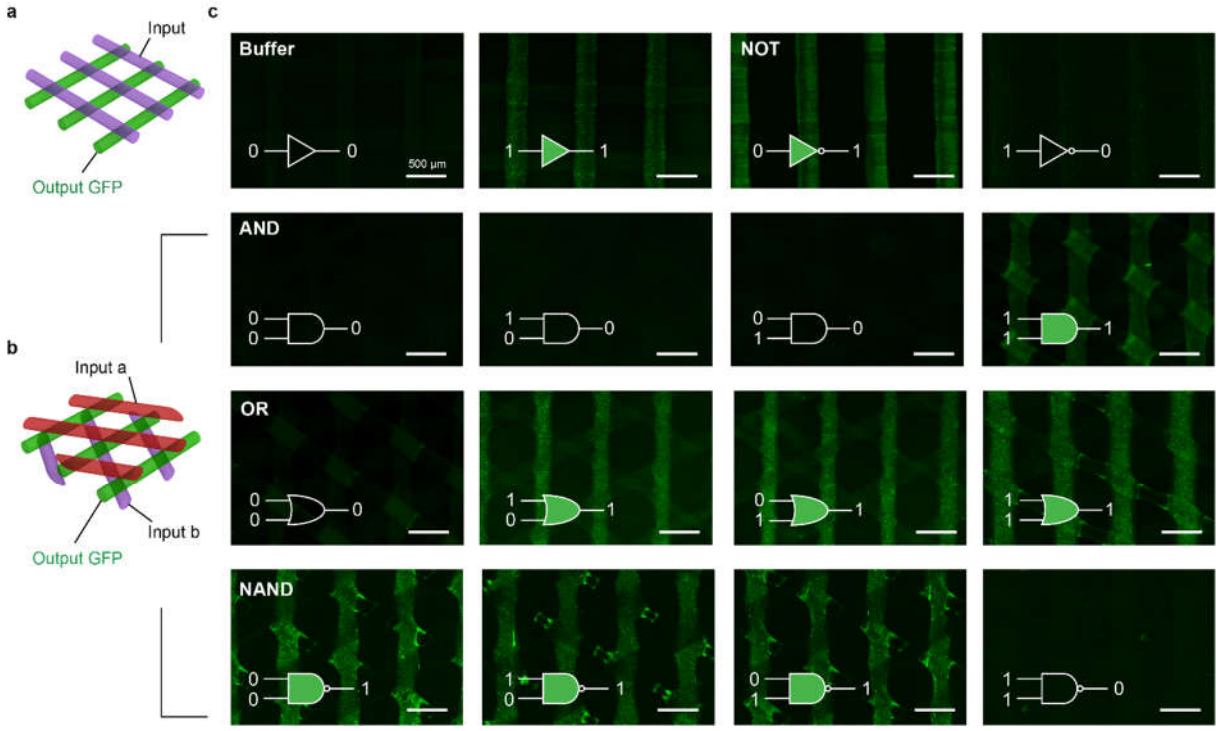

Figure 4-7. Logic gates achieved by multi-ink 3D printing of living materials. (a) Schematic illustration of a 3D-printed living scaffold that can function as a one-input-one-output Boolean logic gate. (b) Schematic illustration of a 3D-printed living scaffold that can function as a two-input-one-output Boolean logic gate. (c) Experimental results of logic gates, indicated by green fluorescence in one layer of the printed hydrogel containing the output. The input hydrogel layer remains dark no matter if it is 0 or 1, while the output hydrogel layer can be either green (1) or

dark (0). The symbols show the inputs, computation, and outputs for each condition. Buffer gate input: AHL in hydrogel, output: AHL/GFP+ bacterial cells in hydrogel. NOT gate input: AHL in hydrogel, output: AHL/GFP- bacterial cells in hydrogel. AND gate inputs: aTc in hydrogel, aTc/AHL+ bacterial cells in hydrogel, output: AHL/GFP+ bacterial cells in hydrogel. OR gate inputs: AHL in hydrogel, Rham in hydrogel, output: a mixture of AHL/GFP+ bacterial cells and Rham/GFP+ bacterial cells in hydrogel. NAND inputs: aTc in hydrogel, aTc/AHL+ bacterial cells in hydrogel, output: AHL/GFP- bacterial cells in hydrogel. Scale bars are 500 μm in c.

Spatiotemporal patterns. Next, we demonstrate the capability of 3D printed living materials to achieve spatiotemporally controlled patterning, due to well-defined spatial distribution and time evolution in the living devices. We choose two exemplary living patterns: a 1D pattern composed of parallel cell lines and a perpendicular chemical line (**Figure 4-8a**), and a 2D pattern composed of concentric cell rings with radial chemical lines (**Figure 4-8e**). The encapsulated cells we use in this particular experiment is AHL/GFP+ and the encapsulated chemical is AHL. For the 1D living pattern, the set of experimental images (**Figure 4-8b**) reveal the spatiotemporal evolution of fluorescence in the living materials over 8 h. Similarly, the spatiotemporal fluorescence in the circular 2D living pattern over 4 h is shown in the experimental images (**Figure 4-8f**). In both cases, the frontline of responded cells (i.e., turning fluorescent) within the hydrogel propagates along the paths for diffusion of signaling chemicals, and the fluorescence intensity of responded regions increases over time. We further develop a coupled diffusion-induction model that accounts for the chemical and cellular behaviors to predict the spatiotemporal responses of the living patterns. The prediction of the spatiotemporal patterns of the 3D printed living materials relies on the understanding of two processes: (i) diffusion of signaling chemicals in hydrogel matrices and (ii) induction of hydrogel-encapsulated bacterial cells by signaling chemicals. The governing equations for these two processes are adopted from classical models (see details in Model of 3D printed hydrogel structures) [55, 411]. To solve the governing equations, numerical models are developed for the living patterns using COMSOL Multiphysics. As shown in **Figure 4-8**, the good agreement between experiments and simulations validates the predictability of our models. Therefore, the design of 3D living materials and devices can be rationally guided by such predictive models that account for the responses of cells and hydrogel matrices.

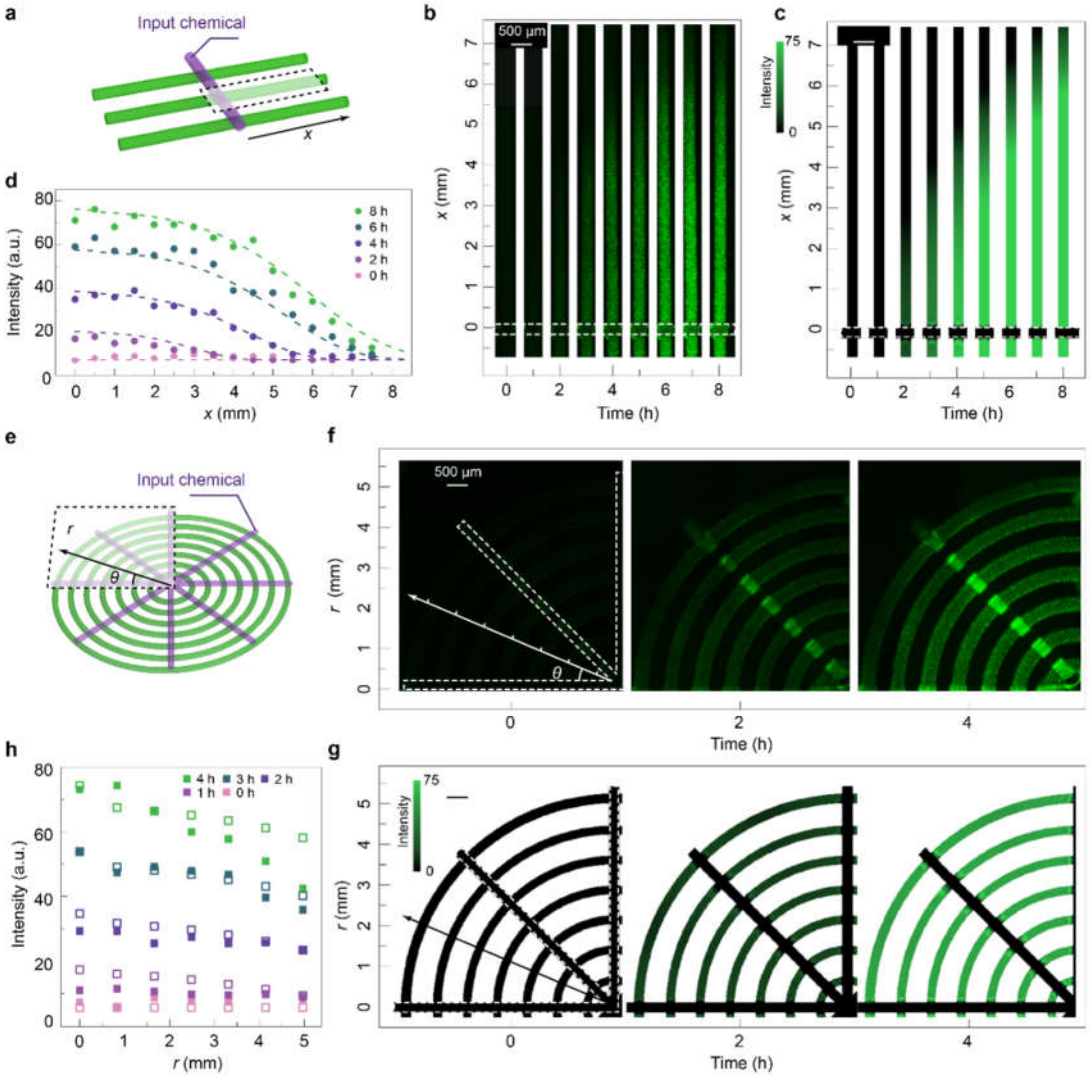

Figure 4-8. Spatiotemporal patterning of 3D printed living materials. (a) Schematic illustration of a one-dimensional living structure. (b) Spatiotemporal evolution of fluorescence in a straight line of the living structure (a) from experiments. (c) Spatiotemporal evolution of fluorescence in a straight line of the living structure (a) from simulation. (d) Quantitative comparison of fluorescence intensity over time in a straight line of the living structure (a) from experiments (solid dots) and simulations (dash lines). (e) Schematic illustration of a two-dimensional living structure. (f) Spatiotemporal evolution of fluorescence in a segment of the living structure (e) from experiments. (g) Spatiotemporal evolution of fluorescence in a segment of the living structure (e) from simulation. (h) Quantitative comparison of fluorescence intensity profiles over time along r in different rings of the living structure (θ = 22.5° in (e) from experiments (solid squares) and simulations (hollow squares). Scale bars are 500 μm in b, c, f and g.

Living tattoos. The 3D printing of programmed cells enables us to explore novel functions of living devices otherwise unachievable with structural design, printing fabrication, or genetic engineering alone. A living tattoo is designed to integrate a collection of multiple chemical-sensing

cells (responsive to AHL, Rham, IPTG) printed on the surface of a bilayer elastomeric sheet, and carefully attached to human skin (**Figure 4-9a**). The thin (~75 μm), flexible, transparent, and gas permeable bilayer elastomeric sheet is fabricated by successive spin-coating deposition of two silicone elastomeric layers, where the upper layer (Sylgard 184) is mechanically robust and flexible, and the lower layer (Silgel 613) is skin-adhesive which gives robust bonding to skin via van der Waals forces alone without the need for any additional fixtures or tape (**Figure 4-9a**). The living device does not impose any mass loading on the skin nor mechanical constraint of the body motion[420]. As shown in **Figure 4-9b**, the skin can deform in different modes (i.e., stretching, compression, and twisting) freely and reversibly without any detachment of the living tattoo. Moreover, robust bonding between the hydrogel and the elastomer sheets and their mechanically soft nature prevents detachment[31, 421]. Further, the elastomer layer effectively reduces water loss from the printed hydrogel, and thus maintains cell viability and device functionality[31]. To examine practical applications of the living tattoo, three signaling chemicals (e.g., AHL, Rham, IPTG) are smeared on the skin, respectively. When the chemicals are received, the adhered tattoos exhibit green fluorescence in corresponding hydrogel printing patterns. The monitoring of different chemicals by the living tattoo device on the skin is shown by experimental (**Figure 4-9c**) results.

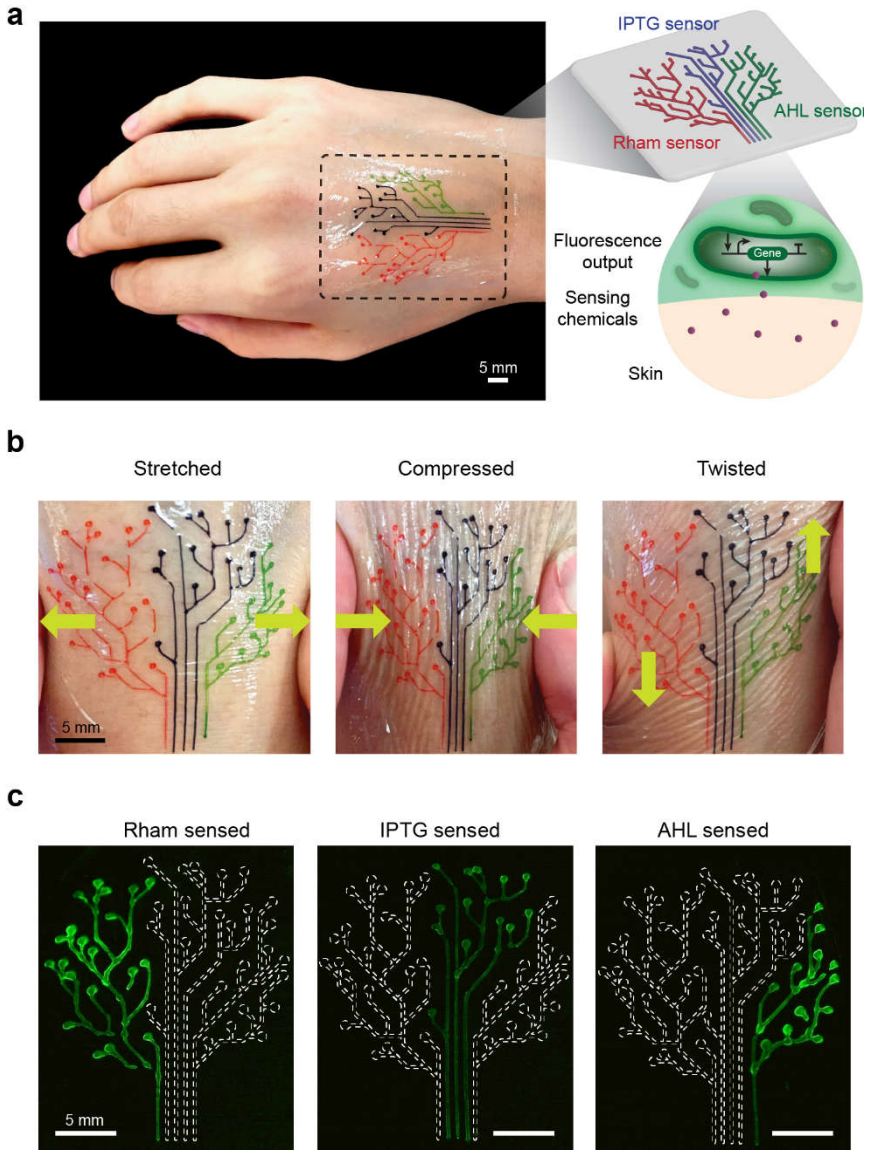

Figure 4-9. 3D printed living tattoo for chemical detection on human skin. (a) The design of the living tattoo. Right: the tattoo is printed as a tree-like pattern on a thin elastomer layer, which is then adhered to human skin. Hydrogels with different colors illustrate the different types of cells encapsulated. Left: schematic illustration of living sensors embedded in the tattoo, which can respond to different chemicals by emitting fluorescence. (b) The living tattoo on skin in different states: stretched (left), compressed (middle), and twisted (right). Food dyes are added to facilitate visualization of the hydrogel pattern in (a-b). (c) The response of the living tattoo on the skin smeared with Rham (left), IPTG (middle), or AHL (right).

4.3. Modeling

4.3.1. Model of hydrogel–elastomer hybrids

The functions of living materials and devices rely on the transportation coupled with the cellular responses. In this section, we develop a model that quantitatively accounts for the physical and

biochemical mechanisms underlying the living sensor (**Figure 4-2**). The framework of the model is also applicable to other living materials and devices. The operation of the living sensor (**Figure 4-2a**) relies on two processes: diffusion of signaling molecules from the environment through the hydrogel window into cell chambers, and induction of the encapsulated bacterial cells by the signaling molecules [411, 422].

Chemical diffusion. The transportation of signaling molecules in the hydrogel window and the cell chamber is assumed to follow the Fick's law. Given the geometry of the senor (**Figure 4-10**), we could approximate the transportation to follow the one-dimensional diffusion equation

$$\frac{\partial I}{\partial t} = D_g \frac{\partial^2 I}{\partial x^2} \quad \text{for } 0 \le x < L_g \tag{4-1}$$

$$\frac{\partial I}{\partial t} = D_c \frac{\partial^2 I}{\partial x^2} \quad \text{for } L_g \le x < L_g + L_c \tag{4-2}$$

where x is the coordinate of a point in the hydrogel window or the cell chamber; L_g and L_c are the thicknesses of the hydrogel window and cell chamber, respectively; t is the current time; I is the moles of the signaling molecules (inducers) per unit volume of hydrogel or medium in the cell chamber (i.e., inducer concentration); and D_g and D_c are the diffusion coefficients of the inducer in hydrogel and medium, respectively.

To prescribe boundary conditions for **Equations 4-1 and 4-2**, the inducer concentration at the boundary between the environment and the hydrogel window is taken to be a constant I_0, the inducer concentration and inducer flux is taken to be continuous across the interface between the hydrogel window and cell chamber, and the elastomer wall of the cell chamber is taken to be impermeable to the inducers. Since the diffusion process begins at $t = 0$, the inducer concentration throughout the hydrogel window and cell chamber is zero when $t \le 0$, as the initial condition for **Equations 4-1 and 4-2**. Furthermore, the consumption of inducers by the bacterial cells is taken to be negligible. In the current experiments, we set $L_g = 5 \times 10^{-4}\ m$, $L_c = 2 \times 10^{-4}\ m$, and $I_0 = 1\ mM$ for IPTG diffusion-induction experiment. The diffusion coefficients of inducers are estimated to be $D_g = 3 \times 10^{-10}\ m^2/s$, $D_c = 1 \times 10^{-9}\ m^2/s$ based on previous measurements [215, 423].

The one-dimensional diffusion equations together with boundary and initial conditions are solved using COMSOL Multiphysics. In **Figure 4-10c**, we plot the inducer concentrations throughout the hydrogel window and cell chamber at different times. It can be seen that the distribution of inducers in the cell chamber is more uniform than that in the hydrogel due to higher inducer diffusion coefficients in media than in hydrogel. We further define the typical inducer concentration in the cell chamber I_c as the inducer concentration at the center of the cell chamber (i.e., $I_c = I(t, x = L_g + L_c / 2)$). In **Figure 4-10d**, we plot the typical inducer concentration in the cell chamber as a function of time.

Cellular induction. To characterize the GFP expression of the bacterial cells in the living sensor, we adopt a model from Leveau [424]. The inducers can bind with repressors or activators in a bacterial cell, and induce the transcription of promoters. The induced promoters initiate the synthesis of nonfluorescent GFP (^{n}GFP). Meanwhile, the ^{n}GFP in the cell are consumed due to their maturation into the fluorescent form of GFP (^{f}GFP), cell division, and protein degradation. The converted ^{f}GFP also undergoes consumption due to cell division and protein degradation. Eventually, the syntheses and consumptions of ^{n}GFP and ^{f}GFP reach steady states in the cell (**Figure 4-10b**). Denoting the numbers of ^{n}GFP and ^{f}GFP in a cell as n and f respectively, their rates of variation can be approximated as [425]

$$\frac{\partial n}{\partial t} = P - m \cdot n - \mu \cdot n - C_n \tag{4-3}$$

$$\frac{\partial f}{\partial t} = m \cdot n - \mu \cdot f - C_f \tag{4-4}$$

In **Equations 4-3 and 4-4**, P is the promoter activity that expresses ^{n}GFP, $m \cdot n$ prescribes the maturation rate of ^{n}GFP into ^{f}GFP where m is the maturation constant, $\mu \cdot n$ and $\mu \cdot f$ prescribe the consumption rates of ^{n}GFP and ^{f}GFP due to cell division where μ is the growth constant, C_n and C_f are the degradation rates of ^{n}GFP and ^{f}GFP, respectively. The promoter activity including transcription and translation induced by an inducer is approximated by a Hill equation [425]:

$$P = P_{\max} \frac{I^h}{I^h + K^h} \tag{4-5}$$

in which $P_{\max}$ is the maximum rate of ^{n}GFP expression (i.e., maximum promoter activity), h is the Hill coefficient, K is the half-maximal parameter (inducer concentration at which P equals $0.5P_{\max}$). Since the inducer concentration in the cell chamber is relatively uniform (**Figure 4-10c**), we take I in **Equation 4-5** to be the typical inducer concentration in the cell chamber (i.e., $I = I_c$). Evidently, the coupling between the transportation of signaling molecules (e.g., inducers) and biochemical responses of cells (e.g., expression of GFP) in the living sensor is through **Equation 4-5**. When $\frac{\partial n}{\partial t} = \frac{\partial f}{\partial t} = 0$, we can obtain the steady-state ^{n}GFP content and ^{f}GFP content as

$$n_{ss} = \frac{P - C_n}{m + \mu} \tag{4-6}$$

$$f_{ss} = \frac{m \cdot n_{ss} - C_f}{\mu} \tag{4-7}$$

Since the half-life of GFP in E. coli is over 24 h in absence of any proteolytic degradation, much longer than the typical responsive time of the living sensor, we assume C_n and C_f are equal to zero throughout the current study. For the IPTG$_{RCV}$/GFP strain, we take $P_{\max} = 1000\ s^{-1}$, $K = 0.3\ mM$, $h = 2$, $m = 1.16 \times 10^{-2}\ s^{-1}$, and $\mu = 1.20 \times 10^{-4}\ s^{-1}$ based on previously reported data on this system [424, 426, 427].

Coupled diffusion-induction. In **Figure 4-10e**, we plot the normalized fluorescence of bacterial cell as a function of time after the inducers are added outside the living device. It can be seen that it takes around 2 h for different strains in the living sensor to demonstrate significant fluorescence (e.g., 0.5 of the maximum fluorescence). For the IPTG$_{RCV}$/GFP strain, the diffusion-induction coupled model matches very well with experimental data (**Figure 4-10e**). Although the responsive time of the current living senor is relatively long (i.e., on the order of hour), it can be significantly shortened by designing bacterial strains with faster response and by using hydrogel window with thinner dimension.

Critical time scales in hydrogel–elastomer hybrids. From the above analysis, we know that the responsive time of a living material or device is determined by two critical time scales: the time for signaling molecules to diffuse and accumulate around a cell to the level that is sufficient for

induction $t_{diffuse}$, and the time to induce GFP expression and reach a steady state t_{induce}. To obtain analytical solutions for $t_{diffuse}$, we develop a simple yet relevant model similar to the geometry of the living sensor (**Figure 4-10a**), but assumes that the cells are embedded in a segment of hydrogel close to the elastomer wall. The inducer concentration in the environment is taken to be constant I_0 and the total thickness of the hydrogel is L (**Figure 4-10f**). By means of multiple imaginary sources [428], the inducer concentration at location L (at the end of hydrogel) and time t can be expressed as

$$\frac{I(L,t)}{I_0} = 2erfc\left(\frac{L}{2\sqrt{D_g t}}\right) - erfc\left(\frac{L}{\sqrt{D_g t}}\right) \tag{4-8}$$

where $erfc(\bullet)$ is the complementary error function. In **Figure 4-10g**, we plot $I(L,t)/I_0$ from **Equation 4-8** and compare it with $I(L_g + L_c/2, t)/I_0$ from the model of the living sensor (**Figure 4-10a**). Despite small deviation ($< 12\ \%$) due to the diffusivity differences between hydrogel and medium and distance variation in two cases, it can be seen that $I(L,t)/I_0$ from **Equation 4-8** can consistently represent the typical concentration profile in the cell chamber of the living sensor at any time. Therefore, the solution of **Equation 4-8** is used to obtain the critical diffusion time scale. From **Equation 4-5**, we assume that only when the inducer concentration at a point reaches the level of K (i.e., $P = P_{\max}/2$), the inducer concentration is sufficient to induce the cells. Therefore, we can calculate the critical diffusion time $t_{diffuse}$ for cells with a typical distance L from the environment (i.e., around the elastomer wall in **Figure 4-10f**) to be

$$t_{diffuse} = \left[\Lambda\left(K/I_0\right)\right]^{-2} \frac{L^2}{D_g} \tag{4-9}$$

where $\Lambda(\bullet)$ is the inverse of function of $\Omega(x) = 2erfc\left(\frac{x}{2}\right) - erfc(x)$, L^2/D_g is the typical diffusion time scale, and the pre-factor $\left[\Lambda\left(K/I_0\right)\right]^{-2}$ accounts for the difference between I_0 and K. We further fit the pre-factor into a power law that approximately gives (**Figure 4-10h**)

$$t_{diffuse} \approx \frac{4}{9}\left(\frac{I_0}{K} - 1\right)^{-0.56} \frac{L^2}{D_g} \tag{4-10}$$

We next evaluate the time scale to induce the cell t_{induce}. When the inducer concentration around a cell reaches the level of K (i.e., P reaches the level of $0.5P_{\max}$ from **Equation 4-5**), significant induction (e.g., expression of GFP) will occur in the cell. To solve **Equations 4-3 and 4-4** analytically, we assume that the induction happens only after P reaches the level of $0.5P_{\max}$, and P maintains at a constant level (between $0.5P_{\max}$ and $P_{\max}$) during the induction. Therefore, we can set $n = f = 0$ as the initial condition for **Equations 4-3 and 4-4** and P as a time-independent constant in **Equations 4-3 and 4-4**. Further setting $C_n = C_f = 0$, we can obtain analytical solutions

$$n = \frac{P}{m+\mu}(1-e^{-(m+\mu)t}) \tag{4-11}$$

$$f = \frac{P}{m+\mu}(e^{-(m+\mu)t}-1) - \frac{P}{\mu}(e^{-\mu t}-1) \tag{4-12}$$

from which two characteristic time scales [i.e., $1/(m+\mu)$ and $1/\mu$] can be identified. From **Equation 4-11**, we know that the characteristic time scale for the expression of ^{n}GFP is $1/(m+\mu)$. In addition, since the maturation constant m is usually much larger than the growth constant μ [424, 429, 430], the second term of **Equation 4-12** has a much larger coefficient than the first term, and thus the second term dominantly characterizes the expression of ^{f}GFP with a characteristic time scale of $1/\mu$. Therefore, we approximate the critical time to induce the cell to reach steady-state fluorescence as

$$t_{induce} \approx \frac{1}{\mu} \tag{4-13}$$

Based on the known parameters for IPTG$_{RCV}$/GFP cells encapsulated in hydrogel at a typical distance of L (0.7 mm) from the environment, we can estimate the critical time scales of diffusion and induction to be $5\times10^{2}\ s$ and $8\times10^{3}\ s$, respectively. The induction of cells takes much longer time than the transportation of signaling molecules, which is consistent with the full model (**Figure 4-10d,e**). In total, the coupled diffusion-induction time scale is 2.4 h, which is also in good agreement with the full model's prediction (**Figure 4-10e**).

The above model and analysis can provide a few guidelines for the design of future living materials and devices. In order to design living materials and devices with faster responses, we

need shorter times for both $t_{diffuse}$ and t_{induce}. In order to decrease $t_{diffuse}$, one can (i) reduce the thickness of the hydrogel window but still maintain its robustness, (ii) increase the diffusivity of signaling molecules in the hydrogel, and (iii) increase the inducer concentration in the environment based on **Equation 4-10**. On the other hand, in order to decrease t_{induce}, one can design cells with higher maturation constants or growth constants, and add negative feedback into genetic circuit [431].

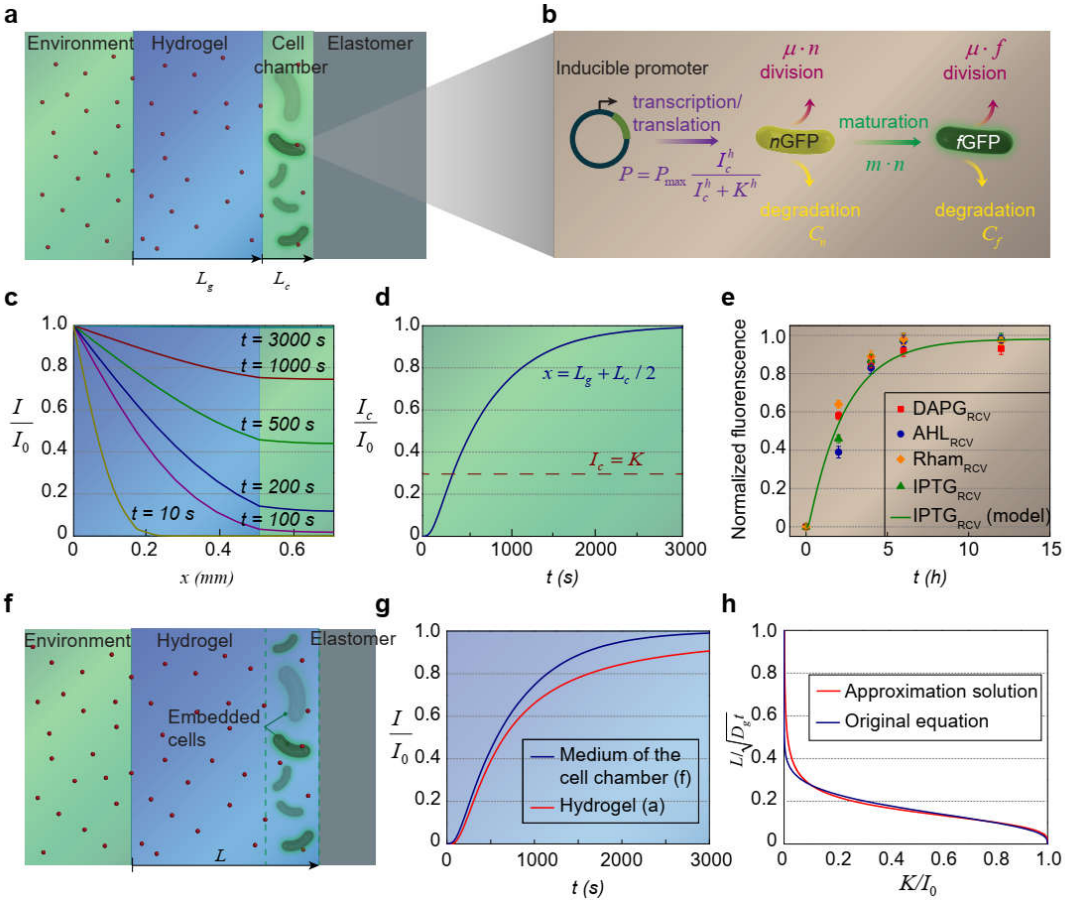

Figure 4-10. Model for the diffusion-induction process in hydrogel–elastomer hybrids. (a) Schematic illustration of the diffusion of signaling molecules from the environment through the hydrogel to cell chambers in the living device. (b) Diagram of GFP expression after induction with a small-molecule chemical. (c) Inducer concentration profile throughout the hydrogel window and cell chamber at different times. (d) Typical inducer concentration in the cell chamber as a function of time. (e) The normalized fluorescence of different cell strains as a function of time after addition of inducer. Dots represent experimental data, and curve represents model. (f) Schematic illustration of signaling molecule diffusion from the environment through the hydrogel in the living device. All cells are embedded in a segment of the hydrogel close to the elastomer wall. (g) Comparison of typical concentration profiles when cells are embedded in hydrogel ($I(L,t)/I_0$) versus cells embedded in medium in the cell chamber ($I(L_g + L_c/2, t)/I_0$). (h) The expression of the original

equation $K / I_0 = 2erfc\left(L / \left(2\sqrt{D_g t}\right)\right) - erfc\left(L / \sqrt{D_g t}\right)$ and its approximate solution $L / \sqrt{D_g t} = 1.5\left(I_0 / K - 1\right)^{0.28}$. Data in (e) are means ± SD, n = 3.

4.3.2. Model of 3D printed hydrogel structures

Quantifying the operation of 3D printed living materials requires a general model that accounts for the transportations of chemicals and the responses of cells in the materials[55, 411, 432]. The chemical diffusion in the hydrogel matrices is taken to follow the Fick's law[55]

$$\frac{\partial C}{\partial t} = -D\nabla C \tag{4-14}$$

where C is the moles of the signaling chemicals per unit volume of hydrogel (i.e., chemical concentration), *t* is the current time, and D is the diffusion coefficient of the chemical in hydrogel. The biochemical reactions in cells depend on the genetic circuits of different cell types. For the inducible GFP expression in cells, we adopt the induction model in previous works, which considers the processes of immature protein synthesis, protein maturation, cell division, and protein degradation[55, 424]. We denote the numbers of immature protein and mature protein in a cell as n and f, respectively, and the numbers of cell per unit volume (i.e., cell density) in the hydrogel as N. Their rates of variation can be expressed as[55, 411]

$$\frac{\partial n}{\partial t} = P_m \cdot \frac{C^h}{C^h + K^h} - m \cdot n - \mu \cdot (1 - \frac{N}{N_m}) \cdot n - k \cdot n \tag{4-15}$$

$$\frac{\partial f}{\partial t} = m \cdot n - \mu \cdot (1 - \frac{N}{N_m}) \cdot f - k \cdot f \tag{4-16}$$

$$\frac{\partial N}{\partial t} = \mu \cdot (1 - \frac{N}{N_m}) \cdot N \tag{4-17}$$

where P_m is the maximum rate of immature GFP expression, h is the Hill coefficient, K is the half-maximal parameter, m is the maturation constant, μ is the cell growth constant, N_m is the maximum cell density in hydrogel, and k is the degradation constant. Note that the measurable fluorescence intensity in the hydrogel is the number of fluorescent proteins per unit of volume in hydrogel, that is $N \cdot f$.

4.4. Materials and methods

4.4.1. Bacterial evaluation

Bacterial strains and plasmids. Plasmid construction and DNA manipulations were performed following standard molecular biology techniques. To create constructs for the expression of output genes under tight regulation by DAPG, IPTG, AHL, aTc, or Rham inducible promoters, pZE-AmpR-pL(lacO)-gfp (IPTG inducible) was used as a starting point. All promoters were amplified using polymerase chain reaction (PCR) and inserted in place of pL(LacO) by Gibson assembly. The corresponding repressors or activators, which can interact with small molecule inducers, were inserted into the E. coli genome or cloned onto the same plasmid that harbors the promoter-gfp output module. For example, the proteins PhlF and LacI repressed DAPG and IPTG inducible promoters, respectively. PhlF was inserted in a plasmid under regulation of proD promoter, whereas the LacI repressor was already present in the genome of DH5αPRO. Similarly, the AHL-inducible transcriptional activator, LuxR, was constitutively expressed from a plasmid and can activate promoter pLuxR upon binding to AHL. The regulatory components necessary for Rham induction were already present in E. coli genome and did not required further engineering. The constitutive promoter pGlpT, aTc-inducible promoter pTet, and output genes, including LuxI and cI, were incorporated in the different plasmids. To construct the AHL sender plasmid, LuxI was put onto a plasmid under the regulation of aTc-inducible promoter PLtetO. For AHL/GFP−, the cI/pLam invertor was cloned under the pLux promoter, and followed by a short-lived gfp-LVA reporter. The constructed plasmids were transformed into E. coli strain DH5αPRO using standard protocols.

Bacterial viability. By utilizing the live/dead BacLight kit in combination with flow cytometry, the cell viability assay was conducted according to kit protocol [433]. The fluorescent live/dead BacLight viability kit consists of two stains: the green fluorescent nucleic acid stain SYTO 9, which stains the nucleic acids of both living and dead bacteria, and the red fluorescent nucleic acid stain propidium iodide, which only stains bacteria that have damaged and leaky membranes. Bacterial suspensions were retrieved from the hydrogel-elastomer hybrids by poking a hole from the hydrogel using metal needles after 12 h culturing. Live-cell controls (untreated) and dead-cell controls (isopropyl alcohol-treated) were set as standards. A diluted bacterial suspension and the live/dead BacLight solution were mixed together and incubated at room temperature protected from light for 15 min. The stained cell samples were then analyzed by an LSRFortessa flow

cytometer (BD Biosciences). For each sample at least 10^4 events were recorded using a flow rate of 0.5 μL/s. FlowJo (TreeStar) was used to analyze the data. All events were gated by forward scatter and side scatter. In the 3D printed hydrogel structures, we stained the cells using the live/dead BacLight bacterial viability kit. 15 min after staining, fluorescent imaging of samples was carried out using an epifluorescence microscope (Nikon Eclipse LV100ND). Live and dead cell counts were obtained using the 3D objects counter plugin in ImageJ software.

Bacterial escape. An intact hydrogel-elastomer hybrid, and a defective living device (with weak hydrogel-elastomer bonding) were tested for comparison. Also, the agar hydrogel with the same dimensions as the hydrogel-elastomer hybrid and encapsulating $Rham_{RCV}$/GFP bacteria was used as a control. We first deformed the living materials, which contained $Rham_{RCV}$/GFP bacteria in different modes (i.e., twisting and stretching), and then immersed them in LB media for 24 h. To test the bacteria leakage, LB solutions surrounding the device were collected for streaking on LB agar plates after 24 h, and optical density (OD) 600 measurements by UV-Visible spectrophotometer (Thermo Scientific) after 6, 12, 20, and 24 h.

4.4.2. Fabrication of hydrogel–elastomer hybrids

Materials. The hydrogel window was composed of two types of crosslinked polymers: ionically crosslinked alginate and covalently crosslinked PAAm. For the stretchy PAAm network in hydrogel window, AAm was used as the monomer, MBAA as the crosslinker, and Irgacure 2959 as the photo-initiator, respectively. Calcium sulfate slurry acted as the ionic crosslinker with sodium alginate for the dissipative network. As for elastomers, Sylgard 184 (Dow Corning) or Ecoflex (Smooth-On) were molded and activated with benzophenone. Purple Nitrile Exam Gloves (Kimberly-Clark) were also used as an elastomer substrate. APS as a thermo-initiator and TEMED as a crosslinking accelerator were used in the fast-curable pre-gel solution for sealing of injection points. For cell induction, DAPG, AHL, Rham, and aTc, were used as the signaling molecules. Carbenicillin was added as antibiotic in the LB-Miller medium for cell culture. Live/dead BacLight bacterial viability and counting kit was used for cell viability assay.

Fabrication. Elastomers with microstructured cavities were prepared by soft lithography with the feature size of 500 μm in width and 200 μm in depth. Then, the prepared microstructured elastomer

was assembled with hydrogel to form robust hydrogel-elastomer hybrid as described in the previous report [31]. Briefly, the surface of the elastomer was treated with 10 wt% benzophenone solution in ethanol for 10 min, then washed and dried with nitrogen. The pre-gel solution (12.05 wt% AAm, 1.95 wt% sodium alginate, 0.2 wt% Irgacure 2959, and 0.012 wt% MBAA was carefully degassed, and mixed with calcium sulfate slurry (2×10^{-2} M in pre-gel solution) to form physically-crosslinked hydrogel. To introduce robust bonding between assembled hydrogel and elastomer, the physically-crosslinked hydrogel was assembled with the surface treated elastomer followed by UV irradiation (365 nm; UVP CL-1000) for 30 min. The resultant hydrogel-elastomer hybrid was washed with phosphate-buffered saline (PBS) for three times, sterilized using germicidal UV irradiation thoroughly, and immersed in LB media with antibiotics for 12 h before bacterial cell seeding.

Cell seeding and induction. Different E. coli strains were picked from overnight growth on LB plates and cultured in LB media at 37°C. 50 μg mL^{-1} carbenicillin was supplemented in LB broth. Cell cultures ($OD_{600} \approx 1$) were infused into the patterned cavities between hydrogel and elastomer by metallic needles (Nordson EFD) through the hydrogel layer. The holes induced by cell injection were sealed with very small amounts of fast-curable pre-gel solution (30.05 wt% AAm, 1.95 wt% sodium alginate, 0.012 wt% MBAA, 0.142 wt% APS, and 0.10 vol% TEMED), which could be cured at room temperature in 5 min. The cell contained device was washed carefully with PBS three times, followed by immersing the device in LB broth with carbenicillin at 37°C. Inducers could be added in LB medium at final concentrations of 100 μM DAPG, 100 nM AHL, 1 mM IPTG, 12 mM Rham, and/or 200 ng mL^{-1} aTc. Alternatively, a piece of sterilized tissue paper (Kimtech) was dipped in LB medium with inducer in it, and was put on top of the hydrogel layer. The device and the tissue paper were kept at 37°C and relative humidity of 90%. The latter method was not only applicable for cell to receive inducers from the environment (e.g., induction of $IPTG_{RCV}$/GFP by IPTG), but also more suitable for intercellular communication when dilution of signaling molecules by the environment was undesirable. Every induction/detection experiment was performed and repeated at least three times.

4.4.3. Fabrication of 3D printed hydrogel structures

Ink preparation. The ink formulation for all experiments contained Pluronic F127-DA as polymer matrices, Irgacure 2959 as photoinitiator, LB broth (Miller) as nutrient, DI water, together with certain chemical inducers, antibiotics (i.e., carbenicillin), and/or bacterial cell pellets. Pluronic F127-DA was synthesized according to a reported protocol[434]. Briefly, 25 g of Pluronic F127 were dissolved into 80 mL of toluene at 60 °C under nitrogen with a condenser with circulating cold water. After 4 h, the solution was cooled down to room temperature, and then to 0 °C in an ice bath. 1.2 mL of trimethylamine was added to the solution, followed by the dropwise addition of 0.5 mL of acryloyl chloride. The mixture was stirred overnight. Afterwards, the precipitated byproduct was filtered away, and the solution was concentrated by rotary evaporator. The white product was precipitated from the viscous solution by adding hexane. Through a second filtration step and drying in a fume hood for 48 h, the Pluronic F127-DA product was obtained. The synthesized Pluronic F127-DA at 27 wt% concentration and Irgacure 2959 at 0.2 wt% were dissolved in DI water in the dark at 4 °C. Then, 0.25 wt% LB broth powder and 50 μg mL^{-1} carbenicillin were added to the mixture. Different active components, including chemical inducers (e.g., 100 nM AHL, 1 mM IPTG, 200 ng mL^{-1} aTc, and 12 mM Rham) and cell pellets (e.g., AHL/GFP± cell, Rham/GFP+ cell, aTc/AHL+ cell, and GFP+ cell), were introduced in different ink systems. The cell density in the printing ink was ~10^9 cells per mL. The freshly prepared inks were loaded into a UV-blocking 5 mL syringe barrel (EFD Nordson), and allowed to defoam at 4 °C for one hour.

Printing and crosslinking. The 3D living materials and devices were fabricated using a three-axis robotic deposition stage (Aerotech) by printing a 3D structure onto a glass slide (Corning) or a chambered coverglass (Lab-Tek) covered with a hydrophobic coating (Rain-X). The structures were designed using commercially available software including Solidworks (Dassault Systèmes) or CADfusion (Aerotech), and translated into G-code using a custom Python script. The prepared inks were housed in the 5 mL syringe barrels, which fitted with nozzles ranging in size from 30 μm (World Precision Instruments), 50 μm (Fisnar), 100 μm (Fisnar), to 200 μm (EFD Nordson). To achieve stable and optimal printing, we chose 90 kPa of air pressure (Ultimus V, Nordson EFD) as printing pressure, and 27 wt% Pluronic F127-DA in the ink for all experiments, where the printed hydrogel filaments were continuous and uniform, and their diameters were nearly the same

as the nozzle diameters. After deposition, the physically crosslinked micelles were then chemically crosslinked by UV irradiation in a UV chamber (365 nm in wavelength, 1 J m^{-2}; UVP CL-1000) for 5 min, and the chamber was saturated with water vapor and nitrogen. After curing, the 3D structures were kept in a humid chamber.

Imaging and image analysis. Photographs of macroscopic 3D architectures were acquired using a DSLR camera (Nikon D7000). Fluorescent dyes, including Rhodamine-B and fluorescein, and food dyes (McCormick) were used to improve visualization of hydrogel-printed structures. The microscopic hydrogel structures were imaged using an epifluorescence microscope (Nikon Eclipse LV100ND) and a confocal microscope (Nikon A1R). ImageJ was used to generate composite microscopy images by combining fluorescent channels. The fluorescence intensities were quantitatively measured using NIS-Element (Nikon).

4.4.4. Mechanical characterization of 3D printed hydrogel structures

Rheological characterization of printing inks. Ink rheology was measured using a controlled stress rheometer (AR-G2, TA Instruments) with a 40-mm diameter 2° cone-plate (54-μm gap) and parallel-plate geometry (250-μm gap). The rheology of chemically crosslinked hydrogel was measured using the same instrument with a 40-mm diameter parallel-plate geometry (3.2-mm gap). Shear viscosity measurements of ink were carried out in steady-state flow mode. The storage shear moduli of ink were measured using an oscillatory stress sweep at a frequency of 1 Hz. To study the time-dependent mechanical properties of physically crosslinked ink and chemically crosslinked hydrogel, the rheometer was used to measure the storage and loss shear moduli at different frequencies of oscillating strain (shear strain is 0.01). Measurements were carried out at 25 °C and 4 °C using an aqueous solvent trap to mitigate drying effects.

Mechanical characterization of printed hydrogels. The mechanical properties of chemically crosslinked hydrogel were further characterized by pure-shear test. The samples with dimensions of 50 mm in width, 10 mm in gauge length, and 1.5 mm in thickness were stretched at room temperature, using a mechanical testing machine (Z2.5, Zwick-Roell) with a 20 N load cell. One sample was notched with a crack and the others were un-notched. The notched sample was

stretched to failure, and the un-notched samples were either stretched to failure or cyclically stretched to evaluate fracture toughness and energy dissipation, respectively.

4.4.5. Fabrication of prototypes

Skin patches fabrication. The robust hybrid patches with wavy microchannels were fabricated by using hydrogel (PAAm-alginate) and silicone elastomer (Sylgard 184) following the previously described method. Bacterial suspension of $Rham_{RCV}$/GFP was infused to the upper two channels, and AHL_{RCV}/GFP to the lower two channels of the patch. Before we adhered the living patch on forearm, the skin was smeared with LB medium of 12 mM Rham and/or 100 nM AHL. Note these two inducers were non-toxic, safe to be applied on skin. The living patch was conformably mounted on the skin with the PDMS layer exposed to air, and fixed on the skin by a clear Scotch tape. To demonstrate the anti-dehydration property of the wearable living patch, a pure hydrogel device without elastomer layer was fabricated by assembling micropatterned hydrogel and flat hydrogel sheet. To compare dehydration of hydrogel-elastomer hybrids and the hydrogel device without elastomer layer, these two types of devices were conformably attached to curved surfaces of plastic beakers. The dehydration tests were carried out at room temperature with low humidity (25°C and 50% relative humidity) for 24 h. To demonstrate the stretchability of living patch, we also fabricated the living skin patch with Ecoflex instead of PDMS in the same design and dimension.

Gloves fabrication. To demonstrate the living chemical sensors at the nitrile glove fingertips, hydrogel-elastomeric glove hybrids with spiral microchannels were prepared. We first laminated thin hydrogel sheets with patterned cell chambers on the fingertips of nitrile gloves, and then encapsulated different inducible cell inside. Different strains of bacteria ($IPTG_{RCV}$/GFP, AHL_{RCV}/GFP and $Rham_{RCV}$/GFP) were injected into spiral-shaped cell chambers at different fingertips, respectively. To test the functionality of the fingertip sensor array, we used a cluster of cotton balls soaked in LB medium with 1 mM IPTG and 12 mM Rham. The glove was worn to grab the wet cotton balls, and hydrogels at the fingertips contacted the inducer-containing cotton balls. The fluorescences at the fingertips were exampled after 4 h of contact with the cotton balls using the bench-top transilluminator.

Living tattoo fabrication. The bilayer elastomeric sheet was fabricated by successive spin-coating deposition of two silicone elastomers, Sylgard 184 (Dow Corning) and Silgel 613 (Wacker). Sylgard 184 was first spin-coated on the glass at 1500 rpm for 60 s, and then cured at 70 °C for 1 h. Then, Silgel 613 was spin-coated on top of the Sylgard 184 at 1500 rpm for 60 s, and then cured at 70 °C for another 1 h. The surfaces of elastomers were treated by absorbing benzophenone. The elastomer surfaces were thoroughly cleaned with methanol and deionized water, and completely dried with nitrogen gas before the benzophenone treatment. Thereafter, a benzophenone solution (10 wt% in ethanol) was applied onto the elastomer to evenly cover the entire elastomer surface for 1 min at room temperature. Then, the elastomer was washed with methanol three times and completely dried with nitrogen gas. The multiple hydrogel inks, which contain different cell sensors, were printed directly on the elastomer with 200-μm size nozzles, followed by 5 min UV curing, which led to the chemically crosslinked hydrogel and the robust bonding between hydrogel and elastomer. Lastly, we carefully peeled off the living tattoo from the glass slide, and adhered it on human skin for further testing.

4.5. Conclusions

We have integrated genetically engineered cells as programmable functional components with stretchable hydrogel-elastomer hybrids and 3D printed hydrogel structures to create a set of hydrogel living devices. We demonstrated the 3D printing of large-scale, high-resolution living materials with precise spatiotemporal control of cell distribution. These living devices can be programmed with desirable functionalities by designing the genetic circuits in the cells as well as the 2D and 3D structures of the hydrogel matrices. Moreover, we developed a quantitative model that accounts for the coupling between physical and biochemical processes in living devices. We further identified two critical time scales that determine the speed of response of the living materials and devices, and provide guidelines for the design of future systems.

While the inducers (such as Rham and AHL) are used as mock biomarkers here, more realistic chemical detections, such as components in human sweat or blood, can be pursued with living devices in the future. It is intriguing to envision a robust and personalized implant in which different cell types are programmed to monitor inflammation biomarkers and release bioactive agents to promote angiogenesis[106, 277]. New ingestible devices based on our 3D printing of living materials may be able to modulate the gut microbiota and treat microbe-mediated diseases

such as obesity and diabetes[435]. Overall, the hydrogel living materials and devices open new technological avenues towards real-world applications, such as on-demand medicine, biotechnology[33, 55, 436], bioremediation[437], and bioenergy via cell programming, structural design, and direct ink writing technologies.

Chapter 5

Hydrogel intestinal retentive devices

The research presented in this chapter has been published in:

- **Xinyue Liu**†, Yueying Yang†, Maria Eugenia Inda†, Shaoting Lin, Jingjing Wu, Yoonho Kim, Xiaoyu Chen, Dacheng Ma, Jianfeng Zang, Timothy K. Lu*, Xuanhe Zhao. Magnetic-hydrogel living devices for intestinal localization, retention and diagnosis. Advanced Functional Materials. 2021.

5.1. Introduction

Over the past few decades, technologies based on electronics and living bacteria have been developed for orally administered diagnostics and therapeutics [438-445]. The service life of existing ingestible devices is limited by the gastrointestinal (GI) transit time, i.e., the time it takes for food to move through the digestive system [97, 446]. In the human body, the GI transit time usually ranges from 6 to 48 h [439, 447, 448]. However, for most GI applications, such as long-lasting biosignal collection [97], prolonged drug delivery[449, 450], and sustained diet control [451, 452], longer retention times are needed. The effective diagnosis and treatment of GI diseases may also require ingestible devices to be positioned at a specific location in the gut. Such positioning would be desirable for the detection and treatment of localized diseases such as Crohn's disease, characterized by patchy inflammation along the GI tract [453, 454].

Although several strategies have been proposed to achieve localization in the GI tract, they all have limitations for intestinal retention. For example, ingestible devices have been developed to reside in the GI tract by floating, unfolding, or swelling [455, 456]; these can be applied to the large-volume gastric cavity but not to tubular structures (e.g., small and large intestines). There are high risks of intestinal blockage caused by the hydrogel swelling and of intestinal perforation caused by stiff or sharp pieces in the intestine [97, 439, 457]. Intestinal peristalsis may also induce the migration of unfolding structures, shortening their service life [458]. Moreover, intestinal

mucus adhesion fails to anchor the materials and devices for more than 4 hours due to the rapid turnover of the mucus layer [110, 459, 460]. Finally, biological scaffolds that are continuously generated by engineered probiotics can persist in the intestine but may have side effects, including the irreversible alteration of the native gut microbiota [461].

Magnetic materials have been of special interest for GI surgery because the magnetic force can be exerted over a distance [126, 462, 463]. Because of the constrained and tortuous architectures of the intestines, magnet-assisted spatial control is a useful feature for the diagnosis, evaluation, and management of localized pathologies, such as inflammation, ulcers, polyps, and tumors [463, 464]. A number of magnet-assisted technologies have been utilized in the GI tract for spatial control, including the placement of enteral tubes [465], the navigation of devices (e.g., capsule endoscopy and micromotors) [464, 466], and the manipulation of surgical instruments (e.g., micro-snares, baskets, and forceps) [467]. However, the existing surgical procedures require sophisticated medical equipment for spatial steering (e.g., X-ray emitter, detector, and robotic arm), and subjects under anesthesia [465-468]. They are applicable only for temporary use because the surgical interventions prevent the free movement of the subjects. In order to have prolonged control over the magnetic materials in the GI tract and permit normal movement of the subject in daily life, we designed a wearable magnet that can allow both spatial localization and temporal retention of ingested magnetic materials.

Here, we build a magnetic hydrogel retentive system, consisting of an ingestible, magnetic hydrogel carrying diagnostic microbes that could be localized by a wearable neodymium magnet, for long-term disease diagnosis in the intestine (**Figure 5-1a**). To prevent dislocation of the magnetic living hydrogel due to peristaltic waves and intestinal fluid flow, we optimize attractive magnetic force between the magnetic hydrogel in the intestine and the magnet by tuning the magnet dimensions (**Figure 5-1d**). Since the ingestible hydrogel is soft and flexible, it conforms to the intestinal surface, minimizing tissue damage to the intestinal lining. The mechanical robustness of the ingestible hydrogel helps maintain its structural integrity during intestinal segmentation (**Figure 5-1d,e**). The wearable magnet is lightweight and portable, and causes minimal tissue compression. Most importantly, the magnetic hydrogel is sufficiently retained by the wearable magnet in both rodent and human models based on our theoretical calculation. We validate the capability of magnet-assisted retention and localization in a human-scale GI tract phantom and in free-moving rodents (for at least a week) without causing any obstruction. Because

the ingestible hydrogels are biocompatible, the living bacteria integrated into the soft hydrogel matrix are functional for 7 days in vitro (**Figure 5-1c**). Bleeding is detected by these biosensing bacteria in the mouse intestine. In contrast to other systems (e.g., magnetically driven position control) which require high-precision medical equipment and comprehensive procedures, the magnetic living hydrogel permits the prolonged monitoring and modulation of the digestive system and adjacent organs and constitutes a non-invasive, accessible platform for the intestinal localization and retention of bacterial biosensors and electronic sensors.

5.2. Design principles

Design and fabrication of magnetic living hydrogels. Neodymium-iron-boron (NdFeB) magnets are hard ferromagnets that can retain high remanent magnetization after being magnetized [462]. Magnetic hydrogels for oral administration and intestinal retention are fabricated by incorporating NdFeB microparticles into a PVA hydrogel matrix (**Figure 5-1a,b**). First, these NdFeB microparticles (5 μm in average diameter) are coated with a nanolayer of silica shell (10 nm in thickness) to protect the alloys from corrosion in the hydrated environment [462]. Overnight cultures of engineered bacteria are centrifuged and resuspended in an equal volume of 10 wt% PVA solution. Then, NdFeB microparticles with volume fractions ranging from 0 to 21% are mixed with the bacteria-containing PVA solution and poured into a mold. The mixture in the mold is subjected to a strong impulse magnetic field (2.5 T) to magnetize the NdFeB microparticles along the applied field direction. This step of magnetization generates a uniform magnetic moment across the bulk mixture [126]. The PVA-NdFeB-bacteria mixture in the mold is then exposed to the temperature of –20 °C for 24 h, which promotes the phase separation of polymers in water and the formation of nanocrystalline domains in the PVA solution, resulting in a hydrogel matrix (**Figure 5-1b**) [288].

The magnetic hydrogels are crosslinked by PVA nanocrystalline domains [124, 288]. Increasing the volume fraction of NdFeB microparticles in the nanocrystalline hydrogel further contributes to a higher Young's modulus, higher toughness, and higher magnetization of the magnetic hydrogel [436]. We determine the amount of NdFeB microparticles in the magnetic hydrogel to be 12 vol%. The hydrogel with 12 vol% NdFeB exhibits a low Young's modulus of 21 kPa, a high toughness of ~ 280 kJ m^{-3}, and a high magnetization of 6×10^4 A m^{-1} [436]. The low Young's modulus of the magnetic hydrogel drastically alleviates the stress concentration on the

intestinal wall, as manifested by the finite element simulations [436]. Low mechanical stiffness of hydrogels is also indispensable for maintaining the viability of encapsulated bacteria, especially in the long-term [436]. The high toughness of the magnetic hydrogel ensures the structural integrity when the hydrogel is subject to intestinal peristalsis and segmentation (**Figure 5-1f**). In addition, the high magnetization enables effective retention of the hydrogel and its localization in spite of intestinal motility.

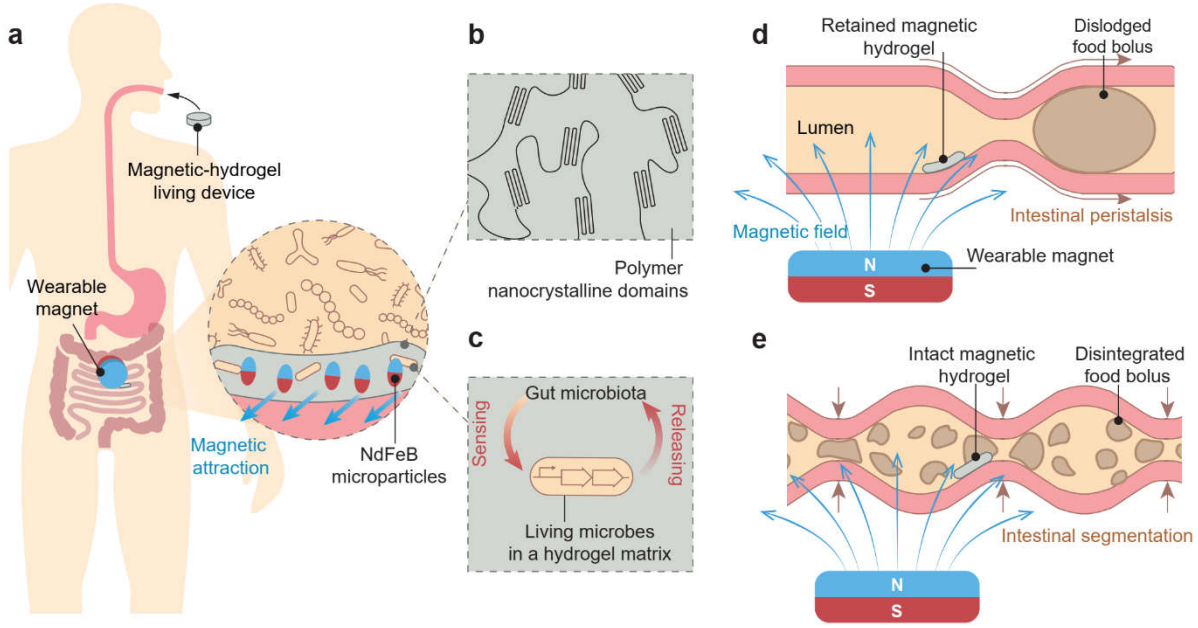

Figure 5-1. Design and mechanism of the magnetic living hydrogels localized and retained in the intestine. (a) The magnetic living hydrogel is orally administrated and retained in the intestine by a magnet worn on the abdominal skin. Inset: magnetized NdFeB microparticles incorporated in the hydrogel matrix provide the attractive magnetic force between the magnetic hydrogel and wearable magnet for intestinal localization and retention. (b) The hydrogel matrix is physically crosslinked by nanocrystalline domains and reinforced by NdFeB microparticles, making it mechanically tough. (c) Living synthetic microbes encapsulated in the hydrogel matrix interact with the gut microbiota when the magnetic hydrogel is retained in the gut, enabling biological functions such as sensing and releasing. (d) Intestinal peristalsis propels a food bolus along the intestinal lumen, while the magnetic hydrogel can be retained due to the magnetic attraction with the wearable magnet. (e) Intestinal segmentation breaks a food bolus into fragments in the intestinal lumen, while the magnetic hydrogel can remain intact due to its mechanical toughness.

5.3. Modeling

5.3.1. Model for intestinal retention and localization

A large wearable magnet can produce a strong magnetic field favorable for the retention and localization of magnetic hydrogels, but may cause a series of side effects including tissue damage

due to the magnetic attraction force and overload caused by a heavy magnet being worn on the body. We develop a model to rationally select the wearable magnet with optimized dimensions. The model includes a disc-shaped wearable magnet and a disc-shaped magnetic hydrogel residing in a lumen with intestinal peristalsis (**Figure 5-2a**). The intestinal peristalsis in the lumen propels the hydrogel to move forward, and the friction between the hydrogel and the lumen wall resists the hydrogel's motion (**Figure 5-2a,b**). The intestinal propelling force is denoted as F^{propel}, and the friction force as F^{friction}. The magnetic force between the wearable magnet and the NdFeB microparticles in the hydrogel may propel or retain the magnetic hydrogel, depending on the direction of the magnetic force (**Figure 5-2b**).

We define a cylindrical coordinate system with the center of the disc-shaped wearable magnet as the origin O, the radial direction of the magnet as the r-axis, and the axial direction of the magnet as the z-axis (**Figure 5-2a**). In addition, the point P(r, z, θ) refers to the center of the magnetic hydrogel, where θ is the angle between the intestinal propelling direction and the projection of OP line segment on the upper surface of the magnet. (**Figure 5-2a**). We next calculated the magnetic force applied on the magnetic hydrogel. The magnetic field **B** around the disc-shaped wearable magnet can be expressed as $\mathbf{B}=B_r\mathbf{e_r}+B_z\mathbf{e_z}$, where $\mathbf{e_r}$ and $\mathbf{e_z}$ are unit vectors in the direction of the r-axis and z-axis, respectively, and B_r and B_z are fully expressed in **Equations 5-3 and 5-4** [469]. The axial direction of the disc-shaped magnetic hydrogel is assumed to be parallel with the axial direction of the wearable magnet. The vertical distance between the adjacent surfaces of the magnet and the hydrogel is D. The magnetic hydrogel is assumed to be uniformly magnetized with the remanent magnetization $\mathbf{M_h}$ formed along the axial direction of the hydrogel (**Figure 5-2b**). We also assume that the magnetization of the magnetic hydrogel is unaffected by the applied magnetic field **B** due to the high coercivity of the NdFeB microparticles in the hydrogel [462]. Given the magnetic field applied by the magnet and the magnetization of the hydrogel, we calculate the magnetic force applied on the hydrogel as

$$\mathbf{F}^{\text{magnetic}}=\nabla\int_0^V \mathbf{M_h}\cdot\mathbf{B}dv \tag{5-1}$$

where V is the volume of the hydrogel and $\nabla=\frac{\partial}{\partial r}\mathbf{e_r}+\frac{\partial}{\partial z}\mathbf{e_z}$. Specifically, the magnetic force acting on the hydrogel can be decomposed into the force component along the z direction F_z and

the force component along the r direction F_r, namely, $\mathbf{F}^{\text{magnetic}} = -F_r\mathbf{e_r} - F_z\mathbf{e_z}$, where F_r and F_z are both positive because the magnetic force is attractive between the magnet and hydrogel (**Figure 5-2b**). The hydrogel can be effectively retained if the forces along r direction satisfy the criterion:

$$F^{\text{friction}} + F_r \cos\theta - F^{\text{propel}} \geq 0 \quad (5\text{-}2)$$

θ ranges from 0 to π/2 when the magnetic hydrogel is on the downstream side of the magnet, and from π/2 to π when the magnetic hydrogel is on the upstream side of the magnet (**Figure 5-2a**). In the current model, we further assume the longitudinal axes of the lumen, the magnetic hydrogel, and the magnet are in the same plane, so that θ = 0 when the magnetic hydrogel is on the downstream side of the magnet, and θ = π when the magnetic hydrogel is on the upstream side of the magnet (**Figure 5-2a,b**).

Based on the calculated intestinal propelling force, friction force, and magnetic force (see Calculation of fields, forces, and positions for details), we apply this criterion to a human model, where the vertical distance between the adjacent surfaces of the magnetic hydrogel and the magnet is 15 mm (**Figure 5-2c**). We fix the thickness (L) of the magnet to be 12.7 mm and vary its radius (a) from 6.4 to 25.4 mm. We found that, when the radius of the magnet is greater than 9 mm, there exists a region in the lumen where the hydrogel can be retained. For example, when the radius of the magnet is 12.7 mm or 25.4 mm, the magnetic hydrogel can be successfully retained on the downstream side of the magnet (**Figure 5-2c**). The solid circles indicate the stably retained locations for the magnetic hydrogels, at which $F^{\text{friction}} + F_r \cos\theta - F^{\text{propel}} = 0$ with θ = 0. To the contrary, the magnetic hydrogel can pass through the lumen without retention when the radius of the magnet is 6.4 mm (**Figure 5-2c**). In addition, as can be seen in **Figure 5-2d**, the normal pressure applied by the retained magnetic hydrogel on the intestinal wall is mild (p_z < 0.6 kPa) at any retained locations around the magnets (a = 25.4 or 12.7 mm, L = 12.7 mm). Therefore, we select the magnet with a radius of 25.4 mm and a thickness of 12.7 mm, due to the portable weight of the magnet (193 g), mild normal pressure applied on the intestinal tissue (0 – 0.6 kPa) [466], and capability of retaining the ingestible hydrogel (**Figure 5-2c,d**).

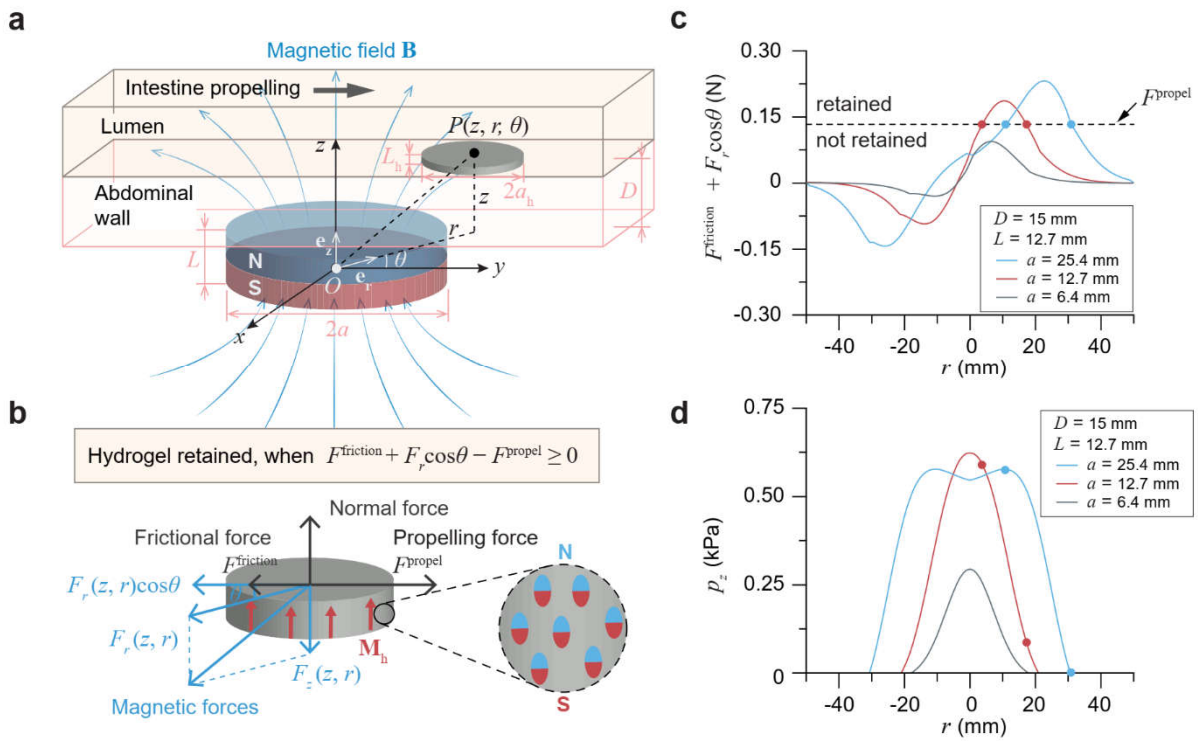

Figure 5-2. Model for intestinal retention and localization of the magnetic living hydrogel. (a) Schematic illustration of a disc-shaped magnetic hydrogel (radius a_h and thickness L_h) residing in a lumen under a magnetic field B generated by a disc-shaped magnet (radius a and thickness L). The vertical distance between the lumen and the magnet is D. (b) Free body diagram of the magnetic hydrogel in the intestinal lumen, when it is moving along the intestinal propelling direction. The magnetization of the hydrogel M_h is uniform and along the axial direction of the hydrogel disc. (c) Net retarding force $(F^{\text{friction}} + F_r \cos\theta)$ of a magnetic hydrogel (radius a_h 10 mm, thickness L_h 1 mm) at a vertical distance of 15 mm away from a magnet (radius a 6.4, 12.7, or 25.4 mm, thickness L 12.7 mm). The magnetic hydrogel can be retained when the net retarding force is higher than the propelling force F^{propel}. (d) Normal pressure p_z applied by a magnetic hydrogel (radius a_h 10 mm, thickness L_h 1 mm) on the intestinal wall at a vertical distance of 15 mm away from a magnet (radius a 6.4, 12.7, or 25.4 mm, thickness L 12.7 mm). Solid circles on each curve in c-d indicate the stably retained locations for the magnetic hydrogel, in which the retarding force $(F^{\text{friction}} + F_r \cos\theta)$ equals the propelling force F^{propel}.

5.3.2. Calculation of fields, forces, and positions

Calculation of the magnetic field. The magnetic field **B** around a disc-shaped magnet can be theoretically expressed as $\mathbf{B} = B_r \mathbf{e}_r + B_z \mathbf{e}_z$, where $\mathbf{e}_r$ and $\mathbf{e}_z$ are unit vectors in the direction of the positive r-axis and z-axis. B_r and B_z can be expressed written as [470]

$$B_r = -\frac{\mu_0}{4\pi} M \int_0^{2\pi} \int_0^a \left[-\frac{R(2r - 2R\cos\Phi)}{2\left(R^2 + (L/2 - z)^2 + r^2 - 2Rr\cos\Phi\right)^{3/2}} + \frac{R(2r - 2R\cos\Phi)}{2\left(R^2 + (L/2 + z)^2 + r^2 - 2Rr\cos\Phi\right)^{3/2}} \right] dRd\Phi \quad (5\text{-}3)$$

$$B_z = -\frac{\mu_0}{4\pi} M \int_0^{2\pi} \int_0^a \left[\frac{R(L/2 - z)}{\left(R^2 + (L/2 - z)^2 + r^2 - 2Rr\cos\Phi\right)^{3/2}} + \frac{R(L/2 + z)}{\left(R^2 + (L/2 + z)^2 + r^2 - 2Rr\cos\Phi\right)^{3/2}} \right] dRd\Phi \quad (5\text{-}4)$$

where (r, z) is the coordinate of the center of the magnetic hydrogel to the origin, μ_0 is the magnetic permeability in a classical vacuum, M is the scalar magnetization of the wearable magnet (the value ~ 1.14×10^6 A m^{-1}) [469], and L and a are the thickness and radius of the magnet, respectively.

Calculation of the intestinal propelling force. We start with the calculation of the intestinal propelling force F^{propel} which is equal to the intraluminal pressure p (i.e., the reported value ~ 6.6 kPa)[471] multiplied by the vertical cross-sectional area of the hydrogel, namely, $F^{\text{propel}} = 2pa_hL_h$, with a_h being the radius and L_h being the thickness of the disc-shaped hydrogel.

Calculation of the friction force. Given the normal force acting on the hydrogel $|F_z|$, we can further estimate the friction force as $F^{\text{friction}} = \mu|F_z|$, where $\mu = \beta(p_z)^{\alpha-1}$ is the frictional coefficient [472] with β = 5.3 and α = 0.54 are parameters fitted by experimental data [436] and $p_z = |F_z|/(\pi a_h^2)$ is the normal pressure.

Calculation of retained positions of magnetic hydrogels. We identify the physiological conditions and estimate the parameters for calculating the hydrogel retention in the mouse and human, including the dimensions of magnetic hydrogels (radius a_h = 1 mm for mouse and 10 mm for human, thickness L_h = 1 mm for both mouse and human), the magnetization of ingestible hydrogel (M_h = 60 kA m^{-1}, θ = 0, θ is the angle between M_h and the z axis), the friction coefficients between hydrogel and intestine under varied normal pressures [436], and the distances between the intestine lumen and abdomen skin (D = 2 mm for mouse and 15 mm for human). The magnetic hydrogel's vertical position z_0 in the coordinate system is determined the distances between the wearable magnet and intestinal lumen, that is, $z_0 = L/2 + D$. To identify the

horizontal position of retained magnetic hydrogels r_0 , we plot the net forces $(F^{\text{friction}} + F_r \cos\theta - F^{\text{propel}})$ in **Figure 5-2c**. The magnetic hydrogel can be retained in the lumen if there are any locations at which net force is greater than or equal to zero, and the stably retained positions r_0 can be identified at which net force equals zero. Otherwise, the hydrogel passes through the tubular structure when the maximum net force is smaller than zero. We further calculate the normal pressures at the (r_0, z_0), that is, the retained positions or positions with the max net force (**Figure 5-2c,d**).

Analysis of magnetic retention in a mouse model. The retained magnetic hydrogel in a mouse model can impart a normal pressure as high as 5 kPa when the hydrogel is 2 mm away from a small magnet (a = 5.6 mm, L = 3.2 mm), which is beyond the safe range for rodent intestinal tissues [436, 466]. Considering the portable weight of the magnet (< 5% of mouse body weight; < 0.3% of human body weight), we further identify the optimal magnet sizes, e.g., a = 25.4 mm, L = 12.7 mm for human and a = 5.6 mm, L = 1.6 mm for mouse intestinal retention [436].

5.4. Results and discussion

5.4.1. In vitro retention

Next, we use transparent plastic tubes with flowing liquids to replicate the geometries and dimensions of mouse and human small intestines, and investigate the in vitro retention and positioning of magnetic living hydrogels based on remote magnetic attraction. In human intestines, the luminal chyme movement is driven by waves of contraction propagating along the intestinal wall [473]. To model the propelling force, fluid flow at different flow rates and viscosities are generated in the tube by a peristaltic pump, which applied a shear stress of 0–10 kPa to the trapped contents close to the wall. As illustrated in **Figure 5-3a,c**, the fluid flow drives the motion of the suspended magnetic hydrogel so that it travelled through the whole conduit. In contrast, a magnet placed beneath the tube at a distance (2 mm for a mouse size and 15 mm for a human size) arrests the smooth movement of the magnetic hydrogel in the tube and kept the hydrogel static for 24 h afterward (**Figure 5-3b,d**). The magnetic force is able to resist a maximum shear stress of 10 kPa in tubes having the same size as the mouse or human small intestines (**Figure 5-3e,f**).

To illustrate the potential utility of the magnetic hydrogel in the clinical setting, we examine the localization and retention of the ingestible magnetic hydrogel with a more clinically

relevant model. We use a life-sized, silicone phantom that replicates the anatomy of human intestines, including the small and large intestine. As seen in **Figure 5-3g**, the tubular structure of the phantom is continuous and tortuous, containing several acute-angled corners, and its inlet and outlet are connected to a peristaltic pump with a flow flux of 3400 mL min^{-1}. The magnetic hydrogel alone automatically passes through the artificial intestine without any navigation [436]. When a magnet is placed on a transparent acrylic sheet right above the winding intestine phantom (distance 15–30 mm), the magnetic hydrogel is retained at several different locations, such as the small intestine, ascending colon, and descending colon [436]. When the magnetic hydrogel encapsulates a miniature temperature sensor (6 mm in diameter and 17 mm in length), the hydrogel piece is effectively pinned by the magnet placed above at several different locations corresponding to the small intestine (**Figure 5-3g**), the ascending colon (**Figure 5-3h**), and the descending colon (**Figure 5-3i**) in the phantom. Since the overall diameter of the electronic sensor-encapsulated magnetic hydrogel is around 8 mm, smaller than the inner diameters of artificial intestines (15 mm for small intestine, 20–43 mm for large intestine), it does not obstruct fluid flow. Furthermore, the strong static magnetic field imposed by the wearable magnet does not affect the temperature sensing and recording functions of the microelectronics. When we infuse 100 mL of cold water (0 °C) through the inlet of the tubular phantom to replicate water drinking, temperature variations at different locations are recorded (points (g)–(h) in **Figure 5-3j**). **Figure 5-3k** indicates that the intake of cold drinks induced temperature variations, and the magnitude and delay time of these variations depended on the locations in the GI tract. When the integrated sensor is close to the inlet (g), the temperature decrease is swift and sharp, whereas there are gradual and gentle temperature fluctuations in the downstream regions, as seen in (h) and (i).

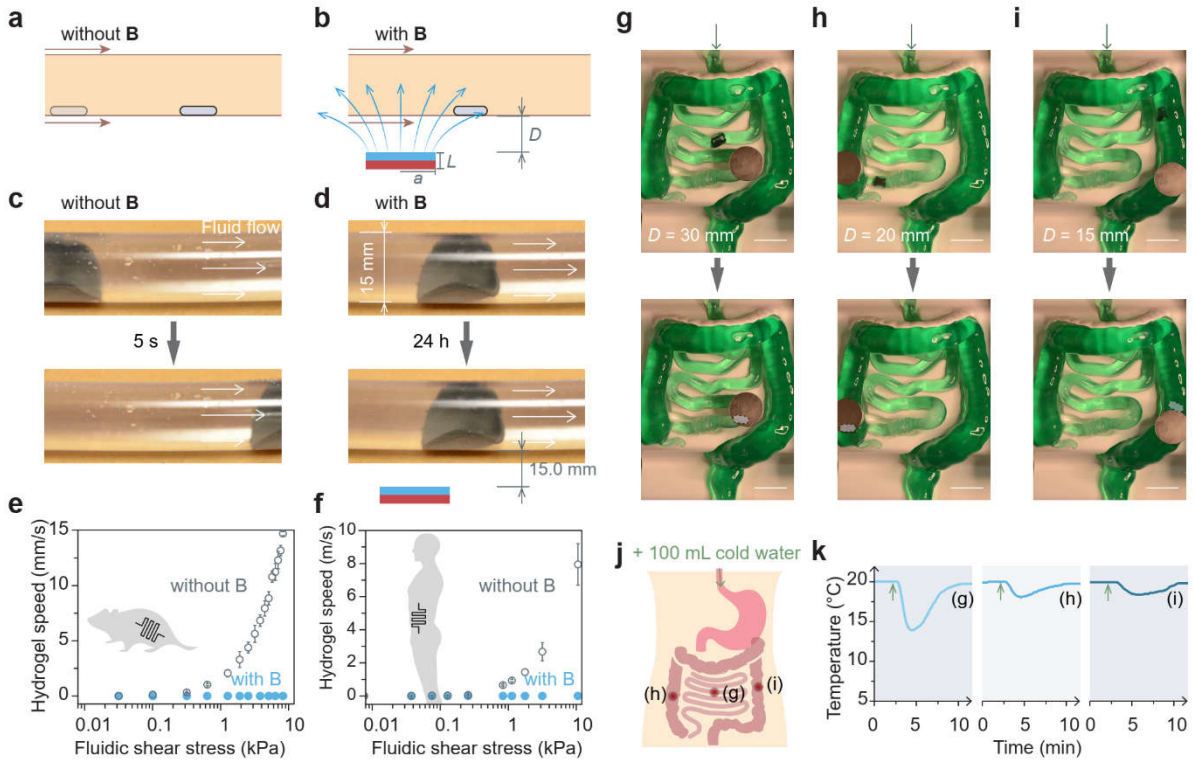

Figure 5-3. In vitro validation of retention and localization of the magnetic living hydrogel. (a) Schematic illustration of the magnetic hydrogel movement propelled by intestinal peristalsis without any external magnet. Magnetic field, B. (b) Schematic illustration of the magnetic hydrogel retention by the magnetic attraction force. (c) Movement of a magnetic hydrogel (radius 10 mm, thickness 1 mm) in a transparent plastic tube (diameter 15 mm) driven by the fluidic flow without any external magnet. (d) Retention of a magnetic hydrogel in a transparent plastic tube (diameter 15 mm) for 24 h with an external magnet (radius 25.4 mm, thickness 12.7 mm) placed 15 mm beneath the tube. (e) Moving speed of a magnetic hydrogel (radius 1 mm, thickness 1 mm) against different fluidic shear stresses in a tube with dimensions similar to those of mouse intestines, with and without an external magnet (radius 5.6 mm, thickness 1.6 mm) at a vertical distance of 2 mm. (f) Moving speed of a magnetic hydrogel (radius 10 mm, thickness 1 mm) against different fluidic shear stresses in a tube with dimensions similar to those of human intestines, with and without an external magnet (radius 25.4 mm, thickness 12.7 mm) at a vertical distance of 15 mm. Localization and retention of an integrated system consisting of a magnetic hydrogel (radius 10 mm, thickness 1 mm) and a miniature temperature sensor in a silicone phantom mimicking the human intestine, and the integrated system is pinned at the (g) small intestine, (h) ascending colon, and (i) descending colon by an external magnet (radius 25.4 mm, thickness 12.7 mm) placed 15–30 mm above the phantom. (j) Schematic illustration of oral intake of cold water to the GI tract and three locations (g)-(i) where the temperature is probed after water intake. (k) Temperature variations after cold water intake measured by a miniature temperature sensor when the integrated system is retained at the three locations in the GI tract. Scale bars are 50 mm in (g)-(i).

5.4.2. In vitro biocompatibility

Interfacing magnetic hydrogels with the human body requires assessments of chemical corrosion and cytotoxicity. We further investigate the corrosion of embedded NdFeB alloys in magnetic hydrogels by element analysis of the leaching solution. The as-prepared magnetic hydrogels are incubated in simulated gastric fluids (pH 1.2) at 37 °C for 1 day and simulated intestinal fluids (pH 6.8) at 37 °C for 10 days to allow the solvent to extract corroded metal ions, including Nd(III) and Fe(III). Element concentrations in these aqueous solutions are obtained by inductively coupled plasma mass spectrometry, from which we calculate the quantity of neodymium and iron ions that are corroded and dissolved from 1 g of magnetic hydrogel in 1 mL of fluids. The lower limits of toxicity, calculated by oral LD50 (i.e., 0.2 g kg^{-1} for $FeCl_3$ and 3.7 g kg^{-1} for $NdCl_3$) times an average human weight (i.e., 62 kg), are orders of magnitude higher than the amounts of corroded ions [Nd(III) and Fe(III)] from 1 g of magnetic hydrogel over 10 days (**Figure 5-4a**), suggesting that the presence of silica shells on the NdFeB particles would help to minimize direct exposure of the alloys to intestinal environments with neutral pH and consequently limit corrosion. The magnetic hydrogels are more severely oxidized and corroded in acidic solution, when they are incubated with simulated gastric fluid (pH 1.2) for 4 h, but the concentrations of corroded metal ions are still much lower than the limits of oral doses that induce toxicity (**Figure 5-4a**).

We then analyze the cytotoxicity of magnetic hydrogels using the Caco-2 cell line, which has been widely used as a model of the epithelial barrier on the intestine [474]. Similar to the trace element analysis mentioned above, leaching experiments are used to collect the chemicals released from magnetic hydrogels in fresh culture media for 1–7 days. Caco-2 cells are then exposed to the culture media containing the released compounds and left for 2 days, and cell viability is analyzed by using live/dead cell stains. As shown in **Figure 5-4b,c**, there is no significant difference in viability for cells kept in the pristine culture medium (positive control), and the media which has been exposed to the magnetic hydrogels and pure PVA hydrogels for 1–7 days.

To determine whether the magnetic hydrogels could maintain living bacteria, as well as to test their in vitro functionality, we use a strain of engineered E. coli Nissle 1917 as a bacterial blood sensor. These probiotic bacteria have been genetically engineered with the gene of $P_{L(HrtO)}$-luxCDABE with HrtR [448]. When they are physically entrapped in the magnetic hydrogel, they express bioluminescence when extracellular heme is present in the surrounding medium. As demonstrated in **Figure 5-4d,e**, bacterial viability in the hydrogel is maintained above 95% for a

week after day 0, and the colony size and density of viable bacteria continuously grew post-encapsulation. A few factors contribute to this lasting survival and growth: the biocompatibility of the chemical components and the fabrication process; chemical permeability, which allows mass transport of nutrient supplies and metabolic products [33]; and mechanical softness, which permits bacterial growth and division within the hydrogel matrix (**Figure 5-4f**) [33, 55]. We then validate the biosensing function of the bacteria encapsulated in the magnetic hydrogels. As shown in **Figure 5-4g**, visible luminescence production in the hydrogels is induced by 0.1 vol% of whole horse blood in vitro. The induction tests are conducted at different time points of hydrogel incubation, during which the normalized luminescence gradually decreases from 33 after 24-h incubation to 7.5 after 7 days (**Figure 5-4g**).

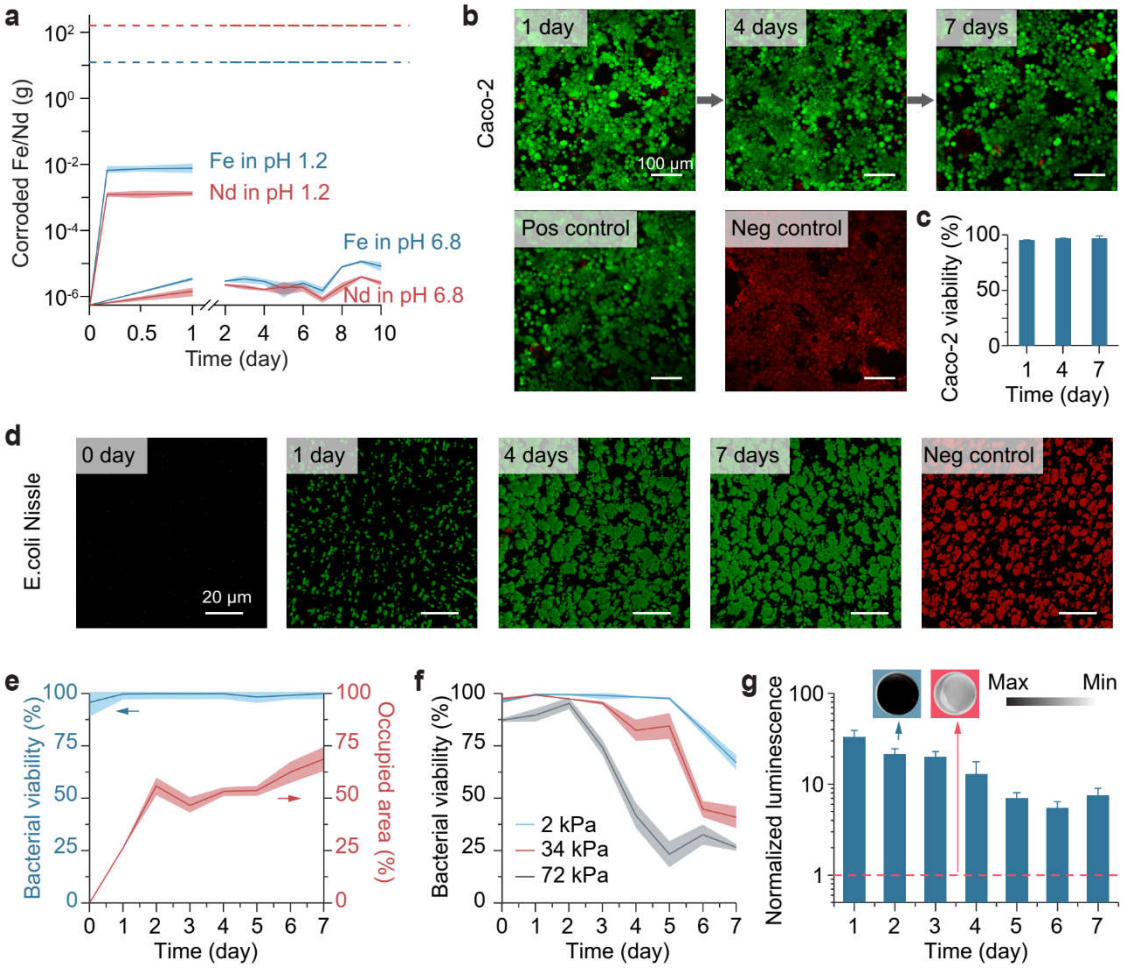

Figure 5-4. Biocompatibility and functionality of the magnetic living hydrogel. (a) Chemical element analysis of the corroded metal ions from the magnetic hydrogel in simulated gastric fluid (pH 1.2) over 24 h and in simulated intestinal fluid (pH 6.8) over 10 days. The values correspond to the corroded metal masses from 1 g of the magnetic hydrogel. Dashed lines represent maximum

oral doses having no significant toxic effect. (b) Biocompatibility of the magnetic hydrogel in a live/dead assay of Caco-2 cells, using a hydrogel-conditioned medium (conditioning time: 1, 4, 7 days) for cell culture. After culture, the Caco-2 cells are stained with calcein-AM (green) and ethidium homodimer-1 (red) to visualize the viable and dead cells, respectively. (c) Caco-2 cell viability using a hydrogel-conditioned medium with varied conditioning time. (d) Encapsulation and visualization of engineered bacteria (E. coli Nissle 1917) in the magnetic hydrogel for 1–7 days. The encapsulated bacteria are stained with SYTO 9 dye (green) and propidium iodide (red) to visualize the viable and dead bacteria, respectively. (e) Bacterial viability and area occupied by viable bacteria (E. coli Nissle 1917) in hydrogels over time. (f) Bacterial viability (E. coli DH5α) in hydrogels with varied Young's modulus over time. (g) Blood-sensing ability of the magnetic living hydrogels that encapsulated engineered bacteria. Insets: typical images of the luminescent hydrogel (left, blue background) and non-luminescent hydrogel (right, red background; negative control). Dashed red line represents values obtained with the negative control. Data in (a), (c), (e), (f) and (g) are means ± SD, n = 3. Scale bars are 100 μm in (b) and 20 μm in (d).

5.5. Applications

5.5.1. In vivo retention

After establishing the retention and positioning of the magnetic hydrogel in vitro, we evaluate the in vivo intestinal retentive ability of magnetic hydrogels in a mouse model (C57BL/6, Jackson Laboratory). Despite differences in size and physiology with the human body, mouse models have been frequently adopted to study the gut microbiota and the interactions of gut microbes with the host; in fact, mice share a similar GI transit time with humans [475, 476]. Magnetic living hydrogels (radius 1 mm, thickness 1 mm) are dispersed in a block of nutritious jelly (DietGel 76A, ClearH_2O) and provided to mice after overnight fasting, so that mice would voluntarily consume the DietGel together with the magnetic hydrogels through oral administration without gavage or other invasive procedures. Owing to high radiographic contrast between magnetic hydrogels and mouse tissues, we employ X-ray microtomography (microCT) to visualize the 3D spatial position of the magnetic hydrogels in the GI tract over time. We observe that fasted mice ingested the magnetic hydrogels within approximately 1 hour after DietGel distribution. Mice with ingested magnetic hydrogels inside their bodies are randomly allocated into two groups: the control group without any treatment (n = 5) and the experimental group carrying a disc-shaped magnet (radius 11 mm, thickness 1.6 mm), which is adhered on the abdomen by skin adhesives (n = 5).

As illustrated in **Figure 5-5a,c**, the ingested magnetic hydrogel is completely cleared from the GI tract in the control group within 6 h. The magnetic hydrogel, in contrast, is magnetically retained in the GI tract for 7 days in the experimental group (**Figure 5-5b,d**). After the removal of the magnet from the abdomen, the magnetic hydrogel is released rapidly and completed its passage

through the remaining tract within 6 h. During its retention period, the magnetic hydrogel is able to resist the mechanical loads caused by intestinal motility and preserve its structural integrity. As indicated in the representative histological images of the small intestine cross-section with (**Figure 5-5f**) and without (**Figure 5-5e**) a magnetic hydrogel, intestinal tissues in contact with the magnetic hydrogel do not exhibit significant inflammatory responses, nor is the intestinal lumen blocked by the retained hydrogel. In addition, although the extracorporeal magnet exerted robust magnetic control of the ingestible hydrogel, no significant change in overall animal well-being, including body weight, movement, and food/water intake, is observed in the animals.

5.5.2. In vivo sensing

To demonstrate that magnetic hydrogels can serve as universal carriers for living sensors in vivo, we verify the biomarker detection in mice enabled by living bacteria encapsulated in the intestinal retentive hydrogel. We choose E. coli Nissle 1917 as a chassis for its excellent safety profile for long-term use and its incapacity to colonize the gut if swallowed [477]. Direct oral administration of E. coli Nissle 1917 resulted in viable cells in stools on the first day of administration (peak at the 6th hour), but bacteria are completely cleared in the subjects afterward [448, 477]. In general, the delivery of bacteria to the small intestine is challenging: colonization by the bacteria of the gut microbiota may cause drastic microbiome perturbation; while competition for nutrients and location with resident microbes may prevent the engrafted bacteria from colonizing, so that they lose their efficacy [478]. Constraining the location of the engineered bacteria by encapsulating them in the magnetic hydrogel offers a solution, because it not only allows long-term, localized residence of bacteria in the GI tract to overcome resistance to colonization but also reduces undesirable dispersion of the gut microbiota. We first feed the animals with the bacteria-encapsulating magnetic hydrogels. After 12 hours, we remove the magnet discs on the abdomen. Then, 1–6 hours after magnet removal, microbes are recovered from the stool samples. In the collected feces with no magnetic hydrogel, few viable bacteria ($0–10^3$ CFU mg^{-1} feces. CFU, colony-forming units) are detected (**Figure 5-5g,h**). In contrast, there are ~ 10^5 CFU of bacteria in 1 milligram of fecal samples containing magnetic hydrogels (**Figure 5-5g,h**). The difference in numbers of living bacteria recovered from collected fecal samples with and without magnetic hydrogels indicates that the hydrogel-encapsulated bacteria are contained in the hydrogel without

significant alteration of the global gut microbiota. It also shows that high loads of bacteria can be retained, which would be useful for efficient therapeutic delivery and accurate biosensing.

To determine whether this system is responsive to GI bleeding elicited by indomethacin, we test the bacterial blood sensor encapsulated in the ingested magnetic hydrogels. C57BL/6J mice carrying the magnetic living hydrogels are administered indomethacin (10 mg kg^{-1}) to induce GI bleeding in the experimental group (n = 5) and PBS in controls (n = 5). Twenty-four hours after indomethacin administration in the experimental group, the magnets on the abdomen are removed and fecal pellets in both groups are collected. We perform the CT scanning to confirm the presence of the magnetic hydrogels, luminescence analysis and CFU enumeration to calculate the bacterial luminescence, and guaiac test to validate the GI bleeding in the mice. As seen in **Figure 5-5i**, normalized luminescence values of fecal pellets are significantly higher in mice administered with indomethacin compared to those of control animals. The results reveal that the 24-h, localized colonization of the bacterial sensors in the mouse intestine allows effective detection of GI bleeding in vivo.

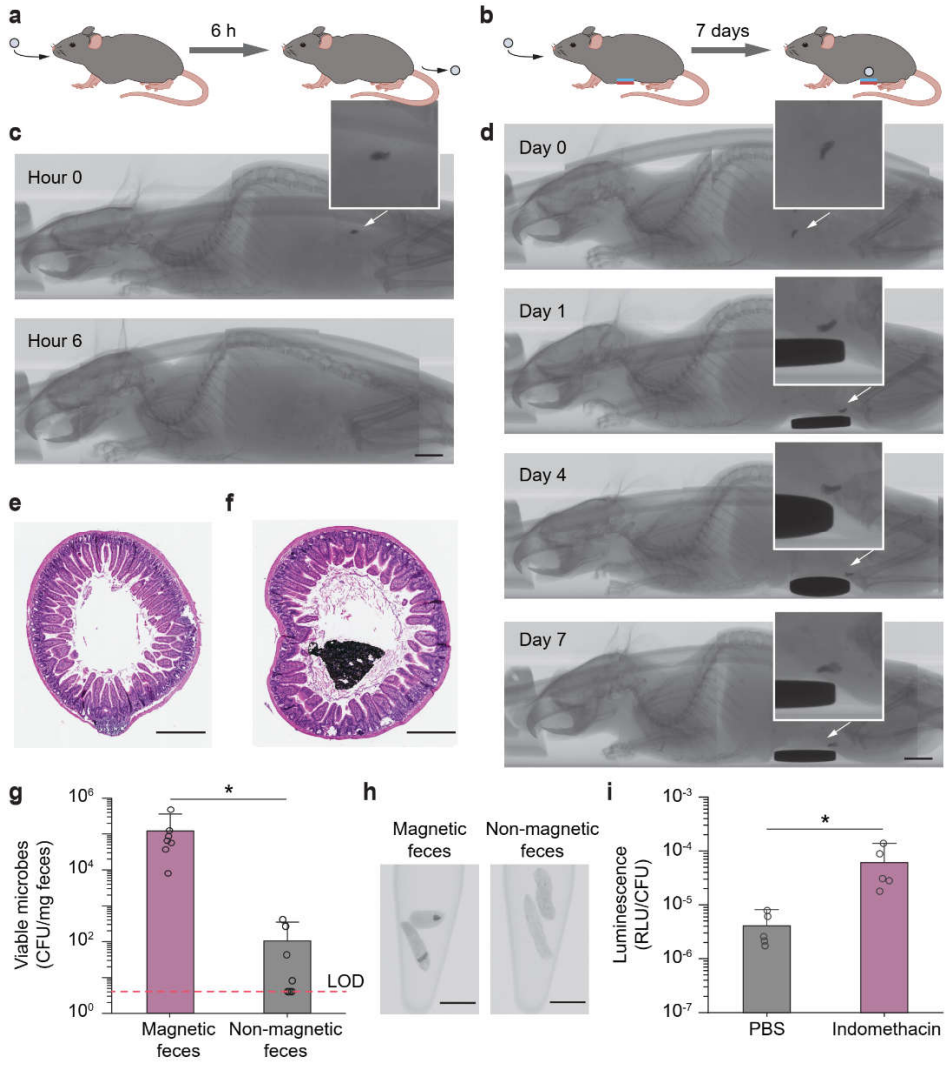

Figure 5-5. In vivo validation of magnet-assisted retention and in vivo heme sensing function of the magnetic living hydrogels. (a) Illustration of an ingested magnetic living hydrogel passing through the whole GI tract of a mouse within ~ 6 h. (b) Illustration of an ingested magnetic living hydrogel retained in the GI tract of a mouse for 7 days by an external magnet attached to the abdomen. (c) CT images of a mouse with an ingested magnetic living hydrogel passing through the whole GI tract of a mouse within ~ 6 h. (d) CT images of a mouse with an ingested magnetic living hydrogel retained in its intestine for 7 days by an extracorporeal magnet attached on the abdomen. Representative histological images stained with haematoxylin and eosin (H&E) for assessment of the small intestine cross-section without (e) and with (f) a magnetic hydrogel after 7-day intestinal retention. (g) Numbers of viable microbes in fecal pellets collected from mice at 12 h post-administration of the hydrogel (containing blood-sensing E. coli Nissle 1917). The fecal samples with and without magnetic hydrogels exhibit significant differences in microbe numbers (*$P < 0.05$; Student's t test; $n = 7$). Dashed line indicates the limit of detection (LOD) of the assay. (h) CT images of fecal pellets with or without magnetic hydrogels. (i) In vivo blood sensing performance. After the magnetic hydrogel (containing blood-sensing E. coli Nissle 1917) is retained in the intestine, mice are administered indomethacin (to induce gastrointestinal bleeding) or PBS. Normalized luminescence values of fecal pellets 24 h post-induction are significantly higher in mice administered indomethacin compared to control animals (*$P < 0.05$; Student's t test;

n = 5). RLU, relative luminescence units. Scale bars are 5 mm in (c) and (d), 500 μm in (e) and (f), and 5 mm in (h).

5.6. Materials and methods

5.6.1. Fabrication of magnetic living hydrogels

Bacterial strains. Plasmid construction and DNA manipulations of bacteria were performed following standard molecular biology techniques. Genetics parts and plasmids used in this study were available from Addgene and the previous paper [448]. All plasmids were constructed by combining PCR fragments generated by Kapa HiFi Polymerase using Gibson assembly [448]. Routine cloning and plasmid propagation were performed in E. coli DH5α, and the gene circuits were transferred into probiotic E. coli Nissle 1917 for bacterial encapsulation.

Silica coating on NdFeB microparticles. NdFeB microparticles were coated with a thin shell of silica based on the condensation reaction of tetraethylorthosilicate (TEOS), which nucleated around the particles to form a cross-linked silica layer [462]. First, 40 g of NdFeB microparticles was dispersed in 1000 mL of ethanol with vigorously stirring to avoid sedimentation at 1500 rpm using a digital mixer (Cole-Parmer). Then, 60 mL of 29% ammonium hydroxide was slowly added to the mixture, followed by slow addition of 2 mL of TEOS. The mixture was stirred for 12 hours at room temperature and then washed with acetone multiple times after the reaction. The suspension was then vacuum-filtered to obtain the silica-coated microparticles.

Fabrication of magnetic living hydrogels. Engineered bacteria were routinely cultured overnight at 37˚C in Luria-Bertani (LB) media (Difco) supplemented with 50 μg mL^{-1} kanamycin. For bacterial encapsulation, overnight cultures of bacteria (E. coli Nissle 1917, 10 mL) were centrifuged at 5000g for 5 minutes, followed by supernatant removal. The remaining bacteria pellets were resuspended in 10 mL of 10 wt% PVA solution (Mw 146,000-186,000, 99+% hydrolyzed) using a planetary mixer (AR-100, Thinky) at 2000 rpm for 2 min. The magnetic hydrogel was prepared by homogeneously mixing silica-coated NdFeB microparticles with an average size of 5 μm (MQFP-B 20441-089, Magnequench) into the bacteria-containing PVA solution using a planetary mixer (AR-100, Thinky) at 2000 rpm for 2 min. The mixture was then magnetized by impulse magnetic fields (about 2.5 T) generated by an impulse magnetizer (IM-10-30, ASC Scientific) to impart magnetic polarities to the NdFeB microparticles embedded in the

uncured PVA solution. Afterward, the magnetized solution was exposed to –20 °C for 24 hours, resulting in a physically crosslinked hydrogel matrix. Magnetic hydrogels with different Young's moduli were fabricated by adjusting the freezing time from 2 h to 48 h. Bacteria (E. coli DH5α) were encapsulated in the magnetic hydrogels with different Young's moduli.

5.6.2. Mechanical characterization

Magnetic living hydrogels based on PVA and NdFeB with different particle concentrations were prepared and then swollen in PBS for 1 h. Subsequently, they were cut into dog bone–shaped specimens with known dimensions (width 4.7 mm, thickness 1.6 mm, gauge length 17 mm) for tensile testing. The specimens were tested on a mechanical testing machine (Z2.5, Zwick/Roell) with a 20-N load cell at a strain rate of 0.01 s^{-1}. A nominal stress–stretch curve was plotted for each specimen, and the Young's modulus and toughness were identified by the initial slope and the area under the stress strain curve, respectively.

5.3.3. Magnetic characterization

Magnetic characterization. The magnetic moment densities of magnetic hydrogels based on PVA and NdFeB with different particle concentrations were measured with a vibrating sample magnetometer (DMS 1660, ADE Technologies). Specimens were prepared from thin sheets of the hydrogels obtained from molding by cutting them into 6-mm circles using a biopsy punch (size 6, Miltex) to fit into the sample holder of the magnetometer. The remanent magnetization of the samples was measured when the applied external magnetic field was zero and then divided by the sample volume to obtain the magnetization or magnetic moment density.

Magnetic field measurement and shielding. We used an AC/DC magnetic meter (PCE-MFM 3000) to measure the magnitude of the magnetic field near the magnet (DY08-N52, K&J Magnetics). A sheet of spring steel (thickness 2.6 mm, McMaster Carr) was attached to the magnet for shielding the magnetic field.

5.6.4. Physical characterization

Diffusion coefficient measurement. Diffusion coefficients of molecules within the magnetic hydrogels (12 vol% NdFeB) were determined using fluorescence recovery after photobleaching

(FRAP). A series of fluorescent probes, that is, fluorescein isothiocyanate-dextran with molecular weights of 500 Da, 4 kDa, 10 kDa, and 70 kDa (FITC-dextran, Sigma-Aldrich) were dissolved in PBS at 5 mg mL^{-1}. The magnetic hydrogels (1 g) were added to the fluorescent solution (50 mL), yielding a final concentration of 5 mg mL^{-1} FITC-dextran in the hydrogels. FRAP measurement of diffusion coefficients was performed on a confocal microscope (SP 8, Leica) with a 5× magnification objective and a 488 nm laser. A circle (radius ω ~15 μm) was selected as the bleaching spot. 20 pre-bleach images were scanned at a low laser intensity (1%), then the bleaching spot was bleached with five iterations (~2.6 s in total) at 100% laser intensity, and followed by detection of the fluorescence recovery in the bleaching spot at low intensity (1%). For each experiment, we obtained a normalized fluorescence recovery curve and a fitting parameter, the characteristic diffusion time τ_D . The diffusion coefficient D_h was then calculated according to $D_h = 0.22\ \omega^2 / \tau_D$.

Friction coefficient measurement. Magnetic hydrogel samples (20 mm × 20 mm × 1 mm) were prepared with 12 vol% NdFeB microparticles. To quantify the friction coefficients, the torque required to shear the specimens at a prescribed shear rate of 1.0 s^{-1} under prescribed normal pressure (from 1.5 to 9 kPa) was measured from a rotational rheometer (AR-G2, TA Instruments) in normal force control mode with a 20-mm-diameter steel plate geometry. In the control group, deionized water was smeared between the hydrogel sample and steel plate before shearing the samples. In the experimental group, a piece of mucus-covered intestinal tissue (Sierra Medical Inc.) was attached to the steel plate and the mucus layer was brought in contact with the magnetic hydrogel. The friction coefficients were calculated following the previously reported protocol [421].

5.6.4. In vitro biocompatibility

Chemical element analysis in leaching solutions. Leaching test of magnetic hydrogels was performed by incubating 1 g of the magnetic hydrogel in 1 mL of simulated intestinal fluid (pH 6.8) [449] for 0–10 days or 1 mL of simulated gastric fluid (pH 1.2) [449] for 0–1 day. Leached elements in the solutions were identified and quantified by inductively coupled plasma mass spectrometry (ICP-MS). ICP-MS analysis was performed on an Agilent 7900 instrument in helium mode (4.5 mL min^{-1} flow rate). 2% HNO_3 was used as a rinse solution, and 10 ppb terbium was

included as an internal standard among all samples. Calibration standards were prepared by volumetric dilution of a multielement standard. Both calibration standards and experimental samples were diluted with 2% HNO_3 to ensure the stability of elements before spectroscopic analysis. Data were collected and analyzed for the following elements of interest: ^{56}Fe and ^{146}Nd.

In vitro cytotoxicity. We conducted in vitro cytotoxicity tests using a magnetic hydrogel-conditioned medium for Caco-2 (American Type Culture Collection) cell culture. There were no bacteria in the magnetic hydrogel for the biocompatibility test. To prepare the magnetic hydrogel-conditioned medium for in vitro cytotoxicity tests, we incubated 20 mg of the magnetic hydrogel in 1 mL of Dulbecco's modified Eagle medium (DMEM, Life Technologies) at 37 °C for 1, 4, 7 days. Caco-2 cells were cultured in DMEM supplemented with 10% fetal bovine serum (Sigma-Aldrich), 1× non-essential amino acids solution (Life Technologies), 1× GlutaMAX (Life Technologies), and penicillin/streptomycin (Life Technologies), and plated in 96-well plates. The cells were then treated with the magnetic hydrogel-conditioned medium and incubated at 37 °C for 48 h in 5% CO_2. Cells grown in pristine DMEM were used as a positive control. Cells grown in pristine DMEM and then treated with 70% ethanol for 30 min were used as a negative control. Cell viability was determined by using a live/dead viability/cytotoxicity kit for mammalian cells (Life Technologies). We used a confocal microscope (SP 8, Leica) to image live cells with excitation/emission at 495 nm/515 nm, and dead cells at 495 nm/635 nm. Live and dead cell numbers were counted using ImageJ, and the ratio of live cells to all cells in the images was calculated as Caco-2 cell viability.

Bacterial viability in hydrogels. 1 g of magnetic hydrogels containing living bacteria were incubated in 20 mL of fresh LB broth at 37˚C for 1–7 days, and the media were changed every 12 h. To test the bacterial viability, the hydrogels were first washed with 0.85% NaCl solution and then stained using the live/dead BacLight bacterial viability kit. 15 min after staining, fluorescent imaging of samples (n = 3) was carried out using a confocal microscope (SP 8, Leica). Magnetic hydrogels treated with 70% ethanol for 1 h were used as a negative control. The occupied areas of green (S_g) and red colonies (S_r) in the images were obtained using ImageJ, and the bacterial viability equals the viable populations over all populations, that is, viability = $S_g / (S_g + S_r)$.

In vitro blood sensing in hydrogels containing bacteria. The heme-sensing ability of bacteria in the magnetic hydrogel was induced by 0.1 vol% defibrinated horse blood (Hemostat) in the culture media and incubated with shaking at 37˚C for 24 hours. Luminescence of hydrogels was visualized via a ChemiDoc Imaging System (Bio-Rad), with an exposure time of 60 s. To quantify the luminescence, 0.1 g of magnetic hydrogels were homogenized in 1 mL of PBS with a 4 mm stainless steel bead using a TissueLyser II (Qiagen) at 30 Hz for 5 minutes. Samples were centrifuged at 1000g for 1 min to deposit large hydrogel debris. The supernatant was serially diluted in sterile PBS and spot plated on MacConkey agar supplemented with 50 μg mL^{-1} kanamycin. Colonies (CFU) were enumerated following overnight incubation at 37˚C. On the other hand, we measured the luminescence in hydrogel homogenate in a BioTek Synergy H1 Hybrid Reader with an integration time of 1 second and a sensitivity of 150. The normalized luminescence of the magnetic hydrogel on different days was calculated as the ratio of the luminescence values (RLU/CFU; RLU, relative luminescence) of the magnetic hydrogel induced by 0.1 vol% blood to that of a non-induced magnetic hydrogel (a negative control) on the same day.

5.6.5. In vitro retention

Retention in a plastic tube. A transparent polyvinyl chloride tube (McMaster Carr) with the inner diameter of 2 mm or 15 mm was filled with liquid (i.e., water, 8.90×10^{-4} Pa·s in viscosity; or glycerol, 1.4 Pa·s in viscosity) aand a magnetic hydrogel. Two ends of the plastic tube were then connected to a soft rubber tube (Masterflex L/S), which was loaded into a peristaltic pump (Masterflex L/S) to drive the fluid flow in the tube. A magnet (D71-N52 or DY08-N52, K&J Magnetics) was placed beneath the tube at a distance. The shear stress at the wall was written as $\tau_w = \frac{4\eta Q}{\pi r_{\text{tube}}^3}$, where η was the fluid velocity, Q was the flow flux of the fluid, and r_{tube} was the radius of the tube.

Retention and localization in a silicone phantom. An intestine phantom model made of silicone (Trandomed 3D) was custom-designed and 3D-printed. This silicone phantom was filled with swollen polyacrylate particles (Iste Lock 770, M2 Polymer) and connected to a peristaltic pump (Masterflex L/S) to simulate the intestinal peristalsis. In the set of demonstrations, the retention

and localization were controlled by a magnet (DY08-N52, K&J Magnetics) on a transparent acrylic sheet which was placed horizontally on top of the phantom at a closest distance of 15 mm.

Temperature sensing in a silicone phantom. The magnetic hydrogel was glued to a temperature sensor (DST nanoT, Star-Oddi) using cyanoacrylate adhesives (Loctite 460 instant adhesive). The temperature sensor has a size of 6 mm in diameter and 17 mm in length, completely encapsulated in the magnetic hydrogel. The sensor contains a tiny silver-oxide battery, which was weakly magnetic. The retention and localization of the integrated device in the artificial intestine were controlled by the external magnet. The presence of the external magnet did not influence the temperature readings of the sensor, and the presence of the sensor did not affect the magnetic retention. 100 mL of cold water (0 °C) was infused from the inlet of the phantom to replicate the water drinking. The temperature sensor was retrieved from the outlet of the phantom and the temperature over time was recorded at different spots in the phantom.

5.6.6. In vivo retention and sensing

Retention in mouse intestine. All mouse experiments were approved by the Committee on Animal Care at the Massachusetts Institute of Technology (protocol number: 0818-075-21). Specific-pathogen free (SPF), male C57BL/6J mice (8-10 weeks of age) were purchased from Jackson Labs and were housed and handled under conventional conditions. Mice were acclimated to the animal facility 1 week prior to the commencement of experiments. Magnetic hydrogels containing engineered bacteria were prepared and incubated in fresh LB broth for 24 h. Then, the hydrogels were cut into small particles (radius 1 mm, thickness 1 mm) by a razor blade and dispersed in a block of nutritious jelly (DietGel 76A, ClearH_2O). The nutritious jelly was provided to mice after overnight fasting. After mice ingested the jelly and magnetic hydrogels, X-ray microtomography (microCT, Bruker) was used to visualize the 3D spatial position of magnetic hydrogels in the GI tract over time. Mice with magnetic hydrogels inside their bodies were allocated into two groups: the control group without any treatment (n = 5), while the experimental group carrying a disc-shaped magnet (D71-52, K&J Magnetics) adhered on the abdomen (n = 5). The disc-shaped magnet was attached to the shaved abdomen skin and adhered by a layer of Histoacryl flexible adhesive (B. Braun Medical Inc.), and then mice were singly housed to prevent magnet-induced physical harm. The magnetic hydrogel retention in the mouse intestine was

monitored by microCT in the experimental group daily for 7 days. All animals were monitored clinically at least twice a day for any evidence of morbidity, including lethargy, inappetence, decreased fecal output, abdominal distension, and decreased body weight.

Blood sensing in mouse intestine. To examine the blood sensing ability of magnetic hydrogels in vivo, we evaluated whether magnetic hydrogels containing engineered bacteria that retained in the intestine could detect upper GI bleeding elicited by oral indomethacin administration. Before indomethacin treatment, mice had taken the magnetic hydrogel containing bacteria and a small magnet disc was fixed on the abdomen skin. After 12-h retention of magnetic hydrogels in the intestine, we induced GI bleeding by indomethacin. Indomethacin solution was prepared by dissolving the compound in absolute ethanol to a concentration of 20 mg mL^{-1}. Immediately prior to mouse gavage, the indomethacin stock solution was diluted to 2 mg mL^{-1} in PBS, and the dilute indomethacin solution was administered to each animal in the treatment group (10 mg/kg). In the control group, mice were fed with 0.2 mL of PBS. In the following morning, gastrointestinal bleeding was confirmed by performing a guaiac test (Hemoccult, Beckman Coulter) on fecal pellets from each animal. Magnet discs on the abdomen were removed and fecal pellets were collected at 1–6 h after magnet removal. The presence of magnetic hydrogels in the fecal pellets was checked by CT scanning of the collected fecal samples. The feces with magnetic hydrogels were used for luminescence analysis and CFU enumeration, and luminescence values were normalized to CFU values and reported in RLU/CFU.

Histology analysis. All mice were sacrificed for histopathological analysis after experiments. Small intestines with and without the magnetic hydrogels were isolated, gently cleaned with PBS, fixed in 10% formaldehyde for 24 h, embedded in paraffin, sectioned, and stained with haematoxylin and eosin. Standard H&E-stained sections for the segments of interest were examined.

5.7. Conclusions

In summary, we have introduced a magnetic hydrogel retentive system that combined an ingestible magnetic living hydrogel with a wearable magnet. This system relied on magnetic attraction to counteract the propelling effects of normal intestinal motility. Using theoretical calculations, we

optimized the dimensions of the extracorporeal magnet for retention of the magnetic hydrogels applicable to either mice or humans. The retention and positioning of the magnetic hydrogel under the control of an extracorporeal magnet were verified by using a mouse-sized tube, a human-sized tube, a human-sized intestine phantom in vitro, and a mouse model in vivo. Similarly, Buss et al. created a slurry of magnetic microparticles and SPION (superparamagnetic iron oxide nanoparticle)-labeled bacterial cells to achieve prolonged retention in mouse gut for 20 days [479]. By incorporating genetically engineered heme-sensing bacteria into the ingestible hydrogel, we demonstrated that the device functioned to detect GI bleeding, as a proof of concept for biosensing in the gut. Engineering bacteria encapsulated in the protective magnetic hydrogel could thus perform diagnostic functions at localized sites in the gut.

There is still room for improvement in the current magnetic hydrogel retentive system. First, the dimensional discrepancy between mouse and human may limit the generalization of the results obtained from mouse studies to clinical settings [475]. The distance between the two parts affects magnetic control: given that the magnetic field varies inversely with the third power of distance and that magnetic force varies inversely with the fourth power of distance [462], validation in large animal species such as pigs and dogs will be required prior to translation to humans. Second, we have shown blood sensing and temperature recording in this work as a proof of concept to demonstrate several functionalities of the intestinal retentive hydrogels. Magnetic hydrogels can also be combined with other actuators, optics, or electronics [126, 451] to enable a range of biomedical applications for these intestinal retentive devices. For example, coupling with bioelectronics to transduce the detected values in real-time [448] and wiring them to next-step actuation would achieve a series of semi-autonomous or autonomous programs while the device is retained in the intestine [126, 445]. Ultimately, spatially localized and temporally retained hydrogel devices may be used to deliver drug-producing bacteria at targeted enteric sites, which can overcome the shortcomings of systemic treatment (e.g., frequent high-dose injections and side effects) and conventional oral administration (e.g., protein degradation in the acidic, protease-rich upper GI tract). Incorporating drug-producing bacteria in the intestinal retentive hydrogel could allow the requisite doses to be reduced by several orders of magnitudes, thus reducing systemic side effects [480, 481].

Chapter 6

Hydrogel gastric retentive devices

The research presented in this chapter has been published in:

- **Xinyue Liu**†, Christoph Steiger†, Shaoting Lin†, Ji Liu, German A Parada, Joy Collins, Siid Tamang, Hon Fai Chan, Hyunwoo Yuk, Nhi Pham, Giovanni Traverso, and Xuanhe Zhao. Ingestible hydrogel device. Nature Communications. 10, 2019.

6.1. Introduction

The integration of technology with the human body requires new devices that are biocompatible, mechanically flexible, and robust over time in biological organisms[447, 482]. For instance, devices that reside in the stomach for days to months can enable new applications as diverse as in-body physiological monitoring and diagnosis[440, 448], bariatric/metabolic interventions[460, 483], and prolonged drug delivery[484, 485]. Prior approaches to gastric retention include using floating particles on the air/fluid interface[486], and size exclusion through unfolding structures[449, 487] or swellable materials[484, 488]. Hydrogels represent an ideal material candidate for gastric residency, owing to their inherent similarities to human tissues (e.g., soft, wet, biocompatible, and bioactive)[55, 277]. For long-term gastric retention, the hydrogel device needs to swell in the gastric environment from an orally administered pill (diameter of 1.0–1.5 cm) to a size large enough to avoid passing through the pylorus (diameter of 1.3–2.0 cm)[489], and fast enough to avert gastric emptying, which generally occurs 0.5–1.5 h after ingestion[490]. Additionally, the hydrogel device is required to withstand long-term mechanical forces from the stomach (~ 1,000 cycles per day of 5–10 kPa)[491] and degrade on demand[484]. Tough hydrogels have been used for gastric retention[484], but their low swelling speed presents a challenge for clinical development. Alternative methods to increase the swelling speed include the incorporation of interconnected pores into hydrogels[492, 493], which tends to adversely affect the hydrogels' swelling ratio and mechanical robustness. Overall, the requirements of high swelling ratio, high

swelling speed, and long-term mechanical robustness in the gastric environment are currently not satisfied among existing hydrogels, limiting the applications of hydrogel devices.

In nature, Tetraodontidae (pufferfish) can rapidly inflate its body into a large and robust sphere when threatened (**Figure 6-1a**)[494, 495]. Its fast inflation abilities and mechanical robustness are enabled by the pufferfish's capacity for rapidly imbibing water (no diffusion here) and its stretchable and anti-fatigue skin. Here, we introduce a pufferfish-inspired hydrogel device, consisting of superabsorbent hydrogel particles that enable the device to quickly imbibe water (instead of diffusion) encapsulated in a soft yet anti-fatigue hydrogel membrane that maintains long-term robustness of the device. The pufferfish-inspired hydrogel device can be ingested as a standard-sized pill (diameter of 1–1.5 cm), rapidly imbibe water and inflate (up to 100 times in volume within 10 min) into a large soft sphere (diameter of up to 6 cm, modulus of 3 kPa), and maintain robustness under repeated mechanical loads over a long time (more than 26,000 cycles of 20 N force over two weeks in vitro). We demonstrate the rapid swelling and long-term gastric retention of the hydrogel device for 9 to 29 days in a large animal model. An embedded sensor in the hydrogel device can continuously monitor in-body physiological parameters (here demonstrated by measuring gastric temperature) throughout the retention period. In addition, the hydrogel device can shrink on demand to exit the body in response to a biocompatible salt solution (**Figure 6-1e**,f). This pufferfish-inspired hydrogel device possesses a set of advantages over conventional ingestible devices made of other materials due to hydrogels' biocompatibility, high water content, and tissue-like softness[55, 277, 447].

6.2. Design principles

The design of the pufferfish-inspired hydrogel device is schematically illustrated in **Figure 6-1**. The hydrogel device consists of superabsorbent hydrogel particles (sodium polyacrylate, ~ 450 μm in diameter) encapsulated in an anti-fatigue porous hydrogel membrane (freeze-thawed PVA, ~ 750 μm in thickness, ~ 200 μm in pore diameter) (see Materials and Methods for detailed fabrication). This design decouples the swelling ratio, swelling speed, and mechanical robustness of hydrogels. Note that the swelling ratio is defined as V_{max}/V_0, and the swelling speed is quantified by the rate constant k in the equation

$$\partial V / \partial t = k(V_{max} - V) \tag{6-1}$$

where V_0 is the initial volume of the hydrogel device, V_{max} the fully swollen volume, and V the volume at swelling time t[496]. The individual superabsorbent particles can swell ~ 160 times in volume within 5–10 min[97]. As the particles swell, water infiltrates through the pores on the membrane into the hydrogel device, mimicking the rapid imbibition of water by pufferfish. This fast swelling is further facilitated by the capillary effect between particles, which promotes water migration inside the hydrogel device (see Modeling for detailed analysis of swelling). The designed hydrogel membrane of the device is capable of sustaining at least 9,000 cycles of 4.3 MPa tensile stress, and thus maintains its robustness under repeated loads, mimicking the anti-fatigue skin of the pufferfish[495]. To enable versatile functionalities such as bio-signal recording and extended drug release, wireless sensors and drug depots can be incorporated inside the hydrogel device. For safe and on-demand exit of the swollen hydrogel device from the gastrointestinal (GI) tract, a calcium chloride solution that flows into the hydrogel device and deswells the superabsorbent particles can be adopted to induce rapid shrinkage of the swollen hydrogel device (**Figure 6-1e,f**). The calcium concentration is within the safe consumption level[497].

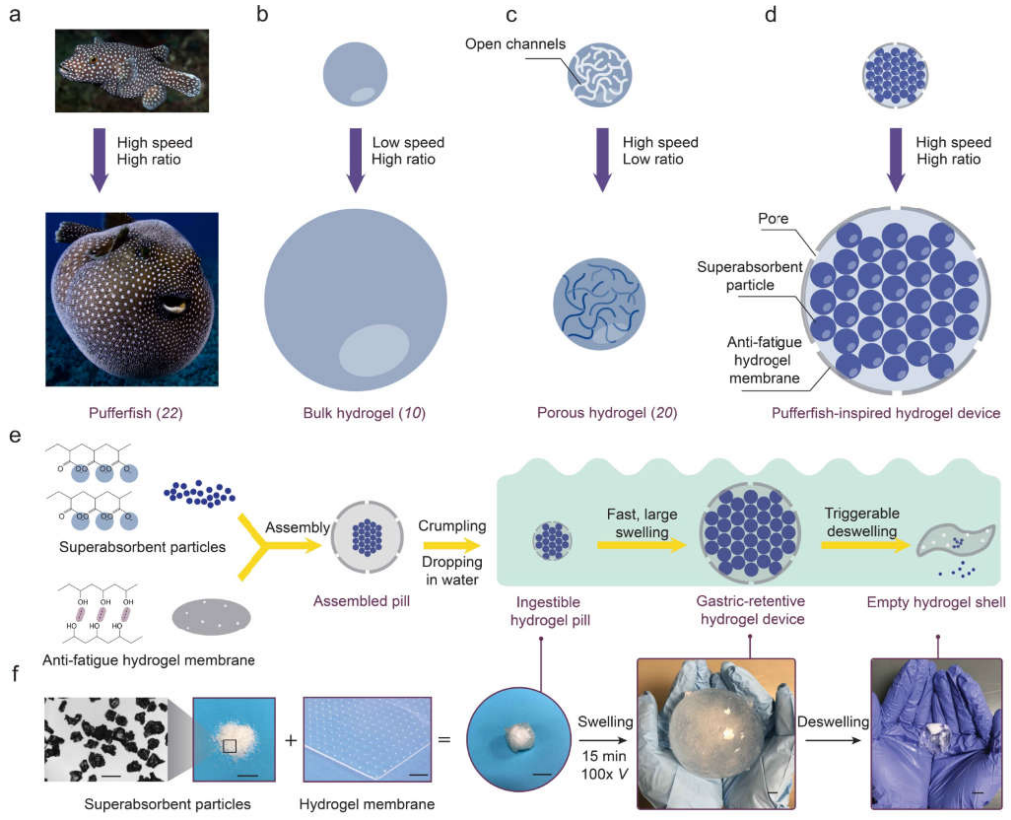

Figure 6-1. Design of the pufferfish-inspired ingestible hydrogel device. (a) A pufferfish inflates its body into a large ball by rapidly imbibing water [494]. (b) Bulk hydrogels swell in water with a low swelling speed [484].(c) Porous hydrogels swell in water with a low swelling ratio [492]. (d) The designed hydrogel device swells in water with both a high speed and a high ratio. (e) Schematic of the fabrication process and working principle of the designed hydrogel device. (f) Photographs of the fabrication process and working principle of the designed hydrogel device. Scale bars are 0.5 mm in (f, first) and 10 mm in (f, others).

6.3. Results and discussion

6.3.1. Swelling characterization

We first investigate the swelling kinetics of the hydrogel device. As shown in **Figure 6-2a**, a hydrogel device with initial size of 1 cm^3 (1 cm in length) swelled into a sphere with a maximum size of 100 cm^3 (5.8 cm in diameter) in 10 min in deionized water (pH 7), indicating a high swelling speed and a high swelling ratio (**Figure 6-2b**). As shown the comparison chart in **Figure 6-2c**, the swelling speed of the designed hydrogel device is orders of magnitude higher than that of bulk hydrogels (such as air-dried PAAm and sodium polyacrylate hydrogels of similar size[97, 484]. The hydrogel device also outperformed the porous hydrogels (such as freeze-dried hydrogels and hydrogel foams) in terms of swelling ratio[97, 492]. By varying the Young's modulus of the PVA hydrogel membrane, we tune the swelling ratio of the hydrogel device while maintaining its high swelling speed (**Figure 6-2d**) (see Modeling for detailed analysis of swelling). We further perform swelling tests of the hydrogel device with a membrane modulus of 3 kPa in porcine gastric fluid and simulated gastric fluid (SGF, pH 3). The hydrogel device swelled ~ 25 times in both media within 10 min, indicating that a hydrogel device with initial size of 3 cm^3 (1.4 cm in length) is capable of swelling to 75 cm^3 (5.2 cm in diameter) within 10 min (**Figure 6-2e**). **Figure 6-2f,g** summarized the swelling ratios and swelling speeds of the hydrogel device with various membrane moduli in water, SGF (pH 3), and porcine gastric fluid. Given that its swelling is faster than the typical gastric emptying time[490], its initial dimension is less than the diameter of the esophagus[498], and its swollen size is greater than the diameter of the pylorus[489], we conclude that the hydrogel device is compatible with oral administration and potential gastric residence.

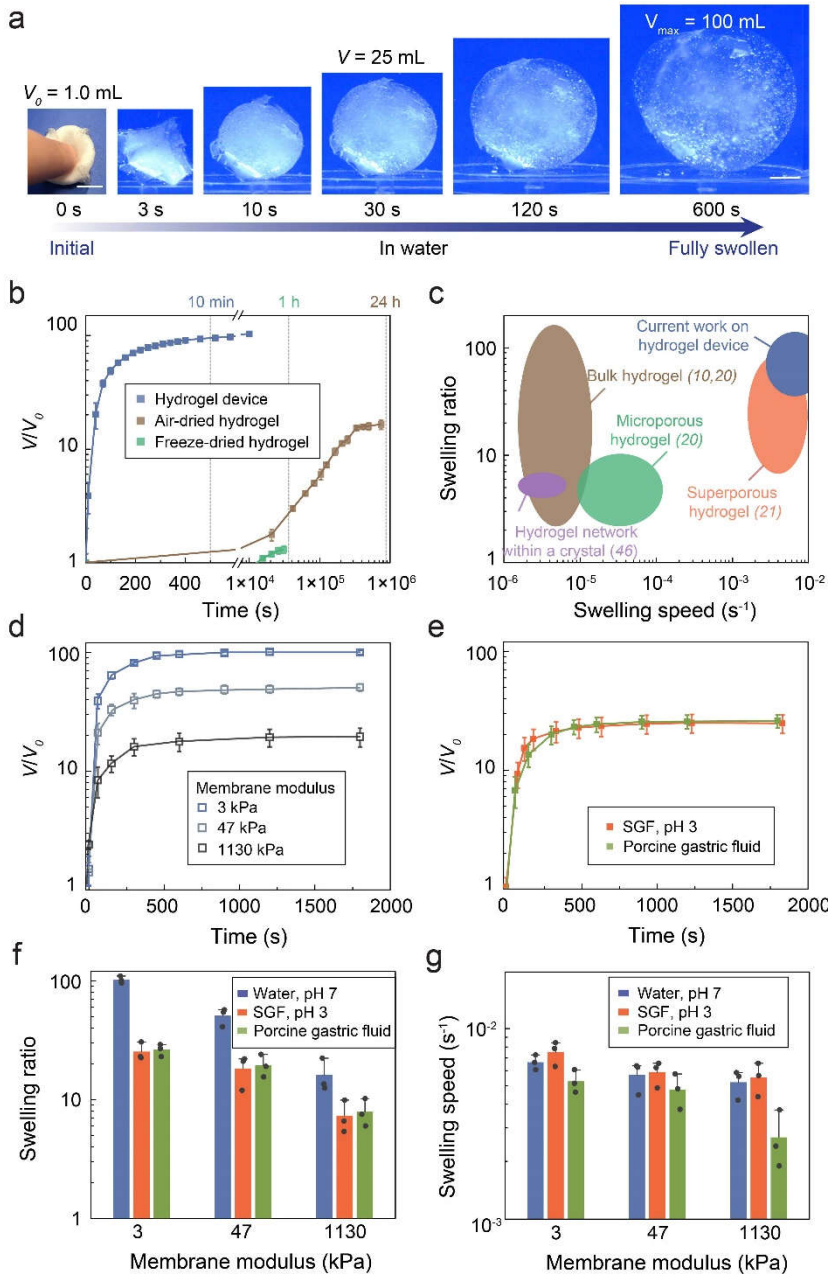

Figure 6-2. High-speed and high-ratio swelling of the ingestible hydrogel device. (a) Time-lapse images of the hydrogel device swelling in water (pH 7). (b) Volume changes of the hydrogel device (membrane modulus 3 kPa), air-dried hydrogel, and freeze-dried hydrogel of the same size as a function of swelling time in water. (c) Comparison of the swelling ratios and speeds in water between the hydrogel device in current work and previously reported hydrogels[484, 492, 493, 499]. (d) Volume changes of the hydrogel devices with various membrane moduli as functions of swelling time in water. (e) Volume changes of the hydrogel devices (membrane modulus 3 kPa) as functions of swelling time in porcine gastric fluid and SGF (pH 3). (f) Swelling ratios of the hydrogel devices with various membrane moduli in water, SGF (pH 3), and porcine gastric fluid. (g) Swelling speeds of the hydrogel devices with various membrane moduli in water, SGF (pH 3),

and porcine gastric fluid. Data in (b), (d), (e), (f) and (g) are means ± SD, n = 3. Scale bars are 10 mm in (a).

To introduce a rescue strategy for potential complications caused by ingestible devices in the GI tract (e.g., bowel obstruction)[500, 501], we demonstrate the rapid shrinkage of the swollen hydrogel device by introducing calcium ions, which flowed into the hydrogel device and bound with the carboxylate groups in the sodium polyacrylate hydrogel. As shown in **Figure 6-3a-c**, the calcium solution (0.6 M) induced the deswelling of superabsorbent particles within 15 min, leading to shrunken particles in an empty hydrogel shell. The hydrogel device is designed such that its shrunken state is small and compliant (~ 1 cm in diameter when compacted, 3–47 kPa in Young's modulus) in order to safely pass through the GI tract[449, 489]. The amount of calcium needed to trigger the shrinkage of hydrogel device (0.6 M; 2.1 g for a typical stomach with 87 mL gastric fluid) is less than the tolerable upper intake level of calcium (2.5–3 g per day)[497], but ~ 20 times greater than the amount in calcium-rich foods (for example, 0.03 M in milk)[502]. Additionally, we demonstrate that a low concentration of calcium (0.03 M) does not significantly affect the SGF-swollen hydrogel device (**Figure 6-3d**), supporting the stability of the hydrogel device in the stomach against the regular calcium intake.

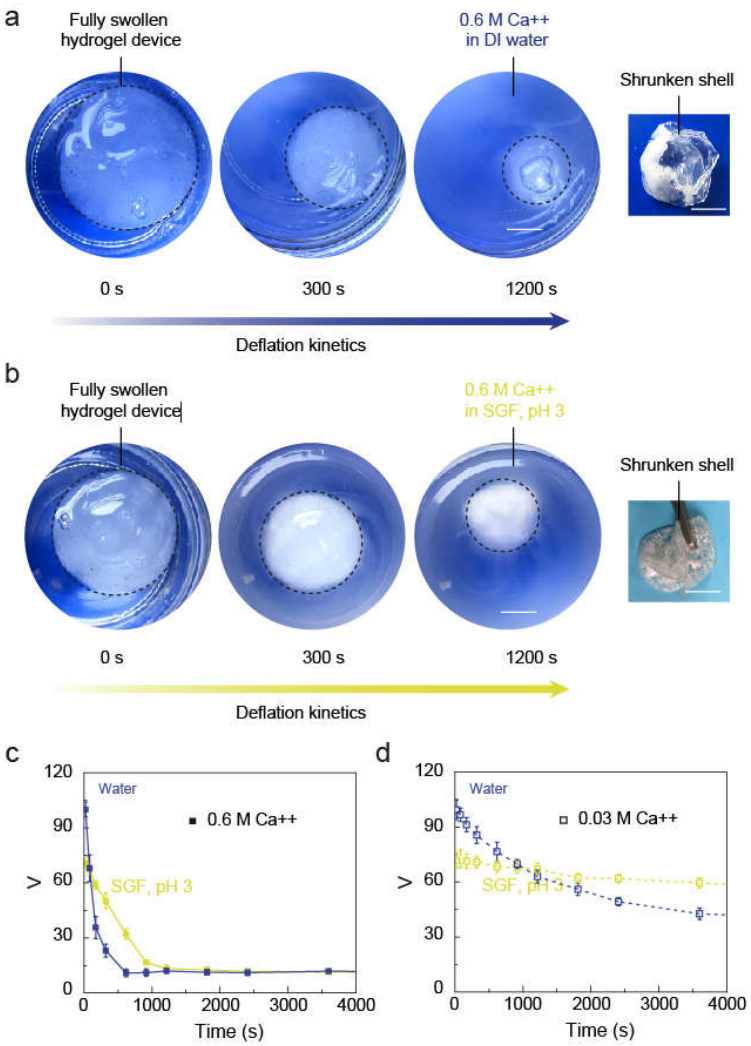

Figure 6-3. Deswelling of the hydrogel devices. (a) Time-lapse images of the $CaCl_2$ (0.6 M) induced deswelling of the hydrogel device in water (pH 7). (b) Time-lapse images of the $CaCl_2$ (0.6 M) induced deswelling of the hydrogel device in SGF (pH 3). (c) Volumetric deflation kinetics of the hydrogel device induced by $CaCl_2$ (0.6 M) in different media. (d) Volumetric deflation kinetics of the hydrogel device induced by $CaCl_2$ (0.03 M) in different media. Data in (c) and (d) are means ± SD, n = 3. Scale bars are 10 mm in (a) and (b).

6.3.2. Mechanical characterization

To provide a mechanically flexible and conformable interface with the stomach, the hydrogel device is designed such that the overall moduli ranged from 3 kPa to 10 kPa with membrane moduli of 3 kPa to 47 kPa (**Figure 6-4**). The hydrogel device is much softer than most existing ingestible devices which contain dry, rigid, and non-degradable materials in order to maintain their structural integrity within the GI tract and to protect electronic components from the harsh environment, such as stomach acid (**Figure 6-5b**)[440, 448, 449, 487, 500]. The compliance of the hydrogel

device is in line with that of common foods (e.g., 15 kPa for noodles[503] and 24 kPa for tofu[504]) and human tissues (e.g., 7 kPa for muscle and 85 kPa for skin[505]). The food and tissue-level softness of the hydrogel device alleviates the potential of GI mucosa injury.

To ensure the long-term robustness of the hydrogel device in the gastric environment, we evaluate its mechanical performance, including the membrane material and the overall device. The stomach generates hydrodynamic flows and cyclic compressive forces in order to grind food into smaller particles, mix them with gastric fluids, and empty them through the pylorus[491]. However, most hydrogels are susceptible to fatigue failure under cyclic mechanical loads, especially in acidic environments[293]. We find that freeze-thawed PVA hydrogels can be used as the anti-fatigue membrane[353] for the hydrogel device under cyclic mechanical loads. The freeze-thawing treatment introduced nano-crystalline domains into the PVA hydrogel, making it strong, tough, and fatigue resistant while maintaining a low modulus (**Figure 6-4**). After being immersed in SGF (pH 3) at body temperature (37 °C) for over two weeks, the hydrogel membrane demonstrated high strength of over 7 MPa (**Figure 6-4b**) and high toughness of over 1,000 J m^{-2} (**Figure 6-4c**). The hydrogel membrane is also capable of sustaining 9,000 cycles of 4.3 MPa tensile stress, and thus maintained the robustness of the swollen hydrogel device under repeated loads[97].

Furthermore, we validate the high robustness of the swollen hydrogel device under mechanical loads. We show that the hydrogel device (diameter ~ 3.6 cm, swollen in SGF) could sustain large compressive strain up to 90% and high force up to 70 N (**Figure 6-4d,e**). Considering the dimension of the hydrogel device, the effective compressive stress is calculated as ~ 70 kPa, which is much higher than the maximum gastric pressure (i.e., ~ 10 kPa)[491]. In addition, we apply 1,920 cycles of 40% compressive strain on a hydrogel device (diameter ~ 4.8 cm) in SGF (pH 3) for 8 h every day (i.e., 26,880 cycles in total for 14 days). The steady-state compressive force reaches 20 N over 14 days, corresponding to an effective compressive stress of ~ 10 kPa (**Figure 6-4f**). We also record the mass of the swollen device after cyclic compression every day, and no mass loss is detected over two weeks (**Figure 6-4g**).

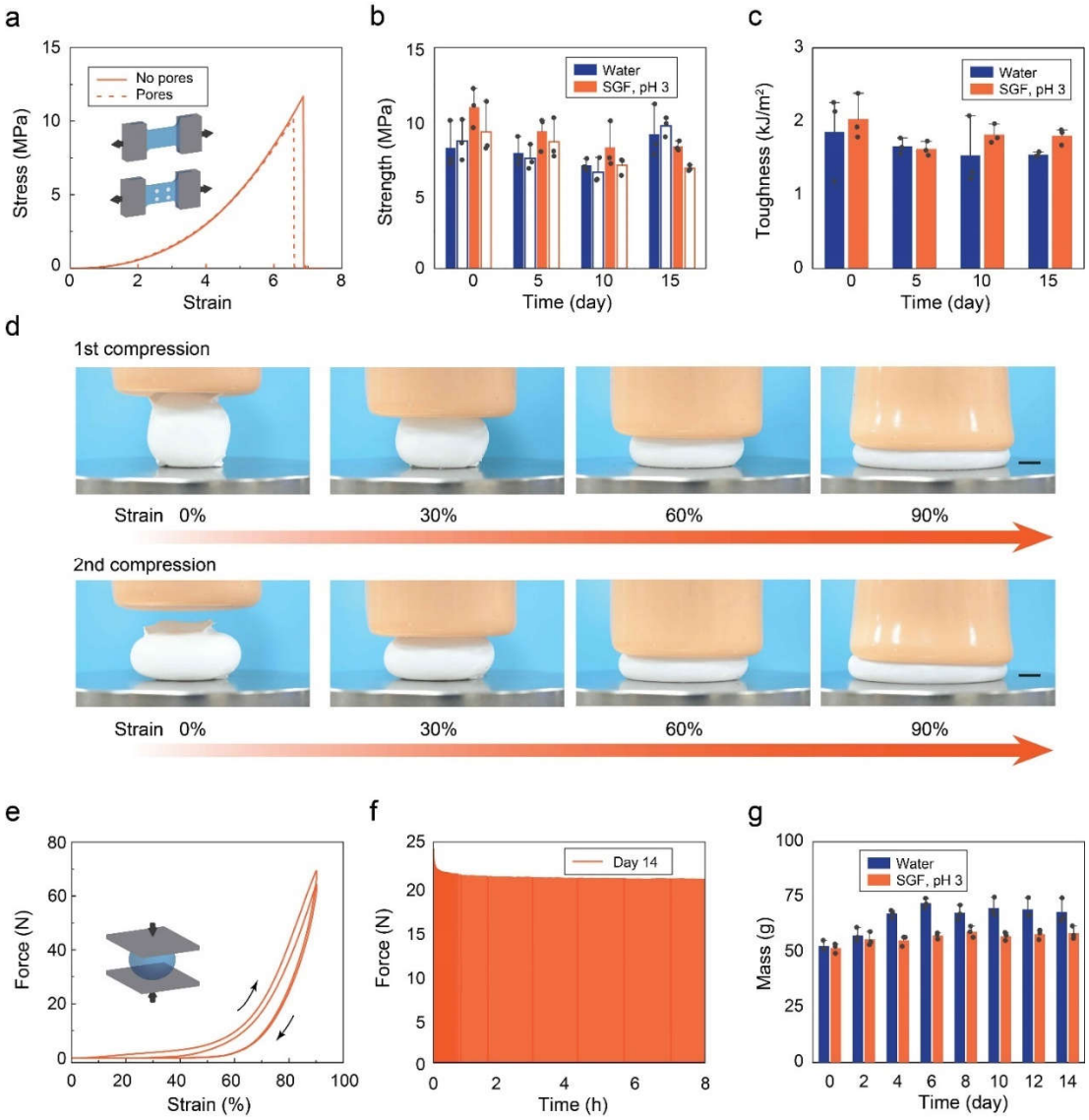

Figure 6-4. Mechanical robustness of the ingestible hydrogel device. (a) True stress-stretch curves of the PVA hydrogel membranes with and without pores, which have been immersed in SGF (pH 3) at 37 °C for 12 h. (b) Tensile strength of the hydrogel membranes with (open) and without (filled) pores, which have been immersed in water or SGF (pH 3) at 37 °C for 0–15 days. (c) Fracture toughness of the hydrogel membranes, which have been immersed in water or SGF (pH 3) at 37 °C for 0–15 days. (d) Time-lapse images of an SGF (pH 3)-saturated hydrogel device (diameter ~ 3.6 cm at undeformed state) exposed to a maximum compressive force of 70 N and a strain of 90%. (e) Force-strain curves of the SGF (pH 3)-saturated hydrogel device exposed to a maximum compressive force of 70 N and a strain of 90% for two cycles. (f) Measured compressive forces applied to a hydrogel device (diameter ~ 4.8 cm at undeformed state) on day 14 (the hydrogel device is immersed in SGF (pH 3), and sustain 1,920 cycles of 40% compressive strains for 8 h per day). (g) Measured mass of the hydrogel device after 1,920 cycles of 40% compressive strain for 8 h per day over 14 days. Data in (b), (c) and (g) are means ± SD, n = 3. Scale bars are 10 mm in (d).

6.4. Applications

6.4.1. Long-term gastric retention

Having demonstrated the significant swelling performance, mechanical softness, and long-term robustness in vitro, we subsequently test the gastric retentive applications of the hydrogel device in a Yorkshire pig model (30–50 kg in weight, N = 3 per group). **Figure 6-5a** illustrates the working principle of the hydrogel device in the GI tract. The ingestible pill enters through the esophagus into the stomach where it resides in its swollen state for a prolonged period of time. As depicted in **Figure 6-5d**, the hydrogel device with the initial size of ~ 3 cm^3 (diameter of 1 cm and length of 3 cm, compatible with oral administration) absorbed gastric fluid and swelled to ~ 50 cm^3 within 60 min in the porcine stomach. Radiographic data suggested that it retained its swollen shape and dimensions in the peristaltic and contractile stomach without being evacuated through the pylorus for a long time (9–29 days; **Figure 6-5c,e**). During its residency in the stomach, the hydrogel device floated freely with no radiographic or clinical evidence of bowel obstruction. In contrast, control samples of the non-swellable hydrogel device with no superabsorbent particles (but otherwise identical design to the original hydrogel device) had a much shorter gastric residence time (3–6 days) in the porcine stomach, indicating that high swelling ratio of the hydrogel device is required for long-term gastric retention (**Figure 6-5c**). One potential limitation of our in vivo tests is that pigs have slower gastric emptying than humans[490, 506]. Also, the gastric compression force in pigs is slightly lower in pigs than that in humans[491, 507] For the successful translation to humans, further testing in other large animal species such as beagle dogs will likely be required[508].

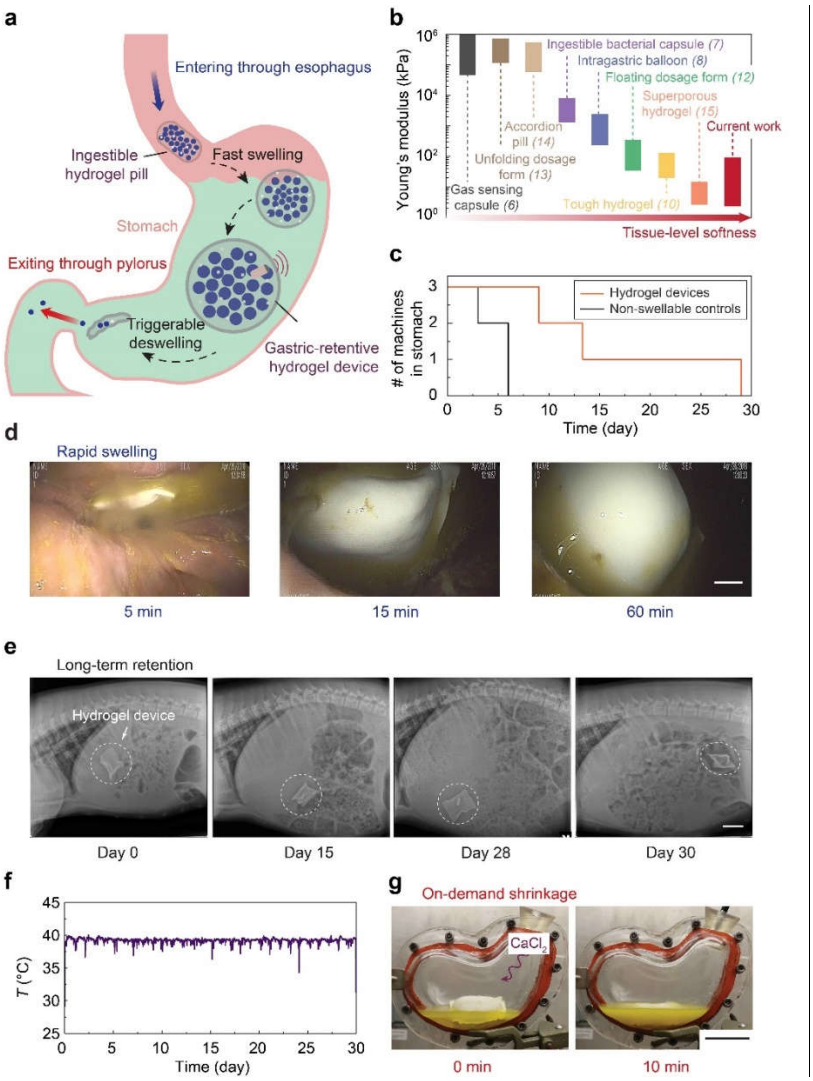

Figure 6-5. Long-term gastric retention and physiological monitoring of the ingestible hydrogel device. (a) Working principle of the gastric retentive hydrogel device, which enters through the esophagus into the stomach as an ingestible pill, resides in the stomach in its swollen state for a prolonged period of time, and exits through the pylorus as a shrunken capsule and small particles. (b) Comparison of the Young's modulus among recently reported ingestible devices[440, 448, 449, 483, 484, 486-488] and the hydrogel device in current work. (c) Number of hydrogel devices and non-swellable devices (i.e., without any superabsorbent particles) being retained in the porcine stomach as a function of time (N = 3 for each group). (d) Endoscopic images depicting the swelling of the hydrogel device in the porcine stomach. (e) X-ray images of the hydrogel device residing in the porcine stomach before being emptied into distal parts of the GI tract (here shown for 29 days in stomach). (f) Continuous measurement of porcine gastric temperature by a sensor embedded in the hydrogel device. (g) Photos of ex vivo shrinkage of the hydrogel device triggered by the addition of 0.6 M calcium chloride solution. Scale bars are 10 mm in (d), and 5 cm in (e) and (g).

6.4.2. Physiological monitoring in a pig stomach

To reveal the hydrogel device's potential application as a prolonged platform in GI tract to carry functional elements, a temperature sensor (DST nanoRF-T, Star-Oddi) is embedded in the hydrogel device. The temperature of the porcine GI tract is recorded for 30 days (**Figure 6-5f**), revealing the capability to monitor in-situ physiological signals for an extended period of time. We replot the temperature profiles in **Figure 6-5f** on a daily basis in **Figure 6-6a**, exhibiting distinct features of day–night cycles. The gastric temperature is known to be linked with the food/drink intake pattern, that is, the consumption on cooler food/drink results in a gastric temperature variation characterized by a sudden drop and subsequent rise[509]. As shown in a detailed temperature profile on day 17 (**Figure 6-6b**), there are different phases with different ingestion activities happening in one day. The pig gastric temperature stabilized at 39.2 ± 0.1 °C when the pig is asleep (from 12 am to 6:30 am). When the pig is awake (from 6:30 am to 12 am), the temperature mostly showed small or moderate fluctuations (39.6 °C ~ 38.5 °C), possibly indicating small or medium amounts of continuous food/drink ingestion. In addition, a sharp temperature drop from 39.2 °C to 37.2 °C within 20 min possibly revealed the massive food/drink intake starting from 11:30 am.

The recorded gastric temperature over a long period of time can be used to characterize the dietary habit of the subject[509, 510]. In order to visually represent the temperature pattern, the heatmaps of temperature (T) and the absolute of temperature derivative (|dT/dt|) are graphically plotted in the **Figure 6-6c,d** as functions of the day and hour. It can be seen that most of the temperature fluctuations occurred between 8 am and 8 pm on different days, indicating the regular dietary habit of the pig are kept within one month. We then assume that there exist food ingestions when $|dT/dt| > 1.75$ (the middle point defined in the heatmap color scale) during one hour, otherwise no food intake. In **Figure 6-6e**, a time slot (one hour) with food intake is marked as an event in terms of three pigs used. The average meal times and standard deviations for three pigs are calculated to be 1:25 pm ± 5.0 h (n = 34 for 9-day recording), 11:25 am ± 3.8 h (n = 41 for 13-day recording), and 1:40 pm ± 4.2 h (n = 88 for 29-day recording). The temperature patterns of three pigs have some common characteristics; for example, 8 am–8 pm is the most active food intake period for all three pigs. The pigs also show diversity in the ingestion time. For instance, pig 1 has more uniformly distributed meal time (SD ~ 5 h), and pig 2 and 3 have more concentrated food intake pattern around noontime (SD ~ 4 h). The information we obtain from the prolonged

biosignal measurement contributes to the understanding of the GI environment, and potentially monitoring of the behavior pattern, analysis of the circadian rhythm, and diagnosis of abnormality[510].

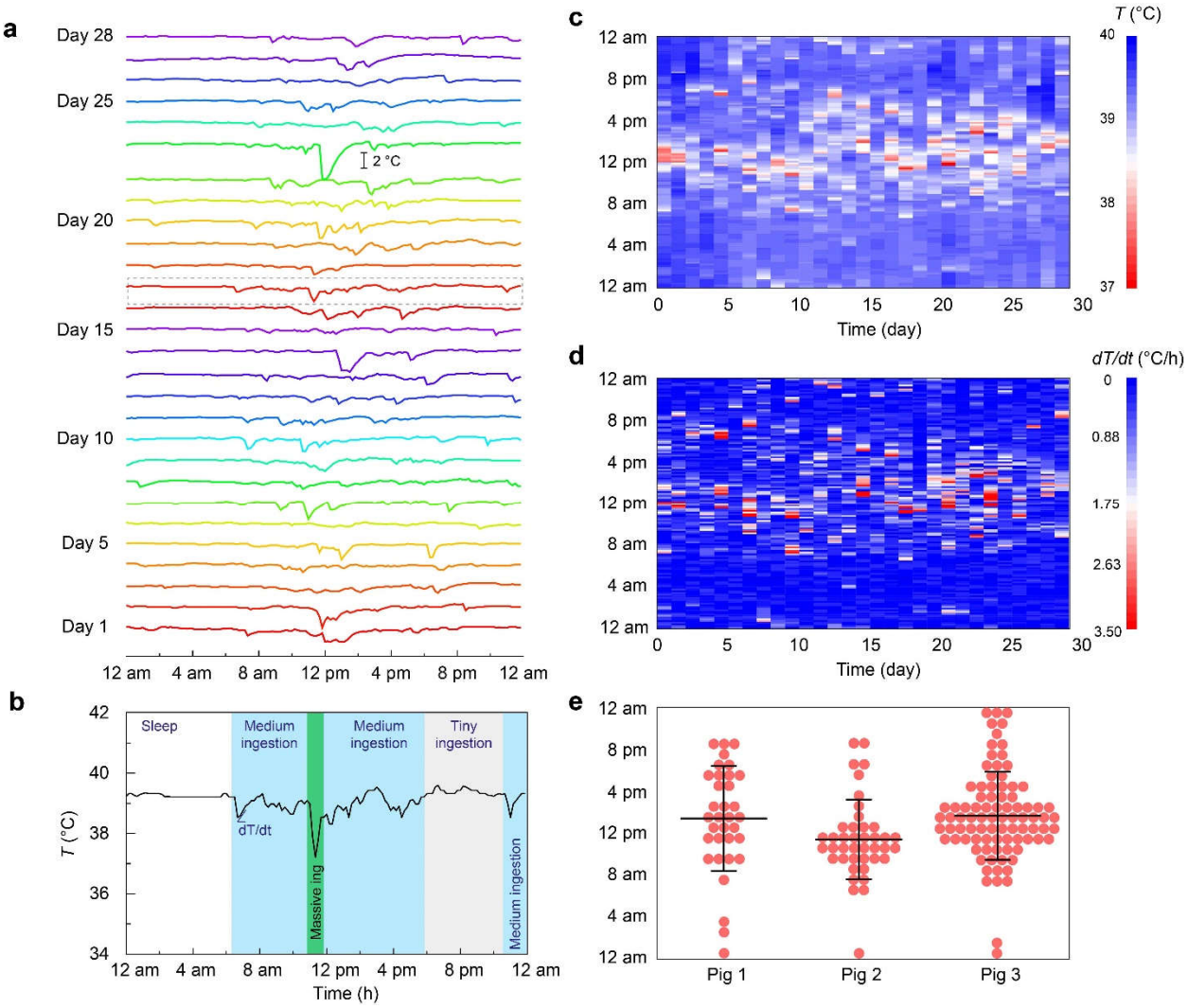

Figure 6-6. Analysis on the prolonged porcine gastric temperature profile measured. (a) The long-term measured gastric temperature are replotted on a daily basis. (b) On a single day (day 17), the temperature profile is divided into different phases with different ingestion activities based on the degree of fluctuations. (c) The heatmap of temperature (T) measured by hydrogel device over 29 days. (d) The heatmap of absolute temperature (|dT/dt|) derivative measured by hydrogel device over 29 days. (e) The time slots (one hour) with food intake (if any $\underline{|dT/dt|}$ >1.75 during the time slot) are marked as events for different pigs. Data in (e) are means ± SD. n = 34 events for pig 1 in 9 days, n = 41 events for pig 2 in 13 days, and n = 88 events for pig 3 in 29 days.

6.4.3. Ex vivo triggerable shrinkage

Additionally, we demonstrat the ex vivo triggerable shrinkage of the hydrogel device for easy and clear visualization. As shown in **Figure 6-5g**, calcium ions (0.6 M) induced deswelling of the

hydrogel device within 10 min in a transparent plastic stomach model containing porcine gastric fluid. On-demand shrinkage of the hydrogel device not only provides a rescue strategy for potential device-related GI tract obstructions, but also serves as an approach to tailorable residence time (e.g., when physiological monitoring is no longer needed)[97].

6.5. Modeling

6.5.1. Analysis of the swelling ratio at equilibrium

To quantitatively analyze the swelling ratio of the hydrogel device, we develop a model that describes the swelling of polyelectrolyte networks as well as the inflation of the elastic membrane. Two primary components determine the swelling kinetics of the hydrogel device being i) superabsorbent particles (polyelectrolyte hydrogel) and ii) the elastic membrane with pores (**Figure 6-7a**). When medium (e.g., water or gastric fluid) flows through the pores within the elastic membrane and subsequently migrates into the aggregation of superabsorbent particles, the particles swells and inflates the elastic encapsulation membrane [118, 511]. The swelling-induced mechanical pressure exerted at the outer surface of the polyelectrolyte hydrogel P_{swelling} decreases as expansion ratio λ in length (or λ^3 in volume) increases. The polyelectrolyte hydrogel continuously swells until P_{swelling} equals the pressure required to inflate the elastic membrane $P_{\text{inflation}}$. To calculate the final swelling ratio λ_{eq}^3 of the hydrogel device, we will focus on the equilibrium state, in which the electrochemical potential of each mobile species is uniform throughout the polyelectrolyte hydrogels and the external solution [3, 118].

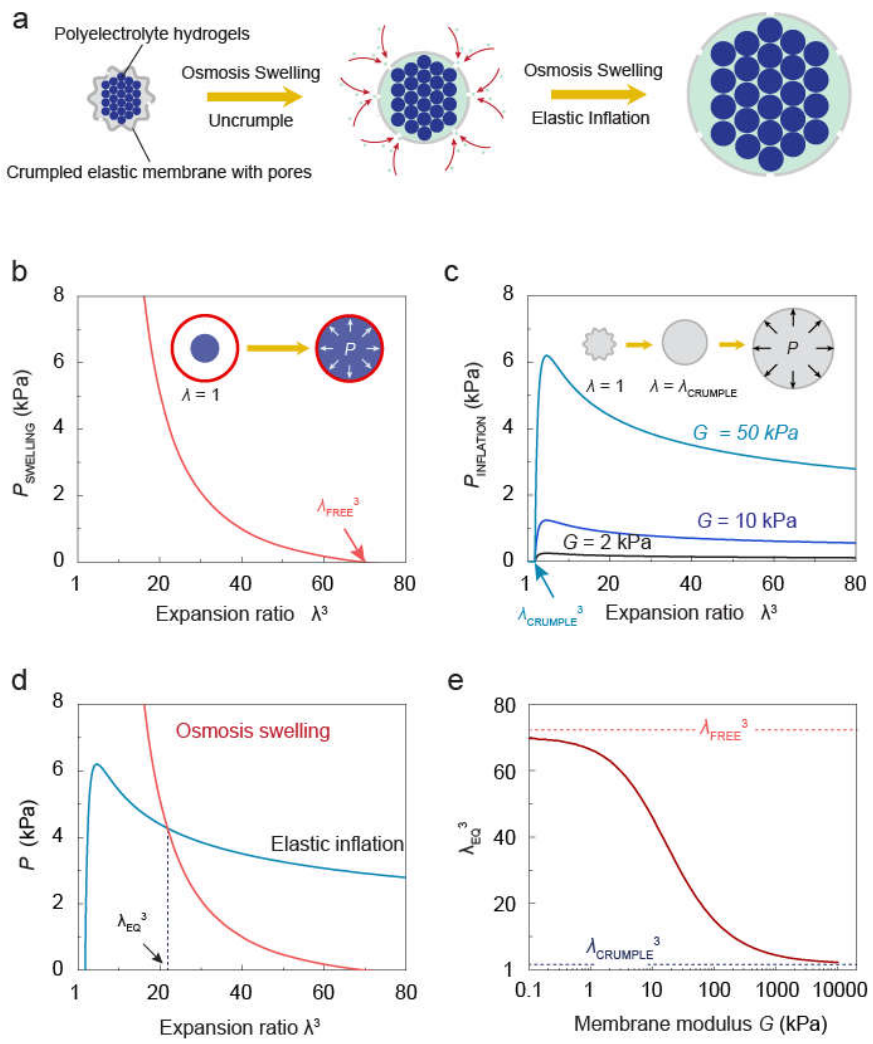

Figure 6-7. Model for equilibrium swelling ratio of the hydrogel devices. (a) Schematic illustration of the hydrogel device expansion. (b) Numerical results depicting swelling-induced pressure versus constrained expansion ratio. Inset: a polyelectrolyte hydrogel in the reference state and constrained swollen state. (c) Numerical results depicting inflation pressure versus expansion ratio for a set of membranes with different moduli. Inset: an elastic membrane in the reference state, uncrumpled state, and inflated state. (d) The overlapped inflation pressure and swelling-induced pressure versus expansion ratio. The intersection of the two curves determines the swelling ratio at equilibrium state of the hydrogel devices. (e) Plot of expansion ratio versus membrane modulus.

To obtain the swelling-induced mechanical pressure exerted at the outer surface of the polyelectrolyte hydrogel P_{swelling}, we start from the free energy density of the polyelectrolyte hydrogel, which can be expressed as [3, 118]

$$W = W_{net} + W_{sol} + W_{ion} + \Pi\left(1 + \sum v_a C_a - \det \mathbf{F}\right) \tag{6-2}$$

where W_{net}, W_{sol} and W_{ion} are the contributions from stretching of the polymer network, mixing the polymers and the solvent, and mixing the solvent and ions. Π is the Lagrange multiplier that enforces the volume conservation of all constituents. v_a is the volume of one mobile species a, C_a is the number of the mobile species a divided by the volume of the dry polymer, $v_a C_a$ is the total volume of species a divided by the volume of the dry polymer, and $\mathbf{F}$ is the deformation gradient of the polymer network. The free energy of stretching the polymer network can be expressed as

$$W_{net} = \frac{1}{2} NkT\left(F_{iK}F_{iK} - 3 - 2\log(\det \mathbf{F})\right) \tag{6-3}$$

where N is the number of polymer chains divided by the volume of the dry polymer, $kT = 4.11\times10^{-21}\,\mathrm{J}$, $\mathbf{F}$ is the deformation gradient of the polymer network and F_{iK} is the corresponding component. Specifically, for a spherical hydrogel with isotropic swelling ratio of λ, $F_{iK}F_{iK} = 3\lambda^2$ and $\det \mathbf{F} = \lambda^3$. The free energy of mixing the polymers and the solvent can be expressed as

$$W_{sol} = \frac{kT}{v_s}\left(v_s C_s \log\frac{v_s C_s}{1+v_s C_s} - \frac{\chi}{1+v_s C_s}\right) \tag{6-4}$$

where v_s is the volume of one solvent molecule (i.e., water), C_s is the number of the solvent molecules divided by the volume of the dry polymer. χ characterizes the enthalpy of mixing of the polymer chains and the solvent molecules. The free energy of mixing the ions and the solvent is taken to be

$$W_{ion} = kT\sum_i C_i\left(\log\frac{C_i}{v_s C_s c_i^0} - 1\right) \tag{6-5}$$

where C_i is the number of the ionic species i divided by the volume of the dry polymer, and c_i^0 defines the reference concentration for zero chemical potential.

For solvents in the external solution, the contribution of free energy only comes from mixing solvents and ionic species; therefore, the chemical potential of the solvent in the external solution is

$$\mu_{s,external} = -kT\sum_i \frac{C_i}{C_s} \tag{6-6}$$

For solvents inside the hydrogel, the free energy additionally covers the contribution from mixing of the polymers. Therefore, the chemical potential of the solvent in the hydrogel is

$$\mu_{s,hydrogel} = kT\left[\log\frac{v_s C_s}{1+v_s C_s} + \frac{1}{1+v_s C_s} + \frac{\chi}{\left(1+v_s C_s\right)^2} - \sum_i \frac{C_i}{C_s}\right] + \Pi v_s \tag{6-7}$$

Here, we focus on the case that highly charged polyelectrolyte hydrogels swell in a dilute solution in which the ion concentration in the external solution is much lower than the fixed charge concentration in the hydrogel. Therefore, the chemical potential in external solution can be approximated to be zero (i.e., $\mu_{s,external} = 0$). The ionizable groups on the polymers are considered to be fully dissociated with C_0 being the number of the fixed negative charge divided by the volume of the dry polymer. Electro-neutrality requires that the number of the counter ions within the hydrogel equals the number of the fixed charges in the polymer, which is denoted by

$$C^- = 0\,,\ C^+ = C_0 \tag{6-8}$$

Equating the chemical potential of the solvent inside the hydrogel to the chemical potential of the external solution (i.e., $\mu_{s,hydrogel} = \mu_{s,external}$), we obtain

$$\Pi = -\frac{kT}{v_s}\left[\log\frac{v_s C_s}{1+v_s C_s} + \frac{1}{1+v_s C_s} + \frac{\chi}{\left(1+v_s C_s\right)^2} - \frac{C_0}{C_s}\right] \tag{6-9}$$

On the other hand, the osmosis swelling of the hydrogel induces the mechanical stress inside the hydrogel when it is constrained at the expansion ratio of λ. The swelling-induced true stress of the hydrogel can be obtained by [511]

$$\sigma_{ij} = \left(\frac{\partial W}{\partial F_{iK}}\right)\frac{F_{jK}}{\det \mathbf{F}} - \Pi\delta_{ij} \tag{6-10}$$

By substituting the deformation gradient, the radial true stress is

$$\sigma_{rr} = NkT(\lambda^{-1} - \lambda^{-3}) - \Pi \tag{6-11}$$

The condition of incompressibility of the polymers and the solvents become

$$1 + v^s C^s = \lambda^3 \tag{6-12}$$

The swelling-induced pressure P_{swelling} (= σ_{rr}) can be obtained by combining **Equations 6-9 to 6-12**

$$P_{\text{swelling}} = NkT(\lambda^{-1} - \lambda^{-3}) + \frac{kT}{v_s}\left[\log\left(1-\lambda^{-3}\right) + \lambda^{-3} + \chi\lambda^{-6} - \frac{v_s C_0}{\lambda^3 - 1}\right] \tag{6-13}$$

Figure 6-7b plots the numerical results for swelling-induced pressure at different constrained expansion ratios. In this numerical calculation, we set $1/Nv = 1000$ with v being the volume of a single monomer $v = 1\times10^{-27}\,\text{m}^3$ [512], which means that each polymer chain contains 10^3 monomers; set $\chi = 0.1$, indicating slightly positive enthalpy of mixing; and assume $v_s = v$ [3]. The swelling-induced pressure increases as the constrained expansion ratio decreases. The intercept of x-axis gives the free swelling ratio λ_{free}.

We next calculate the pressure for inflation of the elastic membrane. We take the membrane as a neo-Hookean solid. The inflation pressure versus the expansion ratio is expressed as [511]

$$P_{\text{inflation}} = 0, \text{ if } \lambda < \lambda_{crump} \tag{6-14}$$

$$P_{\text{inflation}} = \frac{2Gt_o}{R_0}\left[\left(\lambda/\lambda_{crump}\right)^{-1} - \left(\lambda/\lambda_{crump}\right)^{-7}\right], \text{ if } \lambda > \lambda_{crump} \tag{6-15}$$

where G is shear modulus of the membrane, t_0 and R_0 are thickness and radius of the membrane, respectively, and λ_{crump} accounts for the degree of crumple. Here, we set $t_0/R_0 = 0.1$ and $\lambda_{crump} = 1.2$. **Figure 6-7c** plots the numerical results for inflation pressure versus expansion ratio for a set of membranes with different modulus. The intersection of the inflation curve and swelling curve determines the critical swelling ratio λ_{eq} at equilibrium state of the hydrogel device (**Figure 6-7d**). As shown in **Figure 6-7e**, the swelling ratio at equilibrium can be tuned by altering the modulus of the membrane. For an extremely soft membrane, the swelling ratio of the hydrogel device approaches the limit of free swelling ratio λ_{free}^3; for an extremely stiff membrane, the swelling ratio is bounded by the degree of crumple $\lambda_{crumple}^3$.

6.6. Materials and methods

6.6.1. Preparation of the hydrogel devices

Synthesis of the hydrogel membranes. All types of anti-fatigue hydrogel membranes were prepared from PVA powders (Mw 146,000–186,000, 99+% hydrolyzed). An aqueous solution of 10 wt% PVA was dissolved by stirring at 75 °C for 6 h, and mixed and defoamed by using a centrifugal mixer (AR-100, Thinky) for 1 min. The solution was cast in a 0.6-mm-thick custom-made glass mold, frozen at -20 °C for 8 h, and thawed at 25 °C for 3 h. The 8-h-freezing and 3-h-thawing was defined as one freeze-thaw cycle. Samples that underwent one freeze-thaw cycle were the soft hydrogel membranes (Young's modulus 2.6 kPa), and samples that underwent four freeze-thaw cycles were the medium hydrogel membrane (Young's modulus 47 kPa). The PVA hydrogels, after four freeze-thaw cycles, were further air-dried at 37 °C for 1 h, and annealed at 100 °C for 1 h, so that we obtained the stiff hydrogel membranes (Young's modulus 1.13 MPa). For radiographic visualization in vivo, 23 wt% of radio-opaque barium sulfate was incorporated in the hydrogel membrane. The addition of barium sulfate did not affect the mechanical properties as suggested by identical stress-strain curves and moduli (~ 46 kPa for both).

An alternative hydrogel membrane was prepared using a PAAm-agar tough hydrogel. Agar (2 g), AAm (18 g), Irgacure 2959 (0.284 g) as the photoinitiator, and MBAA (0.007 g) as the crosslinker were dissolved in 75 mL water at 90 °C. The solution was degassed thoroughly and poured in the custom-made glass mold (0.6 mm thick). The precursor solution was allowed to cool in the mold at room temperature to form the agar network, and then exposed to UV irradiation (365 nm wavelength, 8 W) for 1 h to form the PAAm network. Unreacted monomer and photoinitiators were leached out from the membrane for 2 days by water.

Fabrication of the hydrogel devices. For water permeation into the hydrogel device, the hydrogel membranes were introduced with uniform pores (~ 200 μm in diameter, two pores per cm^2) using laser cutting (Epilog). The hydrogel membranes were then trimmed based on a Parafilm template (Bemis) and assembled into a pocket or cube structure for subsequent loading with a specific number of superabsorbent particles (sodium polyacrylate homopolymers; Iste Lock 770, M2 Polymer Tech). The edges of the assembled pocket or cube structure were adhered using biocompatible ethyl cyanoacrylate glue (Loctite). After the Parafilm template was removed, the hydrogel device was further crumpled into a pill size.

6.6.2. Swelling tests

Swelling of gastric retentive hydrogel devices. The prepared hydrogel devices were submerged in aqueous media for swelling tests, which included water, SGF (pH 3), or porcine gastric fluid. Compendial SGF was prepared as described previously [513, 514], consisting of sodium chloride (150 mM) and hydrochloric acid (1 mM) in water. Porcine gastric fluid was withdrawn endoscopically when we performed another observational endoscopic study in the pig, and stored at -80 °C. During swelling studies, the increase of volume over time was monitored using a DSLR camera (Nikon D7000), and the mass of hydrogel devices was monitored using analytical balance (Denver Instrument). Swelling of superabsorbent particles was recorded using microscopy (Nikon Eclipse LV100ND). The volume at each time point was obtained by the area to the 1.5th power, and the area was accessible from the time-lapse images. The volume change was expressed as V/V_0, normalized by the initial volume V_0.

Swelling of bulk and porous hydrogels. The air-dried bulk hydrogel and the freeze-dried porous hydrogel were prepared from PAAm-agar following the same procedures described for synthesis of the hydrogel membranes with modifications. Those modifications included that the as-prepared hydrogels were dried at room temperature for 2 days to form bulk hydrogels. To prepare porous hydrogels, the hydrogels were fully swollen in water for 2 days, frozen at -20 °C for 1 day, and lyophilized for 3 days. The mass of each hydrogel was recorded over time during their swelling. The measured swelling times of the air-dried and freeze-dried hydrogels were normalized to the initial sample size of 5 mm.

Deswelling test. Deswelling characteristics of the hydrogel devices were evaluated by inducing deswelling with 0.6 M or 0.03 M calcium chloride in swelling media of water or SGF (pH 3). The mass and volume of the hydrogel devices were recorded over time in the deswelling tests following the procedures described in the swelling tests.

Ex vivo swelling in a stomach model. A stomach model custom-made of plastics and containing 75 mL of porcine gastric fluid was used as an accessible ex vivo model. To trigger the deswelling of the fully swollen hydrogel device, 7.5 mL of calcium chloride solution (50 wt%) was added 30 min after the insertion and swelling of the hydrogel device in gastric fluid. A snare catheter

(Captivator II Single-Use Snare, Boston Scientific) was used to retrieve the shrunken hydrogel through the opening. The process was monitored using a camera (EOS 70D, Canon).

6.6.3. Mechanical characterization

Mechanical characterization of hydrogel membranes. To assess the mechanical properties of hydrogel membranes under simulated physiological conditions, hydrogel membranes with or without pores were incubated in various media of water (pH 7) and SGF (pH 3) at 37 °C before performing mechanical testing. They were cut into dumbbell-shaped samples 6.5 mm in width, 15 mm in gauge length, and 0.75 mm in thickness for all samples, and 1.2 mm in crack length for notched samples[321]. At 12 h, 5 days, 10 days, and 15 days after incubation, true stress-strain curves of the hydrogel membranes were measured using a mechanical testing device (Z2.5, Zwick-Roell) with a 20 N load cell. The strain rate was imposed to 2 s^{-1}.

To test the fatigue properties of hydrogel membranes, we performed cyclic tensile loading on the hydrogel membranes with pores in a water bath (pH 7) at 25°C with a benchtop mechanical tester (UStretch, CellScale), using a 44 N load cell. Forces applied were recorded over time. The strain rate was imposed to 5 s^{-1}.

Mechanical characterization of gastric retentive hydrogel devices. The hydrogel devices, which were fully swollen in SGF (pH 3) or water for 1 h beforehand, were exposed to cyclic compression using a mechanical testing device (Z2.5, Zwick-Roell) with a 2,500 N load cell and a large soft indenter (Ecoflex, diameter 70 mm). The strain rate imposed was 2 s^{-1}. The maximum engineering strain was 40% for long-time compression, and the hydrogel devices (diameter ~ 4.8 cm, cross-section area ~ 20 cm^2 at undeformed state) in the medium underwent 8-h cyclic loading every day. In the short-run test, the maximum engineering strain was 90%, and the devices (diameter ~ 3.6 cm, cross-section area ~ 10 cm^2 at undeformed state) in the air underwent two cycles. The effective compressive stress was calculated by dividing the compressive force by the cross-section area of the undeformed hydrogel device. We used the Hertz model to obtain the effective modulus of whole hydrogel devices from the compression curves[515].

6.6.4. In vivo gastric retention

All procedures were conducted in accordance with protocols approved by the Massachusetts Institute of Technology Committee on Animal Care and as previously described with minor modifications[484]. Six separate female Yorkshire pigs weighing approximately 30–50 kg were used for in vivo evaluation (Experimental group: 39.7 ± 2 kg; Control group: 40.3 ± 8 kg). Following overnight fasting, the animals were sedated with Telazol (tiletamine/zolazepam) 5 mg kg^{-1}, xylazine 2 mg kg^{-1}, and atropine 0.04 mg kg^{-1}, followed by endotracheal intubation and maintenance anesthesia of isoflurane (1-3% in oxygen). The barium sulfate-labeled hydrogel device comprising a temperature sensor (DST nanoRF-T, Star-Oddi) was placed in the stomach using an esophageal overtube (US Endoscopy) with endoscopic guidance. The swelling of the hydrogel device in the stomach was visualized endoscopically at 5, 15, and 60 min after administration. Temperature data was measured every ten minutes. The non-swellable hydrogel device with a temperature sensor but containing no superabsorbent particles inside was delivered as the control experiment. Radiographs were performed every 48–72 h to monitor the integrity and transit of the devices as well as any radiographic evidence of bowel obstruction. Furthermore, all animals were monitored clinically at least twice a day for any evidence of morbidity, including lethargy, inappetence, decreased fecal output, abdominal distension, and vomiting. The temperature sensor in the hydrogel device was retrieved from the pigs' feces after exiting from the GI tract. The temperature data was recorded every 10 min in porcine stomach with resolution of ± 0.032 °C.

6.7. Conclusions

Recently developed soft hydrogel-based ingestible devices (**Figure 6-5b**) are limited by their mechanical weakness, low swelling ratio, and/or low swelling speed, leading to short gastric residence time [484, 486, 488]. The current work represents a non-invasive, self-contained GI-resident device almost entirely made of hydrogels that can be orally administrated as a standard-sized pill, swell in the stomach within 60 min, and remain soft but robust in the gastric cavity for up to 29 days. To our best knowledge, this is the first hydrogel-based device that achieves unprecedented properties of high swelling ratio, high swelling speed, and long-term robustness simultaneously. In addition, this is the first report on an ingestible and gastric retentive device capable of one-month continuous measurement of gastric temperature in a pig model.

Besides the in vitro drug release and in vivo temperature sensing applications we have shown, our hydrogel device can be potentially used as a versatile platform for other functions that closely interact with the digestive system in the human body. For example, long-term measurements of other biosignals may be enabled by the miniature sensors (for motion, salinity, pressure, pH, gas, and other biomarkers) embedded in the hydrogel device. Moreover, the long-acting hydrogel device may be used for monitoring medication-taking patterns, visualizing GI tract disorders by carrying a mini camera, modulating gut microbiota via the addition of probiotics/perbiotics, and inducing satiety to control obesity by volume exclusion. Beyond that, by decoupling the mechanical and swelling properties, the new hydrogel design supports the possibility of achieving osmotic-driven high-force and high-speed actuation, potentially opening new avenues to applications for biomedical devices and soft robotics.

Chapter 7

Hydrogel optical fibers

The research presented in this chapter has been published in:

- **Xinyue Liu†**, Siyuan Rao†, Jiahua Ni, Kayla Felix, Shaoting Lin, Polina Anikeeva, and Xuanhe Zhao. Fatigue-resistant hydrogel optical fibers for peripheral nerve stimulation. In submission.
- Siyuan Rao†, **Xinyue Liu†,** Atharva Sahasrabudhe, Cindy Shi, Shaoting Lin, Xuanhe Zhao, and Polina Anikeeva. Soft and stretchable fiber photometry for studying neural dynamics. In submission.
- Jingjing Guo, **Xinyue Liu**, Nan Jiang, Ali K Yetisen, Hyunwoo Yuk, Changxi Yang, Ali Khademhosseini, Xuanhe Zhao, Seok-Hyun Yun, Highly stretchable, strain sensing hydrogel optical fibers, Advanced Materials. 28, 2016.

7.1. Introduction

Optogenetics allows precise spatiotemporal control of cellular activities to dissect functional wirings in the nervous system[516, 517]. Typically, light is delivered through fiber optics implanted to the targeted site to activate or inhibit a specific cell population, which are rendered photoactive via genetic integration of microbial opsins[517]. Despite the powerful applications of optogenetics, the approach to delivering light to specific locations remains challenging, especially to the regions experiencing vigorous motions[518].

Optogenetics has been applied in the motion-associated regions, ranging from probing neural networks associated with muscle activation for locomotion[519, 520], to precisely creating normal physiological recruitment pattern for muscle control[521], and even to developing therapies for spastic hypertonia by controlling the motor nerve and muscle activity in vivo[522]. However, these optogenetic applications, especially in the peripheral nervous system, are impeded by the light delivery approaches[518, 523]. The conventional optic devices made of stiff materials

(e.g., fused silica with a modulus in GPa) damage the tissues (modulus in kPa-MPa) under repeated deformation and displacement[283, 524], and constrain the natural behaviors of experimental subjects (**Figure 7-1a**). Promising progress has been achieved to optogenetically stimulate the dynamic nerves through microscale light-emitting diodes (μ-LED) that are directly implanted near the targeted positions[525-528]. However, their scalable application requires sophisticated designs of wireless power and control, as well as complex processes of microfabrication and surgical procedures.

Hydrogels exhibit sufficient transparency and tissue-level softness, thus being considered as potential material candidates to develop motion-adaptable optical waveguides for optogenetics[74, 529]. However, under the recurring deformations in vivo, existing hydrogels usually suffer from fatigue failures under cyclic loading[283, 329, 529], as well as de-bonding issues at the light-coupling interfaces. From the perspective of light transmission, because of the low refractive indices in fully hydrated status (~1.34) and the consequent insufficient refractive index contrast between the core and cladding materials, current hydrogel fiber-optic devices experience significant light leakage at the core-cladding interfaces[529].

Here, we present a fatigue-resistant hydrogel fiber-optic technology that can adapt to persistent mouse hindlimb movements during motion-involved behaviors. Introducing nanocrystalline domains in hydrogels prevented crack propagation, and consequently granted high fatigue resistance under repeated stretching (**Figure 7-1b-d**). Nanocrystalline domains were also generated at silica-hydrogel interfaces to establish a robust light coupling with standard external light source systems (**Figure 7-1b-d**). A hydrogel cuff at the end of the fiber-optic device was built to enable motion-adaptable contact with peripheral nerves under deformation (**Figure 7-1d**). To validate its motion-adaptable light delivery functionality, this hydrogel fiber-optic technology was applied in long-distance (~6 cm) optogenetic stimulation on sciatic nerves in *Thy1::Channelrhodopsin-2 (ChR2)-enhanced yellow fluorescent protein (EYFP)* mice with repeated running tests.

7.2. Design principles

Design and fabrication of the hydrogel fiber-optic device. To overcome the limitations of existing light delivery approaches for the peripheral nervous system (**Figure 7-1a**), we designed a hydrogel fiber-optic device that consists of (i) a short segment of silica fiber in a ceramic ferrule

that is exposed to air to prevent hydrogel dehydration (**Figure 7-1b**, up), (ii) a hydrogel fiber consisting of a hydrogel core and a hydrogel cladding, connected to the silica fiber segment (**Figure 7-1b**, middle), and (iii) a monolithic hydrogel cuff anchored to the targeted nerve (**Figure 7-1b**, bottom). To ensure the light transmission along the hydrogel core, we generated nanocrystalline domains of poly(vinyl alcohol) (PVA) in the PVA hydrogel core. To minimize the light loss at the connection between the silica and hydrogel, we anchored the nanocrystalline domains in the PVA hydrogel core onto the silica surface to create a robust and fatigue-resistant interface.

Specifically, a hydrogel core was fabricated via chemical cross-linking of PVA in a mold (inner diameter: 1600 μm), which resulted in an amorphous PVA hydrogel fiber directly connected to a silica fiber segment during synthesis. To create a soft contact between the hydrogel fiber-optic device and the targeted nerve or tissue, a hydrogel cuff was prepared at the distal end of the mold (**Figure 7-1b,d**) via a monolithic casting and puncturing approach (**Figure 7-1d**, also see Methods for details). Subsequently, air drying and high-temperature (100 °C) annealing converted amorphous PVA chains to nanocrystalline domains at the silica-hydrogel interface and in the bulk hydrogels (**Figure 7-1e**). We found that the growth of PVA nanocrystalline domains can be tuned in the high-temperature annealing process. The annealing time was adjusted from 0 to 120 min, and 30 min was selected based on the optimized mechanical properties (i.e., softness and robustness) and optical properties (i.e., absorbance and refractive index). After 30-min annealing and rehydration, the final hydrogel fiber is 600 μm in diameter and 60 mm in length.

To prevent light leakage from the fiber radical directions and unintended optical stimulation on non-targeted tissues, we designed a composite cladding (thickness: 200 μm) with light-absorbing nanomaterials (i.e., reduced graphene oxide, rGO) in PVA hydrogels. The nanomaterials do not diffuse to the PVA hydrogel core, and thus do not affect light transmission[530]. In addition, to enable the robust core-cladding bonding, the PVA polymer chains are allowed to interpenetrate at the hydrogel core-cladding interface during cladding synthesis (**Figure 7-1e**).

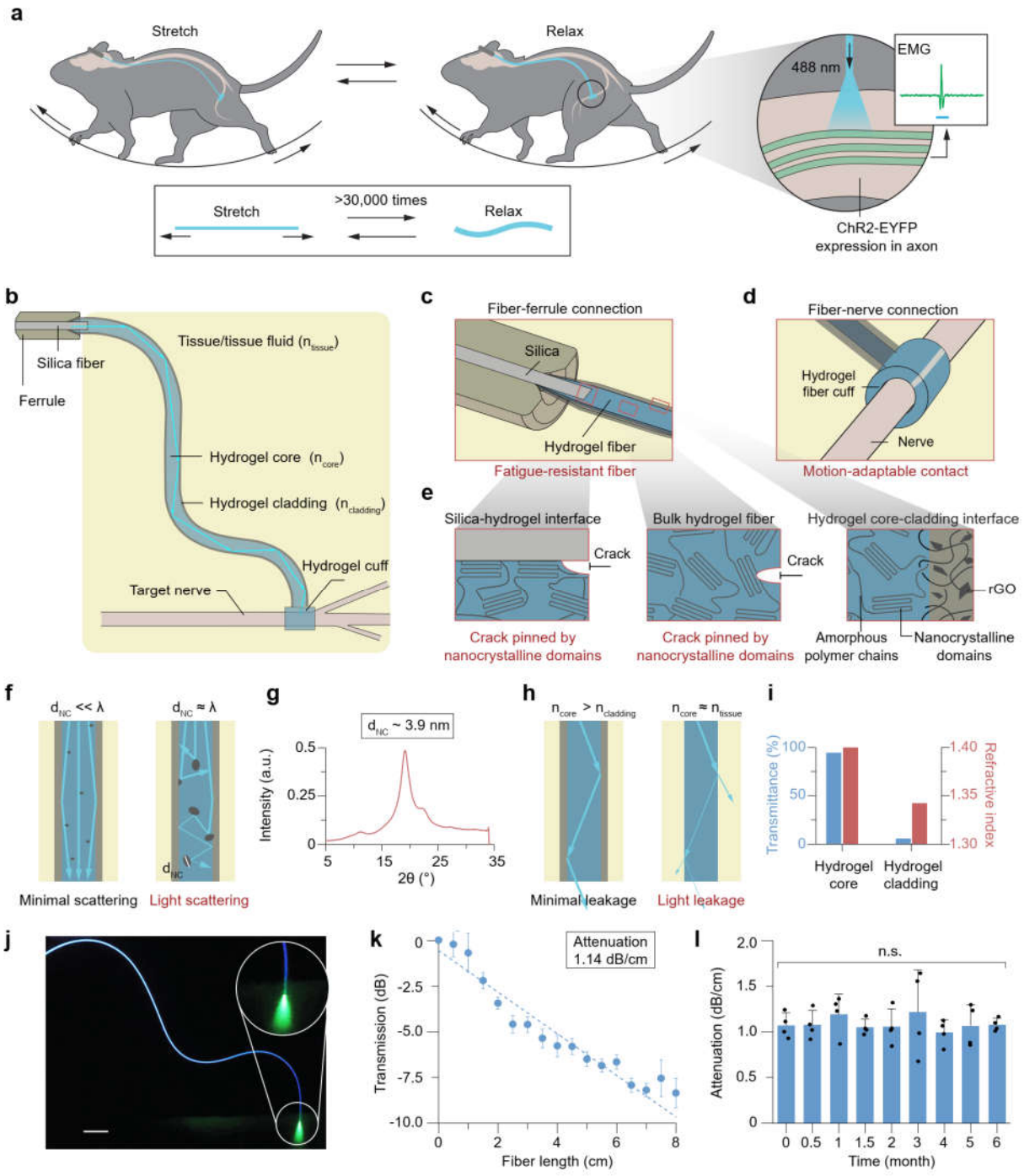

Figure 7-1. Design and mechanisms of the fatigue-resistant hydrogel fiber optics. (a) Peripheral nerves flex with the animal body under persistent locomotion, and implanted fiber optics experiences cyclic stretching and relaxation during the animal movement. Optogenetic activation of peripheral nerves requires motion-adaptable light delivery to the dynamic target. (b) General design of the fatigue-resistant hydrogel fiber-optic device for the optogenetic activation of peripheral nerves, which consists of a short silica fiber in a ceramic ferrule, a hydrogel core that adheres to the silica fiber, a hydrogel cladding that circumferentially covers the hydrogel core, and

a hydrogel cuff that wraps around the targeted nerve. (c) At the connection of the ferrule and fiber, a hydrogel fiber adheres to a short silica fiber extended from a ferrule, and the hydrogel fiber is composed of a hydrogel core and hydrogel cladding. (d) At the connection of the nerve and fiber, a hydrogel cuff wraps around a peripheral nerve for motion-adaptable contact. (e) Silica-hydrogel interface and bulk hydrogel core material are fatigue-resistant as cracks are pinned by nanocrystalline domains, while hydrogel core-cladding interface is achieved by polymer chain interpenetration. (f) When the size of nanocrystalline domains in hydrogels (d_{NC}) is much smaller than the light wavelength (λ), it does not scatter or absorb light; otherwise, it causes significant light scattering and absorption. (g) WAXS profile of the hydrogel core (annealing time: 30 min) in the dry state indicates that the size of nanocrystalline domains is around 3.9 nm. (h) If the reflective index of the hydrogel core n_{core} is much larger than that of the hydrogel cladding $n_{cladding}$, it results in minimal light leakage; however, without the hydrogel cladding, the similarity in reflective indices of the hydrogel core n_{core} and tissue fluid n_{tissue} results in light leakage. (i) Transmittances (wavelength: 488 nm) and refractive indices (wavelength: 400 nm) for the hydrogel core (annealing time: 30 min) and cladding (reduced time: 1 min). (j) Image of a hydrogel fiber-optic device, where the blue light is coupled to the ferrule and the terminal of the hydrogel device is directed to a fluorescein bath. Scale bar: 10 mm. (k) Path attenuation of the hydrogel fiber-optic device in a 1% agarose matrix indicates that the attenuation coefficient is 1.14 dB/cm. (l) Attenuation coefficients of the hydrogel fiber-optic device in a 1% agarose matrix when immersed in PBS over six months at 37 °C. Statistical significance in (l) is determined by one-way ANOVA and Tukey's multiple comparison test; $*P \leqslant 0.05$, n.s., not significant. Values in (k),(l) represent the mean and the standard deviation (n = 3–4 independent samples).

7.3. Results and discussion

7.3.1. Optical performances in the static state

We focus on two aspects to ensure efficient light delivery for in vivo optogenetic stimulation: 1) minimizing the light scattering and absorption caused by the hydrogel core to reduce light loss along the fiber, and 2) creating sufficient refractive index contrast between the hydrogel core and cladding to make sure the total internal reflection at the core-cladding interface (e.g., $n_{core} > n_{cladding}$; n, refractive index). To reduce light loss along the hydrogel core, we optimized the optical properties of the hydrogel materials by controlling nanocrystalline growth. The PVA hydrogels with 30-min annealing treatment exhibit a low normalized absorbance (0.18 for 0.24-mm-thick membrane) and a low normalized autofluorescence (25 for 0.24-mm-thick membrane). Prolonged annealing time (> 60 min) causes 33%–100% enhancement of autofluorescence (excitation wavelength: 470 nm, measured emission wavelength: 510 nm) compared to the shorter annealing time (0 min–30 min). When light transmits along with the hydrogel core, PVA nanocrystalline domains in the hydrogel core may cause light scattering (**Figure 7-1f**). By using wide-angle X-ray scattering (WAXS), we quantified the dimension of nanocrystalline domains (d_{NC}) and found that

30-min annealing produces nanocrystalline domains with the size of ~3.9 nm in the hydrogel core (**Figure 7-1f,g**). This dimension is two orders of magnitude smaller than the wavelength of transmitted light (λ = 488 nm), which prevents significant light scattering by nanocrystalline domains[283, 531].

To reduce the refraction loss at the core-cladding interface, we increased the refractive index difference between the hydrogel core and cladding. We tuned the refractive indices of PVA hydrogels by varying annealing time and PVA polymer fraction. The nanocrystalline hydrogel with 30-min annealing was adopted as the hydrogel core (n_{core} = 1.40) and the amorphous hydrogel without annealing as the hydrogel cladding ($n_{cladding}$ = 1.34) to ensure that hydrogel core-cladding structures effectively confine the light within the waveguide (**Figure 7-1h,i**). This hydrogel core material with nanocrystalline domains exhibited a higher refractive index than other reported synthetic hydrogels in the completely hydrated state[529]. Due to the insufficient refractive index contrast between amorphous hydrogels and water (n_{water} = 1.33), the amorphous PVA hydrogel fibers (n = 1.34) result in severe light leakage. The light power collected from the terminal of amorphous PVA hydrogel fibers is around 17% of the power collected from the nanocrystalline PVA hydrogel fibers (n = 1.40) in water. Additionally, we minimized the undesirable radical illumination by creating a light absorbing cladding layer particularly for the applications in transgenic opsin-expressing animal models. After introducing 2.1 mg/mL of rGO in the amorphous PVA cladding layer, more than 95% of the refracted light can be absorbed in the hydrogel cladding to prevent light rays from escaping to surrounding tissues (**Figure 7-1i**).

Overall, the optimization of PVA nanocrystalline growth contributes to the low attenuation coefficient (1.14 dB/cm for a straight hydrogel fiber-optic device in the fully hydrated state with 488-nm light) (**Figure 7-1k**). When an incident ray of 200 mW transmits through a fiber-optic device (6 cm in length, 600 μm in core diameter), it emits ~145 mW mm^{-2} at the fiber terminal. This light intensity is sufficient to activate Channelrhodopsin in vivo[532, 533]. We further tested the long-term optical performance of the hydrogel fiber-optic device in vitro. After incubating the hydrogel fiber-optic device in phosphate-buffered saline (PBS) at 37 °C over six months, the device still exhibited a stable optical transmission performance (attenuation coefficient < 1.21 dB/cm) (**Figure 7-1l**).

7.3.2. Mechanical and optical performances under mechanical loading

Next, we validated that the hydrogel fiber-optic device maintains sufficient light transmission under cyclic mechanical loading. We first characterized the Young's modulus of the hydrogel fiber and found it exhibits 2.0 MPa (**Figure 7-2a**), which is much lower than that of a silica fiber (~20 GPa)[534]. This suggests an improved modulus matching between the implanted materials and biological tissues (0.1-2 MPa)[535].

To verify the functionality of the hydrogel fiber-optic device in wet and dynamic physiological environment, we conducted cyclic tensile tests in water to evaluate the fatigue performances of the bulk hydrogel material and silica-hydrogel interface under repeated deformation (**Figure 7-2a,b**). We first applied cyclic uniaxial tensile deformation on the hydrogel fiber-optic device with a maximum stress of 1.4 MPa, which is approximate to the mechanical strength of load-bearing tissues (e.g., muscles)[536, 537]. Through the stress-controlled cyclic tests, the maximum strain reached and maintained a constant value (~70%) for 10,000 cycles with no cavity or crack forming at the silica-hydrogel interface (**Figure 7-2c**). This observation indicates the fatigue-resistant performance of nanocrystalline PVA hydrogel fibers and silica-hydrogel interfaces. In addition, the hydrogel fiber-optic device remained its resilience (i.e., 0% hysteresis) and low modulus (i.e., 2.0 MPa) under cyclic loading. When the device was cyclically stretched with a maximum stress of 1.8 MPa, a cavity was generated at the silica-hydrogel interface, leading to severe light loss under dynamic deformation. After 3,347 cycles, the cavity grew larger and led to a complete fracture at the interface. From the stress-life (S-N) curve, we identified a 30,000-cycle fatigue strength as 1.4 MPa (**Figure 7-2b**), which is similar to that of tissues (e.g., 0.4 – 2.0 MPa for skeletal muscles[538]). Moreover, we found that the tensile strength and strain energy density of the hydrogel fiber-optic device stayed nearly constant when incubated in PBS at 37 °C for six months, which demonstrates its long-term mechanical stability in a simulated physiological environment.

We further investigated the optical performances of the hydrogel fiber-optic device under single-cycle and multiple-cycle mechanical loadings. As a comparison, commercial silica fibers (diameter: 400 μm) and polydimethylsiloxane (PDMS) fibers (diameter: 1000 μm) were tested under the same loading conditions. As a key parameter to present optical performance, light transmission was measured for each fiber sample under bending or stretching. Under bending, the light transmission through the hydrogel fibers maintained over 94% when the bending radius was

larger than 7 mm. In contrast, silica and PDMS fibers' transmission decreased to 81% and 62%, respectively at a 7 mm bending radius. Under single-cycle stretching, the hydrogel fiber was still able to transmit light when it was elongated at a strain of 90% (**Figure 7-2d**), while the silica fiber broke at low tensile strains of 1% because of its low fracture energy and the PDMS fiber broke at 20% because of poor PDMS-silica adhesion[309, 539]. During the cyclic stretching with a maximum strain of 25% (25% is the upper limit of tissue deformation), the fiber-optic device made of nanocrystalline hydrogels can consistently maintain above 87% light transmission (**Figure 7-2e,f**)[540].

To demonstrate that the hydrogel fiber-optic device can adapt to motion-involved tissues, we adhered the device longitudinally onto an ex vivo porcine artery powered by pulsed air, which mimics the exaggerated deformation by diastole and systole. Unlike the silica fiber that severely constrained the tissue displacement (**Figure 7-2g,h**), the hydrogel fiber-optic device deformed along with the movement of the artery tissue showing stable light delivery under dynamic loading conditions (**Figure 7-2i,j**).

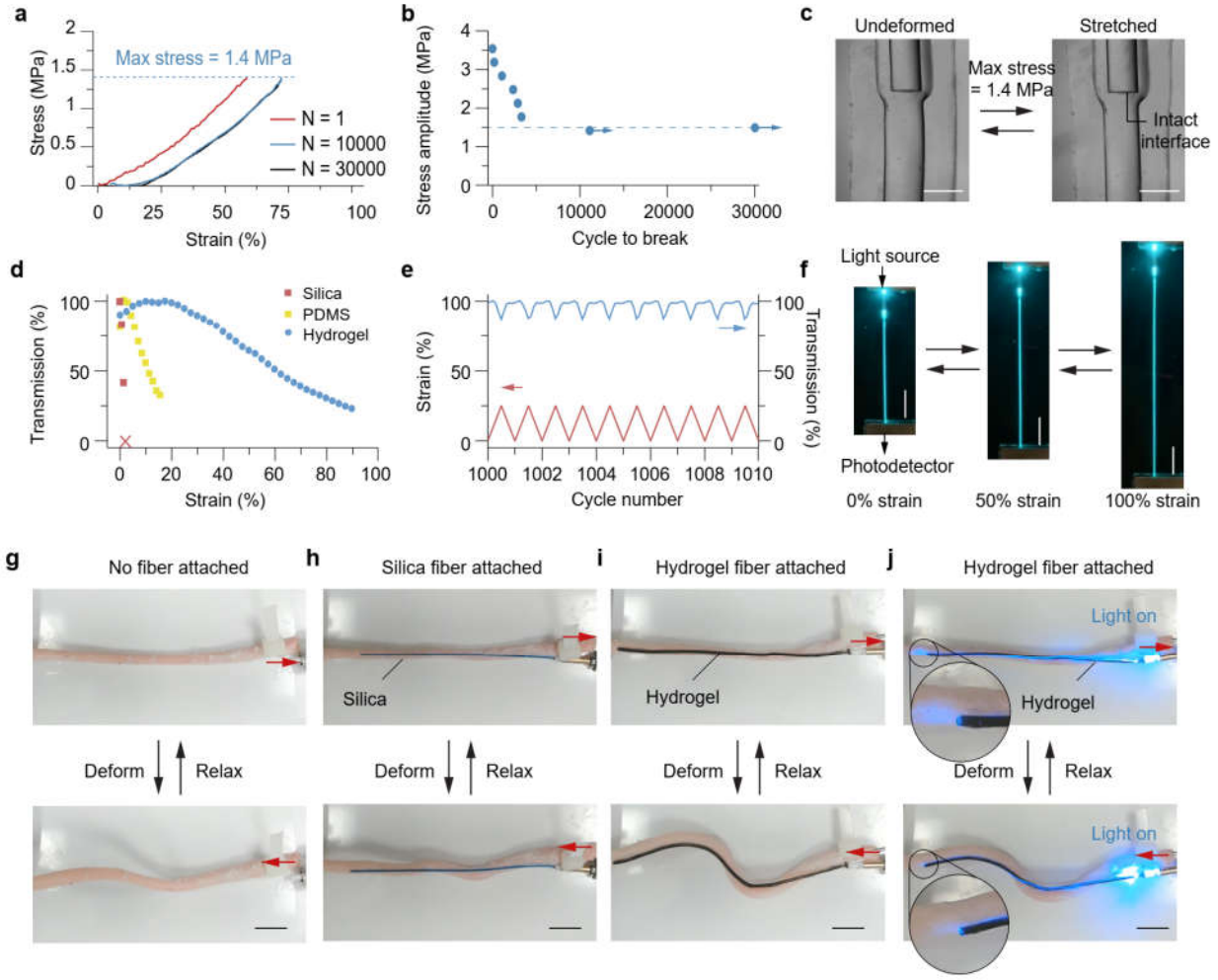

Figure 7-2. Mechanical performance of the fatigue-resistant hydrogel fiber optics. (a) Nominal stress versus tensile strain of the hydrogel fiber-optic device under cyclic loading (applied maximum stress: 1.4 MPa). (b) Stress-life (S-N) curve of the hydrogel fiber-optic device. The plot indicate that the fatigue strength is 1.4 MPa over 30,000 cycles. (c) Microscopic images of the hydrogel fiber-optic device under cyclic loading in PBS. The hydrogel-silica interface remains intact when the applied maximum stress is 1.4 MPa. Scale bars: 500 μm. (d) Light transmission versus tensile strain for the nanocrystalline hydrogel, silica and PDMS fibers. (e) Light transmission under repeated stretching of a hydrogel fiber-optic device, when the maximum tensile strain is 25%. (f) Images of a hydrogel fiber-optic device under repeated stretching. Two ends of the device are coupled with a LED light source and a photodetector, respectively. Scale bars: 10 mm. (g)-(j) Images of an ex vivo porcine artery with free deformation (g), constrained deformation by a silica fiber attached to it (h), unconstrained deformation by a hydrogel fiber attached to it (i). The light can be delivered through the hydrogel fiber attached to the artery under cyclic loading (j). Scale bars: 10 mm.

7.4. Applications

7.4.1. Motion-adaptable hydrogel fiber optics in mouse locomotor tests

To validate its functionality in vivo and test the applicability under intense motion-involved environments, we applied the hydrogel fiber-optic device in mouse voluntary wheel running tests (VWRTs), which have been used to assess the motor function of experimental subjects. The ferrule was fixed on the mouse skull to couple the light source while the cuff terminal was wrapped around the mouse sciatic nerve on the hindlimb. The entire fiber-optic device was tunneled under the skin on the mouse back (**Figure 7-3a,b**). When the implanted mouse was subjected to VWRTs, the stretch of the mouse hindlimb during running caused repeated deformation of the hydrogel fiber-optic device (**Figure 7-3c**).

To quantify the repeated cyclic loading of the implanted hydrogel device in vivo, we performed gait analysis of the test mice in VWRTs using DeepLabCut markless pose estimation[541]. In the side-view gait analysis, mouse skeleton features were labeled with a series of nodes, which can also represent the implanted hydrogel fiber path (**Figure 7-3c,d**). The gait analysis was first used to assess whether the implanted hydrogel fiber-optic device was able to adapt to the intense motion in VWRTs. By comparing the gait of test mice at different time points post-implantation, we found the mouse running behaviors were not constrained by the implanted hydrogel fiber-optic device, although the gait geometry and strain amplitude were slightly altered several days post-surgery (**Figure 7-3c**). Since mouse gait is sensitive to the damage of motor and sensory neurons, we concluded that the hydrogel fiber-optic device did not cause sciatic nerve crush, transection, or constriction (**Figure 7-3c**)[542]. Moreover, by tracking the node positions and counting mouse hindlimb stretching cycle numbers, we calculated the length variation and deformation frequency of the hydrogel fiber-optic device during VWRTs (**Figure 7-3d-f**). Typically, the implanted hydrogel device got deformed with a strain amplitude of ~10% and at a frequency of ~4 cycles per second (**Figure 7-3e-h**). This information helps estimate the overall hydrogel fiber-optic device deformation in long-term mouse VWRTs.

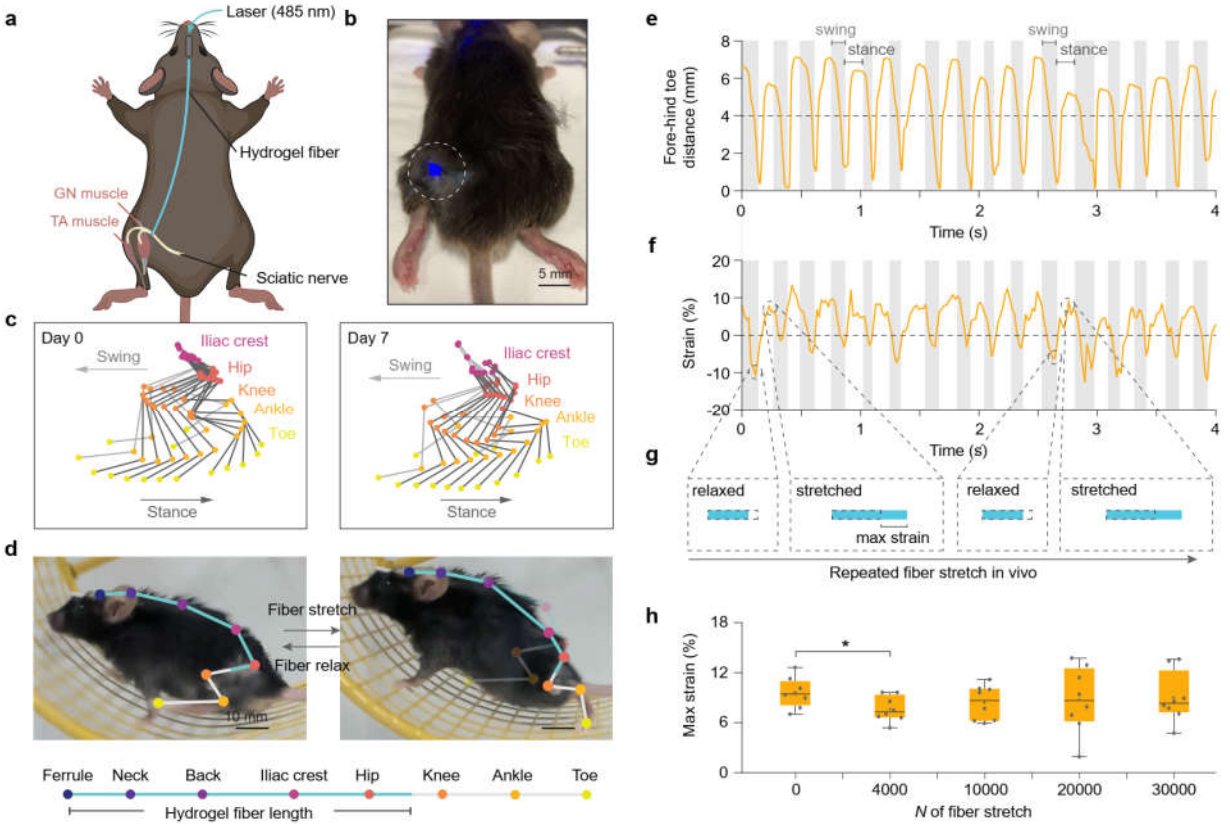

Figure 7-3. Repeated deformation of the fatigue-resistant hydrogel fiber optics led by mouse voluntary wheel running. (a) Schematic of a mouse implanted with a hydrogel fiber-optic device. (b) Image of a mouse implanted with a hydrogel fiber-optic device. Blue light is applied to the mouse sciatic nerve through the implanted hydrogel device. Scale bars: 5 mm. c, Representative stick view decomposition of mouse left hindlimb movements on a running wheel on Day 0 (before surgery, left) and Day 7 (right). A complete gait cycle is composed of a swing phase (light grey) and a stance phase (dark grey) in the stick view decomposition. The nodes represent the iliac crest, hip, knee, ankle, and toe from top to bottom. (d) Pose estimation using DeepLabCut of a mouse implanted with a hydrogel fiber-optic device on a running wheel. The mouse skeleton features are labeled with a series of nodes, including the ferrule, neck, back, iliac crest, hip, knee, ankle, and toe. Scale bars: 10 mm. The hydrogel fiber length is calculated by the total length of the segments starting from the ferrule to the middle point between the hip and knee (highlighted in blue). The hydrogel fiber-optic device is stretched and relaxed per running step. (e) Distance between the fore toe to hind toe of a running mouse, which varies over time on Day 13. (f) Strain of the implanted hydrogel fiber-optic device in a running mouse, which varies over time on Day 13. The total time period in (e) and (f) is separated into a few gait cycles, and each gait cycle is discomposed to a swing phase (light grey) and a stance phase (white) according to the positive or negative slope in (e). (g) Schematic of the hydrogel fiber length variation during mouse running. (h) Maximum strain of the implanted hydrogel fiber-optic device in a running mouse over 30,000 cycles of in vivo fiber stretching. Statistical significance is determined by one-way ANOVA and Tukey's multiple comparison test; $*P \leqslant 0.05$, n.s., not significant.

7.4.2. Optogenetic stimulation with fatigue-resistant hydrogel fiber optics

To examine the light delivery efficacy of the hydrogel fiber-optic device under repeated deformations in vivo, we connected the hydrogel device to a pulsed blue light source and applied it to activate the ChR2-expressing motor axons in sciatic nerves in the *Thy1::ChR2-EYFP* mouse model[525, 532][525, 532] (**Figure 7-4a**). Confocal microscopy images of mouse sciatic nerves confirmed the expression of ChR2, which is fused to an EYFP (**Figure 7-4b**). After implanting the device, we first characterized the hindlimb flexion and electromyographic (EMG) activities to the pulsed blue light illumination (488 nm, 100 mW/mm^2, on: 10 ms/off: 1 s). We observed that light illumination on the sciatic nerve through the hydrogel fiber-optic device was able to consistently evoke muscle twitches and EMG activities in the targeted muscles (**Figure 7-4c-e**). Tetanic muscle contractions and corresponding EMG activity were also observed under high-frequency light stimulation (40 Hz). Although the *Thy1::ChR2-EYFP* mouse model exhibits broad ChR2 expression in the nervous system[525, 532], the stimulation light was effectively delivered to the targeted location without severe light leakage to undesired locations due to the rGO hydrogel cladding design, which contributed to clean results of muscle contractions and EMG activities.

Based on the fatigue-resistant features of the hydrogel fiber-optic device (i.e., fatigue strength of 1.4 MPa over 30,000 cycles), we further investigated the robustness of their mechanical and optical performances with periodic VWRTs (**Figure 7-4a**). The test mice were subjected to 16-minute running tests every three days over four weeks post device implantation. A strain amplitude of ~10% and a running speed of 4 cycles/s (gait analysis) was applied to estimate the hydrogel fiber deformation in periodic VWRTs (**Figure 7-3e,f**). The total running cycles were estimated as 0, 4,000, 10,000, 20,000, and 30,000 cycles after 0, 7, 14, 21, and 28 days respectively, following hydrogel device implantation. The EMG activity and muscle flexion in response to the pulsed light stimulation were still observed at a series of time points corresponding to tens of thousands of device deformation cycles（**Figure 7-4f**), which indicates stable optical performance and fatigue-resistance of the hydrogel fiber-optic device under persistent locomotion in vivo.

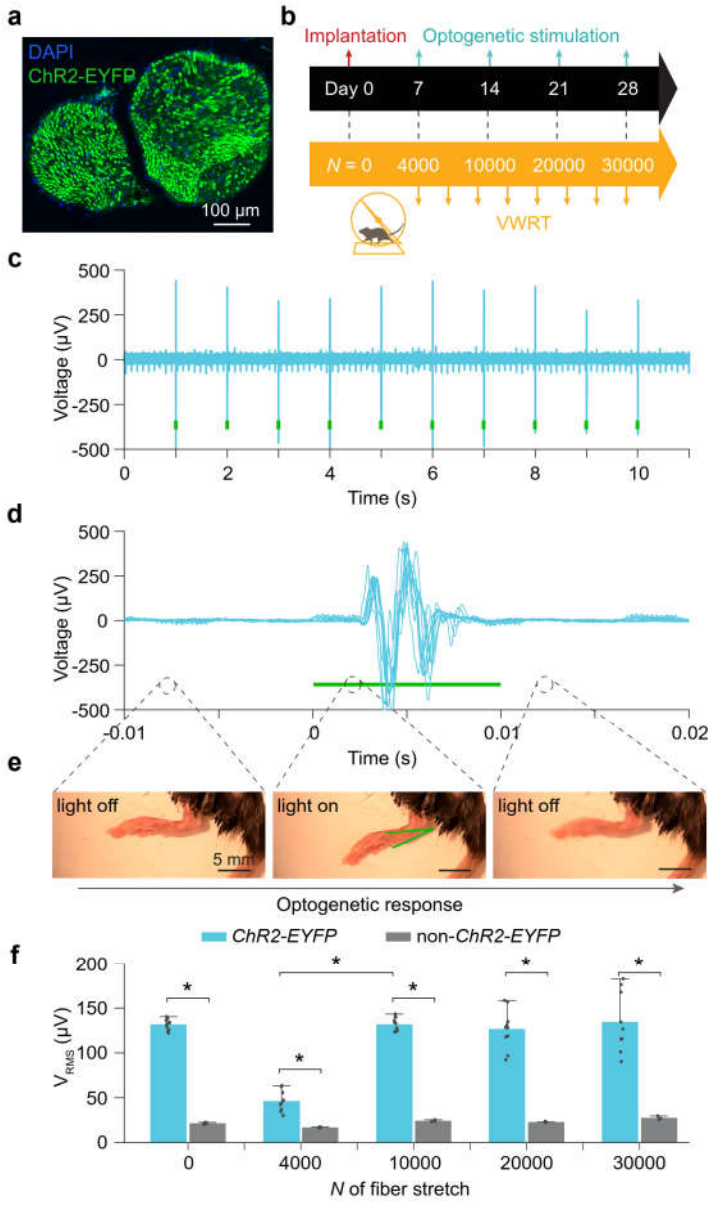

Figure 7-4. Optogenetic activation enabled by the fatigue-resistant hydrogel fiber optics. (a) Confocal image of transverse section of the mouse sciatic nerve. Scale bar: 100 μm. (b) In vivo study design of implantation and optogenetic activation through the hydrogel fiber-optic devices, accompanied by voluntary wheel running of the animal subjects. On Day 0, Day 7, Day 14, Day 21, and Day 28, the subjects have experienced approximately 0, 4,000, 10,000, 20,000, and 30,000 running cycles on a wheel, respectively, and are exposed to optogenetic activation. (c) Representative EMG signals recorded by needle electrodes on Day 0. Green bars indicate the light illumination periods. (d) Overlay plot of EMG spikes on Day 0, aligned to the time of light illumination. The green bar indicates the light illumination periods. (e) Images of the ankle joint movement in response to optogenetic activation through the hydrogel fiber-optic device. Scale bars: 5 mm. (f) Root mean square voltage of the EMG signals in response to optogenetic activation via the hydrogel fiber-optic devices over 30,000 cycles of in vivo fiber stretching. Animal subjects include *Thy1::ChR2-EYFP* and wild-type (non-*ChR2-EYFP*) mice. Statistical significance is

determined by two-way ANOVA and Tukey's multiple comparison test; $*P \leqslant 0.05$. Values represent the mean and the standard deviation (n = 3 independent measurements from different animals).

7.5. Materials and methods

7.5.1. Hydrogel fiber fabrication

Silica pigtail. Hydrogel fiber fabrication. A short silica fiber (core diameter 400 μm, length 15 mm) was stripped from a polyimide-coated multimode fiber (Thorlabs; FG400UEP, NA 0.22) and fixed to a ceramic optic ferrule (outer diameter 1.25 mm, length 10.5 mm; Thorlabs, CFX440-10) using epoxy adhesives (Loctite Eccobond F 112). The silica fiber was extruded out at one end of the ferrule with the length of 3 mm, and both ends of the silica fiber in the ferrule were polished. The extruded silica fiber was treated with 50% sodium hydroxide solution overnight and plasma cleaning (Harrick Plasma) in an oxygen atmosphere for 5 min. 10 wt% PVA (molecular weight of 146,000 to 186,000, 99+% hydrolyzed) was dissolved in water at 90 °C with continuous stirring for 5 hours to obtain a clean PVA solution. A layer of PVA was deposited on the extruded silica fiber by dip coating of the PVA solution. The optic ferrule with a PVA-coated silica segment was then dried at room temperature for 1 hour and heated at 100 °C for 1 hour.

Hydrogel core. 10 mL of 10 wt% PVA solution was mixed with 75 μL of hydrochloric acid (37%) for 30 seconds using a Thinky Mixer (AR-100). 10 mL of PVA solution was mixed with 75 μL of glutaraldehyde solution (25% in water) for 30 seconds using a Thinky Mixer (AR-100). The above two solutions were then mixed for 30 seconds and degassed for 2 minutes using a Thinky Mixer (AR-100). Afterward, the degassed mixture was infused into a silicone tubing (length 120 mm, diameter 1.6 mm; McMaster-Carr, 5233K51) connecting with a disk-shaped compartment (diameter 3 mm). The PVA-coated optic ferrule was then inserted into the silicone tubing. The mixture was allowed to cross-link for 6 hours at room temperature in a humid environment, after which the chemically cross-linked PVA hydrogel was demolded by swelling the silicone mold in dichloromethane (DCM). A hole (diameter 1 mm) was punched with a dispensing tip (18 Gauge; EFD Nordson). The hydrogel was next washed with a large amount of water to remove residual chemicals for two days, dried in the air at room temperature for 12 hours and annealed at 100 °C for 30 min. The process of drying and annealing would induce shrinkage in dimensions (diameter

and length) of the hydrogel. Then hydrogel rehydrated in water was the hydrogel core of the optical fiber.

Hydrogel cladding. After being fully hydrated in water, the hydrogel core was inserted into another silicone tubing (length 60 mm, diameter 1000 μm; McMaster-Carr, 1972T14), and both ends (cuff and ferrule) were exposed. 5 mL of PVA solution was mixed with 50 μL of hydrochloric acid (37%) for 30 seconds using a Thinky Mixer (AR-100). 5 mL of PVA solution was mixed with 50 μL of glutaraldehyde solution (25% in water) for 30 seconds using a Thinky Mixer (AR-100). The above two solutions as well as 5 mL of graphene oxide solution (Ultra highly concentrated single-layer graphene oxide; Graphene Supermarket) were then mixed for 30 seconds and degassed for 2 minutes using a Thinky Mixer (AR-100). The mixture was infused into the silicone tubing containing a hydrogel core, and left for cross-linking for 12 hours, after which the hydrogel was demolded by swelling the silicone mold in DCM. To reduce the graphene oxide in the hydrogel cladding. The hydrogel fiber was incubated in 100 mL of the aqueous solution containing 5 g of sodium hydroxide and 1.5 g of sodium hydrosulfite at 37 °C for 1 min. Lastly, the hydrogel fiber was washed with a large amount of water to remove residual chemicals for another two days.

7.5.2. Structural characterization

Nanocrystals in hydrogel materials. The X-ray scattering measurement was performed on the hydrogel core materials in the dry state with a Pilatus3R 300K detector in an X-ray scattering instrument (Bruker Nanostar, wavelength λ = 1.54 Å). We used a small-angle 2-mm beamstop with a sample-detector distance of 109.1 mm for WAXS measurements. The exposure time was set as 300 seconds. Raw WAXS patterns were processed with corrections by MATLAB-based GIXSGUI software before analysis. After subtracting the instrumental line broadening, we identified the full width at half maximum diffraction peak as β, and the average size of crystalline domains d_{NC} was approximately calculated using Scherrer's equation $d_{NC} = k\lambda/(\beta \cos \theta_0)$, where k is a dimensionless shape factor varying with the actual shape of the crystalline domain (k = 1, approximating the spherical shape of the crystalline domains), λ is the wavelength of X-ray diffraction (λ = 1.54 Å), and θ_0 is the peak of the Bragg angle[543].

Water content measurement. The swollen hydrogels weighing m_S were placed in water at 37°C for 2 hours and weighed m_D after air-drying. Therefore, the water content in the swollen state can be calculated as $(m_S - m_D)/m_S$, and the polymer content in the swollen state can be calculated as m_D/m_S.

Microscopic imaging of hydrogel fibers. Microscopic images of hydrogel fibers at the hydrogel-silica interfaces were acquired with an epifluorescence microscope (Nikon Eclipse LV100ND) in the bright field mode.

7.5.3. Optical characterization

Hydrogel membrane preparation. A series of hydrogel membranes were prepared with a similar procedure as discussed above but using a rectangular mold (thickness 1 mm), including annealed PVA hydrogel with annealing times of 0, 10, 30, 60, and 120 min used for the hydrogel fiber core (denoted as A0, A10, A30, A60, A120), and the black PVA with reduced time of 0, 1 and 5 min for the hydrogel fiber cladding (denoted as B0, B1, B5). In addition, we fabricated chemically cross-linked hydrogel membranes with different cross-linking densities. 10 wt% PVA (molecular weight of 146,000 to 186,000, 99+% hydrolyzed) was dissolved in water at 90 °C with continuous stirring for 5 hours to obtain a clean PVA solution. 10 mL of 10 wt% PVA solution was mixed with 75 μL of hydrochloric acid (37%) for 30 seconds using a Thinky Mixer (AR-100). 10 mL of PVA solution was mixed with 75 μL of glutaraldehyde solution (25% in water) for 30 seconds using a Thinky Mixer (AR-100). The above two solutions were then mixed for 30 seconds and degassed for 2 minutes using a Thinky Mixer (AR-100). Afterward, the degassed mixture was poured into a rectangular mold (thickness 1 mm). The mixture was allowed to cross-link for 6 hours at room temperature. The hydrogel membranes were next immersed in dilute hydrochloric acid (0.36%) for 1 hour and switched to glutaraldehyde solution (0%, 0.25%, 2.5%, 25%) to obtain non-crystalline, chemically cross-linked PVA hydrogels (denoted as C0, C1, C2, C3, C4). The hydrogel was next washed with a large amount of water to remove residual chemicals for two days. The thickness of the hydrogel membranes was measured by a caliper.

Optical measurement of hydrogel materials. The absorbance (488 nm and 600 nm) and fluorescence (excitation: 488 nm, emission: 510 nm) of the hydrogel membranes in water were

measured by a microplate reader (BioTek Synergy H4). The transmission spectra (200 nm – 1000 nm) of the hydrogel membranes were measured by UV-vis spectroscopy (Thermo Fisher Scientific). The refractive indices of hydrogel materials were measured by attaching the hydrogel membranes onto the prism of a digital pocket refractometer (Sper Scientific, 400 nm). The relation between the refractive index and polymer concentration agrees with the rule of mixture[544].

Optical measurement of hydrogel fibers. The propagation loss of the hydrogel fiber in a simulated tissue medium (1% agar) was measured by a cutback method. The hydrogel fiber was inserted into a plastic tube (diameter 3 mm) and 1% agar gel was injected into the tube using a syringe. Laser light at 488 nm (Changchun New Industries) was coupled into a hydrogel fiber using a ferrule mating sleeve. The power of transmitted light through the hydrogel fiber was measured with a power meter (Thorlabs, PM16-122). The 0.5 cm long end of the fiber was cut away using a razor blade, and the output power was measured after each cut. This measurement was repeated at an interval of 0.5 cm. A large-area power meter was placed at the bottom of the tube to measure the transmitted power levels. The input and output of light pulses (100 ms-on/900 ms-off) before and after the hydrogel fiber (5 cm in length) were recorded by a photodetector (Thorlabs, DET36A2) and displayed on an oscilloscope (SDS1202X-E, Siglent), respectively.

7.5.4. Mechanical characterization

Mechanical characterization of the hydrogel fibers. All the mechanical tests were performed in a water bath at 25°C with a U-stretch testing machine (CellScale). The load cells with a maximum force of 4.4 N or 44 N were used. The hydrogel fiber, including an optic ferrule, a hydrogel core, and a hydrogel cladding, with the dimensions in the swollen state of 1000 μm in diameter, 10 mm in gauge length was stretched by the testing machine at the rate of 1 cycle per second. The nominal stress was calculated from the force divided by the cross-sectional area in the swollen state. The strain was measured by the displacement by the gauge length. In a single-cycle tensile test, the hydrogel fiber was stretched until fracture. From the stress-strain curve, we obtained Young's modulus, tensile strength, and work of energy. In a multiple-cycle tensile test, the hydrogel fiber was stretched with constant maximum stress, and the strain was recorded over time.

7.5.5. Coupled optical and mechanical characterization

Optical transmission of hydrogel fibers under mechanical stretching. The amorphous hydrogel fiber is the hydrogel fiber core without any annealing, and the crystalline hydrogel fiber is the hydrogel fiber core with 30-min annealing. For better visualization, there is no light-absorbing cladding in the experiments in **Figure 7-2f**. The hydrogel fibers (50 mm in length) were fabricated with two optic ferrules at each end. Laser light at 488 nm (Changchun New Industries) was coupled into the hydrogel fiber at one end, and the photodiode sensor in a power meter (Thorlabs, PM16-122) was coupled with the hydrogel fiber at the other end. The hydrogel fiber was immersed in a water bath. It was either stretched using a U-stretch testing machine (CellScale) with different tensile strains, or bent along with cylindrical discs with different radii. The power of transmitted light through the hydrogel fiber was recorded at different deformations. In addition to the hydrogel fiber, a silica fiber (length 50 mm, diameter 400 μm; Thorlabs, FT400EMT) adhered to two optic ferrules at each end. A PDMS fiber (length 50 mm, diameter 1000 μm) was fabricated by curing a Sylgard 184 silicone elastomer kit (Dow Inc.) in a silicone mold. Similarly, the optical transmission along silica and PDMS fibers were tested at different deformations.

Ex vivo light delivery by hydrogel fibers. Segments of the porcine artery were purchased from a commercial vendor of research-grade porcine tissue (Sierra for Medical Science). The artery segment (15 mm) was connected with a dispensing system (Nordson EFD), which can pump airflow repeatedly to the artery (1 Hz). The silica fiber and hydrogel fiber were glued to the artery surfaces using cyanoacrylate adhesives (Loctite 460 instant adhesive).

7.5.6. In vivo optical simulation

Animals. All animal surgeries were reviewed and approved by the Committee on Animal Care at the Massachusetts Institute of Technology. Wild-type mice (C57BL/6J) were purchased from the Jackson Laboratory. *Thy1::ChR2-EYFP* mice were also purchased from the Jackson Laboratory and bred by the Division of Comparative Medicine (DCM) at MIT. Mice were given ad libitum access to food and water and were housed in 22 °C ± 1 °C, 50% relative humidity, and on a 12-h light/12-h dark cycle. All experiments were conducted during the light cycle.

In vivo hydrogel fiber implantation. Mice (*Thy1::ChR2-EYFP* or wild type) were anesthetized with 1.5% isoflurane, and body temperature was maintained with a heated surgical table. Under sterile condition, a skin incision exposed the skull. The left sciatic nerve was exposed at the mid-thigh level after a skin incision and blunt separation of the vastus lateralis muscle and biceps femoris muscle. The optic ferrule and hydrogel fiber were threaded subcutaneously from the hindlimb to the skull. Then, the hydrogel cuff was circumferentially wrapped around the sciatic nerve and sealed with Histoacryl flexible adhesives (B. Braun Medical Inc.). The hindlimb skin incision was sewed back together by suturing (Vicryl 6-0, Ethicon). Finally, the optic ferrule was cemented to the skull. The full surgical procedure took, on average, 60 min. The sham surgery protocol was analogous, without hydrogel fiber implantation. A bare ferrule was mounted to the skull so blinded experimenters could not differentiate experimental groups during testing.

Optogenetic stimulation. After implantation and recovery from the surgery, mice (*Thy1::ChR2-EYFP* or wild type) were anesthetized with 1% isoflurane, and body temperature was maintained with a heated surgical table. Pulses of laser light (488 nm, 200 mW, 10 ms-on/1 s-off or 2.5 ms-on/22.5 ms-off) were coupled with the optic ferrule on the mouse skull. To perform EMG measurements, a detection electrode (Natus Ultra Disposable Subdermal Needle Electrodes, Natus Medical) was inserted in the gastrocnemius muscle or tibialis anterior muscle, and a reference electrode (Natus Ultra Disposable Subdermal Needle Electrodes, Natus Medical) was subcutaneously inserted in an electrical unrelated region, such as the right body. EMG data triggered by optical stimulation were collected using an PZ2-32 amplifier (Tucker-Davis Technologies) and RZ5D base processor (Tucker-Davis Technologies). In addition, the left hindlimb flexion in response to the blue light pulses was captured by a camera (Logitech Brio Ultra Pro HD Webcam).

Morphological evaluation and immunohistochemistry. Once the mice were euthanized, the sciatic nerves were then dissected, fixed in the 4% paraformaldehyde (PFA) solution overnight, and embedded in paraffin and cut into 5-μm thick sections for microscopic evaluation of the morphology (ScanScope AT, Leica Biosystems, USA) with hematoxylin and eosin staining. For immunohistochemistry, the fixed nerves were transferred to 30% sucrose in PBS, in which the mouse nerves were kept overnight. The sciatic nerves were then embedded in Tissue-Tek OCT

compound (Sakura Tissue-Tek) and sectioned on a Leica CM1950 cryostat (Leica). For immunohistochemistry, the sciatic nerve was cut in the longitudinal and cross-sectional directions at a 20-μm thickness, then placed onto glass slides, and mounted with Fluoroshield mounting medium with DAPI (4',6-diamidino-2-phenylindole, Abcam). Finally, the slides were photographed with a confocal microscope (SP5, Leica, USA) and a 40X oil immersion objective lens with the excitation wavelengths of 488 nm and 405 nm.

Running poses and gait analysis. All animals were acclimatized to a wire mesh running wheel (20 cm in diameter, Prevue Pet Products) for 16 min, 1 day before surgery. One week after fiber implantation, mice ran on the wheel for 16 min once every three days (on Day 7, 10, 13, 15, 19, 22, 25, 28, 31, 34 following the surgery date). Gait analysis was performed when the voluntary running was recorded by a camera (Logitech Brio Ultra Pro HD Webcam). The 3D markerless pose estimation and hindlimb kinematic analysis was performed using DeepLabCut (Mackenzie Mathis)[541]. Featured nodes on the mouse including ferrule, neck, back, iliac crest, hip, knee, ankle, and toe were tracked during mouse running in the video clips. Other gait parameters, including knee angles, ankle angles and running speed, were also calculated from the trajectories of featured nodes. Running speed was determined by the parabolic nature of the distance between the front and hind toe and MATLAB was used to find the local maximums, which represent the running cycles. Time-dependent hydrogel fiber length during running was calculated by the segments starting from the ferrule end to the middle point of the hip and knee. The original hydrogel fiber length was measured before surgery.

Statistical analysis. Statistical analyses were performed in Excel (Microsoft Corporation, Inc., USA), MATLAB (MathWorks, Inc., USA), and DeepLabCut (Mackenzie Mathis). The normality of data distribution was tested via Shapiro–Wilk test. For the data that showed normal distribution, statistical significance was determined by the analysis of variance with Tukey's multiple comparison test (ANOVA if equal variances or Welch's ANOVA if unequal variances). For gait analysis, where data distributions were found to be non-normal, Kruskal–Wallis test followed by Bonferroni's correction and Dunn–Sidak multiple comparison tests were conducted. P values less than 0.05 were considered significant. The numbers of animals are indicated in the figures, with

each point representing a single experiment. For representative confocal images, a minimum of three animals per experiment was used.

7.6. Conclusions

In the brain, the standard approach for light delivery is based on silica fiber-optics inserted in the any brain structure, which has been readily adopted by neuroscientists. However, in the peripheral nervous system, light delivery has proven to be a lingering challenge for optogenetic applications. There is no universal approach that can access and illuminate diverse peripheries with varied anatomy, location, and locomotion. In this study, we have reported a fatigue-resistant hydrogel fiber-optic technology for light delivery that adapts to animal persistent locomotion. By controlling the growth of nanocrystalline domains during hydrogel synthesis and device fabrication, we have obtained the hydrogel fiber-optic device with good light transmission (1.1 dB/cm), stretchability (75%-150% in strain), and fatigue strength (1.4 MPa) against repeated deformation (30,000 cycles). This technology enables optogenetic stimulation of mouse sciatic nerves with running tests for four weeks: it allows light delivery and adapts to intense motion during animal running. The robust optical and mechanical performance under repeated stretching conditions can be further extended to other applications, such as motor control, somatosensory transduction, and pain processing[517, 518]. The mechanically compatible device-tissue interface offers the promise of delivering light to other peripheral nerves and tubular structures, such as blood vessels, intestines, and tracheas[518]. We envision that the motion-adaptable fiber optics with fatigue-resistant soft materials will provide effective solutions for light delivery to dynamic organs under complicated mechanical environments, such as blood circulation, intestinal peristalsis, and respiration[518].

Chapter 8

Conclusions and future outlook

8.1. Summary of key contributions

Fatigue failure of soft materials and structures is one critical challenge that limits the long-lasting deployment of soft machines and soft robots. The challenge motivates new strategies to design the next generation of hydrogel materials and machines. The answers presented in this thesis use an integrated approach from design and manufacturing, theoretical calculation, experimental characterization, to in vitro and in vivo validation. Following this systematic approach, the thesis specifically focuses on two aspects: (a) designing fatigue-resistant hydrogel materials and adhesions, and (b) designing hydrogel machines that constantly interact with biological organisms. The main contributions of this thesis are summarized as follows:

- Proposed bioinspired optimization of nanostructures in soft materials, significantly enhanced fatigue thresholds of soft materials by orders of magnitude, and addressed fatigue failures of soft materials and structures.
- Constructed hydrogel living devices with genetically engineered cells as active components in a biocompatible hydrogel matrix. Additive manufacturing of living materials results in programmable 3D architectures patterned in space and time.
- Invented ingestible hydrogel devices that can be retained in the stomach and intestine for prolonged monitoring and diagnosis. The localization and retention in the GI tract rely on hydrogel actuation modulated by the osmotic pressure or a magnetic field.
- Developed hydrogel optical fibers that collect and deliver light from/to the nervous system. The tradeoff between optical and mechanical properties is overcome by tuning the nanostructures in the hydrogel.

8.2. Translational challenges and opportunities

Soft machines have their limitations that need to be overcome before translational applications.

8.2.1. Hydrogel living devices

The major limitation of living devices is cell viability. They require sustaining living organisms in the devices for extended periods. Retaining the viability and function of wearable or implantable sensing systems based on living cells requires nutrient delivery and waste extraction, as well as temperature and gas regulation, all of which involve numerous technological hurdles. The living components are usually more susceptible to the harsh environment, such as extreme temperature, low humidity, and chemical insults. We have partially solved this problem by designing the mechanical and structural properties of hydrogels, and hence high viability can be achieved for seven days[436]. A longer operation time of the living devices is expected for clinical translation or daily uses.

Genetically engineered cells can also pose biocontainment or biohazard concerns, particularly if used as consumer-level devices. Complete encapsulation of bacteria in hydrogel structures have effectively prevented environmental escape and fulfilled the regulatory requirements for practical use [55, 437]. Moreover, the mutational pressures on evolving cell populations can result in the loss of the genetic phenotype and function.

8.2.2. Hydrogel GI retentive devices

Oral administration provides an easy and non-invasive approach to applying in-body devices for diagnostics and therapy. Compared with other ingestible materials based on plastics or metals, the food or tissue-level softness of the hydrogel device alleviates the mechanical mismatch between GI mucosa and ingestible devices, especially in the long term [97, 436].

In addition, the potential obstruction of the GI tract is another challenge faced by the GI retentive devices. Hydrogels with programmed degradation or disassembly can help resolve this concern. For example, the shrinkage of swollen hydrogel balloons can be triggered by calcium chloride solution[97], and the release of magnetic hydrogels can be controlled by external magnet removal[436]. Furthermore, ingestible devices generally lack the ability to steer themselves, limiting the possibility to target specific sites in the GI tract, which has been a major problem in capsule endoscopy. To achieve versatile functions, such as localization, steering, and biopsy in the GI tract, hydrogels that are responsive to environmental stimuli or magnetic control are being explored[436].

8.2.3. Hydrogel optical fibers

Light stimulation and therapy are not as widely adopted as electrical counterparts, as optical signals are less ubiquitous than electrical spikes in organisms. Therefore, both optogenetics and fiber photometry require genetic modification to enable optical control and sensing. The hydrogel optical fibers will find more uses in clinical scenarios, such as fluorescence imaging, photoacoustic imaging, and optical coherence tomography for disease monitoring and diagnosis.

Although hydrogels are mechanically soft and stretchable compared with the commercial silica fibers, we should evaluate and optimize the optical transmission of hydrogel optical fibers before clinical translation, because of the size differences between our testing subjects (mouse) and human.

8.3. Future perspectives

This thesis provides a universal paradigm for generating new soft materials and machines for various biomedical applications, including the nervous system modulated by optical fibers, the skeletal system that interfaces artificial cartilages, the digestive system that hosts ingestible hydrogels, and integumentary system that interacts with wearable patches. The burgeoning researches in nanostructures (e.g., nanofibers, nanoparticles, micelles, vesicles) will enable the development of versatile fatigue-resistant hydrogels and open up the design space in nanoscale; the advent of additive manufacturing will allow the device fabrication of any 3D architectures and expand the design space in the micro- and macroscale. The expanded design space in two length scales brings more opportunities for both soft materials and machines; however, there is a lack of guidelines for structure optimization and behavior prediction of soft machines. This is where the paradigm of this thesis has huge potential: the theoretical calculation and experimental validation can guide the manufacturing of soft materials and machines with programmable responses for diverse applications. In this thesis, we focus primarily on the mechanical properties of hydrogels. However, this paradigm can be extended to study other soft material systems (e.g., elastomers and organogels) and other properties (e.g, electrical, optical, and biological). The ultimate goal is to develop soft machines that can interact with the human body in different modes and over the long run.

Bibliography

1. Zhao, X., *Multi-scale multi-mechanism design of tough hydrogels: building dissipation into stretchy networks.* Soft Matter, 2014. **10**(5): p. 672-687.
2. Wichterle, O. and D. Lim, *Hydrophilic gels for biological use.* Nature, 1960. **185**(4706): p. 117.
3. Hong, W., et al., *A theory of coupled diffusion and large deformation in polymeric gels.* Journal of the Mechanics and Physics of Solids, 2008. **56**(5): p. 1779-1793.
4. Li, J. and D.J. Mooney, *Designing hydrogels for controlled drug delivery.* Nature Reviews Materials, 2016. **1**(12): p. 16071.
5. Yuk, H., et al., *Hydraulic hydrogel actuators and robots optically and sonically camouflaged in water.* Nature Communications, 2017. **8**: p. 14230.
6. Yun, S.-H. and C. Myunghwan, *Light-guiding hydrogel devices for cell-based sensing and therapy*. 2017, Washington, DC: U.S. Patent and Trademark Office.
7. Ulijn, R.V., et al., *Bioresponsive hydrogels.* Materials Today, 2007. **10**(4): p. 40-48.
8. Ahn, S.-k., et al., *Stimuli-responsive polymer gels.* Soft Matter, 2008. **4**(6): p. 1151-1157.
9. Chen, F., P.W. Tillberg, and E.S. Boyden, *Expansion microscopy.* Science, 2015. **347**(6221): p. 543-548.
10. Lee, K.Y. and D.J. Mooney, *Hydrogels for tissue engineering.* Chemical Reviews, 2001. **101**(7): p. 1869-1880.
11. Kopeček, J., *Hydrogel biomaterials: a smart future?* Biomaterials, 2007. **28**(34): p. 5185-5192.
12. Zhang, Y.S. and A. Khademhosseini, *Advances in engineering hydrogels.* Science, 2017. **356**(6337): p. eaaf3627.
13. Klebanov, B.M., D.M. Barlam, and F.E. Nystrom, *Machine elements: life and design*. 2007: CRC Press.
14. Engler, A.J., et al., *Matrix elasticity directs stem cell lineage specification.* Cell, 2006. **126**(4): p. 677-689.
15. Caliari, S.R. and J.A. Burdick, *A practical guide to hydrogels for cell culture.* Nature Methods, 2016. **13**(5): p. 405.
16. Huebsch, N., et al., *Matrix elasticity of void-forming hydrogels controls transplanted-stem-cell-mediated bone formation.* Nature Materials, 2015. **14**(12): p. 1269.
17. Chaudhuri, O., et al., *Hydrogels with tunable stress relaxation regulate stem cell fate and activity.* Nature Materials, 2016. **15**(3): p. 326.
18. Tibbitt, M.W. and K.S. Anseth, *Hydrogels as extracellular matrix mimics for 3D cell culture.* Biotechnology and Bioengineering, 2009. **103**(4): p. 655-663.
19. Cushing, M.C. and K.S. Anseth, *Hydrogel cell cultures.* Science, 2007. **316**(5828): p. 1133-1134.
20. Jayawarna, V., et al., *Nanostructured hydrogels for three-dimensional cell culture through self-assembly of fluorenylmethoxycarbonyl–dipeptides.* Advanced Materials, 2006. **18**(5): p. 611-614.
21. Vegas, A.J., et al., *Combinatorial hydrogel library enables identification of materials that mitigate the foreign body response in primates.* Nature Biotechnology, 2016. **34**(3): p. 345.
22. Vegas, A.J., et al., *Long-term glycemic control using polymer-encapsulated human stem cell–derived beta cells in immune-competent mice.* Nature Medicine, 2016. **22**(3): p. 306.

23. Gupta, P., K. Vermani, and S. Garg, *Hydrogels: from controlled release to pH-responsive drug delivery.* Drug Discovery Today, 2002. **7**(10): p. 569-579.
24. Kikuchi, A. and T. Okano, *Pulsatile drug release control using hydrogels.* Advanced Drug Delivery Reviews, 2002. **54**(1): p. 53-77.
25. Kim, S.W., Y.H. Bae, and T. Okano, *Hydrogels: swelling, drug loading, and release.* Pharmaceutical Research, 1992. **9**(3): p. 283-290.
26. Qiu, Y. and K. Park, *Environment-sensitive hydrogels for drug delivery.* Advanced Drug Delivery Reviews, 2001. **53**(3): p. 321-339.
27. Gerlach, G. and K.-F. Arndt, *Hydrogel sensors and actuators: engineering and technology*. Vol. 6. 2009: Springer Science & Business Media.
28. Gong, J.P., et al., *Double-network hydrogels with extremely high mechanical strength.* Advanced Materials, 2003. **15**(14): p. 1155-1158.
29. Sun, J.-Y., et al., *Highly stretchable and tough hydrogels.* Nature, 2012. **489**(7414): p. 133.
30. Yuk, H., et al., *Tough bonding of hydrogels to diverse non-porous surfaces.* Nature Materials, 2016. **15**(2): p. 190.
31. Yuk, H., et al., *Skin-inspired hydrogel–elastomer hybrids with robust interfaces and functional microstructures.* Nature Communications, 2016. **7**: p. 12028.
32. Gladman, A.S., et al., *Biomimetic 4D printing.* Nature Materials, 2016. **15**(4): p. 413.
33. Liu, X., et al., *3D printing of living responsive materials and devices.* Advanced Materials, 2018. **30**(4): p. 1704821.
34. Hong, S., et al., *3D printing of highly stretchable and tough hydrogels into complex, cellularized structures.* Advanced Materials, 2015. **27**(27): p. 4035-4040.
35. Grigoryan, B., et al., *Multivascular networks and functional intravascular topologies within biocompatible hydrogels.* Science, 2019. **364**(6439): p. 458-464.
36. Buenger, D., F. Topuz, and J. Groll, *Hydrogels in sensing applications.* Progress in Polymer Science, 2012. **37**(12): p. 1678-1719.
37. Calvert, P., *Hydrogels for soft machines.* Advanced Materials, 2009. **21**(7): p. 743-756.
38. Griffin, D.R., et al., *Accelerated wound healing by injectable microporous gel scaffolds assembled from annealed building blocks.* Nature Materials, 2015. **14**(7): p. 737.
39. Smith, M.M., *Sensing the past: seeing, hearing, smelling, tasting, and touching in history*. 2007: Univ of California Press.
40. He, X., et al., *Synthetic homeostatic materials with chemo-mechano-chemical self-regulation.* Nature, 2012. **487**(7406): p. 214.
41. Shastri, A., et al., *An aptamer-functionalized chemomechanically modulated biomolecule catch-and-release system.* Nature Chemistry, 2015. **7**(5): p. 447.
42. Miyata, T., N. Asami, and T. Uragami, *A reversibly antigen-responsive hydrogel.* Nature, 1999. **399**(6738): p. 766.
43. Ehrick, J.D., et al., *Genetically engineered protein in hydrogels tailors stimuli-responsive characteristics.* Nature Materials, 2005. **4**(4): p. 298.
44. Han, D., et al., *Soft robotic manipulation and locomotion with a 3d printed electroactive hydrogel.* ACS Applied Materials & Interfaces, 2018. **10**(21): p. 17512-17518.
45. Guo, J., et al., *Highly stretchable, strain sensing hydrogel optical fibers.* Advanced Materials, 2016. **28**(46): p. 10244-10249.
46. Shin, J., P.V. Braun, and W. Lee, *Fast response photonic crystal pH sensor based on templated photo-polymerized hydrogel inverse opal.* Sensors and Actuators B, 2010. **150**(1): p. 183-190.

47. Dong, L., et al., *Adaptive liquid microlenses activated by stimuli-responsive hydrogels.* Nature, 2006. **442**(7102): p. 551.
48. Li, X.-H., et al., *Broadband light management with thermochromic hydrogel microparticles for smart windows.* Joule, 2019. **3**(1): p. 290-302.
49. Ionov, L., *Hydrogel-based actuators: possibilities and limitations.* Materials Today, 2014. **17**(10): p. 494-503.
50. Shibata, H., et al., *Injectable hydrogel microbeads for fluorescence-based in vivo continuous glucose monitoring.* Proceedings of the National Academy of Sciences, 2010. **107**(42): p. 17894-17898.
51. Kim, C.-C., et al., *Highly stretchable, transparent ionic touch panel.* Science, 2016. **353**(6300): p. 682-687.
52. Lei, Z., et al., *A bioinspired mineral hydrogel as a self-healable, mechanically adaptable ionic skin for highly sensitive pressure sensing.* Advanced Materials, 2017. **29**(22): p. 1700321.
53. Usuki, K., H. Onoe, and E. Iwase, *Deformable coloring element using an electroactive hydrogel with bottom-arranged electrodes.* Japanese Journal of Applied Physics, 2015. **54**(6S1): p. 06FP06.
54. Tavakoli, J. and Y. Tang, *Hydrogel based sensors for biomedical applications: An updated review.* Polymers, 2017. **9**(8): p. 364.
55. Liu, X., et al., *Stretchable living materials and devices with hydrogel–elastomer hybrids hosting programmed cells.* Proceedings of the National Academy of Sciences, 2017. **114**(9): p. 2200-2205.
56. Perera, S., et al., *Evaluation of a hydrogel-based diagnostic approach for the point-of-care based detection of Neisseria gonorrhoeae.* Antibiotics, 2018. **7**(3): p. 70.
57. Sepantafar, M., et al., *Engineered hydrogels in cancer therapy and diagnosis.* Trends in Biotechnology, 2017. **35**(11): p. 1074-1087.
58. Richter, A., et al., *Review on hydrogel-based pH sensors and microsensors.* Sensors, 2008. **8**(1): p. 561-581.
59. Zabow, G., S. Dodd, and A. Koretsky, *Shape-changing magnetic assemblies as high-sensitivity NMR-readable nanoprobes.* Nature, 2015. **520**(7545): p. 73.
60. Appel, E.A., et al., *Ultrahigh-water-content supramolecular hydrogels exhibiting multistimuli responsiveness.* Journal of the American Chemical Society, 2012. **134**(28): p. 11767-11773.
61. Culver, H.R., J.R. Clegg, and N.A. Peppas, *Analyte-responsive hydrogels: Intelligent materials for biosensing and drug delivery.* Accounts of Chemical Research, 2017. **50**(2): p. 170-178.
62. Wang, D., et al., *Bioresponsive DNA hydrogels: beyond the conventional stimuli responsiveness.* Accounts of Chemical Research, 2017. **50**(4): p. 733-739.
63. Fu, F., et al., *Bioinspired living structural color hydrogels.* Science Robotics, 2018. **3**(16): p. eaar8580.
64. Schild, H.G., *Poly (N-isopropylacrylamide): experiment, theory and application.* Progress in Polymer Science, 1992. **17**(2): p. 163-249.
65. Yoshida, R., et al., *Comb-type grafted hydrogels with rapid deswelling response to temperature changes.* Nature, 1995. **374**(6519): p. 240.
66. Gao, Y., et al., *Hydrogel microphones for stealthy underwater listening.* Nature Communications, 2016. **7**: p. 12316.

67. Merchant, S.A., et al., *High-sensitivity amperometric biosensors based on ferrocene-modified linear poly(ethylenimine).* Langmuir, 2009. **25**(13): p. 7736-7742.
68. Eggenstein, C., et al., *A disposable biosensor for urea determination in blood based on an ammonium-sensitive transducer.* Biosensors and Bioelectronics, 1999. **14**(1): p. 33-41.
69. Zhai, D., et al., *Highly sensitive glucose sensor based on Pt nanoparticle/polyaniline hydrogel heterostructures.* ACS Nano, 2013. **7**(4): p. 3540-3546.
70. Carrigan, S.D., G. Scott, and M. Tabrizian, *Rapid three-dimensional biointerfaces for real-time immunoassay using hIL-18BPa as a model antigen.* Biomaterials, 2005. **26**(35): p. 7514-7523.
71. Charles, P.T., et al., *Fabrication and characterization of 3D hydrogel microarrays to measure antigenicity and antibody functionality for biosensor applications.* Biosensors and Bioelectronics, 2004. **20**(4): p. 753-764.
72. Kahn, J.S., Y. Hu, and I. Willner, *Stimuli-responsive DNA-based hydrogels: From basic principles to applications.* Accounts of Chemical Research, 2017. **50**(4): p. 680-690.
73. Borisov, S.M., et al., *Composite luminescent material for dual sensing of oxygen and temperature.* Advanced Functional Materials, 2006. **16**(12): p. 1536-1542.
74. Choi, M., et al., *Light-guiding hydrogels for cell-based sensing and optogenetic synthesis in vivo.* Nature Photonics, 2013. **7**(12): p. 987.
75. Heo, Y.J., et al., *Long-term in vivo glucose monitoring using fluorescent hydrogel fibers.* Proceedings of the National Academy of Sciences, 2011. **108**(33): p. 13399-13403.
76. Fine, T., et al., *Luminescent yeast cells entrapped in hydrogels for estrogenic endocrine disrupting chemical biodetection.* Biosensors and Bioelectronics, 2006. **21**(12): p. 2263-2269.
77. Vaddiraju, S., et al., *Enhanced glucose sensor linearity using poly (vinyl alcohol) hydrogels.* Journal of Diabetes Science Technology, 2009. **3**(4): p. 863-874.
78. Ma, Z., et al., *Doping engineering of conductive polymer hydrogels and their application in advanced sensor technologies.* Chemical Science, 2019. **10**(25): p. 6232-6244.
79. Li, L., et al., *All inkjet-printed amperometric multiplexed biosensors based on nanostructured conductive hydrogel electrodes.* Nano Letters, 2018. **18**(6): p. 3322-3327.
80. Li, L., et al., *A nanostructured conductive hydrogels-based biosensor platform for human metabolite detection.* Nano Letters, 2015. **15**(2): p. 1146-1151.
81. Hoffman, A.S., *Hydrogels for biomedical applications.* Advanced Drug Delivery Reviews, 2012. **64**: p. 18-23.
82. Peppas, N.A., et al., *Physicochemical foundations and structural design of hydrogels in medicine and biology.* Annual Review of Biomedical Engineering, 2000. **2**(1): p. 9-29.
83. Tanaka, T. and D.J. Fillmore, *Kinetics of swelling of gels.* The Journal of Chemical Physics, 1979. **70**(3): p. 1214-1218.
84. Amsden, B., *Solute diffusion within hydrogels. Mechanisms and models.* Macromolecules, 1998. **31**(23): p. 8382-8395.
85. Holtz, J.H. and S.A. Asher, *Polymerized colloidal crystal hydrogel films as intelligent chemical sensing materials.* Nature, 1997. **389**(6653): p. 829.
86. Hirokawa, Y. and T. Tanaka. *Volume phase transition in a non-ionic gel*. in *AIP Conference Proceedings*. 1984. Aip.
87. Suzuki, A. and T. Tanaka, *Phase transition in polymer gels induced by visible light.* Nature, 1990. **346**(6282): p. 345.

88. Tanaka, T., et al., *Phase transitions in ionic gels.* Physical Review Letters, 1980. **45**(20): p. 1636.
89. Hendrickson, G.R. and L.A. Lyon, *Bioresponsive hydrogels for sensing applications.* Soft Matter, 2009. **5**(1): p. 29-35.
90. Jones, C.D. and J.W. Steed, *Gels with sense: supramolecular materials that respond to heat, light and sound.* Chemical Society Reviews, 2016. **45**(23): p. 6546-6596.
91. van der Linden, H.J., et al., *Stimulus-sensitive hydrogels and their applications in chemical (micro) analysis.* Analyst, 2003. **128**(4): p. 325-331.
92. Bhattacharya, S. and S.K. Samanta, *Soft-nanocomposites of nanoparticles and nanocarbons with supramolecular and polymer gels and their applications.* Chemical Reviews, 2016. **116**(19): p. 11967-12028.
93. Yang, C. and Z. Suo, *Hydrogel ionotronics.* Nature Reviews Materials, 2018. **3**(6): p. 125.
94. Mirfakhrai, T., J.D.W. Madden, and R.H. Baughman, *Polymer artificial muscles.* Materials Today, 2007. **10**(4): p. 30-38.
95. Huber, J., N. Fleck, and M. Ashby, *The selection of mechanical actuators based on performance indices.* Proceedings of the Royal Society of London, 1997. **453**(1965): p. 2185-2205.
96. Keplinger, C., et al., *Stretchable, transparent, ionic conductors.* Science, 2013. **341**(6149): p. 984-987.
97. Liu, X., et al., *Ingestible hydrogel device.* Nature Communications, 2019. **10**(1): p. 493.
98. Palleau, E., et al., *Reversible patterning and actuation of hydrogels by electrically assisted ionoprinting.* Nature Communications, 2013. **4**: p. 2257.
99. Beebe, D.J., et al., *Functional hydrogel structures for autonomous flow control inside microfluidic channels.* Nature, 2000. **404**(6778): p. 588-590.
100. Cangialosi, A., et al., *DNA sequence–directed shape change of photopatterned hydrogels via high-degree swelling.* Science, 2017. **357**(6356): p. 1126-1130.
101. Kim, Y.S., et al., *Thermoresponsive actuation enabled by permittivity switching in an electrostatically anisotropic hydrogel.* Nature Materials, 2015. **14**(10): p. 1002.
102. Takashima, Y., et al., *Expansion–contraction of photoresponsive artificial muscle regulated by host–guest interactions.* Nature Communications, 2012. **3**: p. 1270.
103. Osada, Y., H. Okuzaki, and H. Hori, *A polymer gel with electrically driven motility.* Nature, 1992. **355**(6357): p. 242-244.
104. Löwenberg, C., et al., *Shape-memory hydrogels: evolution of structural principles to enable shape switching of hydrophilic polymer networks.* Accounts of Chemical Research, 2017. **50**(4): p. 723-732.
105. Ko, H. and A. Javey, *Smart actuators and adhesives for reconfigurable matter.* Accounts of Chemical Research, 2017. **50**(4): p. 691-702.
106. Zhao, X., et al., *Active scaffolds for on-demand drug and cell delivery.* Proceedings of the National Academy of Sciences, 2011. **108**(1): p. 67-72.
107. Chin, S.Y., et al., *Additive manufacturing of hydrogel-based materials for next-generation implantable medical devices.* Science Robotics, 2017. **2**(2): p. eaah6451.
108. Huang, H.-W., et al., *Adaptive locomotion of artificial microswimmers.* Science Advances, 2019. **5**(1): p. eaau1532.
109. Li, T., et al., *Fast-moving soft electronic fish.* Science Advances, 2017. **3**(4): p. e1602045.
110. Yang, S.Y., et al., *A bio-inspired swellable microneedle adhesive for mechanical interlocking with tissue.* Nature Communications, 2013. **4**: p. 1702.

111. English, M.A., et al., *Programmable CRISPR-responsive smart materials.* Science, 2019. **365**(6455): p. 780-785.
112. Kim, J., et al., *Designing responsive buckled surfaces by halftone gel lithography.* Science, 2012. **335**(6073): p. 1201-1205.
113. Nojoomi, A., et al., *Bioinspired 3D structures with programmable morphologies and motions.* Nature Communications, 2018. **9**(1): p. 3705.
114. Wang, C., R.J. Stewart, and J. KopeČek, *Hybrid hydrogels assembled from synthetic polymers and coiled-coil protein domains.* Nature, 1999. **397**(6718): p. 417.
115. Xia, L.-W., et al., *Nano-structured smart hydrogels with rapid response and high elasticity.* Nature Communications, 2013. **4**: p. 2226.
116. Hippler, M., et al., *Controlling the shape of 3D microstructures by temperature and light.* Nature Communications, 2019. **10**(1): p. 232.
117. Wang, E., M.S. Desai, and S.-W. Lee, *Light-controlled graphene-elastin composite hydrogel actuators.* Nano Letters, 2013. **13**(6): p. 2826-2830.
118. Hong, W., X. Zhao, and Z. Suo, *Large deformation and electrochemistry of polyelectrolyte gels.* Journal of the Mechanics Physics of Solids, 2010. **58**(4): p. 558-577.
119. Flory, P.J., *Thermodynamics of dilute solutions of high polymers.* The Journal of Chemical Physics, 1945. **13**(11): p. 453-465.
120. Day, J.C. and I.D. Robb, *Thermodynamic parameters of polyacrylamides in water.* Polymer Gels and Networks, 1981. **22**(11): p. 1530-1533.
121. Cai, S. and Z. Suo, *Equations of state for ideal elastomeric gels.* Europhysics Letters, 2012. **97**(3): p. 34009.
122. Li, J., et al., *Experimental determination of equations of state for ideal elastomeric gels.* Soft Matter, 2012. **8**(31): p. 8121-8128.
123. Jeon, S.-J., A.W. Hauser, and R.C. Hayward, *Shape-morphing materials from stimuli-responsive hydrogel hybrids.* Accounts of Chemical Research, 2017. **50**(2): p. 161-169.
124. Lin, S., et al., *Anti-fatigue-fracture hydrogels.* Science Advances, 2019. **5**(1): p. eaau8528.
125. Yang, C.H., et al., *Ionic cable.* Extreme Mechanics Letters, 2015. **3**: p. 59-65.
126. Kim, Y., et al., *Printing ferromagnetic domains for untethered fast-transforming soft materials.* Nature, 2018. **558**(7709): p. 274.
127. Zrínyi, M., L. Barsi, and A. Büki, *Deformation of ferrogels induced by nonuniform magnetic fields.* The Journal of Chemical Physics, 1996. **104**(21): p. 8750-8756.
128. Kellaris, N., et al., *Peano-HASEL actuators: Muscle-mimetic, electrohydraulic transducers that linearly contract on activation.* Science Robotics, 2018. **3**(14): p. eaar3276.
129. Tondu, B. and P. Lopez, *Modeling and control of McKibben artificial muscle robot actuators.* IEEE Control Systems, 2000. **20**(2): p. 15-38.
130. Baldwin, H.A., *Realizable models of muscle function*, in *Biomechanics*. 1969, Springer. p. 139-147.
131. Ilievski, F., et al., *Soft robotics for chemists.* Angewandte Chemie International Edition, 2011. **50**(8): p. 1890-1895.
132. Mosadegh, B., et al., *Pneumatic networks for soft robotics that actuate rapidly.* Advanced Functional Materials, 2014. **24**(15): p. 2163-2170.
133. Wirthl, D., et al., *Instant tough bonding of hydrogels for soft machines and electronics.* Science Advances, 2017. **3**(6): p. e1700053.

134. Mao, Y., et al., *A large deformation viscoelastic model for double-network hydrogels.* Journal of the Mechanics and Physics of Solids, 2017. **100**: p. 103-130.
135. Hu, Y., et al., *Using indentation to characterize the poroelasticity of gels.* Applied Physics Letters, 2010. **96**(12): p. 121904.
136. Zhang, T., et al., *Predicting fracture energies and crack-tip fields of soft tough materials.* Extreme Mechanics Letters, 2015. **4**: p. 1-8.
137. Lin, S., et al., *Instabilities in confined elastic layers under tension: Fringe, fingering and cavitation.* Journal of the Mechanics and Physics of Solids, 2017. **106**: p. 229-256.
138. Erol, O., et al., *Transformer hydrogels: A review.* Advanced Materials Technologies, 2019. **4**(4): p. 1900043.
139. Ionov, L., *Biomimetic hydrogel-based actuating systems.* Advanced Functional Materials, 2013. **23**(36): p. 4555-4570.
140. Zrinyi, M., L. Barsi, and A. Büki, *Ferrogel: a new magneto-controlled elastic medium.* Polymer Gels and Networks, 1997. **5**(5): p. 415-427.
141. Ilg, P., *Stimuli-responsive hydrogels cross-linked by magnetic nanoparticles.* Soft Matter, 2013. **9**(13): p. 3465-3468.
142. Yang, J., et al., *Hydrogel adhesion: A supramolecular synergy of chemistry, topology, and mechanics.* Advanced Functional Materials, 2020. **30**(2): p. 1901693.
143. Yuk, H., B. Lu, and X. Zhao, *Hydrogel bioelectronics.* Chemical Society Reviews, 2019.
144. Shin, M., et al., *Complete prevention of blood loss with self-sealing haemostatic needles.* Nature Materials, 2017. **16**(1): p. 147.
145. Draper, D.O., et al., *Temperature increases in the human achilles tendon during ultrasound treatments with commercial ultrasound gel and full-thickness and half-thickness gel pads.* Journal of Athletic Training, 2010. **45**(4): p. 333-337.
146. Spencer, K.C., et al., *Characterization of mechanically matched hydrogel coatings to improve the biocompatibility of neural implants.* Scientific Reports, 2017. **7**(1): p. 1952.
147. Green, R. and M.R. Abidian, *Conducting polymers for neural prosthetic and neural interface applications.* Advanced Materials, 2015. **27**(46): p. 7620-7637.
148. Krsko, P. and M. Libera, *Biointeractive hydrogels.* Materials Today, 2005. **8**(12): p. 36-44.
149. Lake, G. and A. Thomas, *The strength of highly elastic materials.* Proceedings of the Royal Society of London, 1967. **300**(1460): p. 108-119.
150. Yuk, H., et al., *Dry double-sided tape for adhesion of wet tissues and devices.* Nature, 2019. **575**(7781): p. 169-174.
151. Yu, Y., et al., *Multifunctional "hydrogel skins" on diverse polymers with arbitrary shapes.* Advanced Materials, 2019. **31**(7): p. 1807101.
152. Yang, J., R. Bai, and Z. Suo, *Topological adhesion of wet materials.* Advanced Materials, 2018. **30**(25): p. 1800671.
153. Kurokawa, T., et al., *Formation of a strong hydrogel–porous solid interface via the double-network principle.* Acta Biomaterialia, 2010. **6**(4): p. 1353-1359.
154. Rao, P., et al., *Tough hydrogels with fast, strong, and reversible underwater adhesion based on a multiscale design.* Advanced Materials, 2018. **30**(32): p. 1801884.
155. LaPorte, R.J., *Hydrophilic polymer coatings for medical devices*. 2017: Routledge.
156. Yun, S.H. and S.J. Kwok, *Light in diagnosis, therapy and surgery.* Nature Biomedical Engineering
2017. **1**(1): p. 0008.

157. Koretz, J.F. and G.H. Handelman, *How the human eye focuses.* Scientific American, 1988. **259**(1): p. 92-99.
158. Davson, H., *The hydration of the cornea.* Biochemical Journal, 1955. **59**(1): p. 24.
159. Fisher, R. and B.E. Pettet, *Presbyopia and the water content of the human crystalline lens.* The Journal of Physiology, 1973. **234**(2): p. 443-447.
160. Keiser, G., *Optical fiber communications*. Wiley Encyclopedia of Telecommunications. 2003.
161. Blout, E.R., M. Fields, and R. Karplus, *Absorption spectra. VI. The infrared spectra of certain compounds containing conjugated double bonds.* Journal of the American Chemical Society, 1948. **70**(1): p. 194-198.
162. Lü, C. and B. Yang, *High refractive index organic–inorganic nanocomposites: design, synthesis and application.* Journal of Materials Chemistry, 2009. **19**(19): p. 2884-2901.
163. de Groot, J.H., et al., *Injectable intraocular lens materials based upon hydrogels.* Biomacromolecules, 2001. **2**(3): p. 628-634.
164. Nichols, J.J. and D.A. Berntsen, *The assessment of automated measures of hydrogel contact lens refractive index.* Ophthalmic and Physiological Optics, 2003. **23**(6): p. 517-525.
165. Lira, M., et al., *The effect of lens wear on refractive index of conventional hydrogel and silicone-hydrogel contact lenses: A comparative study.* Contact Lens and Anterior Eye, 2008. **31**(2): p. 89-94.
166. Kaynak Onurdağ, F., et al., *Candida albicans and Pseudomonas aeruginosa adhesion on soft contact lenses.* Graefe's Archive for Clinical and Experimental Ophthalmology, 2011. **249**(4): p. 559-564.
167. Zhang, Q., et al., *High refractive index inorganic–organic interpenetrating polymer network (IPN) hydrogel nanocomposite toward artificial cornea implants.* ACS Macro Letters, 2012. **1**(7): p. 876-881.
168. Lee, Y., et al., *Transparent and attachable ionic communicators based on self-cleanable triboelectric nanogenerators.* Nature Communications, 2018. **9**(1): p. 1804.
169. Choi, M., et al., *Step-index optical fiber made of biocompatible hydrogels.* Advanced Materials, 2015. **27**(27): p. 4081-4086.
170. Chung, K., et al., *Structural and molecular interrogation of intact biological systems.* Nature, 2013. **497**: p. 332.
171. Ku, T., et al., *Multiplexed and scalable super-resolution imaging of three-dimensional protein localization in size-adjustable tissues.* Nature Biotechnology, 2016. **34**: p. 973.
172. Schägger, H. and G. von Jagow, *Tricine-sodium dodecyl sulfate-polyacrylamide gel electrophoresis for the separation of proteins in the range from 1 to 100 kDa.* Analytical Biochemistry, 1987. **166**(2): p. 368-379.
173. Laurell, C.-B., *Quantitative estimation of proteins by electrophoresis in agarose gel containing antibodies.* Analytical Biochemistry, 1966. **15**(1): p. 45-52.
174. Karlgard, C., et al., *In vitro uptake and release studies of ocular pharmaceutical agents by silicon-containing and p-HEMA hydrogel contact lens materials.* International Journal of Pharmaceutics, 2003. **257**(1-2): p. 141-151.
175. Liu, Z., et al., *Retinal-detachment repair and vitreous-like-body reformation via a thermogelling polymer endotamponade.* Nature Biomedical Engineering, 2019.
176. Hayashi, K., et al., *Fast-forming hydrogel with ultralow polymeric content as an artificial vitreous body.* Nature Biomedical Engineering, 2017. **1**(3): p. 0044.

177. Nicolson, P.C. and J. Vogt, *Soft contact lens polymers: an evolution.* Biomaterials, 2001. **22**(24): p. 3273-3283.
178. Myung, D., et al., *Development of hydrogel-based keratoprostheses: A materials perspective.* Biotechnology Progress, 2008. **24**(3): p. 735-741.
179. Reinhardt, H.M., et al., *High refractive index TiO2-PHEMA hydrogel for ophthalmological applications.* Journal of Materials Science, 2016. **51**(22): p. 9971-9978.
180. Apte, J. and D. Arasteh, *Window-related energy consumption in the US residential and commercial building stock.* 2008.
181. Gao, Y., et al., *Nanoceramic VO2 thermochromic smart glass: A review on progress in solution processing.* Nano Energy, 2012. **1**(2): p. 221-246.
182. La, T.-G., et al., *Highly flexible, multipixelated thermosensitive smart windows made of tough hydrogels.* ACS Applied Materials & Interfaces, 2017. **9**(38): p. 33100-33106.
183. Yang, C.H., et al., *Electroluminescence of giant stretchability.* Advanced Materials, 2016. **28**(22): p. 4480-4484.
184. Lacour, S.P., G. Courtine, and J. Guck, *Materials and technologies for soft implantable neuroprostheses.* Nature Reviews Materials, 2016. **1**(10): p. 16063.
185. Sheng, H., et al., *Neural interfaces by hydrogels.* Extreme Mechanics Letters, 2019. **30**: p. 100510.
186. Wang, L., et al., *Ultrasoft and highly stretchable hydrogel optical fibers for in vivo optogenetic modulations.* Advanced Optical Materials, 2018. **6**(16): p. 1800427.
187. Caló, E. and V.V. Khutoryanskiy, *Biomedical applications of hydrogels: A review of patents and commercial products.* European Polymer Journal, 2015. **65**: p. 252-267.
188. Kim, H.N. and S. Yang, *Responsive smart windows from nanoparticle–polymer composites.* Advanced Functional Materials, 2019: p. 1902597.
189. Ke, Y., et al., *Smart windows: Electro-, thermo-, mechano-, photochromics, and beyond.* Advanced Energy Materials, 2019: p. 1902066.
190. Kuzyk, M.G., *Polymer Fiber Optics: materials, physics, and applications*. 2018: CRC press.
191. Richardson, D.S. and J.W. Lichtman, *Clarifying tissue clearing.* Cell, 2015. **162**(2): p. 246-257.
192. Ranck Jr, J.B., *Which elements are excited in electrical stimulation of mammalian central nervous system: a review.* Brain Research, 1975. **98**(3): p. 417-440.
193. Gong, J., et al., *Electrical conductance of polyelectrolyte gels.* The Journal of Physical Chemistry B, 1997. **101**(5): p. 740-745.
194. Li, H., et al., *Ionic conductivity in polyelectrolyte hydrogels.* Macromolecules, 2016. **49**(23): p. 9239-9246.
195. Sun, J.Y., et al., *Ionic skin.* Advanced Materials, 2014. **26**(45): p. 7608-7614.
196. Sarwar, M.S., et al., *Bend, stretch, and touch: Locating a finger on an actively deformed transparent sensor array.* Science Advances, 2017. **3**(3): p. e1602200.
197. Schroeder, T.B.H., et al., *An electric-eel-inspired soft power source from stacked hydrogels.* Nature, 2017. **552**: p. 214.
198. Pu, X., et al., *Ultrastretchable, transparent triboelectric nanogenerator as electronic skin for biomechanical energy harvesting and tactile sensing.* Science Advances, 2017. **3**(5): p. e1700015.
199. Dvir, T., et al., *Nanowired three-dimensional cardiac patches.* Nature Nanotechnology, 2011. **6**: p. 720.

200. Shin, S.R., et al., *Carbon-nanotube-embedded hydrogel sheets for engineering cardiac constructs and bioactuators.* ACS Nano, 2013. **7**(3): p. 2369-2380.
201. Jo, H., et al., *Electrically conductive graphene/polyacrylamide hydrogels produced by mild chemical reduction for enhanced myoblast growth and differentiation.* Acta Biomaterialia, 2017. **48**: p. 100-109.
202. Xu, Y., et al., *Self-assembled graphene hydrogel via a one-step hydrothermal process.* ACS Nano, 2010. **4**(7): p. 4324-4330.
203. Liu, Y., et al., *Soft and elastic hydrogel-based microelectronics for localized low-voltage neuromodulation.* Nature Biomedical Engineering, 2019. **3**(1): p. 58-68.
204. Lu, B., et al., *Pure PEDOT:PSS hydrogels.* Nature Communications, 2019. **10**(1): p. 1043.
205. Shi, Y., et al., *Conductive "smart" hybrid hydrogels with pnipam and nanostructured conductive polymers.* Advanced Functional Materials, 2015. **25**(8): p. 1219-1225.
206. Feig, V.R., et al., *Mechanically tunable conductive interpenetrating network hydrogels that mimic the elastic moduli of biological tissue.* Nature Communications, 2018. **9**(1): p. 2740.
207. Pan, L., et al., *Hierarchical nanostructured conducting polymer hydrogel with high electrochemical activity.* Proceedings of the National Academy of Sciences, 2012. **109**(24): p. 9287-9292.
208. Stejskal, J., et al., *Solid-state protonation and electrical conductivity of polyaniline.* Macromolecules, 1998. **31**(7): p. 2218-2222.
209. Cayre, O.J., S.T. Chang, and O.D. Velev, *Polyelectrolyte diode: nonlinear current response of a junction between aqueous ionic gels.* Journal of the American Chemical Society, 2007. **129**(35): p. 10801-10806.
210. Koo, H.J., et al., *Towards all-soft matter circuits: prototypes of quasi-liquid devices with memristor characteristics.* Advanced Materials, 2011. **23**(31): p. 3559-3564.
211. Koo, H.-J., et al., *Aqueous soft matter based photovoltaic devices.* Journal of Materials Chemistry, 2011. **21**(1): p. 72-79.
212. Jing, X., et al., *Stretchable gelatin/silver nanowires composite hydrogels for detecting human motion.* Materials Letters, 2019. **237**: p. 53-56.
213. Mottet, L., et al., *A conductive hydrogel based on alginate and carbon nanotubes for probing microbial electroactivity.* Soft Matter, 2018. **14**(8): p. 1434-1441.
214. Peng, H., et al., *Ultra-stretchable hydrogels with reactive liquid metals as asymmetric force-sensors.* Materials Horizons, 2019. **6**(3): p. 618-625.
215. Lin, S., et al., *Stretchable hydrogel electronics and devices.* Advanced Materials, 2016. **28**(22): p. 4497-4505.
216. Han, L., et al., *A mussel-inspired conductive, self-adhesive, and self-healable tough hydrogel as cell stimulators and implantable bioelectronics.* Small, 2017. **13**(2): p. 1601916.
217. Gangopadhyay, R. and A. De, *Conducting polymer nanocomposites: a brief overview.* Chemistry of Materials, 2000. **12**(3): p. 608-622.
218. Zhao, F., et al., *Multifunctional nanostructured conductive polymer gels: synthesis, properties, and applications.* Accounts of Chemical Research, 2017. **50**(7): p. 1734-1743.
219. Gaharwar, A.K., N.A. Peppas, and A. Khademhosseini, *Nanocomposite hydrogels for biomedical applications.* Biotechnology and Bioengineering, 2014. **111**(3): p. 441-453.
220. Leaf, M.A. and M. Muthukumar, *Electrostatic effect on the solution structure and dynamics of pedot:pss.* Macromolecules, 2016. **49**(11): p. 4286-4294.

221. Yao, B., et al., *Ultrahigh-conductivity polymer hydrogels with arbitrary structures.* Advanced Materials, 2017. **29**(28): p. 1700974.
222. Wang, Y., et al., *A highly stretchable, transparent, and conductive polymer.* Science Advances, 2017. **3**(3): p. e1602076.
223. Wei, Q., et al., *Morphological change and mobility enhancement in PEDOT:PSS by adding co-solvents.* Advanced Materials, 2013. **25**(20): p. 2831-2836.
224. Thomas, J.P., et al., *High-efficiency hybrid solar cells by nanostructural modification in PEDOT:PSS with co-solvent addition.* Journal of Materials Chemistry A, 2014. **2**(7): p. 2383-2389.
225. Koo, H.-J. and O.D. Velev, *Ionic current devices—recent progress in the merging of electronic, microfluidic, and biomimetic structures.* Biomicrofluidics, 2013. **7**(3): p. 031501.
226. Guo, Y., et al., *Functional hydrogels for next-generation batteries and supercapacitors.* Trends in Chemistry, 2019.
227. Moss, B.R., *Ecology of fresh waters: man and medium, past to future*. 2009: John Wiley & Sons.
228. Gupta, V.K., et al., *Chemical treatment technologies for waste-water recycling—an overview.* RSC Advances, 2012. **2**(16): p. 6380-6388.
229. Cui, W., et al., *Robust dual physically cross-linked hydrogels with unique self-reinforcing behavior and improved dye adsorption capacity.* RSC Advances, 2015. **5**(65): p. 52966-52977.
230. Ji, X., et al., *Physical removal of anions from aqueous media by means of a macrocycle-containing polymeric network.* Journal of the American Chemical Society, 2018. **140**(8): p. 2777-2780.
231. Lone, S., et al., *Gelatin–chitosan hydrogel particles for efficient removal of Hg (II) from wastewater.* Environmental Science: Water Research & Technology, 2019. **5**(1): p. 83-90.
232. Ma, J., et al., *Efficient removal of heavy metal ions with an EDTA functionalized chitosan/polyacrylamide double network hydrogel.* ACS Sustainable Chemistry & Engineering, 2017. **5**(1): p. 843-851.
233. Li, D., et al., *Stimuli-responsive polymer hydrogels as a new class of draw agent for forward osmosis desalination.* Chemical Communications, 2011. **47**(6): p. 1710-1712.
234. Li, D., et al., *Forward osmosis desalination using polymer hydrogels as a draw agent: Influence of draw agent, feed solution and membrane on process performance.* Water Research, 2013. **47**(1): p. 209-215.
235. Ali, W., et al., *On the potential of using dual-function hydrogels for brackish water desalination.* Polymers, 2018. **10**(6).
236. Zhou, X., et al., *A hydrogel-based antifouling solar evaporator for highly efficient water desalination.* Energy & Environmental Science, 2018. **11**(8): p. 1985-1992.
237. Zhao, F., et al., *Highly efficient solar vapour generation via hierarchically nanostructured gels.* Nature Nanotechnology, 2018. **13**(6): p. 489-495.
238. Kallenberger, P.A. and M. Fröba, *Water harvesting from air with a hygroscopic salt in a hydrogel–derived matrix.* Communications Chemistry, 2018. **1**(1): p. 28.
239. Li, R., et al., *Hybrid hydrogel with high water vapor harvesting capacity for deployable solar-driven atmospheric water generator.* Environmental Science & Technology, 2018. **52**(19): p. 11367-11377.

240. Matsumoto, K., N. Sakikawa, and T. Miyata, *Thermo-responsive gels that absorb moisture and ooze water.* Nature Communications, 2018. **9**(1): p. 2315.
241. Zhao, F., et al., *Super moisture-absorbent gels for all-weather atmospheric water harvesting.* Advanced Materials, 2019. **31**(10): p. 1806446.
242. Ahuja, S., *Handbook of water purity and quality*. 2009: Academic press.
243. Jing, G., et al., *Recent progress on study of hybrid hydrogels for water treatment.* Colloids and Surfaces A, 2013. **416**: p. 86-94.
244. Barakat, M., *New trends in removing heavy metals from industrial wastewater.* Arabian Journal of Chemistry, 2011. **4**(4): p. 361-377.
245. Yamashita, K., T. Nishimura, and M. Nango, *Preparation of IPN-type stimuli-responsive heavy-metal-ion adsorbent gel.* Polymers for Advanced Technologies, 2003. **14**(3-5): p. 189-194.
246. Zheng, Y. and A. Wang, *Nitrate adsorption using poly (dimethyl diallyl ammonium chloride)/polyacrylamide hydrogel.* Journal of Chemical & Engineering Data, 2010. **55**(9): p. 3494-3500.
247. Ma, J., et al., *Water-enhanced removal of ciprofloxacin from water by porous graphene hydrogel.* Scientific Reports
2015. **5**: p. 13578.
248. Vivek, B. and E. Prasad, *Reusable self-healing hydrogels realized via in situ polymerization.* The Journal of Physical Chemistry B, 2015. **119**(14): p. 4881-4887.
249. Van Tran, V., D. Park, and Y.-C. Lee, *Hydrogel applications for adsorption of contaminants in water and wastewater treatment.* Environmental Science and Pollution Research, 2018. **25**(25): p. 24569-24599.
250. Pakdel, P.M. and S.J. Peighambardoust, *A review on acrylic based hydrogels and their applications in wastewater treatment.* Journal of Environmental Management, 2018. **217**: p. 123-143.
251. Pakdel, P.M. and S.J. Peighambardoust, *Review on recent progress in chitosan-based hydrogels for wastewater treatment application.* Carbohydrate Polymers, 2018. **201**: p. 264-279.
252. Li, D., et al., *Composite polymer hydrogels as draw agents in forward osmosis and solar dewatering.* Soft Matter, 2011. **7**(21): p. 10048-10056.
253. Razmjou, A., et al., *Fast deswelling of nanocomposite polymer hydrogels via magnetic field-induced heating for emerging FO desalination.* Environmental Science & Technology, 2013. **47**(12): p. 6297-6305.
254. Fan, X., et al., *Forward-osmosis desalination with poly (ionic liquid) hydrogels as smart draw agents.* Advanced Materials, 2016. **28**(21): p. 4156-4161.
255. Li, D. and H. Wang, *Smart draw agents for emerging forward osmosis application.* Journal of Materials Chemistry A, 2013. **1**(45): p. 14049-14060.
256. Cai, Y., *A critical review on draw solutes development for forward osmosis.* Desalination, 2016. **391**: p. 16-29.
257. Zhou, X., et al., *Architecting highly hydratable polymer networks to tune the water state for solar water purification.* Science Advances, 2019. **5**(6): p. eaaw5484.
258. Guo, Y., et al., *Synergistic energy nanoconfinement and water activation in hydrogels for efficient solar water desalination.* ACS Nano, 2019. **13**(7): p. 7913-7919.
259. Guo, Y., et al., *Tailoring nanoscale surface topography of hydrogel for efficient solar vapor generation.* Nano Letters, 2019. **19**(4): p. 2530-2536.

260. Mauer, L.J. and L.S. Taylor, *Water-solids interactions: deliquescence.* Annual Review Of Food Science And Technology, 2010. **1**: p. 41-63.
261. Kim, H., et al., *Water harvesting from air with metal-organic frameworks powered by natural sunlight.* Science, 2017. **356**(6336): p. 430-434.
262. Kim, H., et al., *Adsorption-based atmospheric water harvesting device for arid climates.* Nature Communications, 2018. **9**(1): p. 1191.
263. Rotzetter, A., et al., *Thermoresponsive polymer induced sweating surfaces as an efficient way to passively cool buildings.* Advanced Materials, 2012. **24**(39): p. 5352-5356.
264. Li, R., et al., *Harvesting water from air: using anhydrous salt with sunlight.* Environmental Science & Technology, 2018. **52**(9): p. 5398-5406.
265. Hall, B.K., *Cartilage V1: structure, function, and biochemistry*. 2012, Cambridge: Academic Press.
266. Taylor, D., et al., *The fracture toughness of soft tissues.* Journal of the Mechanical Behavior of Biomedical Materials, 2012. **6**: p. 139-147.
267. Tavichakorntrakool, R., et al., *K+, Na+, Mg2+, Ca2+, and water contents in human skeletal muscle: correlations among these monovalent and divalent cations and their alterations in K+-depleted subjects.* Translational Research, 2007. **150**(6): p. 357-366.
268. Johnson, G.A., et al., *Tensile and viscoelastic properties of human patellar tendon.* Journal of Orthopaedic Research, 1994. **12**(6): p. 796-803.
269. Connizzo, B.K., S.M. Yannascoli, and L.J. Soslowsky, *Structure–function relationships of postnatal tendon development: a parallel to healing.* Matrix Biology, 2013. **32**(2): p. 106-116.
270. Fratzl, P., *Collagen: structure and mechanics, an introduction*, in *Collagen*. 2008, Springer: New York. p. 1-13.
271. Lee, J.M., D.W. Courtman, and D.R. Boughner, *The glutaraldehyde-stabilized porcine aortic valve xenograft. I. Tensile viscoelastic properties of the fresh leaflet material.* Journal of Biomedical Materials Research A, 1984. **18**(1): p. 61-77.
272. Lee, J.M., D.R. Boughner, and D.W. Courtman, *The glutaraldehyde-stabilized porcine aortic valve xenograft. II. Effect of fixation with or without pressure on the tensile viscoelastic properties of the leaflet material.* Journal of Biomedical Materials Research A, 1984. **18**(1): p. 79-98.
273. Driessen, N.J., C.V. Bouten, and F.P. Baaijens, *Improved prediction of the collagen fiber architecture in the aortic heart valve.* Journal of Biomechanical Engineering, 2005.
274. Peppas, N.A., et al., *Hydrogels in pharmaceutical formulations.* European Journal of Pharmaceutics and Biopharmaceutics, 2000. **50**(1): p. 27-46.
275. Peppas, N.A., et al., *Hydrogels in biology and medicine: from molecular principles to bionanotechnology.* Advanced Materials, 2006. **18**(11): p. 1345-1360.
276. Nguyen, K.T. and J.L. West, *Photopolymerizable hydrogels for tissue engineering applications.* Biomaterials, 2002. **23**(22): p. 4307-4314.
277. Drury, J.L. and D.J. Mooney, *Hydrogels for tissue engineering: scaffold design variables and applications.* Biomaterials, 2003. **24**(24): p. 4337-4351.
278. Kopecek, J., *Hydrogels: From soft contact lenses and implants to self-assembled nanomaterials.* Journal of Polymer Science A, 2009. **47**(22): p. 5929-5946.
279. Jones, A. and D. Vaughan, *Hydrogel dressings in the management of a variety of wound types: A review.* Journal of Orthopaedic Nursing, 2005. **9**: p. S1-S11.

280. Boateng, J.S., et al., *Wound healing dressings and drug delivery systems: a review.* Journal of Pharmaceutical Sciences, 2008. **97**(8): p. 2892-2923.
281. Kamoun, E.A., E.-R.S. Kenawy, and X. Chen, *A review on polymeric hydrogel membranes for wound dressing applications: PVA-based hydrogel dressings.* Journal of Advanced Research, 2017. **8**(3): p. 217-233.
282. Vanderlaan, D.G., et al., *Soft contact lenses*. 2005: Washington, DC.
283. Liu, X., et al., *Hydrogel machines.* Materials Today, 2020.
284. Li, J., et al., *Tough adhesives for diverse wet surfaces.* Science, 2017. **357**(6349): p. 378-381.
285. Cheng, H., et al., *Mussel-inspired multifunctional hydrogel coating for prevention of infections and enhanced osteogenesis.* ACS Applied Materials & Interfaces, 2017. **9**(13): p. 11428-11439.
286. Weightman, B., M. Freeman, and S. Swanson, *Fatigue of articular cartilage.* Nature, 1973. **244**(5414): p. 303-304.
287. Hansson, T., T. Keller, and D. Spengler, *Mechanical behavior of the human lumbar spine. II. Fatigue strength during dynamic compressive loading.* Journal of Orthopaedic Research, 1987. **5**(4): p. 479-487.
288. Lin, S., et al., *Muscle-like fatigue-resistant hydrogels by mechanical training.* Proceedings of the National Academy of Sciences, 2019. **116**(21): p. 10244-10249.
289. Sun, T.L., et al., *Physical hydrogels composed of polyampholytes demonstrate high toughness and viscoelasticity.* Nature Materials, 2013. **12**(10): p. 932.
290. Chen, Q., et al., *A robust, one-pot synthesis of highly mechanical and recoverable double network hydrogels using thermoreversible sol-gel polysaccharide.* Advanced Materials, 2013. **25**(30): p. 4171-4176.
291. Chen, H., et al., *A novel design of multi-mechanoresponsive and mechanically strong hydrogels.* Advanced Materials, 2017. **29**(21): p. 1606900.
292. Gong, J.P., *Why are double network hydrogels so tough?* Soft Matter, 2010. **6**(12): p. 2583-2590.
293. Bai, R., et al., *Fatigue fracture of tough hydrogels.* Extreme Mechanics Letters, 2017. **15**: p. 91-96.
294. Bai, R., et al., *Fatigue fracture of self-recovery hydrogels.* ACS Macro Letters, 2018. **7**(3): p. 312-317.
295. Zhang, W., et al., *Fatigue of double-network hydrogels.* Engineering Fracture Mechanics, 2018. **187**: p. 74-93.
296. Creton, C. and M. Ciccotti, *Fracture and adhesion of soft materials: a review.* Reports on Progress in Physics, 2016. **79**(4): p. 046601.
297. Long, R. and C.-Y. Hui, *Fracture toughness of hydrogels: measurement and interpretation.* Soft Matter, 2016. **12**(39): p. 8069-8086.
298. Rice, J.R. and R. Thomson, *Ductile versus brittle behaviour of crystals.* Philosophical Magazine, 1974. **29**(1): p. 73-97.
299. McMeeking, R. and A. Evans, *Mechanics of transformation-toughening in brittle materials.* Journal of the American Chemical Society, 1982. **65**(5): p. 242-246.
300. Mallick, P.K., *Fiber-reinforced composites: materials, manufacturing, and design*. 2007, Boca Raton: CRC Press.
301. Argon, A.S., *The physics of deformation and fracture of polymers*. 2013, Cambridge: Cambridge University Press.

302. Fung, Y.-c., *Biomechanics: mechanical properties of living tissues*. 2013, New York: Springer.
303. Suresh, S., *Fatigue of materials*. 1998, Cambridge: Cambridge University Press.
304. Bai, R., et al., *Flaw-insensitive hydrogels under static and cyclic loads.* Macromolecular Rapid Communications, 2019. **40**(8): p. 1800883.
305. Baker, M.I., et al., *A review of polyvinyl alcohol and its uses in cartilage and orthopedic applications.* Journal of Biomedical Materials Research B, 2012. **100**(5): p. 1451-1457.
306. Lake, G. and P. Lindley, *The mechanical fatigue limit for rubber.* Journal of Applied Polymer Science, 1965. **9**(4): p. 1233-1251.
307. Li, X., et al., *Mesoscale bicontinuous networks in self-healing hydrogels delay fatigue fracture.* Proceedings of the National Academy of Sciences, 2020. **117**(14): p. 7606-7612.
308. Xiang, C., et al., *Stretchable and fatigue-resistant materials.* Materials Today, 2019.
309. Wang, Z., et al., *Stretchable materials of high toughness and low hysteresis.* Proceedings of the National Academy of Sciences, 2019. **116**(13): p. 5967-5972.
310. Liu, J., et al., *Fatigue-resistant adhesion of hydrogels.* Nature Communications, 2020. **11**(1): p. 1071.
311. Ni, J., et al., *Strong fatigue-resistant nanofibrous hydrogels inspired by lobster underbelly.* Matter, 2020.
312. Figueiredo, K.C., T.L. Alves, and C.P. Borges, *Poly (vinyl alcohol) films crosslinked by glutaraldehyde under mild conditions.* Journal of Applied Polymer Science, 2009. **111**(6): p. 3074-3080.
313. Peppas, N.A. and E.W. Merrill, *Differential scanning calorimetry of crystallized PVA hydrogels.* Journal of Applied Polymer Science, 1976. **20**(6): p. 1457-1465.
314. Chang, J.Y., et al., *Biopolymers· PVA hydrogels anionic polymerisation nanocomposites*. Vol. 153. 2000: Springer Science & Business Media.
315. Hassan, C.M. and N.A. Peppas, *Structure and morphology of freeze/thawed PVA hydrogels.* Macromolecules, 2000. **33**(7): p. 2472-2479.
316. Zhang, R., et al., *Stretch-induced complexation reaction between poly (vinyl alcohol) and iodine: an in situ synchrotron radiation small-and wide-angle X-ray scattering study.* Soft Matter, 2018. **14**(13): p. 2535-2546.
317. Ricciardi, R., et al., *X-ray diffraction analysis of poly (vinyl alcohol) hydrogels, obtained by freezing and thawing techniques.* Macromolecules, 2004. **37**(5): p. 1921-1927.
318. Patterson, A., *The Scherrer formula for X-ray particle size determination.* Physical Review, 1939. **56**(10): p. 978.
319. Otsuka, E., et al., *Effects of preparation temperature on swelling and mechanical properties of PVA cast gels.* Soft Matter, 2012. **8**(31): p. 8129-8136.
320. Lake, G. and P. Lindley, *Cut growth and fatigue of rubbers. II. Experiments on a noncrystallizing rubber.* Journal of Applied Polymer Science, 1964. **8**(2): p. 707-721.
321. Gent, A., P. Lindley, and A. Thomas, *Cut growth and fatigue of rubbers. I. The relationship between cut growth and fatigue.* Journal of Applied Polymer Science, 1964. **8**(1): p. 455-466.
322. Liff, S.M., N. Kumar, and G.H. McKinley, *High-performance elastomeric nanocomposites via solvent-exchange processing.* Nature Materials, 2007. **6**(1): p. 76.
323. Fergg, F., F. Keil, and H. Quader, *Investigations of the microscopic structure of poly(vinyl alcohol) hydrogels by confocal laser scanning microscopy.* Colloid and Polymer Science, 2001. **279**(1): p. 61-67.

324. Sehaqui, H., et al., *Cellulose nanofiber orientation in nanopaper and nanocomposites by cold drawing.* ACS Applied Materials & Interfaces, 2012. **4**(2): p. 1043-1049.
325. Fukumori, T. and T. Nakaoki, *High strength poly (vinyl alcohol) films obtained by drying and then stretching freeze/thaw cycled gel.* Journal of Applied Polymer Science, 2015. **132**(1): p. 41318.
326. Mredha, M.T.I., et al., *A facile method to fabricate anisotropic hydrogels with perfectly aligned hierarchical fibrous structures.* Advanced Materials, 2018. **30**(9): p. 1704937.
327. Zhang, Q., et al., *Stretch-induced structural evolution of poly (vinyl alcohol) film in water at different temperatures: An in-situ synchrotron radiation small-and wide-angle X-ray scattering study.* Polymer, 2018. **142**: p. 233-243.
328. Vatankhah-Varnosfaderani, M., et al., *Chameleon-like elastomers with molecularly encoded strain-adaptive stiffening and coloration.* Science, 2018. **359**(6383): p. 1509-1513.
329. Bai, R., J. Yang, and Z. Suo, *Fatigue of hydrogels.* European Journal of Mechanics A, 2019. **74**: p. 337-370.
330. Haraguchi, K. and T. Takehisa, *Nanocomposite hydrogels: a unique organic–inorganic network structure with extraordinary mechanical, optical, and swelling/de-swelling properties.* Advanced Materials, 2002. **14**(16): p. 1120-1124.
331. Kong, W., et al., *Muscle-inspired highly anisotropic, strong, ion-conductive hydrogels.* Advanced Materials, 2018. **30**(39): p. 1801934.
332. Li, J., Z. Suo, and J.J. Vlassak, *Stiff, strong, and tough hydrogels with good chemical stability.* Journal of Materials Chemistry B, 2014. **2**(39): p. 6708-6713.
333. Lin, S., Y. Zhou, and X. Zhao, *Designing extremely resilient and tough hydrogels via delayed dissipation.* Extreme Mechanics Letters, 2014. **1**: p. 70-75.
334. Stauffer, S.R. and N.A. Peppast, *Poly (vinyl alcohol) hydrogels prepared by freezing-thawing cyclic processing.* Polymer, 1992. **33**(18): p. 3932-3936.
335. Lin, S., et al., *Design of stiff, tough and stretchy hydrogel composites via nanoscale hybrid crosslinking and macroscale fiber reinforcement.* Soft Matter, 2014. **10**(38): p. 7519-7527.
336. Gillies, A.R. and R.L. Lieber, *Structure and function of the skeletal muscle extracellular matrix.* Muscle Nerve, 2011. **44**(3): p. 318-331.
337. Han, W.M., et al., *Microstructural heterogeneity directs micromechanics and mechanobiology in native and engineered fibrocartilage.* Nature Materials, 2016. **15**(4): p. 477-84.
338. Genin, G.M. and S. Thomopoulos, *The tendon-to-bone attachment: Unification through disarray.* Nature Materials, 2017. **16**(6): p. 607-608.
339. Fantner, G.E., et al., *Sacrificial bonds and hidden length dissipate energy as mineralized fibrils separate during bone fracture.* Nature Materials, 2005. **4**(8): p. 612-616.
340. Nair, A.K., et al., *Molecular mechanics of mineralized collagen fibrils in bone.* Nature Communications, 2013. **4**.
341. Rossetti, L., et al., *The microstructure and micromechanics of the tendon-bone insertion.* Nature Materials, 2017. **16**(6): p. 664-670.
342. Gao, H.J., et al., *Materials become insensitive to flaws at nanoscale: Lessons from nature.* Proceedings of the National Academy of Sciences, 2003. **100**(10): p. 5597-5600.
343. Moretti, M., et al., *Structural characterization and reliable biomechanical assessment of integrative cartilage repair.* Journal of Biomechanics, 2005. **38**(9): p. 1846-1854.

344. Bobyn, J.D., et al., *Effect of pore size on the peel strength of attachment of fibrous tissue to porous-surfaced implants.* Journal of Biomedical Materials Research, 1982. **16**(5): p. 571-84.
345. Sidorenko, A., et al., *Reversible switching of hydrogel-actuated nanostructures into complex micropatterns.* Science, 2007. **315**(5811): p. 487-490.
346. Banerjee, I., R.C. Pangule, and R.S. Kane, *Antifouling coatings: recent developments in the design of surfaces that prevent fouling by proteins, bacteria, and marine organisms.* Advanced Materials, 2011. **23**(6): p. 690-718.
347. Yu, C., et al., *Electronically programmable, reversible shape change in two-and three-dimensional hydrogel structures.* Advanced Materials, 2013. **25**(11): p. 1541-1546.
348. Kamata, H., et al., *"Nonswellable" hydrogel without mechanical hysteresis.* Science, 2014. **343**(6173): p. 873-875.
349. Gent, A., *Adhesion and strength of viscoelastic solids. Is there a relationship between adhesion and bulk properties?* Langmuir, 1996. **12**(19): p. 4492-4496.
350. Ahagon, A. and A. Gent, *Effect of interfacial bonding on the strength of adhesion.* Journal of Polymer Science B, 1975. **13**(7): p. 1285-1300.
351. Sudre, G., et al., *Reversible adhesion between a hydrogel and a polymer brush.* Soft Matter, 2012. **8**(31): p. 8184-8193.
352. Ni, X., C. Chen, and J. Li, *Interfacial fatigue fracture of tissue adhesive hydrogels.* Extreme Mechanics Letters, 2020. **34**: p. 100601.
353. Hassan, C.M. and N.A. Peppas, *Structure and applications of poly (vinyl alcohol) hydrogels produced by conventional crosslinking or by freezing/thawing methods*, in *Biopolymers· PVA Hydrogels, Anionic Polymerisation Nanocomposites*. 2000, Springer. p. 37-65.
354. Volinsky, A., N. Moody, and W.W. Gerberich, *Interfacial toughness measurements for thin films on substrates.* Acta Materialia, 2002. **50**(3): p. 441-466.
355. Rose, S., et al., *Nanoparticle solutions as adhesives for gels and biological tissues.* Nature, 2014. **505**(7483): p. 382-385.
356. Zhang, T., et al., *Tough and tunable adhesion of hydrogels: experiments and models.* Acta Mechanica Sinica, 2017. **33**(3): p. 543-554.
357. Lee, H., et al., *Mussel-inspired surface chemistry for multifunctional coatings.* Science, 2007. **318**(5849): p. 426-430.
358. Ghobril, C. and M. Grinstaff, *The chemistry and engineering of polymeric hydrogel adhesives for wound closure: a tutorial.* Chemical Society Reviews, 2015. **44**(7): p. 1820-1835.
359. Pizzi, A. and K.L. Mittal, *Handbook of adhesive technology, revised and expanded*. 2003, Boca Raton: CRC Press.
360. Evans, A.G., J.W. Hutchinson, and Y. Wei, *Interface adhesion: effects of plasticity and segregation.* Acta Materialia, 1999. **47**(15): p. 4093-4113.
361. Raphael, E. and P. De Gennes, *Rubber-rubber adhesion with connector molecules.* The Journal of Physical Chemistry, 1992. **96**(10): p. 4002-4007.
362. Gent, A. and R. Petrich, *Adhesion of viscoelastic materials to rigid substrates.* Proceedings of the Royal Society of London, 1969. **310**(1502): p. 433-448.
363. Baumard, T., A. Thomas, and J. Busfield, *Fatigue peeling at rubber interfaces.* Plastics, Rubber and Composites, 2012. **41**(7): p. 296-300.

364. Zhang, W., et al., *Fatigue-resistant adhesion I. Long-chain polymers as elastic dissipaters.* Extreme Mechanics Letters, 2020: p. 100813.
365. Zhang, Y., et al., *A drip-crosslinked tough hydrogel.* Polymer, 2018. **135**: p. 327-330.
366. Lin, S., et al., *Stretchable Anti-Fogging Tapes for Diverse Transparent Materials.* Advanced Functional Materials, 2021. **n/a**(n/a): p. 2103551.
367. Slomovic, S., K. Pardee, and J.J. Collins, *Synthetic biology devices for in vitro and in vivo diagnostics.* Proceedings of the National Academy of Sciences, 2015. **112**(47): p. 14429-35.
368. Pardee, K., et al., *Rapid, low-cost detection of Zika virus using programmable biomolecular components.* Cell, 2016. **165**(5): p. 1255-1266.
369. Pardee, K., et al., *Paper-based synthetic gene networks.* Cell, 2014. **159**(4): p. 940-954.
370. Mimee, M., et al., *Programming a human commensal bacterium, Bacteroides thetaiotaomicron, to sense and respond to stimuli in the murine gut microbiota.* Cell Systems, 2015. **1**(1): p. 62-71.
371. Chen, A.Y., et al., *Synthesis and patterning of tunable multiscale materials with engineered cells.* Nature Materials, 2014. **13**(5): p. 515-523.
372. Din, M.O., et al., *Synchronized cycles of bacterial lysis for in vivo delivery.* Nature, 2016. **536**(7614): p. 81-85.
373. Daniel, R., et al., *Synthetic analog computation in living cells.* Nature, 2013. **497**(7451): p. 619-623.
374. Friedland, A.E., et al., *Synthetic gene networks that count.* Science, 2009. **324**(5931): p. 1199-1202.
375. Roquet, N., et al., *Synthetic recombinase-based state machines in living cells.* Science, 2016. **353**(6297): p. aad8559.
376. Siuti, P., J. Yazbek, and T.K. Lu, *Engineering genetic circuits that compute and remember.* Nature Protocol, 2014. **9**: p. 1292-1300.
377. Siuti, P., J. Yazbek, and T.K. Lu, *Synthetic circuits integrating logic and memory in living cells.* Nature Biotechnology, 2013. **31**(5): p. 448-452.
378. Yang, L., et al., *Permanent genetic memory with >1-byte capacity.* Nature Methods, 2014. **11**(12): p. 1261-1266.
379. Stricker, J., et al., *A fast, robust and tunable synthetic gene oscillator.* Nature, 2008. **456**(7221): p. 516-519.
380. Danino, T., et al., *A synchronized quorum of genetic clocks.* Nature, 2010. **463**(7279): p. 326-330.
381. Lu, T.K. and O. Purcell, *Machine life.* Scientific American, 2016. **314**(4): p. 58-63.
382. Cheng, A.A. and T.K. Lu, *Synthetic biology: an emerging engineering discipline.* Annual Review of Biomedical Engineering, 2012. **14**: p. 155-178.
383. Ge, Z., P.R. Girguis, and C.R. Buie, *Nanoporous microscale microbial incubators.* Lab on a Chip, 2016. **16**(3): p. 480-8.
384. Kobayashi, H., et al., *Programmable cells: interfacing natural and engineered gene networks.* Proceedings of the National Academy of Sciences, 2004. **101**(22): p. 8414-8419.
385. Feinberg, A.W., et al., *Muscular thin films for building actuators and powering devices.* Science, 2007. **317**(5843): p. 1366-1370.
386. Lind, J.U., et al., *Instrumented cardiac microphysiological devices via multimaterial three-dimensional printing.* Nature Materials, 2016. **advance online publication**.

387. Nawroth, J.C., et al., *A tissue-engineered jellyfish with biomimetic propulsion.* Nature Biotechnology, 2012. **30**(8): p. 792-797.
388. Park, S.-J., et al., *Phototactic guidance of a tissue-engineered soft-robotic ray.* Science, 2016. **353**(6295): p. 158-162.
389. Gerber, L.C., et al., *Incorporation of penicillin-producing fungi into living materials to provide chemically active and antibiotic-releasing surfaces.* Angewandte Chemie International Edition, 2012. **51**(45): p. 11293-11296.
390. Gerber, L.C., et al., *Incorporating microorganisms into polymer layers provides bioinspired functional living materials.* Proceedings of the National Academy of Sciences, 2012. **109**(1): p. 90-94.
391. Annabi, N., et al., *25th anniversary article: rational design and applications of hydrogels in regenerative medicine.* Advanced Materials, 2014. **26**(1): p. 85-124.
392. Seliktar, D., *Designing cell-compatible hydrogels for biomedical applications.* Science, 2012. **336**(6085): p. 1124-1128.
393. Pei, Z., et al., *Mouldable liquid-crystalline elastomer actuators with exchangeable covalent bonds.* Nature Materials, 2014. **13**(1): p. 36-41.
394. Ding, Z., et al., *Direct 4D printing via active composite materials.* Science Advances, 2017. **3**(4): p. e1602890.
395. Villar, G., A.D. Graham, and H. Bayley, *A tissue-like printed material.* Science, 2013. **340**(6128): p. 48-52.
396. Kolesky, D.B., et al., *Three-dimensional bioprinting of thick vascularized tissues.* Proceedings of the National Academy of Sciences, 2016. **113**(12): p. 3179-3184.
397. Lee, J.N., et al., *Compatibility of mammalian cells on surfaces of poly (dimethylsiloxane).* Langmuir, 2004. **20**(26): p. 11684-11691.
398. Darnell, M.C., et al., *Performance and biocompatibility of extremely tough alginate/polyacrylamide hydrogels.* Biomaterials, 2013. **34**(33): p. 8042-8048.
399. Robb, W.L., *Thin silicone membranes-their permeation properties and some applications.* Annals of the New York Academy of Sciences, 1968. **146**(1): p. 119-137.
400. Huh, D., et al., *Reconstituting organ-level lung functions on a chip.* Science, 2010. **328**(5986): p. 1662-1668.
401. Halldorsson, S., et al., *Advantages and challenges of microfluidic cell culture in polydimethylsiloxane devices.* Biosensors and Bioelectronics, 2015. **63**: p. 218-231.
402. Jang, K.I., et al., *Rugged and breathable forms of stretchable electronics with adherent composite substrates for transcutaneous monitoring.* Nature Communications, 2014. **5**: p. 4779.
403. He, Q., et al., *Polymer nanofiber reinforced double network gel composite: Strong, tough and transparent.* Extreme Mechanics Letters, 2016. **9**: p. 165-170.
404. Liao, I.C., et al., *Composite three-dimensional woven scaffolds with interpenetrating network hydrogels to create functional synthetic articular cartilage.* Advanced Functional Materials, 2013. **23**(47): p. 5833-5839.
405. Tamsir, A., J.J. Tabor, and C.A. Voigt, *Robust multicellular computing using genetically encoded NOR gates and chemical 'wires'.* Nature, 2011. **469**(7329): p. 212-215.
406. Bennett, M.R. and J. Hasty, *Microfluidic devices for measuring gene network dynamics in single cells.* Nature Reviews Genetics, 2009. **10**(9): p. 628-638.
407. Duncombe, T.A., A.M. Tentori, and A.E. Herr, *Microfluidics: reframing biological enquiry.* Nature Reviews Molecular Cell Biology, 2015. **16**(9): p. 554-567.

408. Khalil, A.S. and J.J. Collins, *Synthetic biology: applications come of age.* Nature Reviews Genetics, 2010. **11**(5): p. 367-379.
409. Perez-Pinera, P., et al., *Synthetic biology and microbioreactor platforms for programmable production of biologics at the point-of-care.* Nature Communications, 2016. **7**.
410. Chen, Y., et al., *Emergent genetic oscillations in a synthetic microbial consortium.* Science, 2015. **349**(6251): p. 986-989.
411. Dilanji, G.E., et al., *Quorum activation at a distance: spatiotemporal patterns of gene regulation from diffusion of an autoinducer signal.* Journal of the American Chemical Society, 2012. **134**(12): p. 5618-5626.
412. Karzbrun, E., et al., *Programmable on-chip DNA compartments as artificial cells.* Science, 2014. **345**(6198): p. 829-832.
413. Kolesky, D.B., et al., *3D bioprinting of vascularized, heterogeneous cell-laden tissue constructs.* Advanced Materials, 2014. **26**(19): p. 3124-3130.
414. Zhao, X., *Designing toughness and strength for soft materials.* Proceedings of the National Academy of Sciences, 2017. **114**(31): p. 8138-8140.
415. Mironi-Harpaz, I., et al., *Photopolymerization of cell-encapsulating hydrogels: crosslinking efficiency versus cytotoxicity.* Acta Biomaterialia, 2012. **8**(5): p. 1838-1848.
416. Truby, R.L. and J.A. Lewis, *Printing soft matter in three dimensions.* Nature, 2016. **540**(7633): p. 371-378.
417. Xie, Z., et al., *Multi-input RNAi-based logic circuit for identification of specific cancer cells.* Science, 2011. **333**(6047): p. 1307-1311.
418. Komatsu, H., et al., *Supramolecular hydrogel exhibiting four basic logic gate functions to fine-tune substance release.* Journal of the American Chemical Society, 2009. **131**(15): p. 5580-5585.
419. Ikeda, M., et al., *Installing logic-gate responses to a variety of biological substances in supramolecular hydrogel–enzyme hybrids.* Nature Chemistry, 2014. **6**(6): p. 511-518.
420. Kim, D.-H., et al., *Epidermal electronics.* Science, 2011. **333**(6044): p. 838-843.
421. Parada, G.A., et al., *Impermeable robust hydrogels via hybrid lamination.* Advanced Healthcare Materials, 2017.
422. Wessel, A.K., et al., *Going local: technologies for exploring bacterial microenvironments.* Nature Reviews Microbiology, 2013. **11**(5): p. 337-348.
423. Lide, D.R., *CRC handbook of chemistry and physics*. Vol. 85. 2004: CRC press.
424. Leveau, J.H. and S.E. Lindow, *Predictive and interpretive simulation of green fluorescent protein expression in reporter bacteria.* Journal of Bacteriology, 2001. **183**(23): p. 6752-6762.
425. Rogers, J.K., et al., *Synthetic biosensors for precise gene control and real-time monitoring of metabolites.* Nucleic Acids Research, 2015. **43**(15): p. 7648-60.
426. Dreisigmeyer, D.W., et al., *Determinants of bistability in induction of the Escherichia coli lac operon.* IET Systems Biology, 2008. **2**(5): p. 293-303.
427. Kuhlman, T., et al., *Combinatorial transcriptional control of the lactose operon of Escherichia coli.* Proceedings of the National Academy of Sciences, 2007. **104**(14): p. 6043-6048.
428. Socolofsky, S.A. and G.H. Jirka, *Environmental fluid mechanics Part I: Mass transfer and diffusion*, in *Class notes*. 2002.
429. Heim, R., A.B. Cubitt, and R.Y. Tsien, *Improved green fluorescence.* Nature, 1995. **373**(6516): p. 663-664.

430. Cubitt, A.B., et al., *Understanding, improving and using green fluorescent proteins.* Trends In Biochemical Sciences, 1995. **20**(11): p. 448-455.
431. Alon, U., *Network motifs: theory and experimental approaches.* Nature Reviews Genetics, 2007. **8**(6): p. 450-461.
432. Tayar, A.M., et al., *Propagating gene expression fronts in a one-dimensional coupled system of artificial cells.* Nature Physics, 2015. **11**(12): p. 1037-1041.
433. Boulos, L., et al., *LIVE/DEAD® BacLight™: application of a new rapid staining method for direct enumeration of viable and total bacteria in drinking water.* Journal of Microbiological Methods, 1999. **37**(1): p. 77-86.
434. Cellesi, F., N. Tirelli, and J.A. Hubbell, *Materials for cell encapsulation via a new tandem approach combining reverse thermal gelation and covalent crosslinking.* Macromolecular Chemistry and Physics, 2002. **203**(10-11): p. 1466-1472.
435. Ley, R.E., et al., *Microbial ecology: human gut microbes associated with obesity.* Nature, 2006. **444**(7122): p. 1022-1023.
436. Liu, X., et al., *Magnetic living hydrogels for intestinal localization, retention, and diagnosis.* Advanced Functional Materials, 2021. **n/a**(n/a): p. 2010918.
437. Tang, T.-C., et al., *Hydrogel-based biocontainment of bacteria for continuous sensing and computation.* Nature Chemical Biology, 2021.
438. Riglar, D.T. and P.A. Silver, *Engineering bacteria for diagnostic and therapeutic applications.* Nature Reviews Microbiology, 2018. **16**(4): p. 214-225.
439. Steiger, C., et al., *Ingestible electronics for diagnostics and therapy.* Nature Reviews Materials, 2019. **4**(2): p. 83-98.
440. Kalantar-Zadeh, K., et al., *A human pilot trial of ingestible electronic capsules capable of sensing different gases in the gut.* Nature Electroincs, 2018. **1**(1): p. 79-87.
441. Riglar, D.T., et al., *Engineered bacteria can function in the mammalian gut long-term as live diagnostics of inflammation.* Nature Biotechnology, 2017. **35**(7): p. 653-658.
442. Lim, B., et al., *Engineered regulatory systems modulate gene expression of human commensals in the gut.* Cell, 2017. **169**(3): p. 547-558. e15.
443. Pickard, J.M., et al., *Rapid fucosylation of intestinal epithelium sustains host–commensal symbiosis in sickness.* Nature, 2014. **514**(7524): p. 638-641.
444. Kotula, J.W., et al., *Programmable bacteria detect and record an environmental signal in the mammalian gut.* Proceedings of the National Academy of Sciences, 2014. **111**(13): p. 4838-4843.
445. Mimee, M., R.J. Citorik, and T.K. Lu, *Microbiome therapeutics—advances and challenges.* Advanced Drug Delivery Reviews, 2016. **105**: p. 44-54.
446. Hillemeier, C., *An overview of the effects of dietary fiber on gastrointestinal transit.* Pediatrics, 1995. **96**(5): p. 997-999.
447. Bettinger, C.J., *Materials advances for next-generation ingestible electronic medical devices.* Trends in Biotechnology, 2015. **33**(10): p. 575-585.
448. Mimee, M., et al., *An ingestible bacterial-electronic system to monitor gastrointestinal health.* Science, 2018. **360**(6391): p. 915-918.
449. Zhang, S., et al., *A pH-responsive supramolecular polymer gel as an enteric elastomer for use in gastric devices.* Nature Materials, 2015. **14**(10): p. 1065-1071.
450. Abramson, A., et al., *A luminal unfolding microneedle injector for oral delivery of macromolecules.* Nature Medicine, 2019. **25**(10): p. 1512-1518.

451. Payne, S.C., J.B. Furness, and M.J. Stebbing, *Bioelectric neuromodulation for gastrointestinal disorders: effectiveness and mechanisms.* Nature Reviews Gastroenterology & Hepatology, 2019. **16**(2): p. 89-105.
452. Dumonceau, J.-M., *Evidence-based review of the bioenterics intragastric balloon for weight loss.* Obesity Surgery, 2008. **18**(12): p. 1611.
453. Cobrin, G.M. and M.T. Abreu, *Defects in mucosal immunity leading to Crohn's disease.* Immunological Reviews, 2005. **206**(1): p. 277-295.
454. Landry, B.P. and J.J. Tabor, *Engineering diagnostic and therapeutic gut bacteria*. Bugs as Drugs: Therapeutic Microbes for the Prevention. 2018. 331-361.
455. Moës, A.J., *Gastroretentive dosage forms.* Critical Reviews in Therapeutic Drug Carrier Systems, 1993. **10**(2): p. 143-195.
456. Hwang, S.-J., H. Park, and K. Park, *Gastric retentive drug-delivery systems.* Critical Reviews in Therapeutic Drug Carrier Systems, 1998. **15**(3).
457. Sarmast, A.H., et al., *Gastrointestinal tract perforations due to ingested foreign bodies; a review of 21 cases.* British Journal of Medical Practitioners, 2012. **5**(3).
458. Park, J.-S., S. Jeong, and D.H. Lee, *Recent advances in gastrointestinal stent development.* Clinical Endoscopy, 2015. **48**(3): p. 209.
459. Smart, J.D., *The basics and underlying mechanisms of mucoadhesion.* Advanced Drug Delivery Reviews, 2005. **57**(11): p. 1556-1568.
460. Lee, Y., et al., *Therapeutic luminal coating of the intestine.* Nature Materials, 2018. **17**(9): p. 834-842.
461. Praveschotinunt, P., et al., *Engineered E. coli Nissle 1917 for the delivery of matrix-tethered therapeutic domains to the gut.* Nature Communications, 2019. **10**(1): p. 5580.
462. Kim, Y., et al., *Ferromagnetic soft continuum robots.* Science Robotics, 2019. **4**(33): p. eaax7329.
463. Gottlieb, K.T., et al., *Magnets in the GI tract.* Gastrointestinal Endoscopy, 2013. **78**(4): p. 561-567.
464. Wu, Z., et al., *A microrobotic system guided by photoacoustic computed tomography for targeted navigation in intestines in vivo.* Science Robotics, 2019. **4**(32): p. eaax0613.
465. Gabriel, S. and R. Ackermann, *Placement of nasoenteral feeding tubes using external magnetic guidance.* Journal of Parenteral and Enteral Nutrition, 2004. **28**(2): p. 119-122.
466. Laulicht, B., et al., *Localization of magnetic pills.* Proceedings of the National Academy of Sciences, 2011. **108**(6): p. 2252-2257.
467. Yim, S., et al., *Biopsy using a magnetic capsule endoscope carrying, releasing, and retrieving untethered microgrippers.* IEEE Transactions on Biomedical Engineering, 2014. **61**(2): p. 513-521.
468. C Hu, MQH Meng, and M. Mandal, *Efficient magnetic localization and orientation technique for capsule endoscopy.* International Journal of Information Acquisition, 2005. **02**(01): p. 23-36.
469. K&J Magnetics, I. *Demagnetization (BH) curves for neodymium magnets*. Available from: https://www.kjmagnetics.com/bhcurves.asp.
470. Blinder, S.M. *Magnetic field of a cylindrical bar magnet*. 2011; Available from: http://demonstrations.wolfram.com/MagneticFieldOfACylindricalBarMagnet/.
471. Hansen, M., *Small intestinal manometry.* Physiological Research, 2002. **51**(6): p. 541-556.
472. Gong, J., et al., *Friction of gels. 3. Friction on solid surfaces.* The Journal of Physical Chemistry B, 1999. **103**(29): p. 6001-6006.

473. Avvari, R.K., *Biomechanics of the Small Intestinal Contractions*. Digestive System-Recent Advances. 2019: IntechOpen.
474. Sambuy, Y., et al., *The Caco-2 cell line as a model of the intestinal barrier: influence of cell and culture-related factors on Caco-2 cell functional characteristics.* Cell Biology and Toxicology, 2005. **21**(1): p. 1-26.
475. Nguyen, T.L.A., et al., *How informative is the mouse for human gut microbiota research?* Disease Models & Mechanisms, 2015. **8**(1): p. 1-16.
476. Hugenholtz, F. and W.M. de Vos, *Mouse models for human intestinal microbiota research: a critical evaluation.* Cellular and Molecular Life Sciences, 2018. **75**(1): p. 149-160.
477. Isabella, V.M., et al., *Development of a synthetic live bacterial therapeutic for the human metabolic disease phenylketonuria.* Nature Biotechnology, 2018. **36**(9): p. 857-864.
478. Sanders, M.E., et al., *Probiotics and prebiotics in intestinal health and disease: from biology to the clinic.* Nature Reviews Gastroenterology & Hepatology, 2019. **16**(10): p. 605-616.
479. Buss, M.T., et al., *Spatial control of probiotic bacteria in the gastrointestinal tract assisted by magnetic particles.* Advanced Materials, 2021. **33**(17): p. 2007473.
480. Hamady, Z.Z.R., et al., *Xylan-regulated delivery of human keratinocyte growth factor-2 to the inflamed colon by the human anaerobic commensal bacterium Bacteroides ovatus.* Gut, 2010. **59**(4): p. 461-469.
481. Steidler, L., et al., *Treatment of murine colitis by Lactococcus lactis secreting interleukin-10.* Science, 2000. **289**(5483): p. 1352-1355.
482. Someya, T., Z. Bao, and G.G. Malliaras, *The rise of plastic bioelectronics.* Nature, 2016. **540**(7633): p. 379.
483. Nieben, O.G. and H. Harboe, *Intragastric balloon as an artificial bezoar for treatment of obesity.* The Lancet, 1982. **319**(8265): p. 198-199.
484. Liu, J., et al., *Triggerable tough hydrogels for gastric resident dosage forms.* Nature Communications, 2017. **8**(1): p. 124.
485. Bellinger, A.M., et al., *Oral, ultra–long-lasting drug delivery: application toward malaria elimination goals.* Science Translational Medicine, 2016. **8**(365): p. 365ra157-365ra157.
486. Singh, B.N. and K.H. Kim, *Floating drug delivery systems: an approach to oral controlled drug delivery via gastric retention.* Journal of Controlled release, 2000. **63**(3): p. 235-259.
487. Kagan, L., et al., *Gastroretentive accordion pill: enhancement of riboflavin bioavailability in humans.* Journal of Controlled Release, 2006. **113**(3): p. 208-215.
488. Chen, J., et al., *Gastric retention properties of superporous hydrogel composites.* Journal of Controlled Release, 2000. **64**(1-3): p. 39-51.
489. Salessiotis, N., *Measurement of the diameter of the pylorus in man: Part I. Experimental project for clinical application.* The American Journal of Surgery, 1972. **124**(3): p. 331-333.
490. Koziolek, M., et al., *Investigation of pH and temperature profiles in the GI tract of fasted human subjects using the Intellicap® system.* Journal of Pharmaceutical Sciences, 2015. **104**(9): p. 2855-2863.
491. Houghton, L., et al., *Motor activity of the gastric antrum, pylorus, and duodenum under fasted conditions and after a liquid meal.* Gastroenterology, 1988. **94**(6): p. 1276-1284.
492. Sun, B., et al., *Porous double network gels with high toughness, high stretchability and fast solvent-absorption.* Soft Matter, 2017. **13**(38): p. 6852-6857.

493. Chen, J., H. Park, and K. Park, *Synthesis of superporous hydrogels: hydrogels with fast swelling and superabsorbent properties.* Journal of Biomedical Materials Research, 1999. **44**(1): p. 53-62.
494. Wainwright, P.C., R.G. Turingan, and E.L. Brainerd, *Functional morphology of pufferfish inflation: mechanism of the buccal pump.* Copeia, 1995: p. 614-625.
495. Kirti and S.S. Khora, *Mechanical properties of pufferfish (Lagocephalus gloveri) skin and its collagen arrangement.* Marine and Freshwater Behaviour and Physiology, 2016. **49**(5): p. 327-336.
496. Berens, A. and H. Hopfenberg, *Diffusion and relaxation in glassy polymer powders: 2. Separation of diffusion and relaxation parameters.* Polymer, 1978. **19**(5): p. 489-496.
497. Ross, A.C., et al., *Tolerable upper intake levels: Calcium and vitamin D*. 2011.
498. Sultan, M. and R.A. Norton, *Esophageal diameter and the treatment of achalasia.* The American Journal Of Digestive Diseases, 1969. **14**(9): p. 611-618.
499. Zhang, L., et al., *Hyperexpandable, self-healing macromolecular crystals with integrated polymer networks.* Nature, 2018. **557**(7703): p. 86-91.
500. Trande, P., et al., *Efficacy, tolerance and safety of new intragastric air-filled balloon (Heliosphere BAG) for obesity: the experience of 17 cases.* Obesity Surgery, 2010. **20**(9): p. 1227-1230.
501. Cheifetz, A.S., et al., *The risk of retention of the capsule endoscope in patients with known or suspected Crohn's disease.* The American Journal Of Gastroenterology, 2006. **101**(10): p. 2218.
502. Mortensen, L. and P. Charles, *Bioavailability of calcium supplements and the effect of Vitamin D: comparisons between milk, calcium carbonate, and calcium carbonate plus vitamin D.* The American Journal Of Clinical Nutrition, 1996. **63**(3): p. 354-357.
503. Thomas, R., et al., *Quality evaluation of flat rice noodles (Kway Teow) prepared from Bario and Basmati rice.* Sains Malaysiana, 2014. **43**(3): p. 339-347.
504. Kozu, H., et al., *Development of a human gastric digestion simulator equipped with peristalsis function for the direct observation and analysis of the food digestion process.* Food Science and Technology Research, 2014. **20**(2): p. 225-233.
505. McKee, C.T., et al., *Indentation versus tensile measurements of Young's modulus for soft biological tissues.* Tissue Engineering Part B: Reviews, 2011. **17**(3): p. 155-164.
506. Snoeck, V., et al., *Gastrointestinal transit time of nondisintegrating radio-opaque pellets in suckling and recently weaned piglets.* Journal of Controlled Release, 2004. **94**(1): p. 143-153.
507. Houpt, T.R., *Gastric pressures in pigs during eating and drinking.* Physiology & Behavior, 1994. **56**(2): p. 311-317.
508. Cargill, R., et al., *Controlled gastric emptying. II. In vitro erosion and gastric residence times of an erodible device in beagle dogs.* Pharmaceutical Research, 1989. **6**(6): p. 506-509.
509. Sauve, C.C., et al., *Stomach temperature records reveal nursing behaviour and transition to solid food consumption in an unweaned mammal, the harbour seal pup (Phoca vitulina).* PLOS One, 2014. **9**(2): p. e90329.
510. Thouzeau, C., et al., *Adjustments of gastric pH, motility and temperature during long-term preservation of stomach contents in free-ranging incubating king penguins.* The Journal of Experimental Biology, 2004. **207**(15): p. 2715-2724.

511. Verron, E. and G. Marckmann, *Numerical analysis of rubber balloons.* Thin-walled structures, 2003. **41**(8): p. 731-746.
512. Zhao, X., *A theory for large deformation and damage of interpenetrating polymer networks.* Journal of the Mechanics and Physics of Solids, 2012. **60**(2): p. 319-332.
513. Strong, J., D. Cameron, and M. Riddell, *The electrolyte concentration of human gastric secretion.* Experimental Physiology, 1960. **45**(1): p. 1-11.
514. Pharmacopeia, U., *Simulated gastric fluid, TS*. The National Formulary. Vol. 9. 2000.
515. Johnson, K.L. and K.L. Johnson, *Contact mechanics*. 1987: Cambridge university press.
516. Deisseroth, K., *Optogenetics.* Nature Methods, 2011. **8**(1): p. 26-29.
517. Kim, C.K., A. Adhikari, and K. Deisseroth, *Integration of optogenetics with complementary methodologies in systems neuroscience.* Nature Reviews Neuroscience, 2017. **18**(4): p. 222-235.
518. Montgomery, K.L., et al., *Beyond the brain: Optogenetic control in the spinal cord and peripheral nervous system.* Science Translational Medicine, 2016. **8**(337): p. 337rv5-337rv5.
519. Hägglund, M., et al., *Optogenetic dissection reveals multiple rhythmogenic modules underlying locomotion.* Proceedings of the National Academy of Sciences, 2013. **110**(28): p. 11589-11594.
520. Caggiano, V., M. Sur, and E. Bizzi, *Rostro-Caudal Inhibition of Hindlimb Movements in the Spinal Cord of Mice.* PLOS ONE, 2014. **9**(6): p. e100865.
521. Llewellyn, M.E., et al., *Orderly recruitment of motor units under optical control in vivo.* Nature Medicine, 2010. **16**(10): p. 1161-1165.
522. Liske, H., et al., *Optical inhibition of motor nerve and muscle activity in vivo.* Muscle & Nerve, 2013. **47**(6): p. 916-921.
523. Nam, S. and D. Mooney, *Polymeric tissue adhesives.* Chemical Reviews, 2021.
524. Chen, R., A. Canales, and P. Anikeeva, *Neural recording and modulation technologies.* Nature Reviews Materials, 2017. **2**(2): p. 1-16.
525. Park, S.I., et al., *Soft, stretchable, fully implantable miniaturized optoelectronic systems for wireless optogenetics.* Nature Biotechnology, 2015. **33**(12): p. 1280-1286.
526. Kathe, C., et al., *Wireless closed-loop optogenetics across the entire dorsoventral spinal cord in mice.* Nature Biotechnology, 2021.
527. Michoud, F., et al., *Epineural optogenetic activation of nociceptors initiates and amplifies inflammation.* Nature Biotechnology, 2021. **39**(2): p. 179-185.
528. Zhang, Y., et al., *Battery-free, fully implantable optofluidic cuff system for wireless optogenetic and pharmacological neuromodulation of peripheral nerves.* Science Advances, 2019. **5**(7): p. eaaw5296.
529. Guo, J., et al., *Highly stretchable, strain sensing hydrogel optical fibers.* Advanced Materials, 2016. **28**(46): p. 10244-10249.
530. Gurunathan, S., et al., *Green synthesis of graphene and its cytotoxic effects in human breast cancer cells.* International journal of nanomedicine, 2013. **8**: p. 1015.
531. Oster, G., *The scattering of light and its applications to chemistry.* Chemical Reviews, 1948. **43**(2): p. 319-365.
532. Zheng, H., et al., *A shape-memory and spiral light-emitting device for precise multisite stimulation of nerve bundles.* Nature Communications, 2019. **10**(1): p. 2790.
533. Liske, H., et al., *Optical control of neuronal excitation and inhibition using a single opsin protein, ChR2.* Scientific Reports, 2013. **3**(1): p. 3110.

534. Antunes, P., et al., *Mechanical properties of optical fibers*. 2012: INTECH Open Access Publisher.
535. Guimarães, C.F., et al., *The stiffness of living tissues and its implications for tissue engineering.* Nature Reviews Materials, 2020. **5**(5): p. 351-370.
536. Kuthe, C.D., R.V. Uddanwadiker, and A. Ramteke, *Experimental evaluation of fiber orientation based material properties of skeletal muscle in tension.* Mol Cell Biomech, 2014. **11**(2): p. 113-28.
537. Zwirner, J., et al., *Passive load-deformation properties of human temporal muscle.* Journal of Biomechanics, 2020. **106**: p. 109829.
538. Kuthe, C.D. and R.V. Uddanwadiker, *Investigation of effect of fiber orientation on mechanical behavior of skeletal muscle.* Journal of Applied Biomaterials Functional Materials, 2016. **14**(2): p. 154-162.
539. Griffith, A.A.J.P.t.o.t.r.s.o.l.S.A., containing papers of a mathematical or physical character, *VI. The phenomena of rupture and flow in solids.* 1921. **221**(582-593): p. 163-198.
540. Layton, B. and A. Sastry, *A mechanical model for collagen fibril load sharing in peripheral nerve of diabetic and nondiabetic rats.* J. Biomech. Eng., 2004. **126**(6): p. 803-814.
541. Nath, T., et al., *Using DeepLabCut for 3D markerless pose estimation across species and behaviors.* Nature Protocols, 2019. **14**(7): p. 2152-2176.
542. Hamers, F.P., et al., *Automated quantitative gait analysis during overground locomotion in the rat: its application to spinal cord contusion and transection injuries.* Journal of Neurotrauma, 2001. **18**(2): p. 187-201.
543. Lin, S., et al., *Anti-fatigue-fracture hydrogels.* Science Advances, 2019. **5**(1): p. eaau8528.
544. Heller, W., *Remarks on refractive index mixture rules.* The Journal of Physical Chemistry, 1965. **69**(4): p. 1123-1129.